THE UNIVERSITY OF CHICAGO

MEASUREMENT OF Z BOSON PRODUCTION IN ASSOCIATION WITH AT LEAST ONE OR TWO B-JETS IN PROTON-PROTON COLLISIONS AT 13 TEV USING THE ATLAS DETECTOR

A DISSERTATION SUBMITTED TO
THE FACULTY OF THE DIVISION OF THE PHYSICAL SCIENCES
IN CANDIDACY FOR THE DEGREE OF
DOCTOR OF PHILOSOPHY

DEPARTMENT OF PHYSICS

BY
KEVIN ROBERT THOMAS HILDEBRAND

CHICAGO, ILLINOIS
DECEMBER 2019

To my family

Table of Contents

List of Figures

All figures are the author's work unless otherwise cited.

List of Tables

ABSTRACT

This thesis presents a measurement of the production cross-section of a Z boson in association with at least one or two b-jets. This final state occurs in the Standard Model and can be used to test predictions from perturbative quantum chromodynamics. It is also an important background for several processes including Higgs production, with the Higgs decaying to a b-quark pair, in association with a vector boson as well as searches for physics beyond the Standard Model which contain leptons and b-jets in the final state. The measurement is done using data collected by the ATLAS detector from proton-proton collisions at a center-of-mass energy of 13 TeV at the LHC corresponding to an integrated luminosity of 35.6 fb^{-1}. The integrated and differential cross-sections are measured at the particle level for both the electron and muon decay channels of the Z boson. The results are compared to predictions from several Monte Carlo predictions.

CHAPTER 1

INTRODUCTION

This thesis presents a measurement of Z boson production in association with b-jets (Z+b-jets) in proton-proton collisions at a center-of-mass energy of 13 TeV produced at the Large Hadron Collider (LHC) using the ATLAS detector. The measurement focuses on a leptonically decaying Z boson and is separated into two channels based on the flavor of the lepton pair produced by the Z boson. The data was collected during 2015 and 2016 and corresponds to a total integrated luminosity of 35.6 fb^{-1}.

This measurement can provide an important test of perturbative quantum chromodynamics. The Z+b-jets processes are sensitive to heavy flavor quarks in the initial state. In perturbative quantum chromodynamics two common methods are used to generate these processes: four-flavor number scheme (4FNS) and five-flavor number scheme (5FNS)[1, 2, 3]. They differ in the inclusion of the b-quark in the initial state. The former only considers parton densities of gluons and of the first two quark generations in the proton. In the 5FNS the b-quark density is included in the initial state by including the b-quark in the parton distribution function of the proton. This means that precise measurements of Z+b-jets processes could be used to constrain the b-quark parton density function of the proton.

The Z+b-jets signal is also an important background to other processes such as top production, Higgs boson production, as well as many beyond the Standard Model processes including SUSY. For example, in Higgs boson production in association with a vector boson, with the Higgs decaying into a b-quark pair, Z+b-jets is an irreducible background.

The measurement of Z boson production in association with b-jets has been performed previously. The CDF and D0 experiments [4, 5] performed measurements using proton-antiproton collisions at a center-of-mass energy of 1.96 TeV. Measurements were also performed using proton-proton collisions at a center-of-mass energy of 7 TeV by the ATLAS

and CMS experiments [6, 7].

The total integrated cross section is presented for events with at least one b-jet and for events with at least two b-jets. The differential cross sections are measured as a function of a number of different variables. They can be grouped into the following categories:

1. Jet multiplicity and jet properties. This category is of primary importance for tests of QCD predictions and for the modeling of Monte Carlo event generators.

    - transverse momentum, p_T, of the leading b-jet
    - rapidity, y, of the leading b-jet
    - p_T of the two leading b-jets system divided by its invariant mass

2. Dijet distributions. This category is important for topologies of Higgs and new physics.

    - azimuthal angle difference between the 2 leading b-jets
    - rapidity difference between the 2 leading b-jets
    - difference in radius between the 2 leading b-jets
    - invariant mass of the 2 leading b-jets
    - p_T of the Z boson
    - p_T of the 2 leading b-jets

3. Boson and Boson-jet distributions. This category is important for parton density functions understanding.

    - rapidity of the Z boson
    - rapidity difference between the Z boson and the leading b-jet.

A general description of the steps taken in making the measurement is as follows. First Monte Carlo samples are produced for the different signal and background processes. Three

different generators are used to produce the Z+jets samples. Selections are then defined to select events with a Z boson and b-jets. The event selection is applied to the Monte Carlo samples and data collected by ATLAS. Not all events passing event selection are signal. For example, a c-jet could be misidentified as a b-jet. The amount of background passing event selection in the data is predicted using the Monte Carlo samples. The different Monte Carlo generators used to produce the Z+jets samples give different predictions for the flavor composition of the jets, so a fit to data is performed to extract normalization factors for the different flavor components of the Z+jets samples. At this point the distributions produced from events passing event selection are at the detector level. That is they include detector effects, for example, electron reconstruction efficiencies. A process, known as unfolding, is used to take the detector level distributions to the particle level.

The thesis is structured as follows. Chapter 2 provides a brief overview of the Standard Model and QCD physics. Chapter 3 gives a brief description of the LHC and of the ATLAS detector. Chapter 4 briefly describes the data used in this analysis. The Monte Carlo samples used to simulate signal and the different background process are described in chapter 5. Chapter 6 gives a description of how the different physics objects are reconstructed in the ATLAS detector. Chapter 7 defines the selections used to select events. Chapter 8 goes over the data driven method for estimating QCD multijet background. Chapter 9 describes the top validation region. Chapter 10 gives a description of the systematics uncertainties at the detector level. These include the systematics associated with object reconstruction as well as systematics associated with the top background modeling. Chapter 11 describes the flavor fit. Chapter 12 presents plots of the different variables at the detector level both with and without the scale factors from the flavor fit applied. Chapter 13 describes unfolding. It begins by introducing the method of unfolding. The fiducial region in which the particle level measurement is made in is also defined. It also describes how the systematics are propagated through the unfolding. The results are summarized and shown in Chapter 14.

In Appendix E a brief description of some of the contributions I made to the analysis in this thesis is given.

CHAPTER 2

THEORY

2.1 The Standard Model

The Standard Model (SM) of particle physics is a quantum field theory that describes all known fundamental particles and their interactions with each other through three of the four fundamental forces [8, 9]. Since its formulation in the latter half of the 20th century the Standard Model has been very successful in predicting experimental results. It successfully predicted the existence of the W and Z Bosons [10] over a decade before their discovery [11, 12]. The Higgs boson, whose existence was predicted several decades prior to its discovery [13], was finally discovered at the LHC [14, 15] completing the discovery of all the fundamental particles predicted by the standard model. Since the introduction of the Standard Model, numerous experiments have been built to perform measurements of an immense range of physical processes and so far no such experiments have shown statistically significant results that contradict those predicted by the Standard Model. The ATLAS detector, which will be described in more detail later on, has been used to measure the production cross-section rates of a number of physical processes. In fig. 2.1 a summary of some the measurements made using the ATLAS detector are compared to the corresponding Standard Model predictions. The results show further the success the Standard Model has had in describing the interaction of the known fundamental particles in particle physics.

Although the Standard Model has been very successful, it has deficiencies. For one, it does not include the gravitational force. Also, naturally one would believe the early universe would be symmetrically composed of matter and anti-matter. However, the observable universe at present is composed of mostly matter and there exists no confirmed physical process within the Standard Model that explains the huge asymmetry in matter/anti-matter. There are also cosmological observations, such as the rotation of galaxies [17] and inflation in the universe

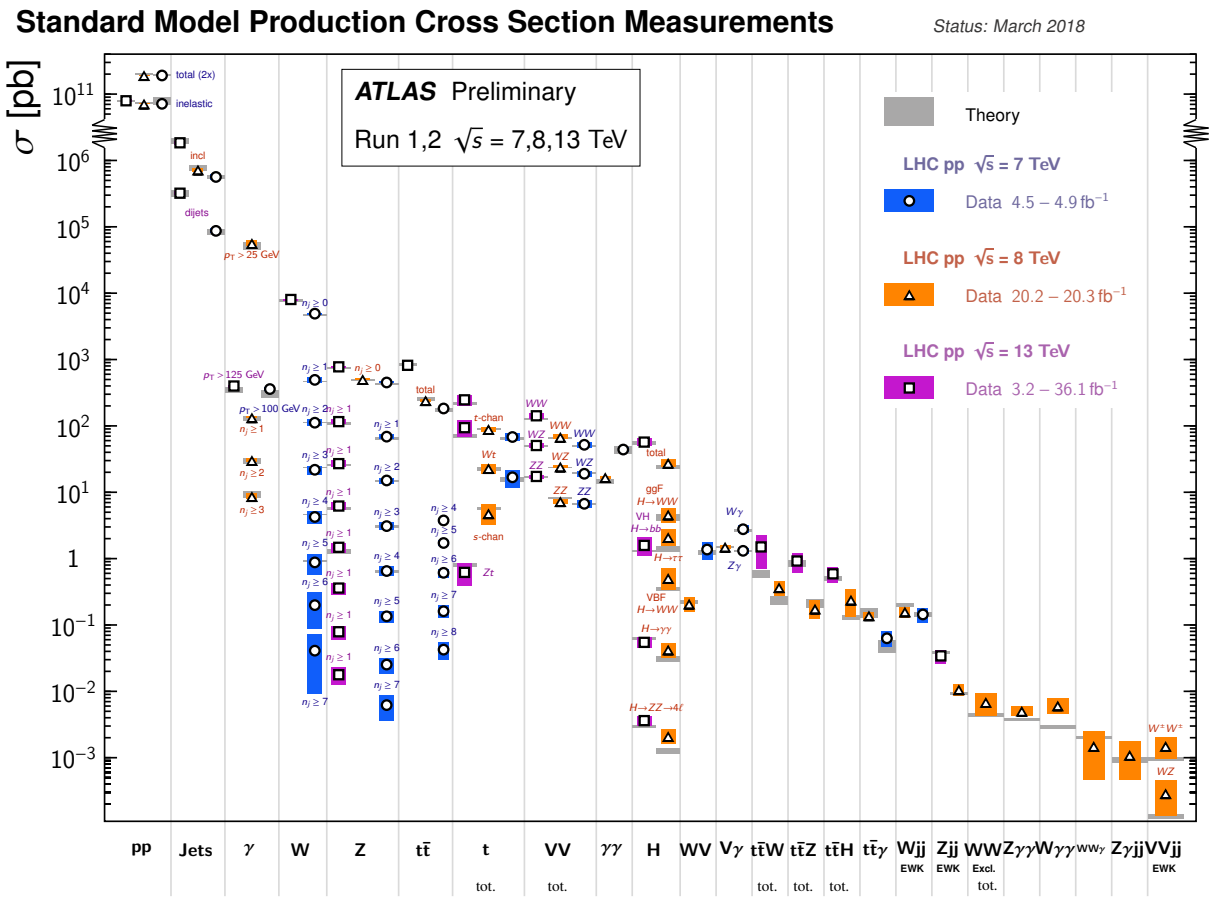

Figure 2.1: Many of the Standard Model cross-sections experimentally measured by the ATLAS detector along with there theoretically predicted values.[16]

[18], which gives overwhelming evidence for the existence of dark matter and dark energy including that the two account for over 90% of the energy in the universe. However, the Standard Model does not contain any description for either of these phenomena. These deficiencies have led to new theories that extend beyond the Standard Model and provide solutions to these problems. The ATLAS detector allows one to probe these new theories while at the same time make Standard Model measurements. The Standard Model consists of seventeen fundamental particles. These are shown in fig. 2.2. The fundamental particles are divided into two groups, fermions and bosons. The fermions have half-integer spin and are further divided into two categories, quarks and leptons. The bosons have integer

spin. There are three generation of quarks. Each generation has an up-type quark and

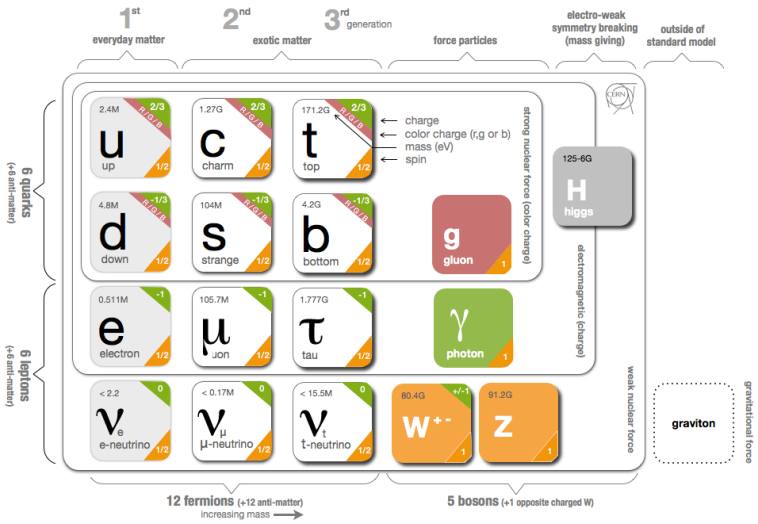

Figure 2.2: The fundamental particles in the Standard Model. [19]

down-type quark. Up-type quarks have electric charge $+\frac{2}{3}$ while down-type quarks have electric charge $-\frac{1}{3}$. Each quark also has color charge, which can be either red, green or blue. Each generation is heavier than the previous generation. There are three generations of leptons. Each generation has a charged lepton and a nearly massless neutrino. Like quark generations each lepton generation is heavier than the previous generation. Each charged lepton has electric charge -1. Neutrinos do not have electric charge and interact weakly with ordinary matter. Leptons do have color charge and therefore do not interact through the strong force. Each fermion has a corresponding anti-particle which has the same mass but opposite quantum numbers. The three fundamental forces that the Standard Model describes are the electromagnetic,strong and weak force. Ordinary every day matter one encounters is made up of the first generation of quarks and leptons. For example, a proton is made up of two up quarks and one down quark.

There are five bosons, the Higgs boson and the four force carrying bosons. The fundamental particles interact through the fundamental forces by exchanging force carrying

bosons. The photon is the force carrier for the electromagnetic force and interacts with all particles with non-zero electric charge. The photon is massless and has no electric charge and their force cannot interact with itself. The gluon is the force carrier for the strong force and interacts with all particles that have color charge. The gluon is massless and does have color charge so gluons can interact among themselves. The $W^{\pm}$ and Z bosons are the force carries of the weak force. These bosons are massive and interact with all the fundamental particles.

2.2 QCD and Collider Physics

The strong force is described by the theory of quantum chromodynamics (QCD). This section will give a brief description of its use that is most relevant to this thesis. A more complete description can be found in [20]. Feynman diagrams are used to graphically represent the transition from an initial state to the final state. For a given initial state and final state there are an unlimited number of Feynman diagrams that describe the transition from the initial state to the final state. Each diagram can be categorized by the number of QCD interaction vertices and the number of electroweak (EW) vertices that it contains. For a given process, the leading order Feynman diagrams are the diagrams with the least number of vertices needed to take an initial state to the final state. The Feynman diagram for leading order Z boson production at the LHC is given in fig. 2.3.

When calculating the cross-section, each additional QCD and EW vertex in the Feynman diagram will add an additional factor of α_S and α_{EW}, respectively, where α_S is the strong coupling constant and α_{EW} is the EW coupling constant. This means that if $\alpha_S \ll 1$ and $\alpha_{EW} \ll 1$ a perturbitive expansion of the cross-section in orders of the coupling constants would work well because each successive higher order correction should result in a smaller correction. The leading order diagrams for Z + 1-jet are shown in fig. 2.4. Interesting features start to appear when considering higher order corrections.

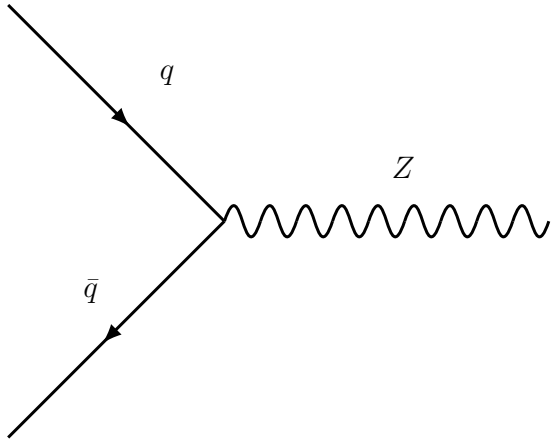

Figure 2.3: Leading order Feynman diagram for Z boson production.

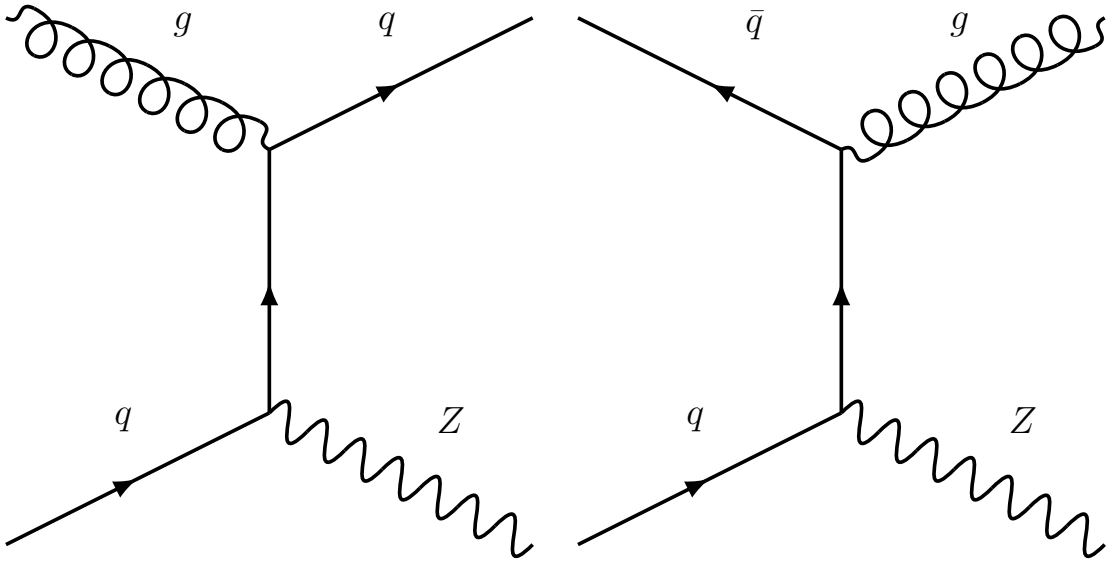

Figure 2.4: Leading order Feynman diagram for Z boson + 1-jet production.

The addition of higher order diagrams results in diagrams containing loops. The integration of these loop diagrams over all possible momentums result in divergent integrals. This is resolved by a procedure known as renormalization [21] which absorbs the divergences into renormalized definitions of the coupling constants. This results in a coupling constant which is not actually constant and depends on the renormalization scale, μ_R. Its value for transferred momentum, Q^2, relative to a renormalization scale is given by the following equation

[22]:

$$\alpha_S(Q^2) = \frac{\alpha_S(\mu^2)}{1 + \frac{\alpha_S(\mu^2)}{12\pi}(33 - 2n_f)log(Q^2/\mu^2}, \tag{2.1}$$

where n_f is the number of quark flavors. For the Standard Model there are six quark flavors. Therefore eq. (2.1) shows that as Q^2 goes to infinite, α_S goes to zero, allowing for perturbative calculations. However, in the other direction, as Q^2 goes to zero the coupling constant grows larger and the perturbative approach breaks down. This breakdown at low energy scales leads to the confinement of quarks and gluons and a non-perturbative approach must be taken.

To combine the low energy region with the high energy region the factorization theorem [21] is used, which introduces a factorization scale, μ_F, which separates the short-range perturbative calculation of the hard scatter from the long-range non-perturbative calculation that describes the hadron structure with the PDFs. The cross section can then be written as:

$$\sigma_{AB\to X} = \sum_{a,b} \int dx_a dx_b f_{a/A}(x_a, \mu_F^2) f_{b/B}(x_b, \mu_F^2) \times [\hat{\sigma_0} + \alpha_S(\mu_R^2)\hat{\sigma_1} + \cdots]_{ab\to X}, \tag{2.2}$$

where A and B are the colliding hadrons (the two protons for the case of the LHC) and X is the final state. a and b are the partons of the hadrons A and B, respectively. The sum is over the different partons contained in the hadrons. $f_{a/A}(x_a, \mu_F^2)$ is the Parton Distribution Function (PDF), which is the probability for parton a to carry the fraction x_a of the hadron's momentum. The PDFs depends on the factorization scale. The factorization scale determines whether a parton emission is treated within the PDF or partonic cross section of eq. (2.2). A parton emitted with transverse momentum less than the factorization scale is absorbed into the PDF definition and is considered part of the structure of the proton. Where as a parton emitted with transverse momentum greater than the factorization scale will be developed as part of partonic hard scatter.

2.2.1 Parton Distribution Function

The parton density function (PDF) of the proton describes the probability of finding a parton of a given flavor, from the proton interacting at a momentum scale Q^2, with momentum fraction x. The PDF cannot be calculated directly. It is derived from performing fits to experimental data [23]. The general procedure is to parametrize the PDFs as a function of x at given energy scale. The DGLAP equations [24] are then solved to obtain the distributions at any scale for all momentum fractions x. The PDFs obtained are then used to perform fits on the data to obtain the best fit parameters for the PDFs. Many different PDF sets exist and are produced by different groups. Common global PDFs sets used at the LHC include the NNPDF3.0, MMHT14, and CT14 sets [25]. An example of the PDF set MMHT14 is shown in fig. 2.5 for two different Q^2 scales.

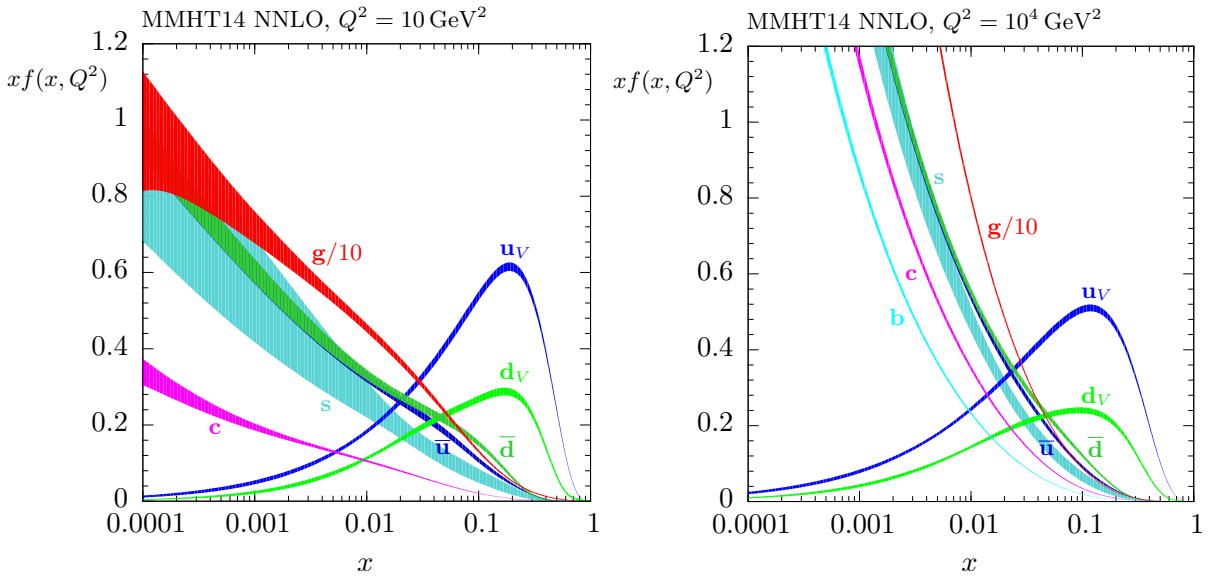

Figure 2.5: The MMHT14 NNLO parton distribution functions at energy scale Q^2= 10 GeV^2 (left) and Q^2= 10^4 GeV^2 (right).[26]

2.2.2 Monte Carlo generators

The simulation of events by Monte Carlo generators is done by a series of sequential steps that will briefly be described in this section. A graphical representation of the different steps involved is shown in fig. 2.6. The red circle represents the hard scatter. The purple circle represents secondary interactions between partons and beam-beam remnants which are referred to as the underlying event. From the hard scatter the high energy partons shower according to perturbative QCD which is shown as the red lines. The lower energy partons resulting from the parton showers then hadronize, which is represented by the light green circles.

Monte Carlo simulation begins with simulation of the hard scatter. This is described by matrix element calculations. The matrix elements corresponding to Feynman diagrams relevant to the hard-scatter process being simulated are all generated. Using these, along with a PDF set describing the initial state partons, the generator will produce a list of final state partons along with their momenta.

A procedure referred to as parton showering is used to evolve the final state partons from the high interaction scale of the hard scatter down to a lower interaction scale where confinement takes over and hadronization can occur. The high energy partons coming from the hard scatter will radiate gluons and photons. The gluons in turn can then radiate quark anti-quark pairs. This leads to showers of particles. The showering continues until the energy scale reaches approximately 1 GeV. At this point the energies are low enough that hadronization can occur.

At the low energies where perturbative theory becomes invalid color confinement takes over resulting in hadronization, ie the formation of colorless hadrons. There are two models that are commonly used to approximate the non-perturbative behavior of QCD that confines the partons into hadrons. The string model and the cluster model. [28]. These two models are depicted in fig. 2.7.

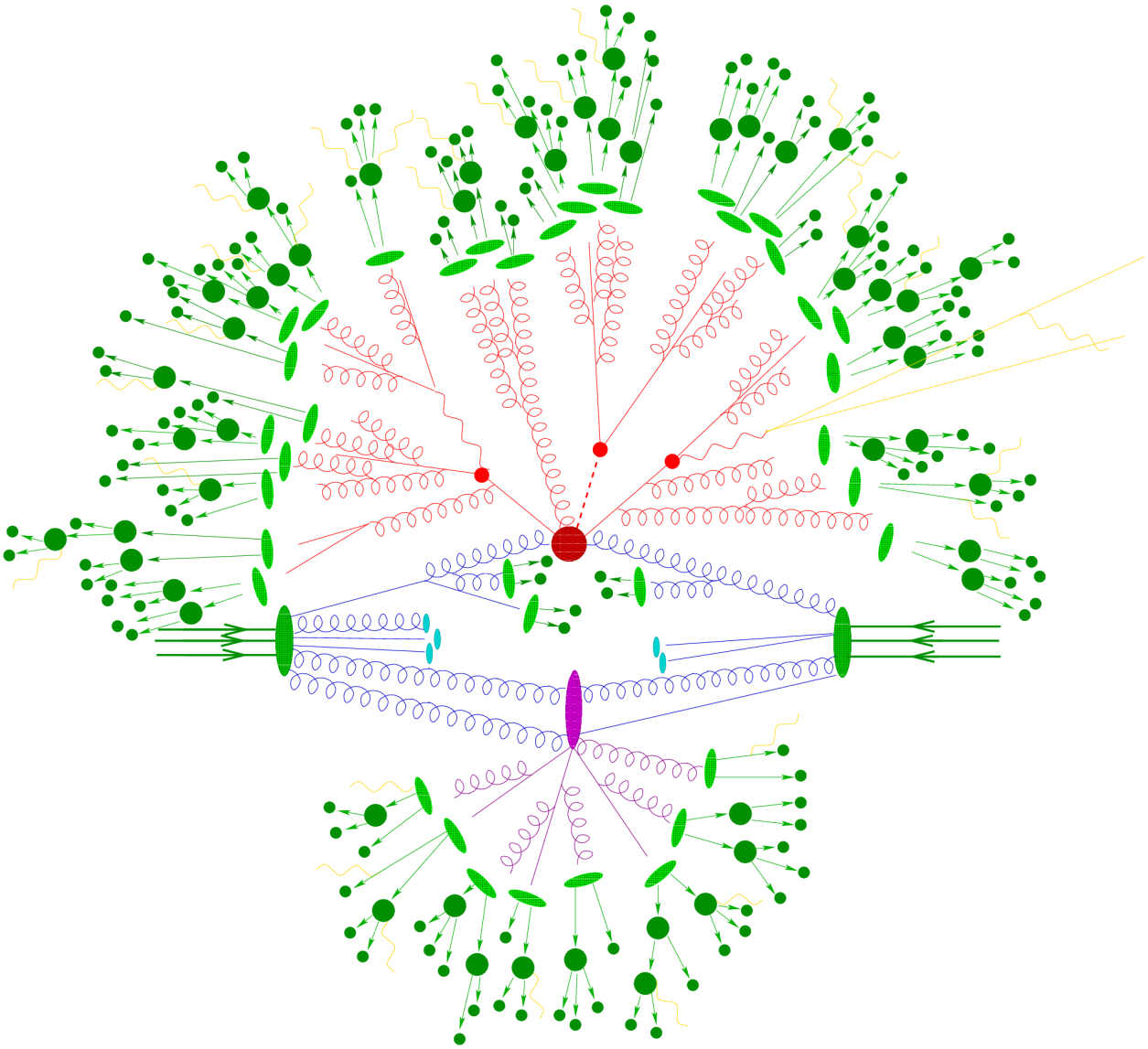

Figure 2.6: Sketch of a hadron-hadron collision as simulated by a Monte-Carlo event generator. The red blob in the center represents the hard collision, surrounded by a tree-like structure representing Bremsstrahlung as simulated by parton showers. The purple blob indicates a secondary hard scattering event. Parton-to-hadron transitions are represented by light green blobs, dark green blobs indicate hadron decays, while yellow lines signal soft photon radiation.[27]

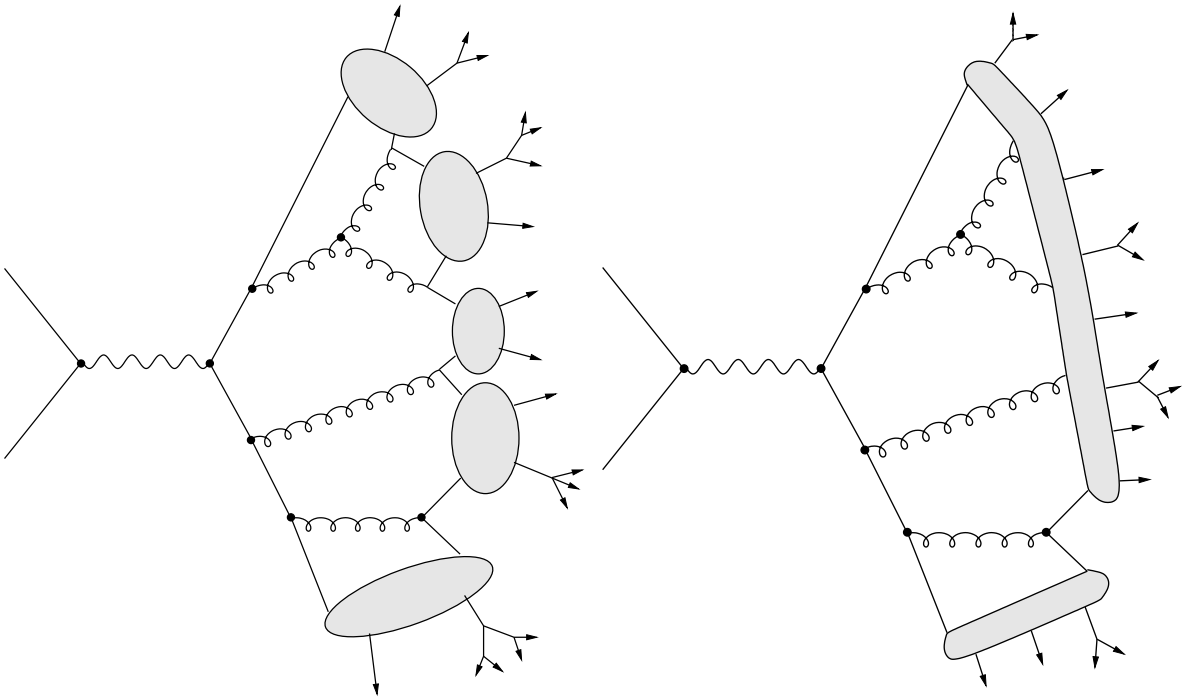

Figure 2.7: Illustration showing the cluster (left) and string (right) hadronization model.[29]

CHAPTER 3

THE LARGE HADRON COLLIDER AND THE ATLAS DETECTOR

3.1 The Large Hadron Collider

The Large Hadron Collider [30] is a 27 km circular collider located approximately 100m underground at the European Organization for Nuclear Research (CERN). CERN is located outside of Geneva, Switzerland. The LHC accelerates two proton beams up to an energy of 7 TeV. The two beams travel in opposite directions and are collided at four different interaction points along the ring. Detectors are located at each interaction point to analyze the resulting interaction. The location of the detectors and the LHC on France-Switzerland border is shown in fig. 3.1. There are two general purpose detectors and two more specialized

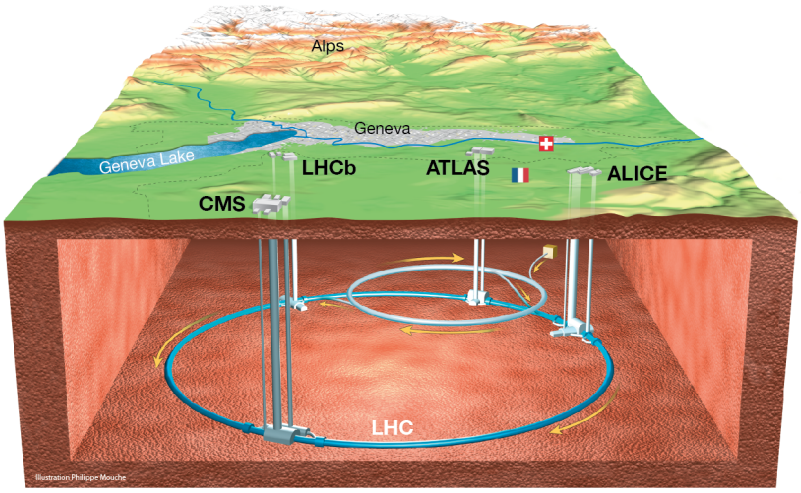

Figure 3.1: Illustration showing the location of the LHC at CERN along with the four detectors (ATLAS,CMS,LHCb, and ALICE).[31]

detectors. The Compact Muon Solenoid (CMS) experiment and A Toroidal LHC ApparatuS (ATLAS) experiment are the general purpose detectors which were designed to measure

proton-proton collisions at center of mass energies,$\sqrt{s}$, up to 14 TeV. The Large Hadron Collider Beauty (LHCb) experiment is designed to perform precision measurements involving b physics. A Large Ion Collider Experiment (ALICE) is designed for the study of heavy ion collisions which the LHC is also capable of accelerating and colliding.

Protons cannot be accelerated up to high energies by the LHC alone. They are accelerated up in steps of energy by other accelerators prior to being injected into the LHC ring. The accelerators the protons pass through are illustrated in fig. 3.2. First the protons must be produced which is done by ionizing hydrogen gas. Linac2 (LINear ACcelerator 2) takes these protons and accelerates them to an energy of 50 MeV before injecting them into the Proton Synchrotron Booster (PSB) which then accelerates them up to 1.4 GeV. From there the protons pass through the Proton Synchrotron (PS) which increases the beams energy to 25 GeV. The final step before being injected into the LHC is the Super Proton Synchrotron (SPS) which accelerates the protons to 450 GeV. The protons are then inserted into the two beam pipes of the LHC which accelerates the protons up to there maximum energy of 6.5 TeV. One beam pipe circulates the protons clockwise while the other beam pipe circulates the protons counterclockwise.

The protons are not uniformly distributed along the LHC. Starting at the PS accelerator, acceleration occurs by the application of an oscillating electric field in resonant frequency (RF) cavities. The 40 MHz frequency of the RF cavities results in the protons being in bunches with 25 ns spacing. Each bunch contains approximately 10^{11} protons. These bunches are steered around the LHC by superconducting dipole magnets that provide a magnetic field of up to 8.3 T. Quadrapole magnets along ring continuously focus the beam to maintain emittance. The two beams are collided at the four interaction points where the experiments are located. The term luminosity is used to describe both the beam and the data that is recorded. The instantaneous luminosity is proportional to the number of interactions per second and the LHC was designed to achieve an instantaneous luminosity

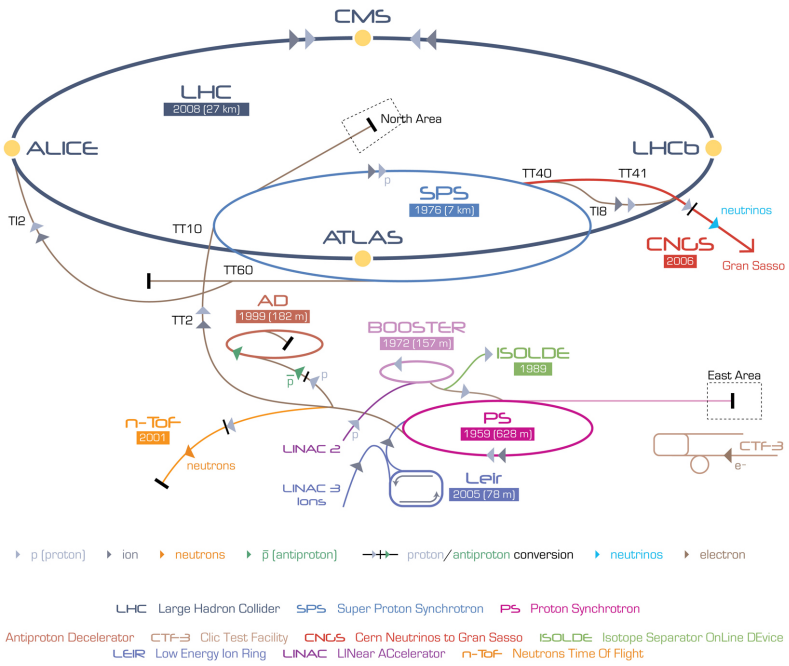

Figure 3.2: Accelerators proton pass through prior to be injected into the LHC.[32]

of up to $10^{34} cm^{-2} s^{-1}$.

During Run 1 of data taking the LHC successfully delivered an integrated luminosity of approximately 20 fb^{-1} at $\sqrt{s}$ of 8 TeV to the ATLAS detector. Run 2 of data taking began in 2015 with a center of mass energy of 13 TeV. The data used in this thesis was taken from the first two years of Run 2 (2015-2016). The integrated luminosity delivered to ATLAS during this period is about 40 fb^{-1}. 3.9 fb^{-1} of which came during 2015, while the remaining 35.6 fb^{-1} was recorded in 2016 as is shown in fig. 3.3. During 2015 the LHC delivered a peak luminosity of $5.0 \times 10^{33} cm^{-2} s^{-1}$ with an average number of pp interactions per bunch crossing, $\langle \mu \rangle$, of 13.4. While in 2016 the LHC delivered a peak luminosity of $1.38 \times 10^{34} cm^{-2} s^{-1}$ with $\langle \mu \rangle$ of 25.1. The peak luminosity per fill is shown in fig. 3.4.

Not all pp collisions result in interesting physics. Most are elastic or soft inelastic collisions. The hard inelastic collisions, which are much more interesting physics events, occur at much smaller rate. So increasing the number of interactions per bunch crossing will increase the rate at which the more interesting collisions occur. The trade-off with increasing the

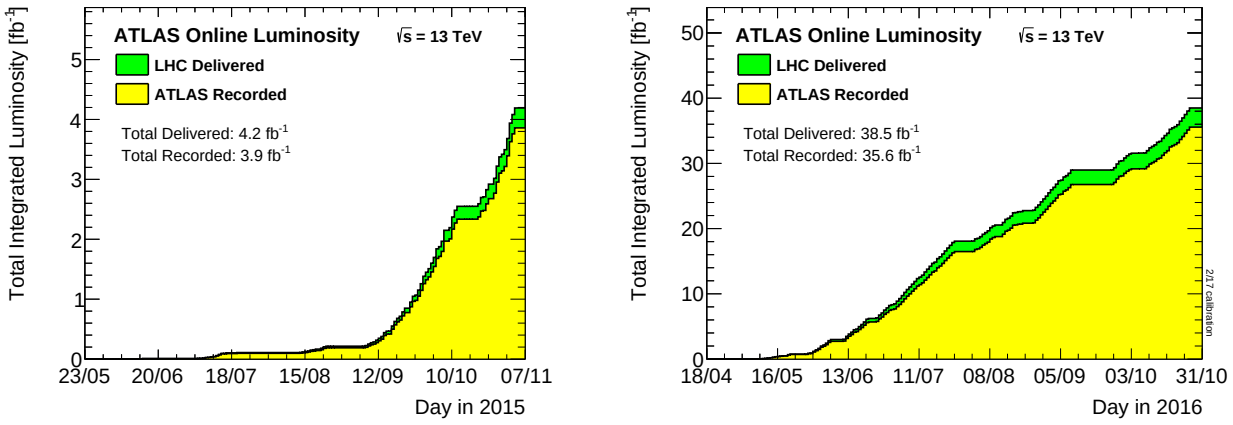

(a) (b)

Figure 3.3: Cumulative luminosity versus time delivered to (green) and recorded by ATLAS (yellow) during stable beams for pp collisions at 13 TeV center-of-mass energy in (a) 2015 and (b) 2016. The delivered luminosity accounts for luminosity delivered from the start of stable beams until the LHC requests ATLAS to put the detector in a safe standby mode to allow for a beam dump or beam studies. The recorded luminosity reflects the DAQ inefficiency, as well as the inefficiency of the so-called warm start: when the stable beam flag is raised, the tracking detectors undergo a ramp of the high-voltage and, for the pixel system, turning on the preamplifiers. Shown is the luminosity as determined from counting rates measured by the luminosity detectors. These detectors have been calibrated with the use of the van-der-Meer beam-separation method, where the two beams are scanned against each other in the horizontal and vertical planes to measure their overlap function. The luminosity shown represents the preliminary 13 TeV luminosity calibration based on van-der-Meer beam-separation scans in 2016.[33]

number of interactions per bunch crossing is that you are also increasing the rate at which the less interesting collisions occur along side the interesting ones. This results in events having multiple *pp* collisions, of which only one contains the interesting physics that one is trying to study. The other *pp* collisions are referred to as pile-up. The average number of interactions per bunch crossing for 2015-2017 data is shown in fig. 3.5.

3.2 The ATLAS detector

The ATLAS detector [34],shown in fig. 3.6, is a general purpose detector located at one of the interaction points in the LHC. It is a cylindrical detector that provides almost full phase

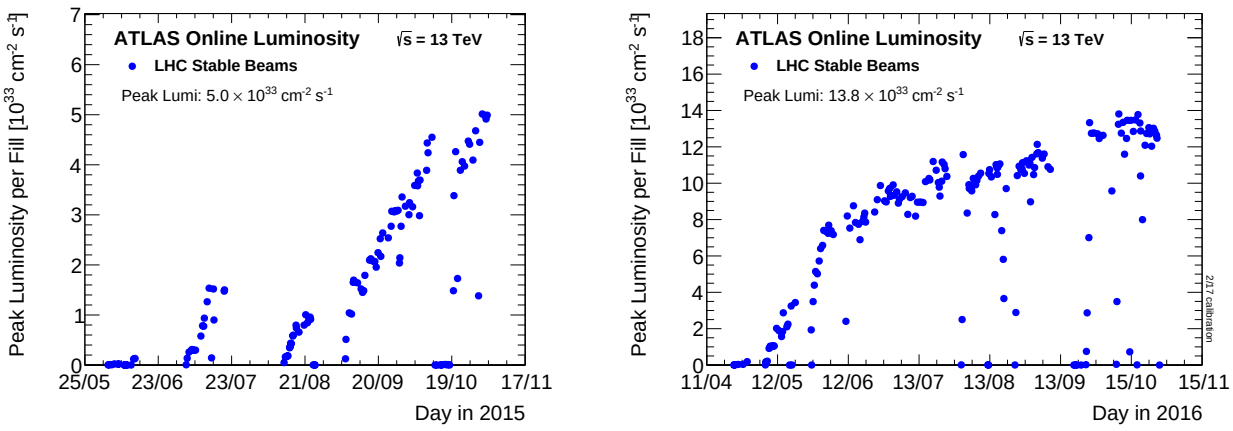

(a) (b)

Figure 3.4: The peak instantaneous luminosity delivered to ATLAS during stable beams for pp collisions at 13 TeV centre-of-mass energy is shown for each LHC fill as a function of time in (a) 2015 and (b) 2016. The luminosity is determined using counting rates measured by the luminosity detectors, and is based on a preliminary 13 TeV calibration determined using van-der-Meer beam-separation scans.[33]

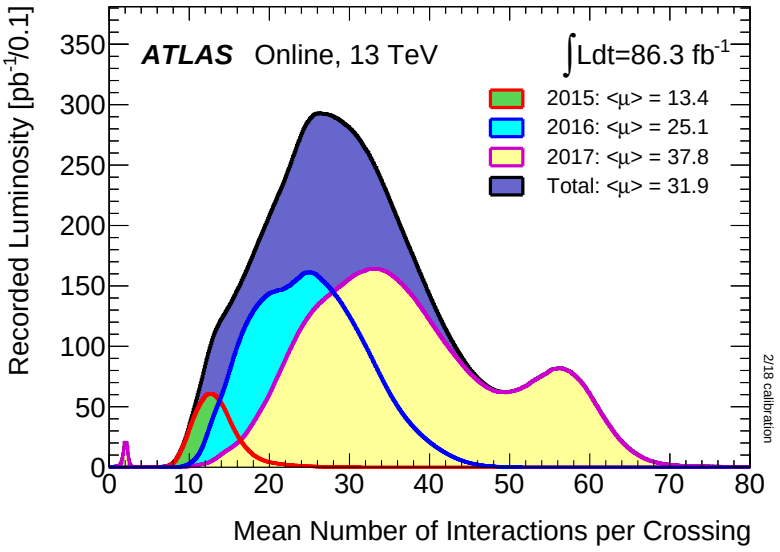

Figure 3.5: The average number of proton-proton interactions per bunch crossing for data from 2015-2017. 2017 data is not used in this thesis.[33]

space coverage around the interaction point (IP) located at the center of the detector. It was designed to detect and measure the particles produced by proton collisions over a wide range of energies. This is accomplished by the three main subsystems that make up ATLAS. They

are the inner detector, the calorimeters, and the muon spectrometer. The interaction of particles with the different sub-detectors that make up these subsystems is shown in fig. 3.7. These will be described in further detail in the sections that follow.

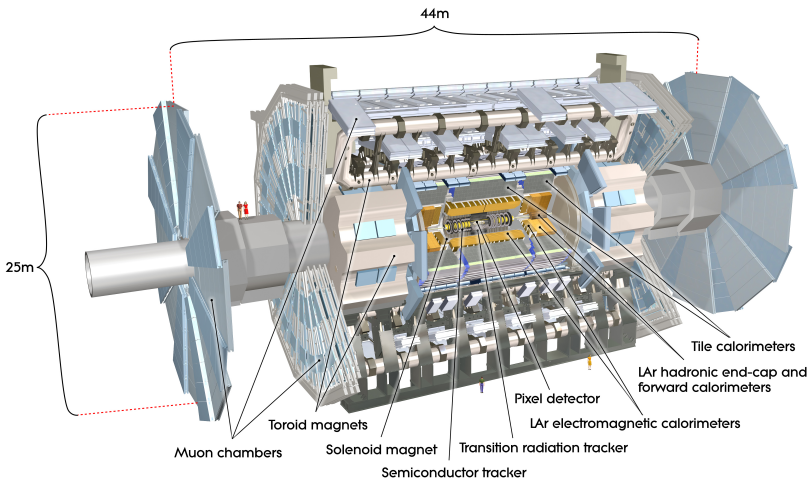

Figure 3.6: Overview of the main components of the ATLAS detector.[35]

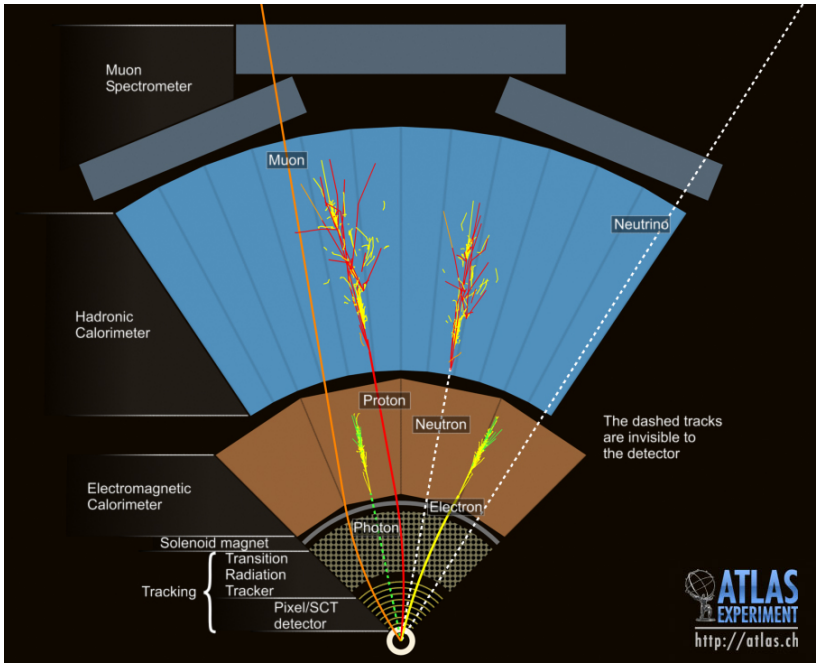

Figure 3.7: A cross section view of the atlas detector in a plane perpendicular to the beam axis illustrating different particle interactions with the different components that make up the ATLAS detector.[34]

ATLAS uses a right-handed coordinate system with the nominal interaction point used as the origin. The beam line is used to define the z-axis and the x-y plane is transverse to the beam direction. The positive x-axis is defined as pointing from the IP to the center of the LHC ring and the positive y-axis is defined as pointing upwards. Cylindrical coordinates (r, ϕ) are used in the transverse plane, where the azimuthal angle, ϕ, is measured around the beam axis and the radial distance, r, is measured from the beam axis. The polar angle, θ, is the angle from the beam axis and is used to define the pseudorapidity, $\eta = -ln[\tan\frac{\theta}{2}]$. η of zero corresponds to a direction in the transverse plane, where as high values of η correspond to directions closer to the beam line. The relationship between the polar angle, θ, and the pseudorapidity, η, are shown in fig. 3.8. Finally, the angular separation between two points in the detector is defined as $\Delta R = \sqrt{(\Delta\eta)^2 + (\Delta\phi)^2}$.

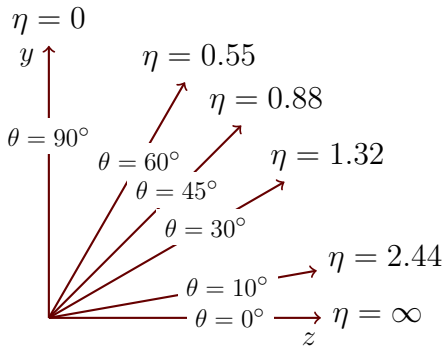

Figure 3.8: The relationship between the polar angle,θ, and the pseudorapidity, η. Here the horizontal axis is the beam axis (z-axis) and the vertical axis is the plane transverse to the beam axis. Image created with TikZ [36]

3.2.1 The Inner Detector

The inner detector (ID) [37] is the subsystem located closest to the interaction point. It is made up of three sub-detectors and sits inside a magnetic field as illustrated by the components labeled tracking in fig. 3.7. The ID is designed to reconstruct the trajectories of charged particles and provides tracking out to $|\eta| < 2.5$. The pixel detector, the semiconduc-

tor tracker (SCT), and the transition radiation tracker (TRT) are the three sub-detectors that make up the ID and cover different radii from the beam axis as shown in fig. 3.9 and fig. 3.10. Figure 3.10 also shows how each sub-detector is split into cylindrical concentric barrel modules. The ID sits inside a superconducting solenoid that produces a roughly uni-

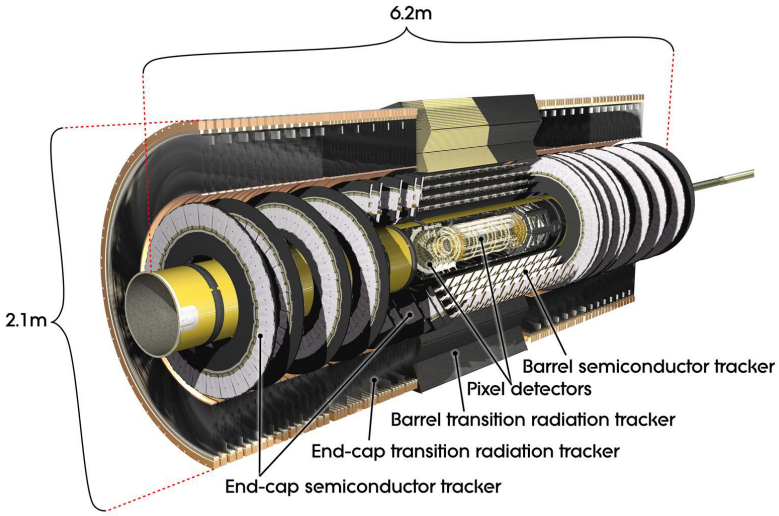

Figure 3.9: Illustration showing layout of the inner detector's sub-detectors.[34]

form 2 T magnetic field along the beam axis. This causes charged particles passing through the ID to follow helical trajectories and allows the momentum of charged particles to be measured in the transverse direction.

The pixel detector is the in the innermost subdetector. It is made up of 80 million pixels that measure 50 μm by 400 μm. A charged particle passing through a pixel generates an electron hole pair which then drifts in the applied electric field. Measuring this drift current can allow one to detect a hit in the pixel. The pixels are arranged in two different configurations. In the barrel region they are arranged in three concentric cylinders and in the forward region they are arranged in three endcap layers. Pixel provides coverage for $|\eta| < 2.5$.

Surrounding the pixel detector is the SCT. It functions similarly to the pixel detector, however instead of reading out individual pixels that allows a two-dimensional position mea-

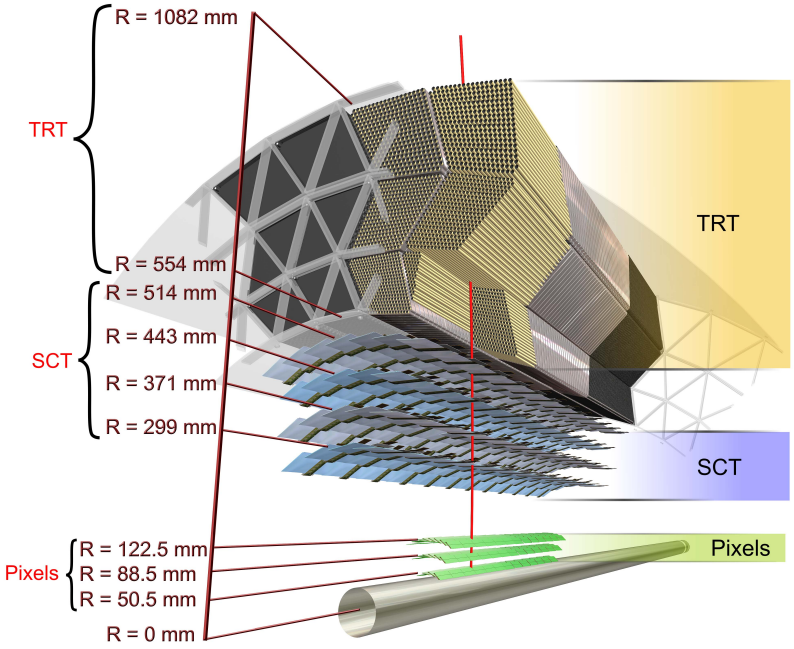

Figure 3.10: Cross section view of the different inner detector sub-detectors illustrating their radial layout.[34]

surement, the silicon sensors are arranged as strips of width 80 μm. The strips only allow a spatial measurement in one dimension. A second layer of strips is placed on top of the first layer at an angle of 40 mrad relative to the first layer. The intersection of two strips with hits in them allows the position in angular space to be known. As with the pixel detector the SCT has two different configurations. In the barrel region there are four double layers and in the forward region there are nine endcap double layers. The SCT provides coverage for $|\eta| < 2.5$.

The TRT is the outermost subdetector in the ID. Instead of using silicon sensors the TRT uses 4 mm diameter straw drift tubes filled with a gas mixture of xenon, carbon dioxide, and oxygen with a gold plated tungsten wire running through the center of the tube. The wire is kept at a high voltage relative to the drift tubes. When a charged particle passes through

the straw it ionizes the gas which creates a drift current that can then be measured. The position along the width of the straw can be determined by looking at the time of arrival of the signal. A charged particle traveling closer to the wire will have a shorter drift time. The space between the straws is filled with a polypropylene radiator. Electrons passing through the radiator will produce larger amounts of transition radiation than pions or other heavier charged hadrons. Thus, TRT also provides discrimination between electrons and heavier charged particles. Like the other two sub-detectors the TRT has two configurations. The barrel region has 73 layers of straws that are aligned along the beam axis and in the endcap the straws are arranged in disks with a total of 160 layers. The TRT provides coverage for $|\eta| < 2.0$.

3.2.2 The Calorimeters

The ATLAS detector uses two different calorimeter types, an electromagnetic calorimeter and a hadronic calorimeter. They are located just outside the solenoid for the ID as shown in fig. 3.11. Together, the calorimeters are used to measure the energy of all particles except muons and neutrinos. The calorimeters are the only part of ATLAS capable of measuring neutral particles and therefore are crucial for the reconstruction of jets. The sub-detectors that make up the atlas calorimeters are considered non-compensating sampling calorimeters. Sampling means that the energetic particles are showered using a dense passive absorber material (e.g. steel) which is then sampled with an active material (e.g. plastic). The calorimeters are made of alternating layers of these two materials. Since the entire shower is not contained in the active layers, the energy measured in the active layers is less then the initial energy of the particle entering the calorimeter. This is corrected for with an energy calibration during offline reconstruction.

The electromagnetic (EM) calorimeter [38] is designed to measure the energy of electrons and photons. It is divided into a barrel part ($|\eta| < 1.475$) and two endcap components

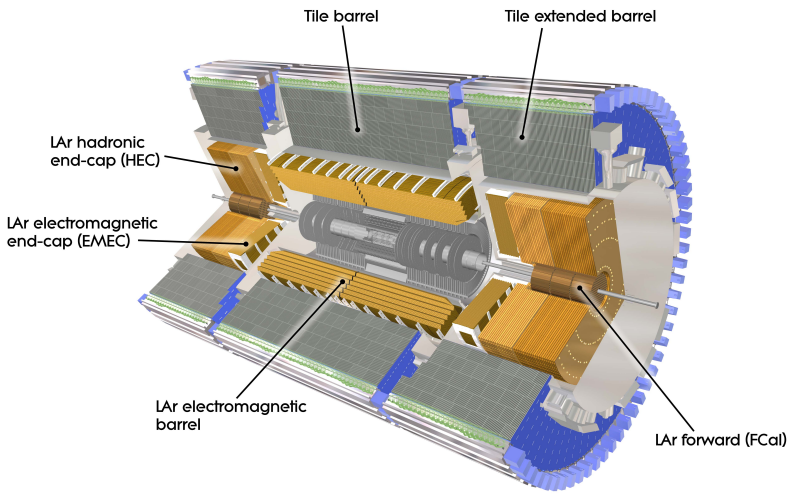

Figure 3.11: Illustration showing layout of the subsystems that make up the electromagnetic calorimeter and hadronic calorimeter in the ATLAS detector.[34]

($1.375 < |\eta| < 3.2$). Both parts use liquid argon (LAr) as the active material and lead as the absorber. The lead plates are organized into an accordion structure designed for complete ϕ symmetry without azimuthal cracks. The EM calorimeter is designed so that most of the EM shower are contained in it while allowing hadrons to pass through with minimal energy loss. Absorbers can be classified by both their radiation length and interaction length. Radiation length is the distance an electron will travel before its energy drops by a fraction of $\frac{1}{e}$. Interaction length is the average distance a hadronic particle will travel before it inelastically interacts with another nucleus. The barrel of the EM calorimeter is 22 radiation lengths and about 2 interaction lengths ensuring that most of the energy from electrons and photons entering the EM calorimeter is contained while minimizing the degradation of the hadronic energy resolution. If a charge particle enters the EM calorimeter, it either directly ionizes the LAr or if it was a hadronic particle it can first shower in the lead and then ionizes the LAr. The electrons that get produced then get collected by readout cathodes which allows the measurement of the total collected charge with is calibrated to represent the total energy that was deposited in that calorimeter cell. Each cell is defined by the segmentation of the

calorimeter which is shown in fig. 3.12. As can be seen, the EM barrel is made up of three layers longitudinally with differing granularity and radiation lengths.

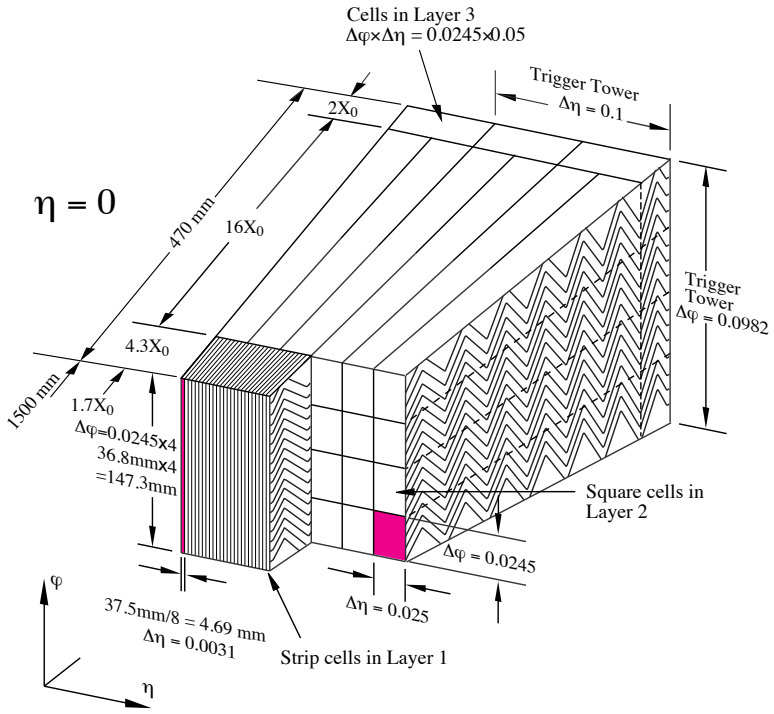

Figure 3.12: Schematic showing the segmentation and granularity of the three layers of the electromagnetic calorimeter barrel section.[34]

The hadronic calorimeter [39] surrounds the EM calorimeter and is designed to measure the energy of hadrons with $|\eta| < 4.9$ and limit hadrons from reaching the muon spectrometer by containing most of the hardonic shower. It consists of the three sub-detectors that cover different $|\eta|$ ranges. The tile calorimeter (TileCal) cover $|\eta| < 1.7$, the LAr hadronic endcap (HEC) covers $1.5 < |\eta| < 3.2$, and the LAr forward calorimeter (FCal) covers $3.1 < |\eta| < 4.9$. TileCal uses steel plates as the absorber and scintillating plastic tiles as the active material. The arrangement of the tiles for a module is shown in fig. 3.13. The steel plates initiate the shower and get converted to light by the plastic tiles. The light signal gets transmitted along wave-shifting fibers, that run along each side of the plastic tiles, to photomultiplier tubes (PMTs) that converts it to an electrical signal which is read out for each cell. The

segmentation of TileCal into cells is shown in fig. 3.14. TileCal is segmented into three layers longitudinally. HEC sits directly behind the EM calorimeter end-cap and is made up of 2 wheels with copper plate absorbers oriented perpendicular to the beam axis. Similar to the EM calorimeter it uses LAr as the active material. FCal is made up of three segments. The first segment uses copper absorbers, while the other two segments use tungsten absorbers. LAr is once again used as the active material to read out ionization charge.

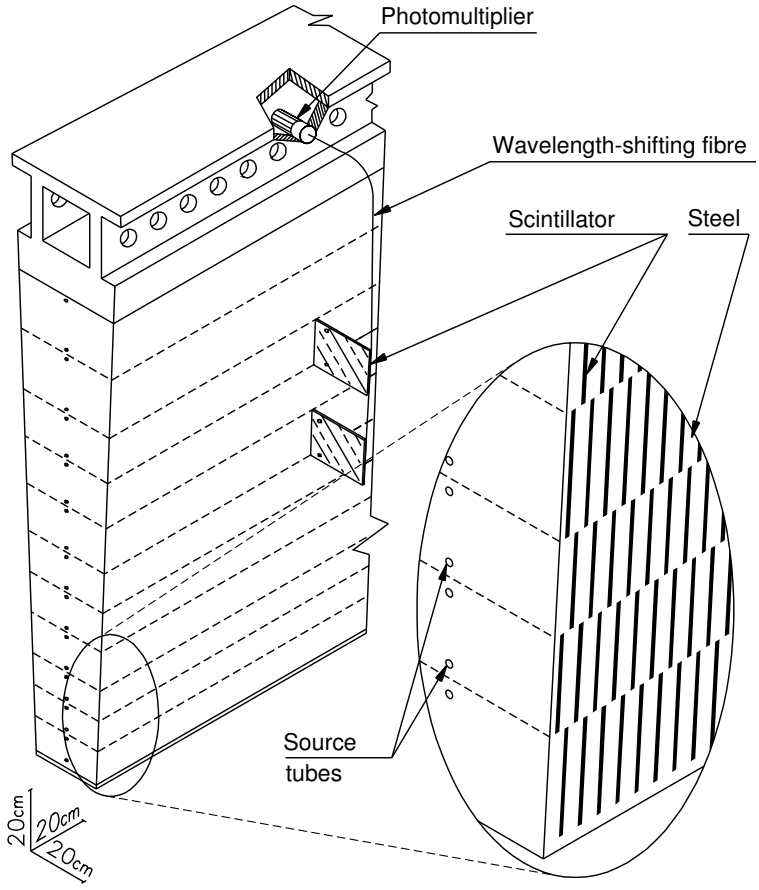

Figure 3.13: Schematic of TileCal showing arrangement of plastic and steel tiles.[34]

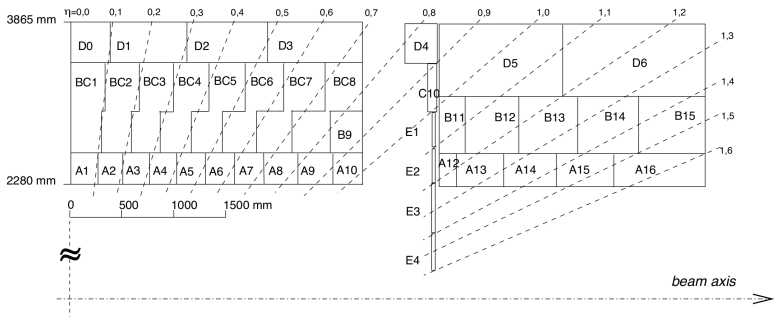

Figure 3.14: Segmentation of TileCal into cells for the central barrel and extended barrel modules.[34]

3.2.3 Muon Spectrometer

The muon spectrometer [40] is the outermost subsystem of the ATLAS detector and provides coverage up to $|\eta| < 2.7$. It is designed to identify and measure the momentum of muons passing through the inner detector and calorimeters. The muons trajectories are bent by large superconducting toroid magnets and detected using four different technologies shown in fig. 3.15. The four technologies used in the muon spectrometer are monitored drift tubes (MDT), cathode strip chambers (CSC), resistive plate chambers (RPC), and thin gap chambers (TGC). All four function similarly to the transition radiation tracker in the detector. They detect the muons by measuring a drift current produced in a large electric field by muons passing through and ionizing a gas.

The MDT has three layers and covers out to $|\eta| < 2.7$, except for the first layer that only extends out to $|\eta| < 2.0$. Its design and function is similar to the straw tube design of the TRT. The CSC covers the forward gap in the first layer of the MDT. The CSCs are multiwire proportional chambers containing many anode wires between two segmented cathodes. These two sub-detectors provide good spatial resolution, however have relatively large drift times. Up to 700 ns for the MDT. This makes them unsuitable for the trigger, discussed in more detail in the next section. The RPC and TGC have much shorter response times and are used for the muon trigger. The RPC covers up to $|\eta| < 1.05$. It consists of two resistive

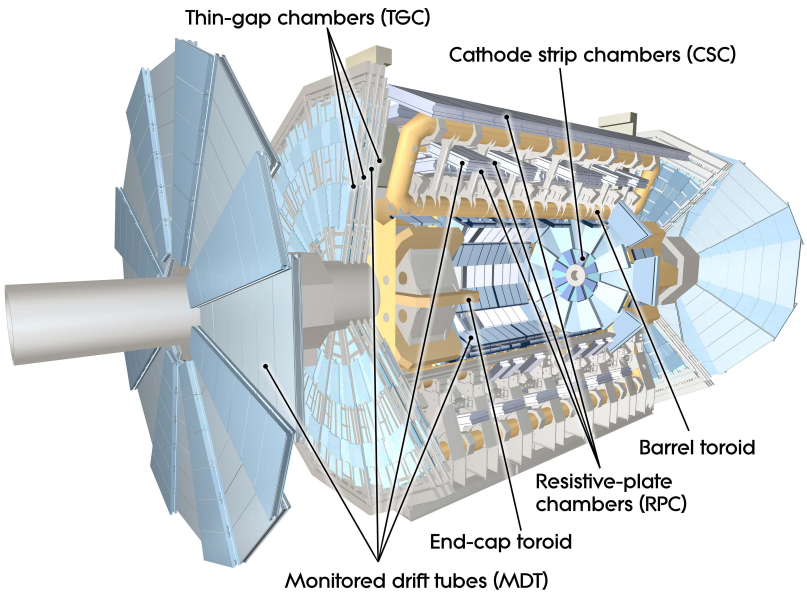

Figure 3.15: Illustration showing the four sub-detectors that make up the Muon Spectrometer in the ATLAS detector.[34]

plates separated by a small gap. The strong electric field applied allows avalanches to form along the ionizing tracks towards the anodes. This provides a fast readout for triggering. The TGC provides a coverage of $1.05 < |\eta| < 2.4$. It is also a multiwire proportional chamber like the CSC with the main difference being the smaller spacing between the wires and cathodes and a strong electric field. The smaller distances between electrodes and stronger electric fields in the RPC and TGC results in shorter drift times necessary for muon triggers.

3.2.4 Trigger and Data Acquistion

The LHC collides protons at a rate of 40 MHz. The recording of a single event in ATLAS requires about 1 MB of data. Which means recording every event would require the writing of 40 TB/s of data. Both reading out data at this rate and the amount of storage that would be needed would be extremely difficult to build with today's technology. The ATLAS Trigger and Data Acquisition (TDAQ)[41, 42] system selects which events are recorded and which are discarded. The trigger reduces the recording rate of events of interest to about 1 kHz.

During Run 2 the trigger consisted of two levels. The Level 1 trigger (L1) is implemented in dedicated hardware to produce a trigger decision within 2.5 μs. The second level is the high-level trigger (HLT) and is software based. There are numerous criteria that are used to decide whether an event passes the L1 and HLT triggers, for example the p_T of the reconstructed object or the multiplicity of identified objects, and for each criteria a unique trigger exists.

The L1 system makes a decision using data from the calorimeters and muon spectrometer. It searches for signatures from high-p_T muons, electrons, photons, jets, and τ and identifies the regions of interest (ROI) containing the candidate objects. Events with large missing transverse energy (E_T^{miss}) are also selected. It does not use the full granularity of the calorimeters and muon spectrometers. L1 reduces the event rate to about 100 kHz.

Events passing the L1 trigger are processed by the HLT. The HLT uses finer-granularity calorimeter information, precision measurements from the muon spectrometer, and tracking information from the inner detector to perform reconstruction on the ROIs. To reduce processing time most HLT triggers use a two-stage approach with a fast first-pass reconstruction that rejects the majority of events and a slower precision reconstruction for the events that pass the first stage. The HLT reduces the event rate to about 1 kHz.

CHAPTER 4

COLLISION DATA QUALITY CUTS

The measurement presented in this thesis is based on pp collision data collected using the ATLAS detector during 2015 and 2016. During the data collection periods used, the LHC delivered proton beams with a center-of-mass energy, $\sqrt{s}$, of 13 TeV. During this time ATLAS recorded a total integrated luminosity of 39.5 fb^{-1}. Not all this data was used in this analysis. Events are used only if they occurred during stable beam conditions and with all ATLAS sub-systems functioning nominally. These requirements result in the loss of about 10% worth of data due to quality. The periods in which the data quality is considered good for analysis is maintained in what is called good run list (GRL). The GRL reduced the total integrated luminosity used in this measurement to 36.1 fb^{-1}.

During 2016 data taking the bunch train structure included eight filled bunches follow by four empty bunches. During high pile-up periods this introduced saturation in the electronics of the inner wheel of the electromagnetic calorimeter end-cap (EMEC-IW). The EM calorimeter was described in section 3.2.2 and the location of the EMEC is show in fig. 3.11. The EMEC-IW covers the region $2.5 < |\eta| < 3.2$. The electronics would become saturated at the end of the bunch train and would recover over the first few bunches of the next bunch train. This caused two effects. The first is that the energy in the EM calorimeter for the first few bunches would be lower. This effect is accounted for, on average, by the eta-intercalibration (section 6.3). The second, and more significant, effect is that while the EMEC-IW electronics are recovering, large electronic noise is observed. This effect results in a large number of fake jets being reconstructed in the corresponding η region in a small fraction of data from the beginning of bunch trains and can result in fake E_T^{miss}. Since these fake jets appear at $|\eta|$ 2.9, JVT cuts are not applied (section 7.3) and hence JVT can not reject these jets. A cleaning cut was developed based on the number of high p_T clusters with poor quality in this region. The cleaning cut removes 1.66% of 2016 data reducing the total

integrated luminosity from 36.1 fb^{-1} to 35.6 fb^{-1}. This remaining 35.6 fb^{-1} of data is what is used to perform the measurement.

CHAPTER 5

MONTE-CARLO SAMPLES

Monte-Carlo (MC) simulations [43, 44] play an important part in this analysis. They are used to emulate signal events observed in collision data as well the background events from various processes observed in the collision data. Both of which are crucial for unfolding the data to the particle level. MC simulations are also used to simulate signal events at the particle level for comparison to the unfolded data.

The simulation of events at ATLAS is carried out through a series of steps. The first step is simulating the hard scatter. For ATLAS this is the interaction of the partons coming from the colliding protons. The generator begins by calculating all the matrix elements that are relevant to the hard scatter process. The phase space is then randomly sampled so that the hard scatter in each event is produced according to the probability distribution of kinematic configurations described by the calculated matrix elements. Resulting partons from the hard scatter then undergo parton showering and hadronization. The partons coming from the hard scatter are able radiate gluons through QCD and photons through QED. Since gluons themselves carry color charge, they can further radiate partons. This leads to showers of particles. This process is called parton showering. Due to confinement, once the showering partons lose enough energy they will recombine into colorless baryons and mesons.

In addition to the hard scatter, each simulated event gets overlaid with multiple additional simulated proton-proton collisions. These additional collisions are to simulate the soft QCD processes that occur when the proton beams collide. This is simulated with Pythia using the A2 tune [45] and the MSTW2008LO PDF [46]. The number of additional collisions that will occur on top of the hard scatter is taken from the distribution of the average number of interactions per bunch crossing, μ, that is predicted during data taking in 2015. Since this is only a prediction, the distribution for μ between the MC samples and the data samples differ. A reweighting, referred to as pileup reweighting, is applied to MC events so that the

μ distribution of the MC samples matches the μ distribution of the data. The μ distribution for data used in this analysis is shown in fig. 3.5.

The final-state stable particles from the previous steps are then propagated through the ATLAS detector using the GEANT4 [47] simulation tool. GEANT4 uses Monte Carlo methods to simulate the interaction of the particles with all the materials of the ATLAS detector. The simulations uses a comprehensive model of the detector which includes not only the active materials that make up the sub-systems but also includes support structures, electronics, cabling, etc.

Following the GEANT4 simulation event reconstruction is performed. Event reconstruction is done the same for MC simulation as is done for collision data. This is covered further in chapter 6.

A list of the physics processes considered in this analysis as well as there production cross-section at $\sqrt{s} = 13$ TeV is shown in table 5.1. A brief description on how all the processes are simulated is the topic of the following sections. Appendix A contains tables summarizing details of the samples such as there more detailed name, as would be found in the ATLAS database, and the initial number of events generated to produce the sample.

Initially all samples are normalized to the cross-section calculated by the MC generator used. For some samples, a higher order inclusive cross-section has been calculated. For these samples a scaling factor, called the k-factor, is applied. The k-factor is defined by dividing the higher order inclusive cross-section that has been calculated by the inclusive cross-section from the generator. Scaling the sample by this k-factor normalizes it to the higher order cross-section.

5.1 Z+Jets

The Z+jets samples contain both signal and background events depending on the flavor of the jet produced. The flavor of jets will discussed in more detail in section 7.3.2. Three

Physics process	Cross section (pb) [× BR]
W$\to \ell\nu$ $(\ell = e, \mu, \tau)$	20080
Z$\to \ell\ell$	1906
$t\bar{t}$	831
single top t-channel	217
single top Wt-channel	72
single top s-channel	10
$Z \to \ell\ell + Z \to qq$	2.17
$W \to \ell\nu + W \to qq$	49.4
$Z \to \ell\ell + W \to qq$	3.4
$W \to \ell\nu + Z \to qq$	11.4
$W \to \ell\nu + H \to b\bar{b}$	0.269
$Z \to \ell\ell + H \to b\bar{b}$	0.045

Table 5.1: Production cross section of the different physics processes considered, multiplied by the relevant branching ratios when appropriate

different generators are used to produce the Z+jets samples. For the remainder of this thesis they will be labeled as Sherpa, Alpgen, and MadGraph. A brief description of these generators will be given in the following sections. Sherpa is the generator that is used in unfolding the data. Alpgen is used to determine a systematic uncertainty from the modeling used in unfolding. Madgraph is used as a further comparison of measured cross sections. For the Z+jets samples k-factors are applied to normalize the samples to the inclusive NNLO Z cross section as calculated by FEWZ [48, 49].

5.1.1 Sherpa

The Z+jets Sherpa samples are generated using Sherpa 2.2.1 [50]. Sherpa is a general purpose MC event generator which does both the matrix-element generation and the parton showering using the ME+PS@NLO prescription [51]. Matrix elements are calculated at next-to-leading order (NLO) for Z+jets processes with 0, 1, or 2 additional partons. While processes with 3 or 4 additional partons are only generated at leading order (LO). Any additional jets are produced by the parton shower. The parton density functions (PDFs) Sherpa uses are provided by the NNPDF3.0nnlo set [52]. It uses the five-flavor number scheme (5FNS). In the 5FNS only gluons as well as the first five flavors of quarks are considered in the PDF.

All partons are considered massless in the matrix elements while massive quarks are used in the parton shower. For Sherpa the samples are generated in intervals of the variable $max\,[p_T(Z), H_T]$ at the parton level. The transverse momentum of the Z boson, $p_T(Z)$, is determined from the two parton-level leptons, while the parton-level H_T is defined as the scalar sum of the transvere momentum, p_T, of all patron-level jets with $p_T > 20$ GeV. Here, patron-level jets are constructed from all the remaining matrix-element-level patrons, excluding the two leptons from the Z boson, using the anti-k_t algorithm with a jet radius of 0.4. Jet reconstruction and the anti-k_t algorithm are discussed in more detail in section 6.3. The intervals of $max\,[p_T(Z), H_T] < 500$ GeV are further split based on their b-hadron and c-hadron content at the particle level. A table showing the samples used can be found in Appendix A.

5.1.2 Alpgen

Z+jets samples were also produced using Alpgen v2.14 [53]. Alpgen is a LO matrix-element generator. Alpgen does not model the parton shower and therefore it must be interfaced to another generator that can perform the parton showering. For our samples it is interfaced to Pythia v6.426 [54] for the parton showering using the Perugia2012C [55] tune. Alpgen uses the CTEQ6L1 PDF set [56]. It uses a four-flavor number scheme (4FNS). In the 4FNS the PDF contains only gluons and the first two generations of quarks. Alpgen is able to generate matrix elements at LO for up to five additional partons in the final state. Samples are generated based on the number of additional partons in the final state. These samples make no distinction on the flavor of the parton used in the matrix element calculation. Therefore, these samples contain events with both light-flavor jets and heavy-flavor jets and will be referred to as the inclusive samples.

Alpgen can also be used to produce samples that explicitly contain massive c- or b-quarks in the matrix elements that are calculated. Doing so is useful for improving statistics

in events with heavy flavor jets. This is possible for the processes that include $Z + c\bar{c}$ and $Z + b\bar{b}$. This calculation like in the inclusive samples can include up to five partons. The five partons include the explicit ones. These explicit samples will be referred to as the heavy-flavor samples.

To avoid double counting when combining the inclusive samples and heavy-flavor samples a heavy-flavor overlap removal (HFOR) procedure is used. Double counting occurs because heavy-flavor quarks are produced by both gluon splitting in the parton shower and by the explicit matrix-element calculations. This is illustrated using the Feynman diagram in fig. 5.1. In the heavy-flavor samples this diagram would be included in the matrix element calculation and in this case the two b's are coming from the hard scatter. However, in the inclusive samples, this same diagram without the two b's drawn would be included in the matrix element calculation. The gluon in the diagram from the hard scatter could then split into two b's in the parton showering resulting in the double counting of the event. The HFOR procedure is used to avoid this double-counting. The procedure applies to events with two heavy-flavor quarks and is based on the angular separation, ΔR, and origin of the two heavy-flavor quarks. If the two heavy-flavor quarks originate from the parton shower with $\Delta R\,(q, \bar{q}) > 0.4$ then the event is removed. If the two heavy-flavor quarks originated from the matrix element with $\Delta R\,(q, \bar{q}) < 0.4$ then the event is removed. This HFOR procedure is only applied to same flavor quarks, b or c, and between particle/anti-particle pairs.

5.1.3 Madgraph

The Z+jets samples produced with what is labeled as Madgraph in this thesis are produced using MadGraph5_aMC@NLO v2.2.2 [57] interfaced to Pythia v8.186 [58]. Similar to Alpgen, Madgraph generates matrix elements at LO. Madgraph does not perform the parton showering and hence needs to be interfaced with another generator, which in this case is Pythia8 using the A14 tune [59]. It can calculate matrix elements for Z plus up to 4 ad-

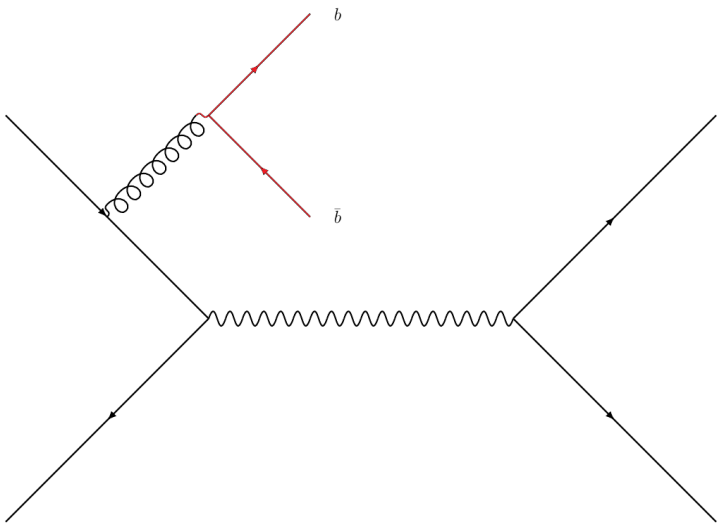

Figure 5.1: Feynman diagram used for illustrating double counting in Alpgen samples

ditional partons. The Madgraph samples produced used the NNPDF3.0nlo PDF set [52]. Like Sherpa, it uses a 5FNS with massless c- and b-quarks in the matrix element calculation and massive quarks in the parton shower. Samples produced with Madgraph are generated in intervals of the variable H_T (defined in section 5.1.1) and further split based on their b-hadron and c-hadron content at the particle level similar to the Sherpa samples. A full list of the samples used is shown in Appendix A.

5.2 Background Samples

Almost all background processes are modeled using MC simulations. The exception is QCD multijet (MJ) production. This background is estimated using data driven techniques. This will be discussed further in chapter 8. A summary of the simulated background processes was included in table 5.1. The W+jets background samples are produced just like Z+jets samples. The Diboson processes, WW, WZ, and ZZ, are generated using Sherpa 2.2.1, which calculates up to one additional parton at NLO and three additional partons at LO. Only semi-leptonic decay samples are produced.

Samples are produced for WH and ZH processes (collectively referred to as VH) with zero or one additional jet. These samples are generated using POWHEG-BOX v2 + MINLO [60, 61]. POWHEG-BOX calculates the matrix-elements of the hard scatter at NLO precision using the POWHEG method. It is interfaced with Pythia8 to perform the particle showering. The samples are produced with the requirement that the vector boson decays leptonically and that the Higgs boson decays to $b\bar{b}$. The mass of the Higgs boson was fixed at 125 GeV and the $H \to b\bar{b}$ branching fraction was fixed at 58%. As is shown in table 5.1 these processes are relatively rare. However, in the case of ZH the final state ($ZH \to \ell\ell + b\bar{b}$) is identical to the final state in the 2B signal region. In order for events from the ZH process to make it into the 1B signal region one of the b-quarks would have to be lost or misidentified.

Top production is a large source of background for the measurement of a Z plus b-jets produced in QCD interactions because of the similar signature that results from the $t \to Wb$ decay. It is divided into two categories based on the number of tops produced ($t\bar{t}$ and single top). The samples for simulating $t\bar{t}$ production are generated at NLO using POWHEG-BOX v2 interfaced with Pythia8. Events were produced with the requirement that at least one W boson in the event decays leptonically. For producing the samples, the top quark mass was set to 172.5 GeV. The parameter referred to as hdamp, which controls the matrix element to parton shower matching in POWHEG and effectively regulates the high-p_T radiation, was set to 1.5 times the top quark mass. This choice of hdamp was used because it was found to give the best modeling of $t\bar{t}$ for both $\sqrt{s} = 7$ TeV and $\sqrt{s} = 13$ TeV [62]. For $t\bar{t}$ a k-factor is applied to normalize the sample to the cross section calculated at NNLO with the Top++2.0 program [63].

Single top production is further divided into three channels distinguished by the way the W boson is involved in the production. In the t-channel, the top quark is produced via the exchange of a virtual, time-like W boson ($Q_W^2 < 0$, where Q_W is the four-momentum of the W boson). Where as in the s-channel, the top quark is produced via the exchange of a virtual,

space-like W boson ($Q^2_W > 0$). The Wt-channel is distinguished from the other two channels by the production of a single top quark in association with a real W boson ($Q^2_W = M^2_W$). Diagrams representing these three channels are shown in fig. 5.2. The samples used for these three channels were produced using POWHEG-BOX v1 interfaced with Pythia6 using the Perugia 2012 tune.

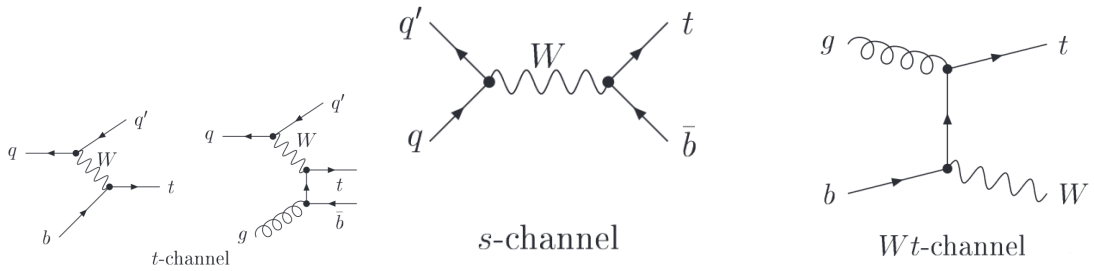

Figure 5.2: Example Feynman diagrams showing the three different single top production channels.[64]

Since top production represents a significant amount of the background, systematics associated with the modeling of the top production are estimated using additional samples. This is discussed in more detail in section 10.3.

CHAPTER 6

PHYSICS OBJECT RECONSTRUCTION

In order to perform any measurement at a particle collider one has to be able to identify and reconstruct the physics objects produced by the collision from the electronic readouts of the detector. The physics objects that are used in this analysis are electrons, muons, jets and missing transverse energy(E_T^{miss}). Conservation of momentum means that the vector sum of the transverse momentum should be zero, however since neutrinos are not directly detected there will be an imbalance in the transverse momentum in events involving them. Thus reconstructing E_T^{miss} allows one to indirectly reconstruct neutrinos. The procedures for reconstructing these physics objects using the subsystems that make up the ATLAS detector is described in this chapter.

6.1 Electrons

Electrons are reconstructed using information from the EM calorimeter and inner detector [65]. It begins by searching for clusters of energy deposited in the EM calorimeter. The EM calorimeter is divided into a grid of 200 $\times$ 256 towers of size 0.025 $\times$ 0.025 in $\eta \times \phi$ space. These towers correspond to the granularity of the middle layer of the calorimeter. The energy in all three layers of the calorimeter in each tower are summed up to define the energy in that tower. A sliding-window algorithm [66] is then used to search for seeds for electron clusters. The size of the window used is 3 $\times$ 5 towers. A clustering algorithm is then used to form clusters around these seeds. A region of interest with a cone $\Delta R = 0.3$ around the seed cluster barycenter is defined for EM clusters that pass loose shower shape requirements.

The next step is track reconstruction in the inner detector. This is carried out in two steps: pattern recognition and track fit. In the first step the pattern recognition algorithm [67] first

uses the pion hypothesis for energy loss due to interactions with the detector material. A track seed is made up of three hits from the pixel and SCT detector. If a track seed with $p_T > 1$ GeV cannot be successfully extended to a full track of at least 7 hits using the pion hypothesis, but it falls within one of the EM clusters region of interest, then a second attempt is performed using a modified pattern recognition which uses an electron hypothesis. The electron hypothesis allows for up to 30% energy loss to account for possible bremsstrahlung at each intersection of the track with the detector material. In the second step the track candidates are fitted with the same hypothesis as was used for pattern recognition using the ATLAS Global χ^2 Track Fitter [68]. If the fit fails under the pion hypothesis, but is within a region of interest for an EM cluster, then the fit is redone under the the electron hypothesis. If a track is within $\Delta\eta < 0.05$ and $\Delta\phi < 0.05$($\Delta\phi < 0.2$ if the track is on the side of the cluster that the track is bending towards to account for loss in energy due to bremsstrahlung) of an EM cluster then it is refitted using an optimized Gaussian Sum Filter (GSF) [69], which takes into account the non-linear bremsstrahlung effects.

Electron candidates are then created by matching GSF fitted tracks to EM clusters. The requirement for a track to be matched to a cluster is that the track must be within $\Delta\eta < 0.05$ and $\Delta\phi < 0.05$($\Delta\phi < 0.1$ if the track is on the side of the cluster that the track is bending towards) of the cluster. If more than one track matches, then the track closest to the cluster is selected.

A full description of the calibration of electron energy is given in [70]. Several corrections are applied. The energy reconstructed in the electron cluster is corrected to account for the energy lost in the material upstream of the calorimeter, for the energy deposited in cells neighboring the cluster in η and ϕ, and for the energy lost beyond the EM calorimeter. A single correction factor for these corrections is derived by training a multivariate regression algorithm on different features of the EM shower and the position of it within the detector and comparing cluster energies with truth electron energies in simulated events. An electron

energy scale correction is applied to the energies in data events and a smearing correction is applied to the energies in MC events so that the electron energy scale and resolution match between data and MC.

In order to determine whether the reconstructed electron candidates are signal-like objects (ie electron coming from the hard-scatter) or background-like objects (for example, hardonic jets or converted photons), algorithms for electron identification (ID) are applied. The algorithm used is a likelihood-based (LH) method. It is a multivariate analysis technique that simultaneously evaluates several properties of the electron candidates when deciding whether they are signal-like or background-like. The inputs to the LH algorithm include measurements from the tracking system, the calorimeter system, and variables that combine both tracks and calorimeter information. Three levels of identification operating points are provided for electron ID. They are called loose, medium, and tight in reference to their background rejection. The operating points each use the same variables to define the LH discriminant. They differ in the selection on the discriminant.

Another important property of the electron candidate is how isolated it is. Two discriminating variables are defined to quantify the amount of energy of particles produced around the electron candidate. One defines how isolated the electron track is ($p_T^{varcone20}$) while the other defines how isolated the EM cluster is (E_T^{cone20}). The calorimetric isolation energy,E_T^{cone20}, is defined as the sum of transverse energy of topological clusters within a cone of $\Delta R = 0.2$ around the electron candidate's EM cluster, but not including the electrons transverse energy. The track isolation momentum, $p_T^{varcone20}$, is defined as the sum of the transverse momentum of all tracks within a cone of $\Delta R = min(0.2, 10GeV/p_T)$ around the electron candidate's track. Cuts applied to these isolation variables are used to further discriminate between signal and background.

6.2 Muons

Muons are reconstructed using information from the inner detector (ID) and muon spectrometer (MS). The reconstruction of muon tracks is first performed independently in the ID and MS. Information from individual subdetectors is then combined to form muon tracks that are used for physics analyses [71].

In the ID, muon tracks are reconstructed like they are any other charged particle [72]. The primary algorithm for reconstructing tracks in the ID is the inside-out algorithm. It starts with a track seed and adds hits moving away from the interaction point using a combinatorial Kalman filter. The algorithm extends tracks into the TRT.

In the MS, muon tracks are reconstructed using an algorithm called MUONBOY [73]. The algorithm is summarized into four main steps. First, it identifies regions of activity by using hits in the trigger chambers (RPC and TGC). Within these regions of activity it then reconstructs local track segments in the MDT by performing straight-line fits to the hits found in each layer. At this stage the hits are close enough in space for the straight line approximation to be valid locally. The local track segments are then combined in muon track candidates by considering which combinations of the segments would be compatible with the path the muon would take through the magnetic field. A global fit is then done using all the hits associated with segments that make up the muon track candidate.

Four different muon types are defined depending on which sub-detectors are used in their reconstruction. For this thesis only one type is used, however they all will be briefly mentioned.

A combined (CB) muon is a muon where track reconstruction is performed independently in the ID and MS and then a combined track is formed with a global refit that uses the hits from both the ID and MS sub-detectors. During this refit, hits in the MS may be added or removed from the track to improve the fit quality.

Segment-tagged (ST) muons are tracks in the ID that are classified as muons if they can

be extrapolated to the MS and associated with at least one local track segment in the MDT or CSC. ST muons are used when muons don't cross the entire MS either because they have low p_T or because they pass through a region that has reduced MS acceptance.

Calorimeter-tagged (CT) muons are tracks in the ID that are classified as muons if it can be matched to an energy deposit in the calorimeter compatible with a minimum-ionizing particle. This type uses no information from the MS.

Extrapolated (ME) muons are muon tracks reconstructed based only on the MS track and requiring a loose requirement on compatibility that it originated from the interaction point. The muon is required to travel through at least two layers of MS chambers. The primary use of ME muons is to extend the acceptance for muon reconstruction out to the region $2.5 < |\eta| < 2.7$, which is not covered by the ID.

To identify and select muons a few quality requirements are applied to suppress background. The main source of background muons come from pion and kaon decays. Muons coming from W/Z decays are considered signal, where as muons that come from the decays of light-hadrons are considered background. A muon candidate that originates from the in-flight decay of a charged hadron in the ID can often be identified by a distinct kink in the topology of the reconstructed track. Either the direction the muon travels in may differ from that of the charged hadron resulting in a poor fit quality of the resulting combined track from the ID and MS, or the muon will carry less momentum then the charged hadron potentially resulting in the momentum measured in the ID and MS to not be compatible. One of the variables used to discriminate signal muons from background muons is the q/p significance. It is defined as the absolute value of the difference between the ratio of the charge and momentum of the muons measured in the ID and MS divided by the sum in quadrature of the corresponding uncertainties. In addition a few quality cuts are applied based on the number of hits in the ID. An ID track is required to have at least one pixel hit, at least five SCT hits, and fewer than three pixel or SCT holes. A hole is defined as an active

sensor that lies on the path transversed by the track that contains no hits. Only holes which fall between hits successfully assigned to the track are considered in this requirement on the number of holes. If the track falls in the region of full TRT acceptance ($0.1 < |\eta| < 1.9$) then a requirement is also place on the number of TRT hits. The requirement is that at least 10% of the TRT hits originally assigned to the track were included in the final fit.

The muon quality identification has four different categories: loose, medium, tight, and high-p_T. This thesis uses medium identification of muons and so only that category is described. The medium identification is described as the default selection for muons in ATLAS. These muons are made from CB and ME tracks only. The ME tracks are only used for $2.5 < |\eta| < 2.7$ and we require our muons to have $|\eta| < 2.5$ (see section 7.2 for muon selection) so that all muons come from CB tracks in this thesis. The tracks are required to have at least 3 hits in at least two layers in the MDT for $|\eta| > 0.1$. For the $|\eta| < 0.1$ region, tracks are required to have hits in at least one layer in the MDT and have at most one hole in the MDT. The q/p significance is required to be less then seven. This selection is used to reduce the contamination coming from hadrons being misidentified as muons.

Like for the electron, muon isolation is an important property used to improve background rejection. It is quantified similarly to how electron isolation is quantified using two variables. The track based isolation variable, $p_T^{varcone30}$, quantifies how isolated the muon track is. It is defined as the sum of the transverse momentum of all tracks within a cone of $\Delta R = min(0.3, 10GeV/p_T)$ around the muon's track. The calorimeter based isolation variable, $E_T^{topocone20}$, quantifies how isolated the muon's energy that is deposited in the calorimeter is. It is defined as the sum of transverse energy of topological clusters within a cone of $\Delta R = 0.2$ around the muon, but not including the muon's transverse energy. Cuts are applied to these isolation variables to further discriminate between signal and background.

A full description of how the muon momentum is calibrated in MC is given in [71]. The p_T and resolution of muons in MC simulated events does not initially match that of muons

observed in data. This is measured using $J/\Psi \rightarrow \mu\mu$ and $Z \rightarrow \mu\mu$ decays. The p_T in simulated events is corrected by applying scale factors. The scale factors are determined in bins of η and ϕ and are applied to the tracks of the ID and MS separately. The result is then propagated to the combined muon p_T measurement.

6.3 Jets

Electrons and muons can be directly observed as they pass through the detector. However, due to confinement, individual quarks and gluons cannot be directly observed. Due to the strong coupling of QCD, the quarks and gluons originating from the proton-proton collisions at the LHC will radiate gluons and create $q\bar{q}$ pairs. This process of showering continues until enough energy is lost and the remaining partons hadronize. The reconstruction of these collimated sprays of particles are what are referred to as jets.

Jets are reconstructed using a clustering algorithm. The goal of the jet algorithm is to reconstruct an object that accurately represents the original parton that initiated the collimated spray of particles. Over the past decades there have been many algorithms developed to reconstruct jets [74]. Jets are obviously not unique and depend on the algorithm used to define them. A good jet algorithm should be collinear-safe and infrared-safe. Collinear-safe means splitting a high-p_T particle into two or more collinear particles will not effect jet clustering. Infrared-safe means the jet clustering should not be effected by soft radiation. The clustering algorithm used for jets in this thesis is the anti-k_T algorithm [75] with a radius parameter of $R = 0.4$. This is a standard algorithm used within the ATLAS collaboration. It is implemented in the FastJet software package [76]. The anti-k_t algorithm is a sequential recombination jet algorithm. It uses the energy deposited in the EM and hadronic calorimeters as input. Before the jet clustering algorithm is performed a three-dimensional topological clustering of the individual calorimeter cells is performed to produce clusters called topo-clusters[77]. It is these topo-clusters that are used in the jet reconstruction.

The reason for using the topo-clusters instead of the individual calorimeter cells directly as inputs to the jet reconstruction is because the topo-clusters have better noise suppression and energy resolution after calibrations are applied.

The anti-k_t algorithm is a specific case of a more generalized sequential recombination jet algorithm. It takes a set of input objects and two different definitions for distances and uses a series of steps to cluster these objects into jets. One distance is defined to measure the distance between two input objects, d_{ij}. The other distance is defined to measure the distance between the object and the beam, d_{iB}. The algorithm then follows these steps:

1. Calculate d_{iB} for all objects and d_{ij} for all possible combinations of particles.

2. Find the minimum distance from the set of all distances computed in step 1.

3. If the minimum distance corresponds to a d_{ij}, then the objects i and j are combined into a new object k. Object i and j are replaced by object k in the list of objects. Return to step 1.

4. If the minimum distance corresponds to a d_{iB}, then object is removed the list of objects and labeled as a jet. Return to step 1.

These steps are repeated until all input objects have been clustered into jets. Three commonly used jet algorithms are defined by the following choices for the distances:

$$d_{ij} = min(p_{Ti}^n, p_{Tj}^n)\frac{\Delta R_{ij}^2}{R^2} \tag{6.1}$$

$$d_{iB} = p_{Ti}^n \tag{6.2}$$

and are differentiated by the choice of n. R is the radius parameter and roughly corresponds to the radius of the jet. Choosing $n = 2$ corresponds to the k_t algorithm, $n = 0$ corresponds to the Cambridge/Aachen algorithm, and $n = -2$ corresponds to the anti-k_t algorithm.

Since this thesis uses the anti-k_t algorithm a general qualitative description of how it clusters jets will be given. Consider an event with several hard particles and many soft particles. Here hard means high-p_T and soft means low-p_T. Consider a hard particle 1 and a soft particle i. The distance d_{1i} given by equation eq. (6.1) with $n = -2$ is determined exclusively by the transverse momentum of the hard particle and the ΔR_{1i} separation because $1/p_{T1}^2 \ll 1/p_{Ti}^2$. If another soft particle j exists with a similar separation $\Delta R_{ij} \sim \Delta R_{1i}$ then the only difference between the distances d_{1i} and d_{ij} comes from the differences in the $p_T s$ involved in which case the transverse momentum of the hard particle (p_{T1}) dominates. That is $d_{1i} \ll d_{ij}$. This shows that soft particles will tend to cluster to hard particles long before they cluster among themselves. If no other hard particles exist within a distance of $2R$ of hard particle 1, then hard particle 1 will simply be clustered with all soft particles within a circle of radius R, resulting in a perfectly canonical jet. This is simply seen because once all clusters within a circle of radius R are combined with the hard particle 1's cluster then the remaining soft particles will necessarily have $\Delta R_{1i} > R$. This then implies that d_{1B} is a minimum and thus this object is labeled as jet and removed. If however there exists another hard particle 2 such that $\Delta R_{12} < R$, then the two hard particles will be clustered together and form a single jet. The resulting jet shape will be the union of two circles with radius $< R$ along with a third circle of radius R centered on the final jet. If instead $R < \Delta R_{12} < 2R$ then the two hard particles will not be clustered together and instead two separate jets will be constructed. If $p_{T1} \gg p_{T2}$ then jet 1 will be circular while jet 2 will be missing the part that overlaps with jet 1. Instead if $p_{T1} \sim p_{T2}$, then neither jet will be circular and the overlapping part will be divided approximately by a straight line. An example of an event clustered using the anti-k_t algorithm is shown in fig. 6.1 and illustrates many of the properties described.

Topo-clusters are formed through an iterative procedure which identifies seed cells and then adds neighboring cells with significant signal to the cluster. The basic observable that

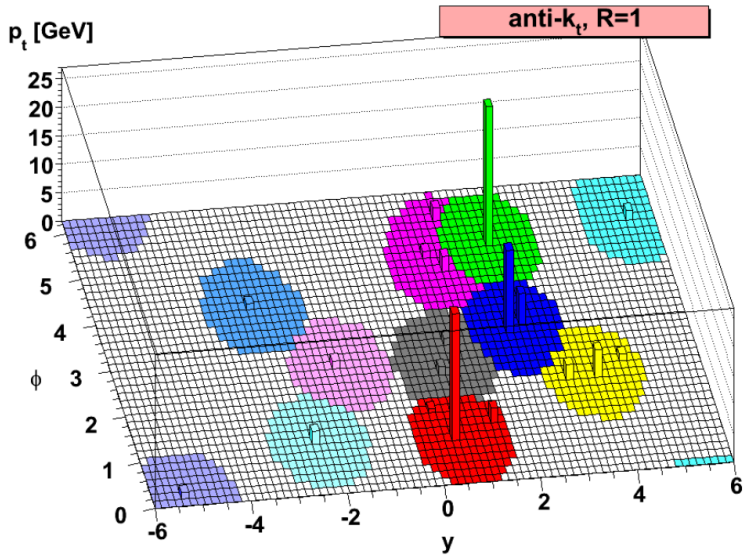

Figure 6.1: Resulting jets reconstructed using the anti-k_t algorithm.[78]

controls the cluster formation is the cell signal significance, S, defined as:

$$S = \frac{E^{EM}_{cell}}{\sigma^{EM}_{noise,cell}}, \tag{6.3}$$

where E^{EM}_{cell} is the cell energy and $\sigma^{EM}_{noise,cell}$ is the expected noise in the cell, both measured at the EM energy scale. The procedure first identifies all seed cells as cells with $S > 4$. Topo-clusters are then formed around these seed cells. All cells with $S > 2$ adjacent to the seed cell are added to the topo-cluster. This procedure is repeated until all neighboring cells of the topo-cluster with $S > 2$ are added to the topo-cluster. If a neighboring cell belongs to two different topo-clusters than the two topo-clusters are merged. Once all cells passing the noise threshold requirements are added to the topo-cluster all surrounding cells, regardless of their energy, are added to the topo-cluster. This procedure can produce topo-clusters that are too large to provide a good measurement of the energy flow from the particles generated in the event because the spatial structures inside the clusters is not explicitly taken into account in the formation procedure. For example, a topo-cluster with multiple local signal

maxima would indicate the presence of more than one particle depositing energy in close proximity. A cluster splitting algorithm is used to split clusters that have multiple local maximum. Figure 6.2 shows an example of the formation of topo-clusters.

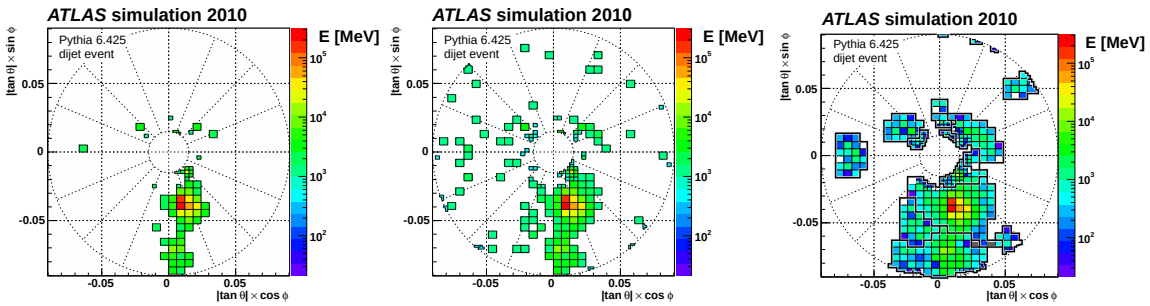

(a) Cells with $S > 4$ (b) Cells with $S > 2$ (c) Reconstructed topo-clusters

Figure 6.2: Stages of topo-cluster formation in the first module of the FCal for a simulated dijet event with at least one jet entering this calorimeter. (a) shows the seed cells, (b) shows cells with $S > 2$ which are the cells that get iteratively added to the seed cells, and (c) shows the resulting topo-clusters outlined by thicker black lines.[77]

The jets reconstructed from topo-clusters are originally at the EM scale. A series of steps are done to calibrate the jets to the particle-level energy of the initial particle that produced the jet. Referred to as the jet energy scale(JES). These steps correct for detector effects, pile-up, and MC mismodeling. The stages of calibration are summarized in fig. 6.3. A detailed description of the calibration is given in [79], which is summarized below.

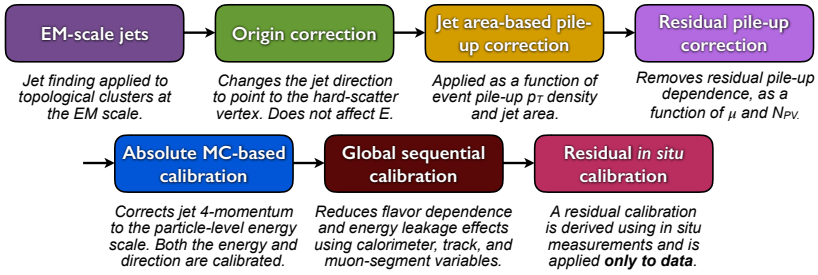

Figure 6.3: Calibration stages for EM-scale jets.[79]

The first is the origin correction. A jets four-vector is initially reconstructed to point back to the center of the detector. However, particles will actually point back to the position

of the interaction that produced them, most likely not the center of the detector. These vertices (position of the interaction) are identified by the extrapolation of tracks in the inner detector. The vertex corresponding to the hard scatter is taken as the primary vertex with the largest Σp_T^2 of tracks. The jets four-vector is adjusted so that it points back towards this primary vertex while keeping the jet energy constant. This correction improves the η resolution of jets.

The next step is pile-up correction. This correction is to account for the additional energy deposited in the jet from in-time and out-of-time pile-up. The first correction assumes that pile-up deposits energy uniformly in η and ϕ. It is an area-based method that subtracts the per-event event pile-up contribution to the p_T of each jet according to its area. For each event the p_T density in the η-ϕ plane is calculated for each jet. The area of the jet is calculated using ghost association. The pile-up density, ρ, is taken as the median of the p_T density. An example of the ρ distribution is shown for MC simulation in fig. 6.4. The p_T of each jet in the event is then corrected by subtracting off $A \times \rho$, where A is the area of the jet. After this correction a dependence on the p_T of anti-k_t jets on the amount of pile-up still remains as is shown in fig. 6.5. It shows that there is still a dependence on the number of primary vertices, N_{PV}, which is sensitive to in-time pile-up, and μ, which is sensitive to out-of-time pile-up. A residual correction is applied based on these variables and the position of the jet in η. The correction for in-time pile-up is taken as $\alpha(\eta) \times (N_{PV} - 1)$, where $\alpha(\eta)$ is taken from a fit to the purple band in fig. 6.5a. The correction for out-of-time pile-up is taken as $\beta(\eta) \times \mu$, where $\beta(\eta)$ is taken from a fit to the purple band in fig. 6.5b. The overall pile-up correction is summarized in the following equation:

$$p_T^{corr} = p_T^{EM} - \rho \times A - \alpha \times (N_{PV} - 1) - \beta \times \mu \tag{6.4}$$

The next step in jet calibration uses MC to take the jet from the EM scale to the particle-

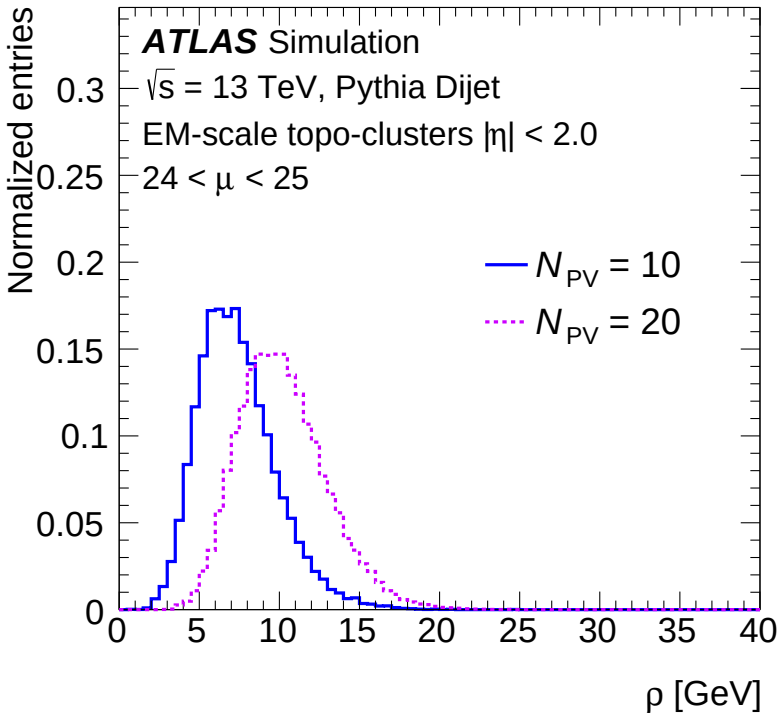

Figure 6.4: Per-event median p_T density, ρ, at $N_{PV} = 10$ (solid) and $N_{PV} = 20$ (dotted) for $24 < \mu < 25$ as found in MC simulation.[79]

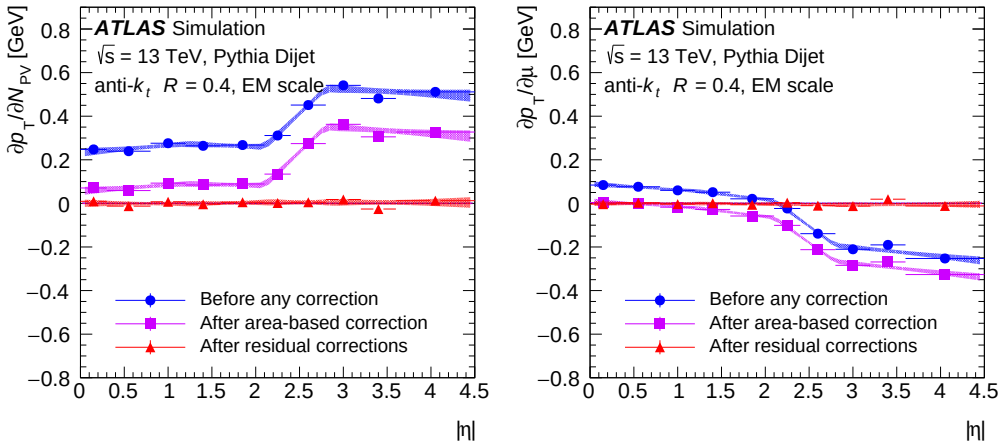

(a) In-time pile-up dependence (b) Out-of-time pile-up dependence

Figure 6.5: Dependence of EM-scale anti-k_t jet p_T on (a) in-time pile-up and (a) out-of-time pile-up as a function of η for p_T^{truth}= 25 GeV. The dependence is shown before pile-up corrections (blue), after the area-based correction (purple), and after the residual correction (red).[79]

level scale and correct for biases in the jet η reconstruction. The corrections are derived by comparing reconstructed information to truth information in MC simulations. Reconstructed jets are matched to truth jets if $\Delta R < 0.3$ between the two jets. The reconstructed jets are also required to be isolated. The isolation requirement is that there are no other calorimeter jets within $\Delta R = 1.0$. The truth jets are also required to be isolated. The energy response is defined as the ratio of the energy of the reconstructed jet (E_{reco}) to the energy of the truth jet (E_{truth}) and is binned in E_{truth} and η_{det}. η_{det} is the original η of the original reconstructed jet before the origin correction is applied. The reason for using η_{det} instead of the corrected η is to remove the ambiguity as to which region of the detector is measuring the jet. Each bin is fit with a Guassian and the mean of the fit is taken as the average jet energy response. The average jet energy response is shown in fig. 6.6 for different values of E_{truth}. A numerical inversion procedure is used to parameterize the average energy response

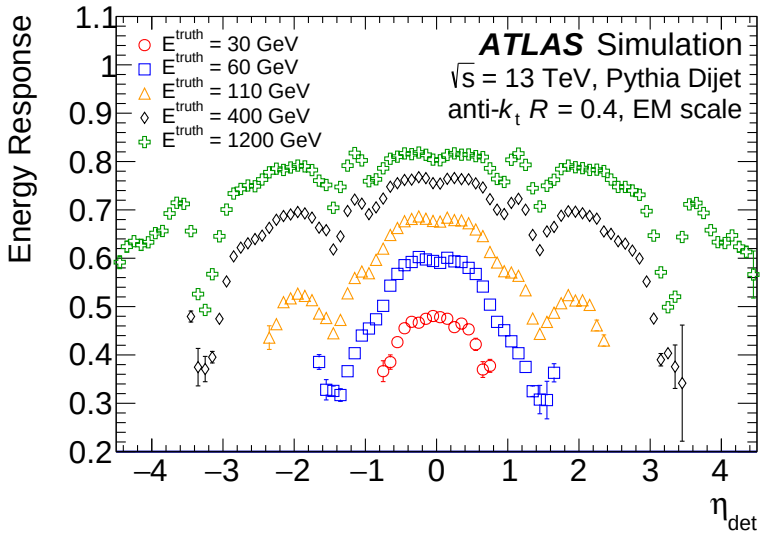

Figure 6.6: The average energy response as a function of η_{det} for jets of truth energy 30, 60, 110, 400, and 1200 GeV. The energy response is shown after origin and pile-up corrections are applied.[79]

as a function of E_{reco} and the jet calibration factor is taken as the inverse of the average jet energy response. After applying the jet calibration factor a bias can be seen in the reconstructed jet η. This bias is shown in fig. 6.7. The cause of this bias comes from the

jet energy response not being uniform over the entire region a jet encompasses. The bias is largest in jets that encompass two calorimeter regions with different energy responses caused by changes in calorimeter geometry or technology. The energy of topo-clusters in regions with lower energy response will artificially be lower than the energy of topo-clusters in regions with a higher energy response. The effect is that it causes the direction of the jet to be biased towards the region with the higher energy response. To reduce this bias another correction is derived similar to that of the average energy response except instead using the average difference $\Delta\eta = \eta_{reco} - \eta_{truth}$.

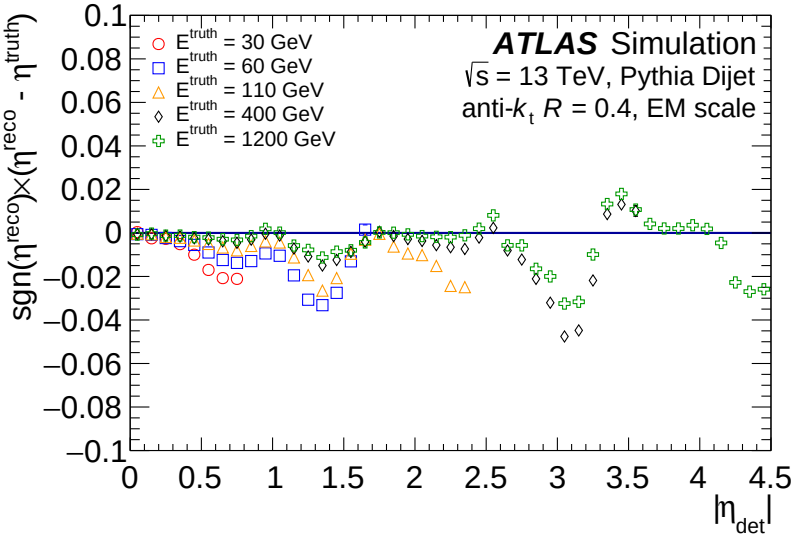

Figure 6.7: The signed difference between the truth jet η_{truth} and the reconstructed jet η_{reco} after calibration is applied.[79]

Following all the jet calibrations discussed up till now there still exists residual dependencies of the jet energy on longitudinal and transverse features of the jet. The cause of this is primarily due to the differences in the shower profiles between jets initiated by quarks and jets initiated by gluons. A jet initiated by a quark will often include hardons with a higher fraction of the jet p_T that penetrate further into the calorimeter, while a jet initiated by a gluon will typically contain more particles of softer p_T which leades to a lower calorimeter response and a wider transverse profile. In order to remove these dependencies

a global sequential calibration (GSC) procedure [80, 81] is used to improve the resolution of the JES while maintaining the average energy response derived in the previous jet energy scale calibration. Five variables are used in the GSC procedure and their corrections are applied sequentially. The five variables used, in order are:

1. The fraction of jet energy measured in the first layer of the Tile calorimeter
2. The fraction of jet energy measured in the third layer of the EM calorimeter
3. The number of tracks associated with the jet
4. The width of the tracks associated with the jet
5. The number of muon segments associated with the jet

The final step in jet calibration is the in-situ correction. This correction is designed to account for differences between the jet response between data and MC simulation. The sources of the difference can come from imperfections in the simulation of the hard scatter, underlying event, pile-up, jet formation, and EM and hadronic interactions with the detector. The differences are quantified by balancing the p_T of a jet against other well-measured reference objects. The response, $\mathcal{R}$, is defined in data and MC simulation as the average ratio of jet p_T to reference object p_T. The ratio of this response in data to MC is taken as the in-situ correction. The different in-situ calibrations that are performed are:

1. η-intercalibration: Corrects the average response of forward jets ($0.8< |\eta_{det}| <4.5$) to that of well-measured central jets ($|\eta_{det}| <0.8$) using dijet events.
2. Boson Balance: Calibrates central jets through the p_T balance of a jet against a Z boson or a photon. The Z boson is required to decay to either a electron or muon pair. The Z boson provides calibration over the p_T range $20 < p_T < 500$ GeV while the photon provides calibration over $36 < p_T < 950$ GeV.

3. Multijet Balance: Calibrates central jets by balancing a high-p_T jet against a system composed of several lower-p_T jets. The p_T of the lower-p_T is low enough that they have been calibrated by the boson balance calibration. The Multijet Balance calibration extends the calibration to a p_T of 2 TeV.

The corrections derived from the boson and multijet balance calibrations are combined into a single correction over the full p_T range. The combination is show in fig. 6.8.

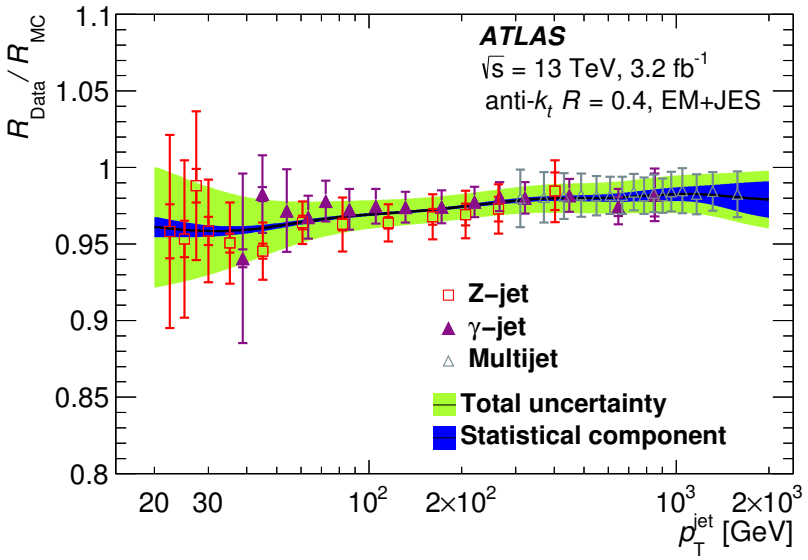

Figure 6.8: The in-situ calibrations for the boson balance (Z+jet,γ+jet) and multijet balance as well as the final combined calibration (black line).[79]

6.4 Jet B-Tagging

Identifying jets containing b-hadrons is referred to as b-tagging. The lifetime of b-hadrons is $\sim$ 1.5 ps, which is longer than the lifetime of most other hadrons, and allows them to travel a few mm before decaying. This results in a secondary vertex, corresponding to the b-hadron decay, that is displaced from the primary hard-scatter vertex. This is exploited in b-tagging algorithms to identify b-jets. The ATLAS experiment uses three different b-tagging algorithms whose output are combined in a multivariate discriminant algorithm to identify b-jets[82, 83].

The first b-tagging algorithm, called IP3D, is based on the impact parameters of the tracks associated with the jet. The transverse impact parameter, d_0, is defined as the distance of closest approach in the r-ϕ plane of the track to the primary vertex. The longitudinal impact parameter, $z_0 \sin\theta$, is defined as the distance of the track to the primary vertex in the longitudinal plane at the point of closest approach in r-ϕ. Tracks generated from b-hadron decays tend to have large impact parameters due to the long lifetime of b-hadrons. The sign of the impact parameter is determined based on if the primary vertex is in front or behind the secondary vertex relative to the jet direction. IP3D uses the transverse impact parameter significance, d_0/σ_{d_0}, and the longitudinal impact parameter significance, $z_0 \sin\theta/\sigma_{z_0 \sin\theta}$. MC simulations are used to determine probability density functions used as references for the different jet flavor possibilities (b, c and light flavor). Examples of the distributions of the impact parameters significances is shown in fig. 6.9. From the probability density functions a log-likelihood ratio discriminant is computed, which is is shown in fig. 6.10. The IP2D tagger is also used and is similar to the IP3D algorithm. The difference is that the IP2D tagger only uses the transverse impact parameter significance. The log-likelihood ratio discriminants are what are used as input in the multivariate algorithm discussed further below.

The next b-tagging algorithm used is the secondary vertex finding algorithm (SV) that explicitly reconstructs a secondary vertex within the jet. The algorithm takes all track pairs within a jet and constructs all possible two-track vertices. Any two-track vertices reconstructed that are compatible with the decay of a long-lived non b-hadron or hadronic interactions with the detector material are removed. A secondary vertex is then reconstructed by fitting all the tracks from the accepted two-track vertices, removing tracks that are not compatible with the fit iteratively. Several requirements are placed on the tracks and two-track vertices [82], for example a two-track vertex is required to be significantly displaced from the primary interaction vertex. Several properties of the reconstructed secondary vertex

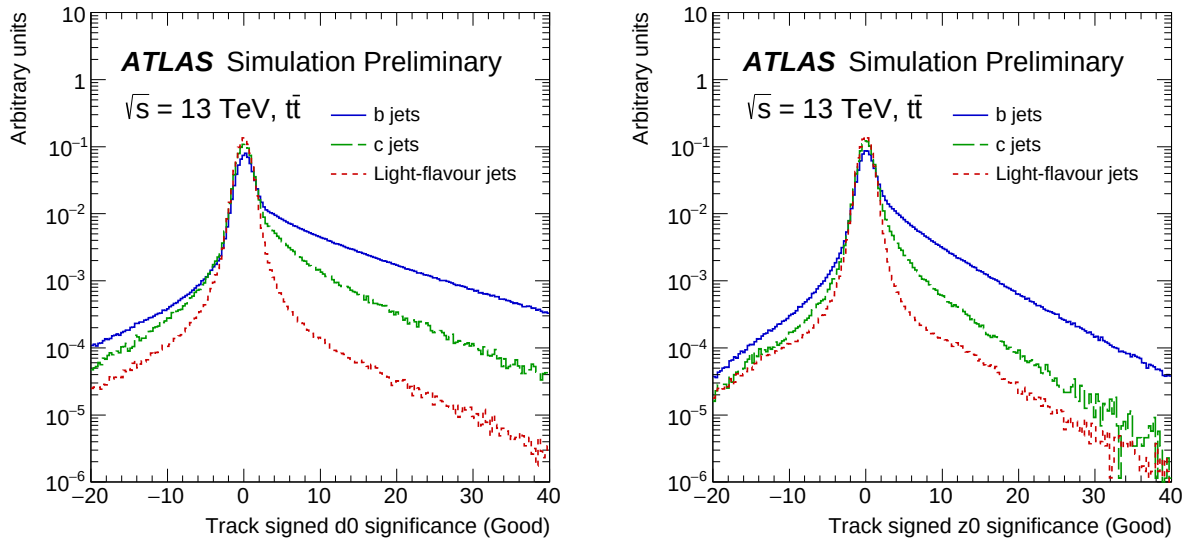

(a) (b)

Figure 6.9: The transverse (a) and longitudinal (b) signed impact parameter significance of tracks in $t\bar{t}$ events for the different flavor of jets.[82]

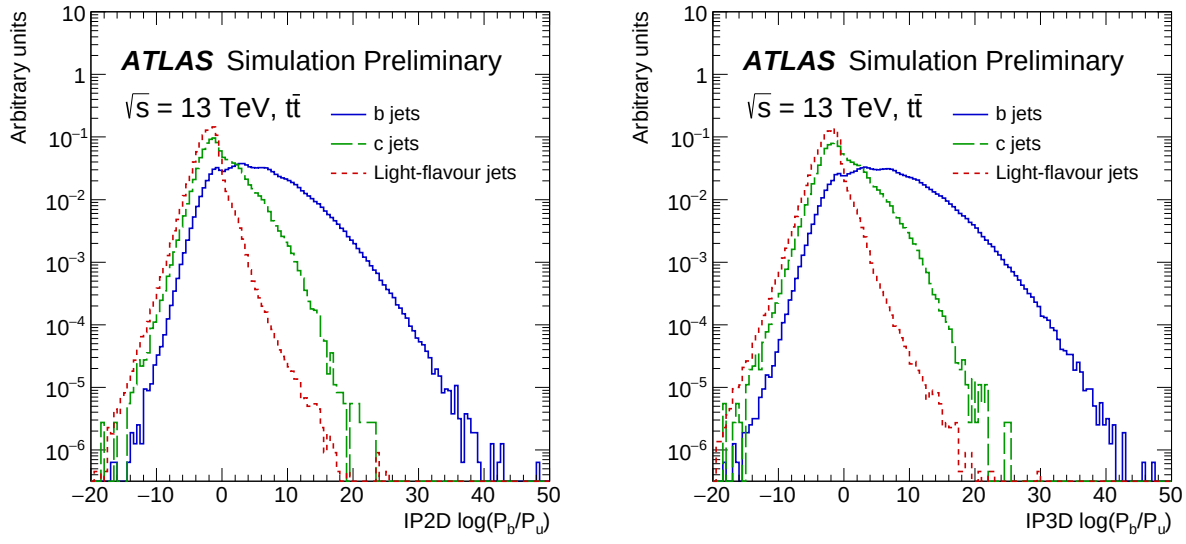

(a) (b)

Figure 6.10: The log-likelihood ratio for the IP2D (a) and IP3D (b) b-tagging algorithm in $t\bar{t}$ events for the different flavor of jets. The log-likelihood ratio shown is computed as the ratio of the b-flavor and light-flavor probability density functions.[82]

are then used as inputs in the multivariate algorithm discussed further below. Two such properties are the number of tracks associated to the secondary vertex and the invariant mass of the secondary vertex. Examples of these distributions are shown in fig. 6.11 for different jet flavors.

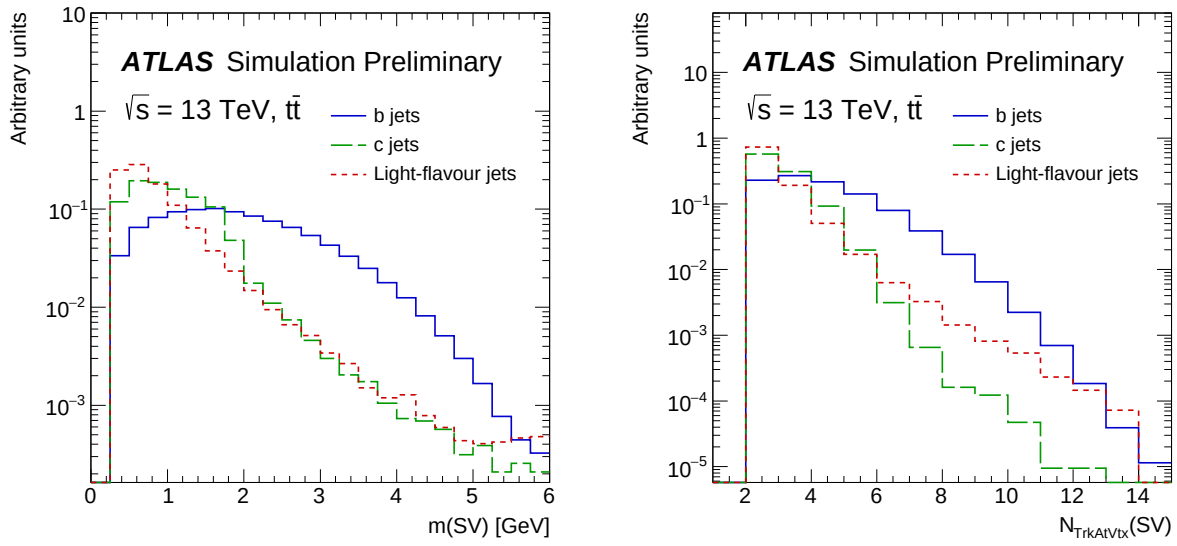

(a) (b)

Figure 6.11: The invariant mass (a) and number of tracks (b) of the secondary vertex reconstructed by the secondary vertex finding algorithm in $t\bar{t}$ events for the different flavor of jets.[82]

The final b-tagging algorithm used is a decay chain multi-vertex reconstruction algorithm called JetFitter[84]. It attempts to reconstruct the full decay chain, PV $\rightarrow b \rightarrow c$, by exploiting the topological structure of b-hadron and c-hadron decays inside the jet. A Kalman filter is used to find a common line on which the primary vertex and the bottom and charm vertices lie along, approximating the b-hadron flight path, as well as their positions. This method, when resolution allows, is able to resolve b-hadron and c-hadron vertices even when only a single track is attached to each of them. Several properties of the reconstructed decay chain, similar to the properties from the secondary vertex finding algorithm, are used as inputs in the multivariate algorithm. Three such properties are the number secondary

vertices reconstructed with one track, the number of secondary vertices reconstructed with more than one track, and the invariant mass of the tracks associated with the secondary vertices. Examples of these distributions are shown in fig. 6.12 for different jet flavors.

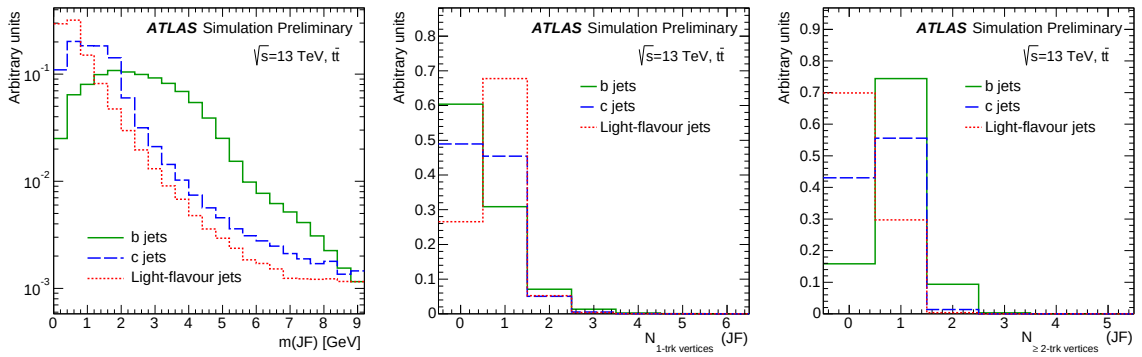

(a) (b) (c)

Figure 6.12: The invariant mass (a), number of secondary vertices with only one track (b), and number of secondary vertices with more than one track (c) using the JetFitter algorithm in $t\bar{t}$ events for the different flavor of jets.[83]

The outputs of the previously described b-tagging algorithms are combined using a multivariate algorithm called MV2, which is a boosted decision tree algorithm. The MV2 algorithm gives better discrimination than any of the previous b-tagging algorithms described can give individually. MV2 uses twenty-four input variables (the complete list of them can be found in [83]): the p_T and η of the jet, six from IP2D and IP3D (three each), eight from the secondary vertex finding algorithm, and eight from JetFitter. The p_T and η of the jet are included in the algorithm to take advantage of any correlations of them with the other input variables. The MV2 algorithm is trained using jets from $t\bar{t}$ events with b-jets being considered signal, and c-jets and light-flavor jets being considered background. Three different variants of the MV2 algorithm were developed during run 2 of ATLAS, differentiated by the amount of c-flavor jets in the background. They are labeled MV2c00, MV2c10, and MV2c20. For the initial 2015 configuration the cXX corresponded to the percentage of the background that was made up of c-flavor jets. So for example, MV2c10 was trained on a background consisting of 10% c-flavored jets and 90% light-flavored jets. However, in 2016

these numbers were changed to improve c-flavor jet rejection and maintain similar light-flavor jet rejection. For the 2016 configuration, which is the one used in this thesis, MV2c00 corresponds to no c-flavored jets in the background training sample, MV2c10 corresponds to 7% c-flavored jets in the background training sample, and MV2c20 corresponds to 15% c-flavored jets in the background training sample. The performance of the three variants of MV2 are shown in fig. 6.13 for rejecting light flavor and c-flavor jets as a function of the b-flavor jet efficiency. Also shown is the comparison of the 2015 configuration to that of the 2016 configuration. It can be seen that MV2c20 does provide the best c-jet rejection, but also the worse light-flavored jet rejection. As this analysis is sensitive to both light and c-flavor jets the MV2c10 variant is chosen as the algorithm used. This also corresponds to the standard algorithm used by most analyses. Also shown in fig. 6.13 is the improvement in the c-jet rejection from the 2015 configuration to the 2016 configuration for MVc10 as well as the light-jet rejection staying very similar between the two configurations.

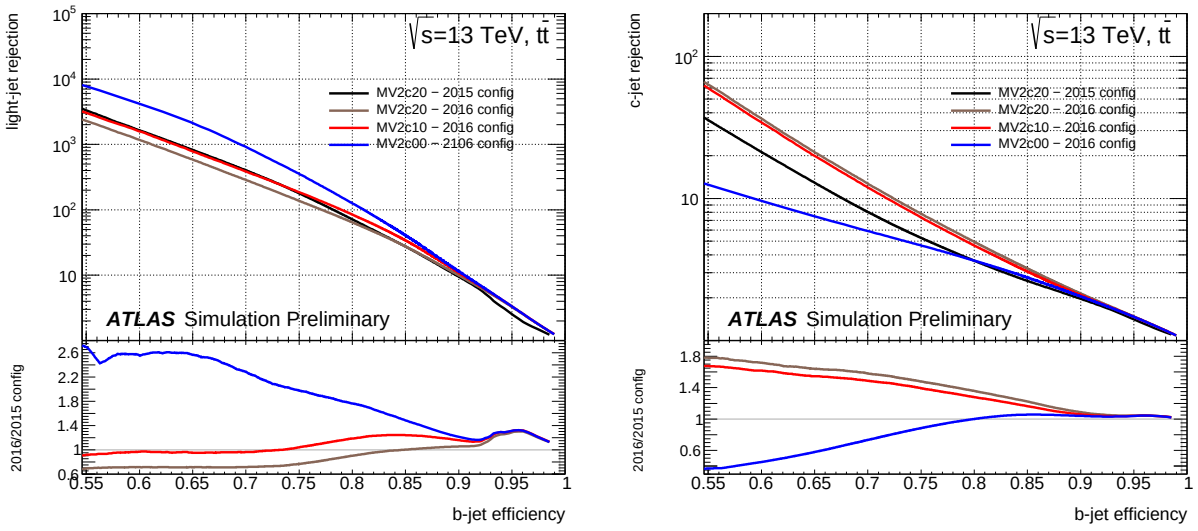

(a) (b)

Figure 6.13: Light-flavor jet (a) and c-flavor jet (b) rejection versus b-jet efficiency for the 2015 configuration and 2016 configuration of the MV2 b-tagging algorithm evaluated on $t\bar{t}$ events.[83]

The output of the MV2c10 algorithm for the signal and background components are

shown in fig. 6.14. Operating points are defined by a single cut value on the MV2 output and are chosen to provide a specific b-jet efficiency on a $t\bar{t}$ sample. Different operating points as well as the background rejection rates at those operating points is shown in table 6.1.

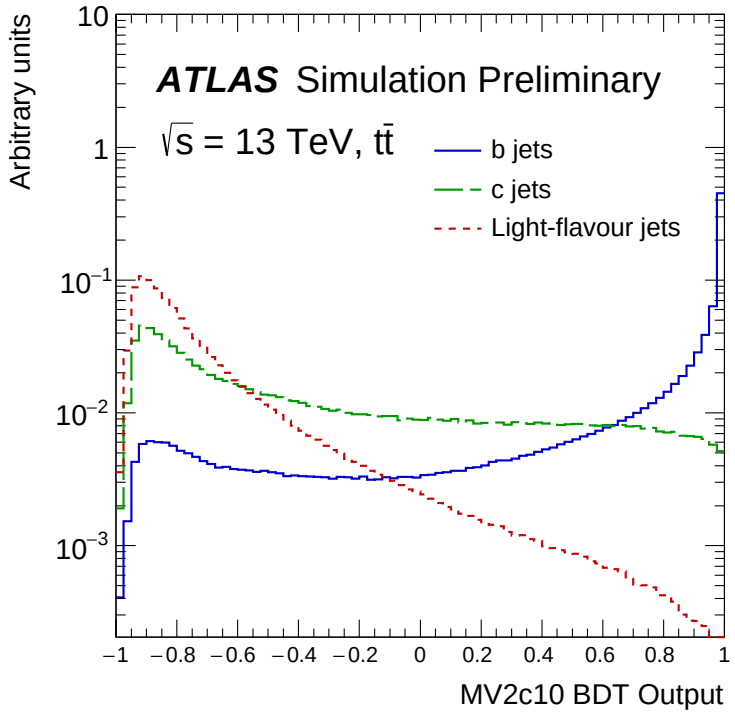

Figure 6.14: Output of MV2c10 algorithm for different flavored jets evaluated with $t\bar{t}$ events.[82]

Operating Point	MV2c10 Cut Value	c-jet Rejection	light-jet Rejection	τ Rejection
50	0.9769	106	5701	614
60	0.9349	35	1539	184
70	0.8244	12	381	55
77	0.6459	6	134	22
85	0.1758	3	33	8

Table 6.1: Different operating points of the MV2c10 algorithm.

6.5 Missing Transverse Momentum

Conservation of momentum in the plane transverse to the beam axis implies that the vector sum of the transverse momentum of all the particles produced in the collision should sum to zero. A momentum imbalance in the transverse momentum implies that particles invisible to the detector systems, such as neutrinos, were produced in the collision. This momentum imbalance is referred to as the missing transverse momentum (E_T^{miss}).

The E_T^{miss} is reconstructed by calculating the sum of the negative vectors of the selected hard objects: electrons, photons, muons, hadronically decaying τ-leptons, and jets. Reconstructed momentum not associated to any hard objects are also included in E_T^{miss} and referred to as the soft term. The vector sum of E_T^{miss} can in general be written as:

$$-E_T^{miss} = \sum p_T^{\mu} + \sum p_T^{e} + \sum p_T^{\gamma} + \sum p_T^{\tau} + \sum p_T^{jets} + \sum p_T^{soft}. \tag{6.5}$$

The hard objects used in E_T^{miss} are selected and calibrated the same as they are outside of E_T^{miss}. For example, an electron selected as coming from $W \to \ell\nu$, will also be selected to be included in the calculation of E_T^{miss}. The soft term is made up of all tracks that are not associated with a reconstructed physics object. The tracks are also required to be originating from the hard scatter. More details on E_T^{miss} including its performance can be found in [85].

CHAPTER 7

EVENT SELECTION

This chapter covers the requirements placed on the reconstructed objects described in the previous chapter used in this analysis. Only events that were recorded during optimal running conditions are considered. This was determined by the GRL. Two separate GRLs were used, one for data taken during 2015[1] and one for data taken during 2016[2]. This analysis is divided into two channels depending on the flavor of the lepton in the decay of the Z (Z$\rightarrow \ell\ell$). The electron and muon channels are further divided into two regions depending on the number of b-jets produced along with the Z boson. A region for events with at least one b-jet and a region for events with at least two b-jets. How these regions are defined is the subject of the following sections.

7.1 Electron Selection

Electron events are selected using triggers that require at least one electron meeting a certain p_T threshold. The lowest unprescaled triggers available are used and follow the recommendations by the electron group. The triggers used depends on the data acquisition period and are summarized in table 7.1. Electrons are reconstructed as described in section 6.1. Electrons are required to pass the tight operating point of the electron identification likelihood algorithm. The electron passing the identification requirement must also be the electron that corresponds to the trigger. Electrons are also required to be isolated. For electrons with $p_T < 60$ GeV, the electron is considered isolated if it passes the "FixedCutTight" selection [70] ($p_T^{varcone20}/p_T < 0.06$ and $E_T^{cone20}/p_T < 0.06$). Electrons with $p_T >$60 GeV are

1. data15_13TeV.periodAllYear_DetStatus-v79-repro20-02_DQDefects-00-02-02_PHYS_StandardGRL_All_Good_25ns.xml

2. data16_13TeV.periodAllYear_DetStatus-v88-pro20-21_DQDefects-00-02-04_PHYS_StandardGRL_All_Good_25ns.xml

considered isolated if they satisfy "isLooseTrackOnlyIso" and "FixedCutHighPtCaloOnly" selections [70] ($E_T^{cone20} < 3.5GeV$). The selected electron must also have a minimum p_T of at least 27 GeV and lie within the region of $|\eta| < 2.47$, but not within the calorimeter crack region between $1.37 < |\eta| < 1.52$.

Requirements are also placed on the electrons tracks to ensure that the electron is associated with the primary vertex. This is done by placing requirements on the transverse impact parameter, d_0, and the longitudinal impact parameter, z_0, of the electron with respect to the primary vertex. The requirement is that $|d_0|/\sigma(d_0) < 5$ and $z_0 \sin(\theta) < 0.5mm$, where θ is the polar angle.

2015	2016
HLT_e24_lhmedium_L1EM20VH	HLT_e24_lhtight_nod0_ivarloose
HLT_e60_lhmedium	HLT_e26_lhtight_nod0_ivarloose
HLT_e120_lhloose	HLT_e60_lhmedium_nod0
	HLT_e60_medium
	HLT_e140_lhloose_nod0
	HLT_e300_etcut

Table 7.1: Triggers used to select events with at least one electron.

7.2 Muon Selection

Muon events are selected using triggers that require at least one muon meeting a certain p_T threshold. The lowest unprescaled triggers available are used and follow the recommendations by the muon group. The triggers used depends on the data acquisition period and are summarized in table 7.2. Muons are reconstructed as described in section 6.2. Muons are required to pass the medium operating point of the muon identification algorithm. Muons that pass the identification requirement must also be the muon matching to the trigger selection. Muons are also required to be isolated. They are considered isolated if they satisfy the "FixedCutTight" selection [71] ($p_T^{varcone30}/p_T < 0.06$ and $E_T^{cone20}/p_T < 0.06$). Muons

are required to be in the region $|\eta| < 2.5$ and like electrons must have a minimum p_T of at least 27 GeV. Similar to electrons requirements are placed on the muons tracks to ensure that the muon is associated with primary vertex. The requirements are that $|d_0|/\sigma(d_0) < 3$ and $z_0 \sin(\theta) < 0.5mm$.

2015	2016
HLT_mu20_iloose_L1MU15	HLT_mu24_iloose
HLT_mu40	HLT_mu24_ivarmedium
	HLT_mu26_ivarmedium
	HLT_mu40
	HLT_mu50

Table 7.2: Triggers used to select events with at least one muon.

7.3 Jet Selection

The jets used in this analysis are reconstructed with the anti-kt jet algorithm using radius parameter $R = 0.4$ using topological clusters in the calorimeter and calibrated as described in section 6.3. Jets are required to have a p_T greater than 20 GeV and lie in the region $|\eta| < 4.5$. Jets are required to pass loose jet cleaning requirements which are described in [86]. The "LooseBad" working point is used. These requirements are designed to reject fake jets caused by beam induced background, cosmic-ray showers, and calorimeter noise while maintaining a high efficiency of selecting real jets.

To reduce the effects of pileup, a multivariate combination of properties of the jet is used to identify a jet as coming from pileup or not. This algorithm is called the jet vertex tagger (JVT) [87] and uses information of the tracks associated with the jet among other variables to produce a discriminant that can be used to identify pileup jets. For example, a pileup jet would tend to have smaller fraction of tracks associated with the primary vertex than a jet coming from the hard scatter would have. The output of the JVT is a number between 0 and 1, where 0 corresponds to a more pileup like jet and 1 corresponds to a more hard scatter

like jet. The JVT requirement is only applied to jets with 20 GeV $< p_T <$ 60 GeV and $|\eta| <$ 2.4. The "Medium" working point of the JVT is used, which corresponds to requiring that the discriminant of the JVT to be greater than 0.59.

7.3.1 B-Jets

Jets passing the selection in the previous section are considered to be b-jets, that is b-tagged, if the MV2c10 weight is larger than 0.8244273. As shown in table 6.1 this corresponds to the 70% working point. In addition to the MV2c10 requirement, b-jets are also required to fall within the rapidity range of $|y| <$2.5.

7.3.2 Jet Flavor

In the MC simulations, jets are classified as either coming from b, c, or light quarks using the truth hadrons. They are classified using cone-based matching. A jet is labeled a b-jet if a b-hadron is contained in a cone of $\Delta R = 0.3$ within the jet. If a b-hadron can be matched to two jets, only the jet closest in ΔR to the b-hadron is labeled as a b-jet. Similarly jets are labeled as a c-jet or tau-jet. Any remaining jets that are not labeled as b-, c- or tau-jets are labeled as light jets.

It should be noted that we have now introduced two different definitions of b-jets. One based on the value of MV2c10 and one based on if the jet has a matching truth b-hadron. The latter is only used when considering the Z+jets samples produced by the three different generators used (Sherpa, Alpgen, and Madgraph) and is used to divide up the samples into the different flavor components to allow for a comparison between generators and for use in the flavor fit. In this thesis it should be clear from the context which one is being used.

Using this labeling of jet flavor, events in the Z+jets samples are divided into five categories:

1. $Z + bb$: contains at least 2 b-jets

2. $Z + b$: contains only one b-jet

3. $Z + cc$: contains at least 2 c-jets

4. $Z + c$: contains only one c-jet

5. $Z + light$: does not fall under previous 4 categories

If an event falls into more than one of the above categories than it is only included in the category highest on the list. For example, if an event contains only 1 b-jet and 1 c-jet, it would only be included in the $Z + b$ category. This results in the five categories being mutually exclusive.

7.4 Overlap Removal

It is possible for the same signal in the detector to be reconstructed as two different objects. For example an electron being reconstructed as both an electron and a jet. In this case we would want to remove the jet from the event. This procedure is known as overlap removal. The overlap removal procedure is done using only leptons that pass the lepton selections and jets with $p_T > 20$ GeV. The procedure is performed sequentially with the following steps:

1. Remove jet if $\Delta R < 0.2$ within a selected electron.

2. Remove electron if $\Delta R <$min(0.4,0.04 + 10 GeV/p_T^e) within a jet selected with JVT>0.59 if $p_T < 60$ GeV and $|\eta| < 2.4$.

3. Remove jet if $\Delta R < 0.2$ within a selected muon, if the jet has less than three tracks in the ID or if both $p_T^\mu / SumPtTrk^{jet}$ >0.7 and p_T^μ / p_T^{jet} >0.5. Here $SumPtTrk^{jet}$ is the sum of the p_T of the tracks associated with the jet.

4. Remove muon if $\Delta R <$min(0.4,0.04 + 10 GeV/p_T^μ) within a jet selected with JVT>0.59 if $p_T < 60$ GeV and $|\eta| < 2.4$.

Jets that have survived the overlap procedure above are removed if they are within $\Delta R < 0.4$ of any selected leptons. The choice for using the value of ΔR=0.2 comes from studies that show electron clusters plus bremsstrahlung should be contained in such a cone. Therefore the first step removes jets that are primarily formed from the showering of a prompt electron. The second step is to remove electrons that are produced from the decay of hadrons. The third step is to remove jets that are primarily formed by high-p_T muons that lose energy due to bremsstrahlung as they pass through the calorimeter. These jets usually have very few tracks associated with them. The fourth step is to remove muons that are produced from the decay of hadrons.

7.5 Scale Factors to Correct Efficiencies in Monte Carlo Samples

The same algorithms are used in reconstruction and identification of physics objects in collision data and Monte Carlo (MC) simulations. However the efficiency of these algorithms can differ between the two sample types. This can be caused by a number of things, for example the mismodeling of a muon's energy loss as it passes through the calorimeter to the muon spectrometer. The differences in efficiencies are corrected for in MC by applying efficiency Scale Factors (SF), which are derived from calibration analyses performed by various ATLAS Combined Performance groups. The scale factor in general is defined as the ratio of the efficiency in data to the efficiency in MC and summarized in the following:

$$SF^x = \frac{\epsilon^x_{Data}}{\epsilon^x_{MC}}, \tag{7.1}$$

where x is the effect the SF is accounting for.

The trigger efficiencies are measured for data and MC for each of the electron trigger algorithms listed in table 7.1 and each of the muon trigger algorithms listed in table 7.2. Electron trigger efficiencies are measured as a function of p_T and η using $Z \to ee$ events.

Muon trigger efficiencies are measured as a function of η and ϕ using $Z \to \mu\mu$ events. More details on the measurement of these efficiencies can be found in [41].

Events containing a muon have a muon scale factor applied. This muon scale factor is made up of a couple of scale factors associated with the muon. One scale factor accounts for the efficiencies of the working point of the muon identification. Another scale factor accounts for the efficiencies of the working point of the muon isolation. These two scale factors are multiplied together to form the muon scale factor. A description of the measurement of these efficiencies can be found in [71].

Events containing an electron have an electron scale factor applied. Similar to the muon scale factor, the electron scale factor is composed of several individual scale factors associated with electron reconstruction. The first scale factor accounts for the efficiency of reconstructing an electron given that an EM cluster has been found. The second scale factor accounts for the efficiency of the working point of the electron identification. That is, the efficiency of the electron to pass electron identification requirements given that an electron has been reconstructed. The final scale factor accounts for the efficiency of the working point of the electron isolation. These three scale factors are multiplied together to form the electron scale factor. More details on the measurement of electron efficiencies can be found in [65].

Events that have jets passing the JVT requirement have a JVT scale factor applied to them. The JVT scale factor accounts for the efficiency of the "medium" working point of the JVT algorithm. Details of the measurement of this efficiency can be found in [87].

A b-tag scale factor is applied to each event. This scale factor accounts for the efficiency differences between data and MC in the b-tagging efficiency for b, c, and light-flavor jets. The b-tag scale factor is computed using a pseudo-continuous b-tagging calibration [88]. This is necessary for performing the flavor fit and extracting the c-jet and light-flavor jet backgrounds from the flavor fit. This will be discussed further in the chapter 11. For each jet that passes the b-tagging selection, an efficiency scale factor is applied as a function of

the jet flavor, jet p_T (in the case of light-flavor jets, also jet η), and MV2c10 variable. A description of how these efficiencies are measured is given in [89].

7.6 Z Final State

We are only interested in events containing a single Z boson decaying leptonically to either an electron pair or muon pair. These events are selected by requiring exactly two "good" leptons of the same flavor which are oppositely charged. Where a good lepton is defined as an electron passing the event selection described in section 6.1 or a muon passing the event selection described in section 6.2. The invariant mass of the di-lepton pair is required to be within 76 GeV $< m_{ll} <$ 106 GeV.

As mentioned earlier top is a significant background in this analysis. To reduce it an additional selection cut is placed on the missing transverse energy. The cut requires $E_T^{miss} <$ 60 GeV and only applied if the transverse momentum of the Z boson is less than 150 GeV. A summary of the selection for Z boson candidate events is given in table 7.3.

Selection	Requirement
Number of leptons	exactly 2 good leptons, same flavor and oppositely charged
E_T^{miss}	$<$ 60 GeV if $p_T^Z < 150GeV$
mass window	76 GeV $< m_{ll} <$ 106 GeV

Table 7.3: Requirements to be considered Z Boson candidate.

Additionally, for each lepton flavor, we have two signal regions defined by the number of b-jets in the event. Where a b-jet is as defined in section 7.3.1. The "≥1b-jet region" is defined as events with at least 1 b-jet. The "≥2b-jets region" is defined as events with at least 2 b-jets. These will be referred to as the Z1B and Z2B signal regions.

Having defined the signal regions, the next two chapters will investigate some of the backgrounds. Chapter 8 investigates whether or not QCD multi-jet events are present in the signal region. The top background modeling is checked in validation regions in chapter 9.

Chapter 10 goes over the systematic uncertainties that are considered at the detector level. The flavor fit is then described in chapter 11 which includes how the systematic uncertainties are treated in the fit. Data is compared to the Monte Carlo predictions in chapter 12. Comparisons are made with and without the use of the scale factors extracted from the flavor fit.

CHAPTER 8

QCD MULTI-JET ESTIMATION

This chapter investigates whether or not QCD Multijet (MJ) events appear as a background in the signal region and shows that they do not.

QCD (MJ) events are events with multiple jets where the hard scatter only involves quarks and gluons with no electroweak vertices. A QCD event could enter this analysis if jets are misidentified as leptons. These fake leptons are largely suppressed by requiring the lepton to be isolated, however due to the large production cross section of QCD jets at the LHC it is possible that some of these types of events can be present in our signal region due to these jets faking leptons. The type of QCD events that can make it into the signal region can arise from heavy quark leptonic decays, conversions in the detector material, and hadrons in general. The simulation of such events is difficult to accurately model in MC. Instead, a data driven method is used to estimate the amount of MJ present in our signal regions.

In this thesis the number of events coming from QCD jets faking leptons in both the ee and $\mu\mu$ final sates are estimated from data using a template fit method. In this method, a MJ template is determined from a control region (CR) that consists of a data sample enriched in jets faking leptons. The template is then normalized in a normalization region (NR), which is selected to be similar to the signal region (SR) of the measurement, but background-enriched. The normalization is done using a maximum-likelihood template fit to the data in the NR, with templates for signal and backgrounds other than MJ being taken from MC simulation. The number of MJ events present in the signal region is then taken as the number of fake template events satisfying the SR selection multiplied by the resulting scale factor. The next two sections describe this procedure in more detail for the two different lepton channels.

8.1 Fake Estimate in the $Z \to \mu\mu$ channel

For the muon channel, the CR used to extract the MJ template is defined similar to the selection criteria of the signal region. The two differences are that in the CR the Z-mass cut is not applied and instead of requiring opposite-sign (OS) muons, two same-sign (SS) muons are required. In the CR the MJ template is estimated in a region inclusive in the number of jets and without counting b-jets ($\mu^{\pm}\mu^{\pm}+ \geq 1$ jet). The resulting CR is shown in fig. 8.1, comparing data and MC with the described selections. The difference seen in the number of events between data and MC suggests that the chosen CR is indeed enriched by MJ background.

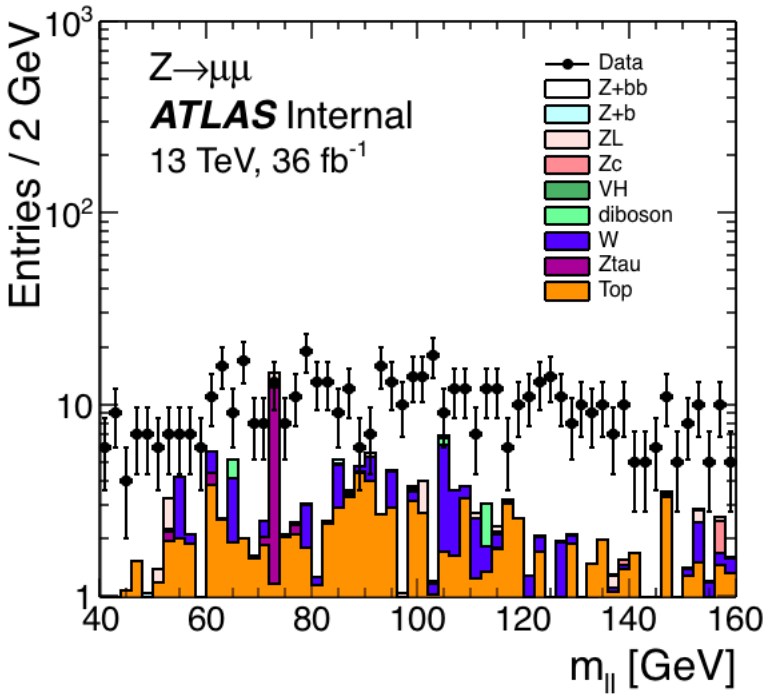

Figure 8.1: Comparison of data and MC in the MJ CR for the muon channel as a function of $m_{\mu\mu}$

The MJ template is extracted from the CR defined previously by subtracting the non-MJ backgrounds from the data $m_{\mu\mu}$ distribution shown in fig. 8.1. The normalization of

the MJ template is determined by fitting the invariant mass distribution in data in a NR. The NR is defined by the same selection that is used in the CR except that in the NR, OS muons are required as is required in the signal region. The fit is performed in the window 60 GeV $< m_{\mu\mu} <$ 160 GeV. In the fit, the template for MJ background is taken as described above, while the templates for all other backgrounds and signal are taken from MC. When fitting, the normalization for the MJ template is floating while the normalizations of the other templates have 5% Gaussian constraints. The resulting fit is shown in fig. 8.2.

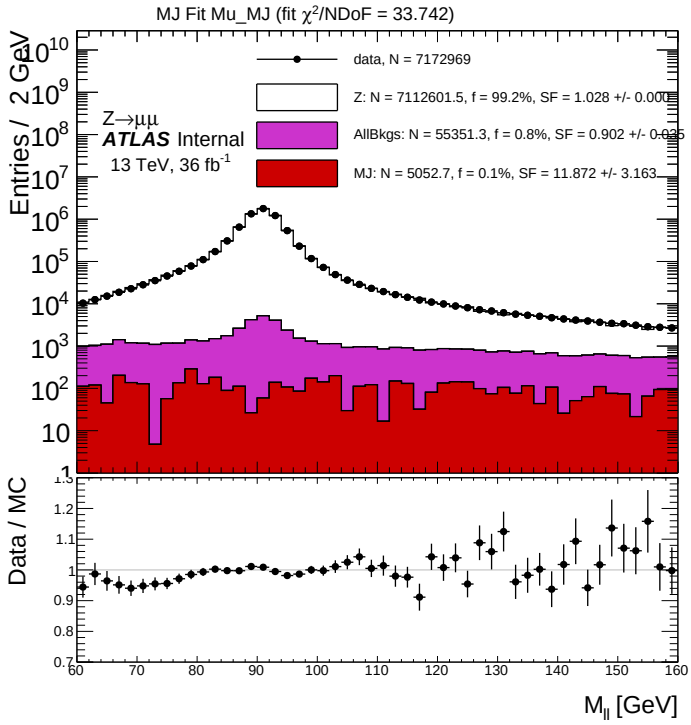

Figure 8.2: The MJ contribution in the muon channel estimated by a fit template on data in the mass range 60$GeV < m_{\mu\mu} <$ 160 GeV for inclusive jet multiplicities ($Z+ \geq 1$ jet) in the NR.

The amount of MJ in the two signal regions ($Z \to \mu\mu+ \geq 1$ b-jet and $Z \to \mu\mu+ \geq 2$ b-jets) is then obtained by applying the ≥ 1 and ≥ 2 b-tags requirement on top of the CR definition, subtracting off the electroweak contamination, and then scaling the resulting yield by the factor obtained from the fit in the NR. This method of estimating the MJ requires

the assumption that the shape of the MJ template is unchanged and that the ratio of OS muons to SS muons is the same for $Z+ \geq 1$ jet, $Z+ \geq 1$ b-jet, and $Z+ \geq 2$ b-jets selections.

For the $Z+ \geq 1$ b-jet region the MJ contribution was estimated to be 269 ± 1213 events which corresponds to 0.08% of data. While for the $Z+ \geq 2$ b-jets region, the MJ contribution was estimated to be 112 ± 239 events which corresponds to 0.52% of data. The uncertainty given is taken from the fit scaled by the reduced chi-square of the fit. These results confirm that the event selection used in this analysis are sufficient to reduce the QCD background.

As an alternative, the MJ normalization for the $Z(\rightarrow \mu\mu)+ \geq 1$,2 b-jets regions were also extracted by directly fitting in a NR with the corresponding b-tagging requirements. This resulted in a consistent estimate to the one using the other NR but less stable fit behavior.

In order to estimate the validity of the MJ estimation, the procedure was performed using different definitions of the CR from which the MJ template was extracted from. The alternative CRs that were looked are listed below:

- 2 OS muons both with reversed d_0 significance selection ($|d_0 sigBL| > 3$)
- 2 OS muons with one passing the reversed d_0 significance selection ($|d_0 sigBL| > 3$)
- 2 SS muons with one passing the reversed d_0 significance selection ($|d_0 sigBL| > 3$)

The first alternative CR selection suffered from very low statistics. The second was affected by a large contamination of signal events around the Z peak. The third alternative CR provided a MJ estimate close to zero (close here meaning much smaller than 0.1% of data) and was consistent with the nominal result.

In addition to looking at alternative CRs, other variations of the procedure were performed. The other variations include:

- Varying the fitting di-muon mass range
- Allowing the top background and all other other background components to vary independently in the fit (still with the Gaussian constraint)

Signal Region	Number of Multijet events	Fraction to Data (MJ/Data)
Nominal procedure		
≥ 1	269 $\pm$ 1213 (stat)	0.08%
≥ 2	112 $\pm$ 239 (stat)	0.52%
mass range 40–160 GeV		
≥ 1	211 $\pm$ 1084 (stat)	0.07%
≥ 2	92 $\pm$ 213 (stat)	0.43%
Independent SFs for Top/W/Other		
≥ 1	5 $\pm$ 180 (stat)	0.00%
≥ 2	3 $\pm$ 232 (stat)	0.01%
Binning $\times 2$ finer		
≥ 1	332 $\pm$ 929	0.11%
≥ 2	139 $\pm$ 183	0.64%
Binning $\times 2$ larger		
≥ 1	85 $\pm$ 1786	0.03%
≥ 2	39 $\pm$ 352	0.18%
Exclude Z peak region		
≥ 1	312 $\pm$ 817	0.10%
≥ 2	145 $\pm$ 135	0.67%

Table 8.1: Multijet event yield and fraction to data in the two signal regions of the $Z \to \mu\mu$ channel.

- Varying the binning of the templates
- Excluding the Z peak region (76 GeV $< m_{\mu\mu} <$ 106 GeV) from the fit and extrapolation to the Z mass region assuming flat shape of the template (similar to the nominal procedure in the electron channel described below)

The resulting MJ yields in the signal regions from the modifications to the nominal procedure are given in table 8.1. The results are all consistent with zero. From these results the overall impact of the MJ contribution on the cross-section measurement can be taken as negligible and is not considered further in the analysis procedure.

8.2 Fake Estimate in the $Z \to ee$ channel

The estimating of the MJ present in the electron channel follows a similar procedure to that described for the muon channel. As was done for the muon channel, several control regions were studied. Common among these CR was the requirement of two SS electrons without the mass cut, and without the d_0 significance requirement ($|d_0 sigBL| < 5$). The control regions were differentiated by the following requirements on the electrons:

- Both electrons fail the isolation cut
- Both electrons fail the isolation cut and are loose
- The isolation requirement is not applied
- One electron is loose and fails the tight identification and the isolation is not applied
- One electron fails both the identification (it is loose failing tight) and the isolation requirement.

Of these CR, only one provided a sizeable MJ contribution to the m_{ee} template. Here, sizeable meaning that there was significant excess of data over estimated MC electroweak contribution and that it was positive over most of the m_{ee} range. The CR that gave this was the one that required both electrons to fail the isolation requirement without applying the identification cut. This CR is shown in fig. 8.3 comparing the m_{ee} distributions in data and MC as well the resulting MJ template. As can be seen, the CR still has a significant contribution at the Z peak which is not reliably subtracted by using MC. As a result, the Z peak region (76 GeV $< m_{ee} <$ 106 GeV) is excluded when fitting the MJ template.

Following the procedure for the muon channel, a fit is performed in a NR using the MJ template. The NR is defined as inclusive in the number of jets with the nominal electron selection and a wider mass window (60 GeV $< m_{ee} <$ 160 GeV) excluding the Z peak. The resulting fit is shown in fig. 8.4.

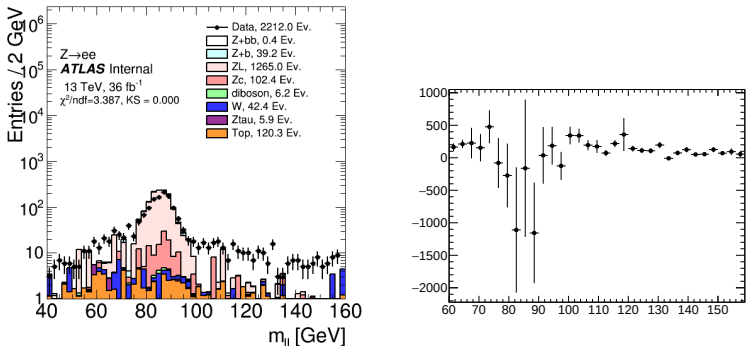

(a) (b)

Figure 8.3: Comparison of data and MC in the MJ CR for the electron channel as a function of m_{ee}(a). The MJ template shape after subtracting the electroweak contribution MC estimates from the data (b).

In order to estimate the MJ contribution in the signal region with ≥ 1 (2) b-jets, the ≥ 1 (2) b-tag requirements are applied on top of the CR definition. The electroweak contamination is then subtracted and the resulting yield is scaled by the factor obtained from the fit in the NR. This gives the yield outside the Z mass peak. In order to get the yield inside the Z peak, the linear shape of the MJ template outside of the Z peak is assumed through the Z peak and this yield is extrapolated into the signal mass region ($76 < m_{ee} < 106$ GeV). This procedure gives a MJ yield of 150 ± 286 for the $\geq 1b - jet$ region and 11 ± 21 for the $\geq 2b - jets$ region. This corresponds to approximately 0.1% of data.

Similar to the muon channel, the MJ yields are estimated with variations to the procedure. The resulting MJ estimates are shown in table 8.2 along with the nominal procedure. The results are all consistent with zero and, hence, consistent with each other. Therefore, as was the case in the muon channel, the contribution of this background is negligible and is not considered further in this analysis.

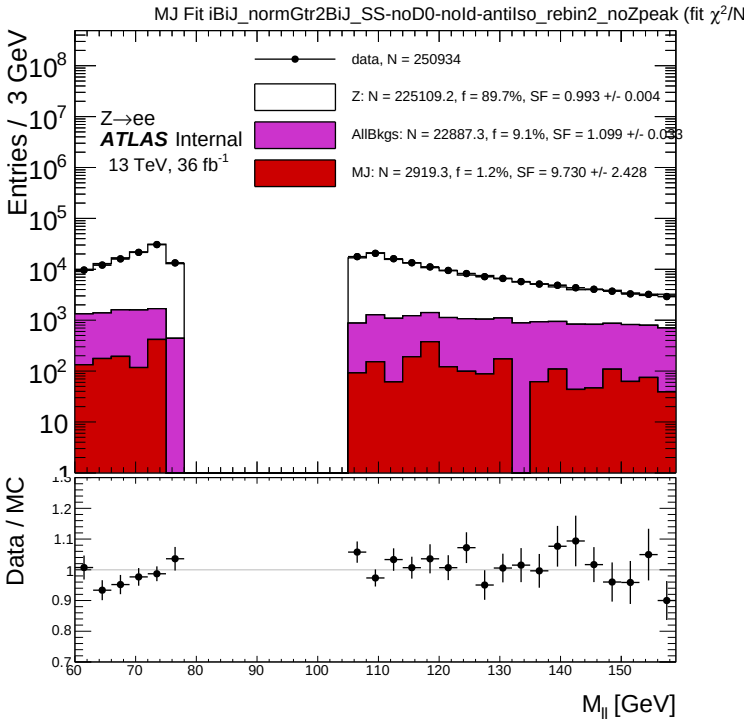

Figure 8.4: The MJ contribution in the electron channel estimated by a fit template on data in the mass range $60 < m_{\mu\mu} < 160$GeV (excluding the Z peak $76 < m_{ee} < 106$ GeV) for inclusive jet multiplicities.

Signal Region	Number of Multijet events	Fraction to Data (MJ/Data)
Nominal procedure		
≥ 1	150 $\pm$ 286 (stat)	0.08%
≥ 2	11 $\pm$ 21 (stat)	0.07%
Lower fit bound down to 40 GeV		
≥ 1	96 $\pm$ 255 (stat)	0.05%
≥ 2	3 $\pm$ 15 (stat)	0.02%
Independent SFs for Top/W/Other		
≥ 1	127 $\pm$ 283 (stat)	0.06%
≥ 2	9 $\pm$ 21 (stat)	0.06%
Perform the fit in $\geq 1/2b$ region rather than in the inclusive one		
≥ 1	58 $\pm$ 47	0.03%
≥ 2	1 $\pm$ 1	0.01%
Binning $\times 3$ finer		
≥ 1	78 $\pm$ 151 (stat)	0.04%
≥ 2	6 $\pm$ 11 (stat)	0.04%
Binning $\times 2$ larger		
≥ 1	237 $\pm$ 428 (stat)	0.12%
≥ 2	18 $\pm$ 29 (stat)	0.12%

Table 8.2: Multijet event yield and fraction to data in the two signal regions of the $Z \to ee$) channel.

CHAPTER 9

TOP BACKGROUND MODELING AND VALIDATION

The di-top and single-top production are one of the larger sources of background for the measurement of a vector boson plus b-jets produced in QCD interactions because of the similar signature that arises from the $t \to Wb$. For example, di-top events where both W bosons decay leptonically will have a final state that can mimic $Z \to$. As a result, some of the cuts for event selection are used implemented to reduce the contamination coming from top-quark events. For example, the requirement of same-flavor oppositely charged leptons or the requirement of $E_T^{miss} < 60$ GeV for $p_T^Z < 150$ GeV both reduce top background.

Although the cuts used in event selection reduce the top background present in this analysis, a large amount is still present and must be correctly modeled in the background subtraction and the measurement of the unfolded $Z+b(b)$ cross section. As mentioned in section 5.2, $t\bar{t}$ is modeled using Powheg+Pythia8 and single-top is modeled using Powheg+Pythia6. Systematics associated with the top modeling and cross section uncertainties will be described in more detail in section 10.3.

The top-modeling is validated using dedicated validation regions (VR) which are defined to be close to the nominal region but where the top-background is enhanced. These VR are defined to mainly enhance $t\bar{t}$ because of its larger cross section compared to single-top. The VR is defined almost identically to the signal region except it removes the same flavor lepton requirement and instead requires different flavor leptons. The use of different flavor leptons allows for the selection of a very pure sample of dileptonic $t\bar{t}$ decays with kinematic characteristics very close to the top background events entering in the nominal selection. The top modeling in the VR for the ≥ 1 and ≥ 2 b-jet selections are shown in fig. 9.1 and fig. 9.2, respectively. Included in the systematics in the plots are the top systematics described in section 10.3.

One can see from the plots that the agreement in the VR is good for the nominal samples

that are used in this thesis and that the differences between data and MC are contained in the top-simulation uncertainties that will be further described in section 10.3.

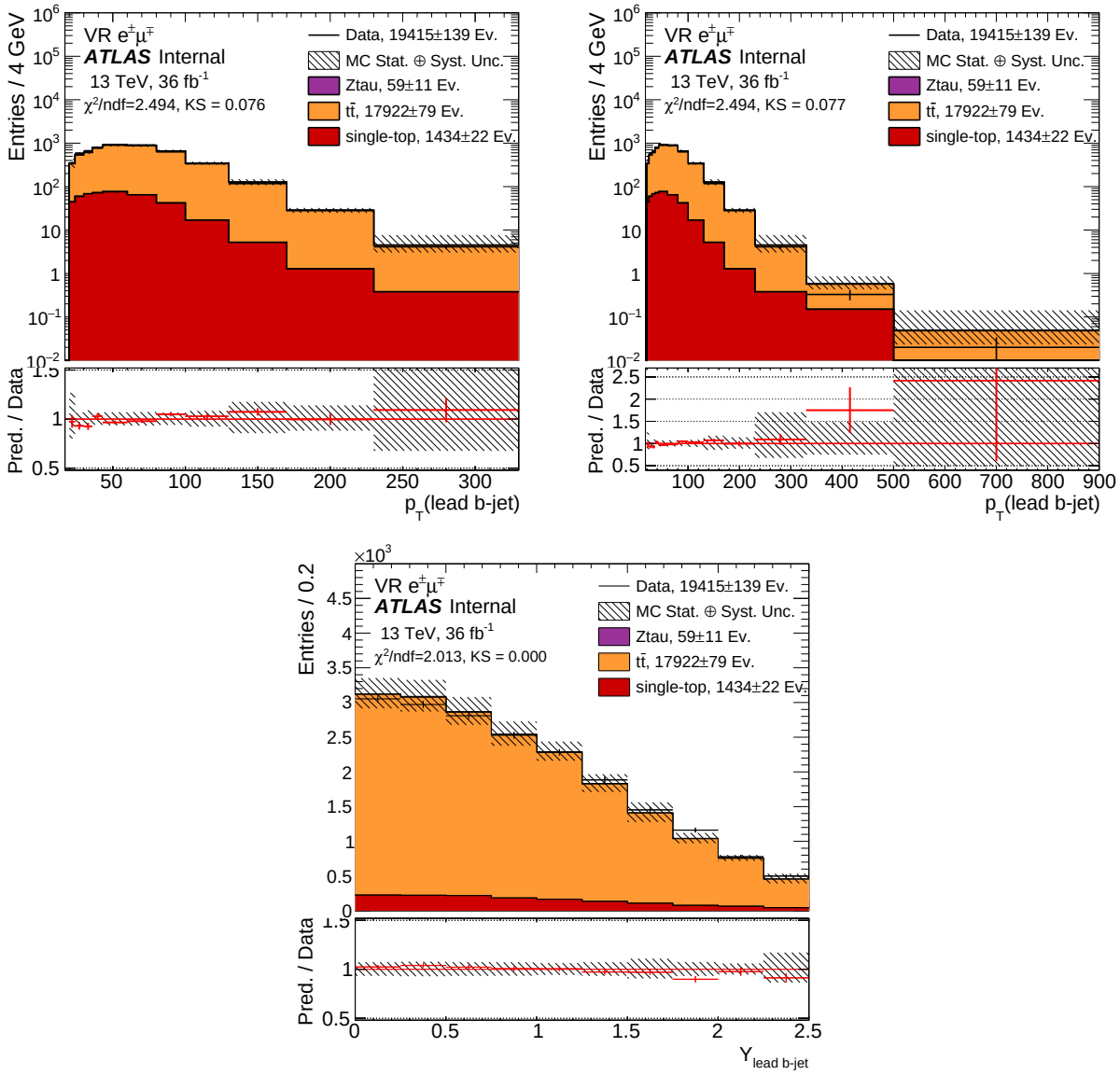

Figure 9.1: Background estimate modeling in the Top VR for the $Z + b(b)$ channel (defined by the different flavor lepton requirement) for ≥ 1 b-jet selection. Top Left:p_T of the leading b-jet in the first part of the spectrum. Top Right: p_T of the leading b-jet in the full spectrum to appreciate the tails. Bottom: Rapidity ,Y, of the leading b-jet. The $t\bar{t}$ systematic uncertainties described in section 10.3 are included in the dashed band.

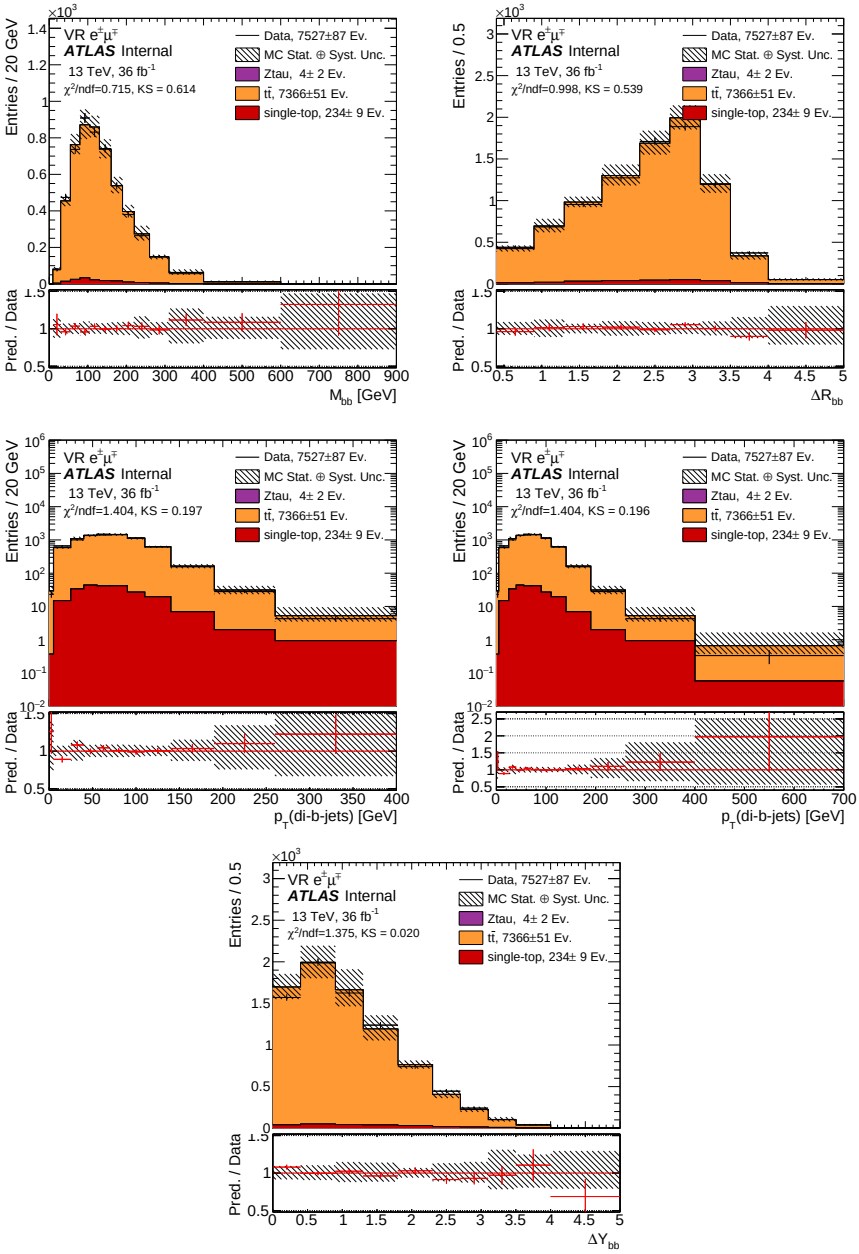

Figure 9.2: Background estimate modeling in the Top VR for the $Z + b(b)$ channel (defined by the different flavor lepton requirement) for $\geq 2b$-jets selection. Top Left: di-jet invariant mass. Top Right: di-jet ΔR. Center Left: di-jet p_T in the first part of the spectrum. Center Right: di-jet p_T in the full spectrum to appreciate the tails. Bottom: di-jet ΔY. The $t\bar{t}$ systematic uncertainties described in section 10.3 are included in the dashed band.

CHAPTER 10

SYSTEMATIC UNCERTAINTIES AT DETECTOR LEVEL

10.1 Detector Systematics

In this chapter the systematic uncertainties related to object reconstruction will be described. The systematic uncertainty is evaluated by varying the corresponding variable associated with the effect by one standard deviation. This results in two different distributions of the event yields, an up variation ($+1\sigma$) and a down variation (-1σ) with respect to the nominal distribution. A few of the systematic uncertainties have only one variation, for example the jet energy resolution (JER), in which case the uncertainty is symmetrized around the nominal distribution. These uncertainties are summed in quadrature to obtain the total systematic uncertainty shown in the plots in chapter 12. Their treatment in the flavor fit and unfolding will be discussed further in those corresponding sections.

10.1.1 Jets

The uncertainty in the jet energy scale calibration is originally made up of 88 components that have been propagated from the individual calibrations and studies that are performed to arrive at the final jet energy scale [90]. The majority (75) of these components come from the in situ calibrations and account for assumptions made in the event topology, MC simulation, sample statistics, and the propagated uncertainties of the electron, muon, and photon energy scales. The remaining components come from the following:

- 3 components come from the eta-intercalibration
- 4 components come from pile-up corrections
- 1 component comes from the behavior of high-p_T jets using single-hadron response

- 1 component for non-closure in the absolute JES calibration of fast-simulation jets (only applies when using MC samples that have used fast-sim to model detector response instead of full-sim)
- 3 components to account for flavor response and composition
- 1 component to account for punch-through jets

In order to decrease computations the original 75 components that come from the in situ calibrations are reduced to 8 parameters using a global reduction scheme [91]. An eigen-decomposition of these 75 components is performed. The eignenvectors corresponding to the 7 largest eigenvalues are kept as independent parameters and the remaining components are quadratically combined into a single parameter. This reduction results in only a few percent loss in correlation information between jets. The remaining 21 parameters describing the uncertainty in the jet energy scale are treated as independent.

Another uncertainty comes from the jet energy resolution. This uncertainty is derived by comparing the resolution in data to the resolution is MC. This uncertainty is described by a single parameter. There is also an uncertainty associated with the JVT scale factor. It is also described by a single parameter.

10.1.2 b-tagging

A description of the measurement of the b-tagging efficiencies is given in [89]. The systematic uncertainties associated with b-tagging are split according to jet flavors to account for the different efficiency calibration procedures that are used. The number of individual parameters that are used to describe the uncertainty in b-tagging is on the order of 50 for each flavor. The number of individual parameters is large not just because of the number of systematic uncertainties associated with each calibration method, but because each calibration bin contributes an individual statistical error, and calibrations are extracted in bins

of jet p_T (in the case of light-flavor jets, also jet η) and bins of the MV2c10 discriminant. An eigen-decomposition is performed, similar to the one done for the JES systematics, in order to reduce the number of variations that need to be evaluated in this analysis. This is implemented in the analysis by using a tool provided by the flavor tagging group. The medium reduction scheme is used which results in a total of 28 parameters for b-jets, 28 for c-jets, and 36 for light-flavor jets. This reduction results in only a few percent loss in correlation information.

10.1.3 Electrons

There are several sources of uncertainty associated with electrons. The first source comes from the scale factors used to correct the electron's reconstruction, identification, isolation, and trigger efficiencies. The measurement of these efficiencies as well as their uncertainties is described in [65]. A single parameter for each efficiency scale factor is used to describe its uncertainty. The total uncertainty coming from the efficiency corrections is around 1%. The other sources of uncertainty comes from the measurement of the electron energy scale and resolution and are described in [70]. Again, each uncertainty is described by a single parameter. The uncertainty in the electron energy scale and resolution is approximately 0.2%. To summarize, the uncertainty coming from electrons is broken down into six parameters, one parameter for each of the four scale factors, one parameter for the electron energy scale, and one parameter for the electron energy resolution.

10.1.4 Muons

The uncertainties associated with muons are very similar to those of electrons with a few additions. The first sources come from the uncertainties in the scale factors used to correct the muons identification, isolation, track to vertex association, and trigger efficiencies. Each of these sources of uncertainty is described with a single parameter. Another source of

uncertainty for muons is the uncertainty in the measurement of its momentum scale and resolution. The uncertainty in the momentum scale is described by a single parameter, however the uncertainty in the momentum resolution is divided into two components that are treated independently. The two components are the momentum resolution in the Inner Detector and the momentum resolution in the Muon Spectrometer. Another source of uncertainty comes from the sagitta-bias correction that is described in [92]. The total systematic uncertainty contributed by muon reconstruction at the detector level is less than 1%.

10.1.5 Missing Transverse Energy

As mentioned in section 6.5, E_T^{miss} is composed of a hard term and soft term. The hard term is made up of the jets, muons and electrons that pass event selection. The effects of the resolution and scale on E_T^{miss} coming from these objects own resolution and scale is taken into account by recalculating E_T^{miss} when considering these systematic variations on the hard objects. This results in the uncertainty of E_T^{miss} resolution and scale being implicitly included in the resolution and scale of the hard objects. The uncertainties associated with the resolution and scale of the soft term of E_T^{miss} are evaluated by comparing MC to data as described in [85].

10.2 Luminosity and Pileup Reweighting

Two other sources of systematic uncertainties at the detector level come from the luminosity measurement and pileup reweighting. The uncertainty from pileup reweighting is calculated by shifting the weighting factor up and down by 0.09. The uncertainty on the combined integrated luminosity that corresponds to the 2015 and 2016 datasets is 2.1%. A description of the measurement of the luminosity as well as it uncertainty can be found in [93].

10.3 Top Background Modeling

The largest source of background comes from Z+c-jets and Z+light-flavored jets. The next largest background contribution comes from top production because it can produce the same final state as the signal. For this reason it is important to evaluate systematics associated with its modeling. The uncertainty on the production cross-section is taken as scaling uncertainty on the overall normalization of the nominal top samples. A summary of the cross sections for top pair production and the three single top channels is given in table 10.1.

Sample	Central Value (pb)	Scale Uncertainty	PDF Uncertainty
$t\bar{t}$	831.76	+19.77 -29.20	+35.06 -35.06
single top t-channel	216.99	+6.62 -4.64	+6.16 -6.16
single top Wt-channel	71.7	+1.80 -1.80	+3.40 -3.40
single top s-channel	10.32	+0.29 -0.24	+0.27 -0.27

Table 10.1: Top Production Cross Sections.

Three different systematics uncertainties are considered for the modeling of the top background. The modeling of the hard scatter, parton shower, and the amount of radiation. The systematic uncertainties are evaluated by comparing top samples generated using different configurations.

10.3.1 $t\bar{t}$ Samples

As described in section 5.2 the nominal $t\bar{t}$ sample is Powheg+Pythia8. The systematic uncertainty from the modeling of the hard scatter is determined by comparing events generated with Powheg to those generated with MadGraph5_aMC@NLO and both using the same parton shower model. Samples generated with Powheg are showered using Pythia8 and Herwig7 to determine the systematic uncertainty on the parton shower model. To determine the effect of the modeling of the amount of radiation Powheg+Pythia8 samples are produced with a different tune and scale variations to give higher and lower amounts of radiation. For the

radiation samples, the variations are halved since we are comparing two shifted samples and not to the nominal sample. The samples compared are summarized in table 10.2.

Modeling Source	First Sample (MCID)	Second Sample (MCID)
Hard Scatter Generator	Powheg+Pythia8, FullSim (410501)	aMcAtNlo+Pythia8, FullSim (410225)
Parton Shower Model	Powheg+Pythia8, AFII (410501)	Powheg+Herwig7, AFII (410525)
3*Additional Radiation	Powheg+Pythia8, AFII (410511) Powheg hdamp=3.0* top mass A14 tune var3c up,scale =0.5	Powheg+Pythia8, AFII (410512) Powheg hdamp=1.5* top mass A14 tune var3c down,scale =2.0

Table 10.2: Samples compared for modeling systematics in $t\bar{t}$

10.3.2 Single top Samples

For single top the nominal samples are generated using Powheg+Pythia6. Single top is divided into three separate channels: s-channel, t-channel, Wt-channel. As is done for $t\bar{t}$, the systematic uncertainty from the modeling of the hard scatter is determined by comparing events generated with Powheg to events generated with MadGraph5_aMC@NLO using the same parton shower model, namely Herwigpp. Similarly to $t\bar{t}$, samples generated with Powheg are showered using Pythia6 and Herwigpp to determine the systematic uncertainty on the parton shower model. The effect of the modeling of the amount of radiation is also determined similarly to what is done for $t\bar{t}$. For the s-channel samples are only available to look at the systematic uncertainty from the modeling of the amount of radiation. However, the s-channel is a very small background. For the Wt-channel a fourth systematic is considered because of interference at NLO with top-quark pair production. Different methods for treating this interference are used. The nominal sample used in this analysis uses the diagram removal scheme(DR). The systematic uncertainty associated with using this scheme is determined by comparing it with a sample produced using the diagram subtraction (DS) scheme. The samples compared for the modeling of the different single top channels are summarized in tables 10.3 to 10.5.

Table 10.3: Samples compared for modeling systematics in single top t-channel

Modeling Source	First Sample (MCID)	Second Sample (MCID)
Hard Scatter Generator	Powheg+Herwigpp (410047+410048)	aMcAtNlo+Herwigpp (4100141)
Parton Shower Model	Powheg+Pythia6 (410011+410012)	Powheg+Herwigpp (410047+410048)
2*Additional Radiation	Powheg+Pythia6 (410018+410020) Perugia 2012 radHi tune, scale=0.5	Powheg+Pythia6 (410017+410019) Perugia 2012 radLo tune, scale=2.0

Table 10.4: Samples compared for modeling systematics in single top Wt-channel

Modeling Source	First Sample (MCID)	Second Sample (MCID)
Hard Scatter Generator	Powheg+Herwigpp (410145+410146)	aMcAtNlo+Herwigpp (4100164)
Parton Shower Model	Powheg+Pythia6 (410013+410014)	Powheg+Herwigpp (410147+410148)
2*Additional Radiation	Powheg+Pythia6 (410099+410101) Perugia 2012 radHi tune, scale=0.5	Powheg+Pythia6 (410100+410102) Perugia 2012 radLo tune, scale=2.0
Single-Top Interference	Powheg+Pythia6 DR scheme (410013+410014)	Powheg+Pythia6 DS scheme (410062+410063)

Table 10.5: Samples compared for modeling systematics in single top s-channel

Modeling Source	First Sample (MCID)	Second Sample (MCID)
2*Additional Radiation	Powheg+Pythia6 (410107+410109) Perugia 2012 radHi tune, scale=0.5	Powheg+Pythia6 (410108+410110) Perugia 2012 radLo tune, scale=2.0

10.3.3 Top Background Systematics

Single top production contributes a very small amount to the background estimate in the signal regions of the Z analysis. It makes up approximated 0.3% of the total data yields in the $\geq$ 1b-jet signal region and approximately 0.6% of the total data yields in the $\geq$ 2b-jets signal region. As a result, it was checked that the impact of the different single top sample variations described above gave a negligible impact on the background estimates and only the uncertainty on production cross-sections were taken as a systematic uncertainty on the single top background yield.

For top-quark pair production, this is not the case. As was mentioned at the beginning of this section, top production is was one of the most significant backgrounds contributing to the signal region and this is almost exclusively coming from the top-quark pair production. In the $\geq$ 1b-jet signal region approximately 4% of the total data yield comes from $t\bar{t}$ and in the $\geq$ 2b-jets signal region $t\bar{t}$ contributes even a larger fraction to the data yield at approximately 20%. Because of the size of this contribution, uncertainties on both the shape and rate are included for $t\bar{t}$ using the samples described above.

The effects of these top systematics on the total background estimates are shown in fig. 10.1 for both lepton channels and both signal regions for two different variables.

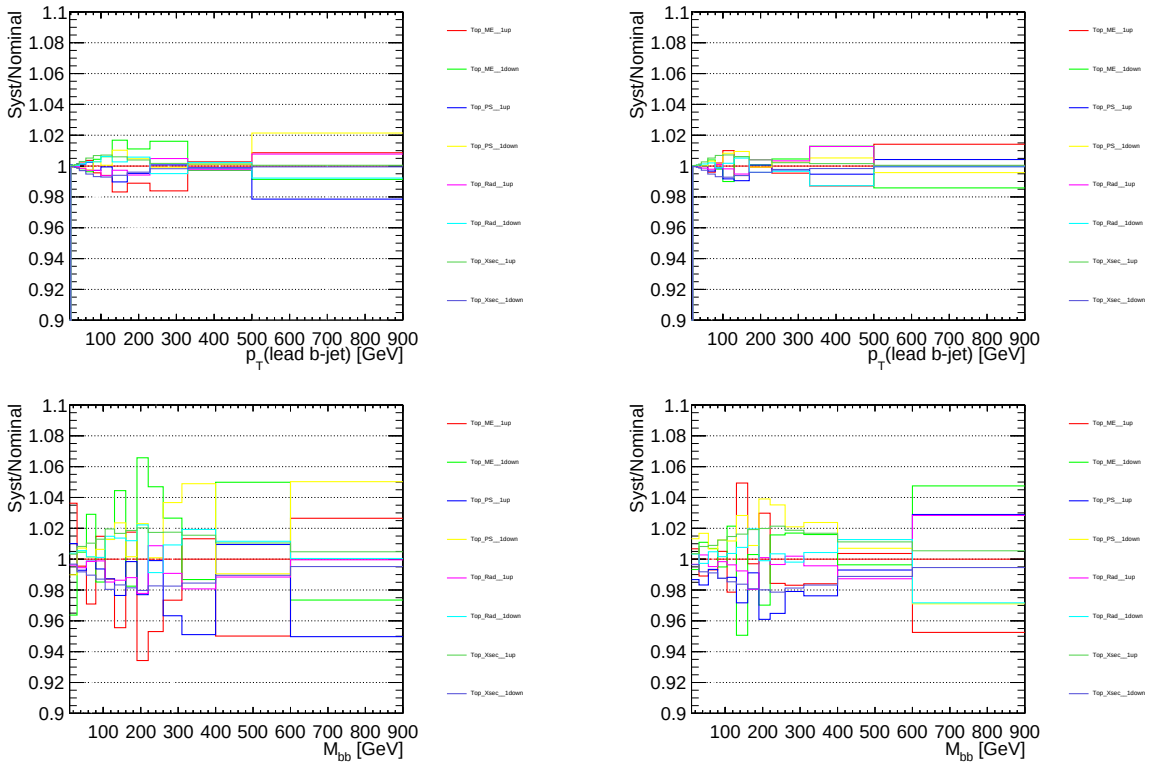

Figure 10.1: Relative variation of the total background estimate in the electron (left) and muon (right) channels, for the $\geq 1b$-jet signal region, leading b-jet p_T (top), and for the $\geq 2b$-jets signal region, di-b-jet invariant mass (bottom) distributions. Both shape and rate variations are applied to the $t\bar{t}$ estimate, while only rate variations are applied to the single top estimate.

CHAPTER 11

FLAVOR FIT

To motivate the use of the flavor fit a few distributions comparing MC predictions to data are shown in fig. 11.1 at the detector level using the selections described in chapter 7. Shown are the lead b-jet p_T distributions in the Z + $\geq 1b$-jet signal region as well as the invariant mass of the 2 leading b-jets in the Z + $\geq 2b$-jets signal region for both lepton channels. As can be seen the agreement qualitatively looks alright, but that it varies strongly depending on the generator that is used. This is further illustrated in Tables 11.1, 11.2, 11.3, and 11.4, which shows the prefit yields of the different processes passing event selection. There, it is easy to see how the flavor composition differs among the choice in generator used. As a result a flavor fit is necessary so that the different flavor components predicted by the different generators can be corrected to give the best description of the data. The objective of the flavor fit is to determine the normalizations of the different flavor components and calculate scale factors that can applied to the detector level distributions chapter 12 and also propagated to the unfolding procedure chapter 13.

This is done using a binned likelihood fit to extract the normalizations of the different components of the Z+jets samples. The fits are done separately in the two signal regions: the Z +$\geq 1b$-jet signal region (Z1B), and the Z +$\geq 2b$-jets signal region (Z2B). The fit is also performed separately in the electron and muons channels as well as by combining the electron and muon channels. The compatibility of the individual lepton channel fits is compared to the combined lepton fit.

The detector level systematics described in chapter 10 are propagated through the fit using the offset method. The fit is rerun for each systematic variation and the resulting scale factors extracted are then propagated to the unfolding procedure.

In the following sections scale factors are determined for both the signal components and background components of the Z+jets samples. Only the scale factors associated with the

background components are applied to the inputs prior to unfolding. The signal components are not scaled by the flavor fit scale factors prior to unfolding because their cross sections are obtained from the unfolding procedure.

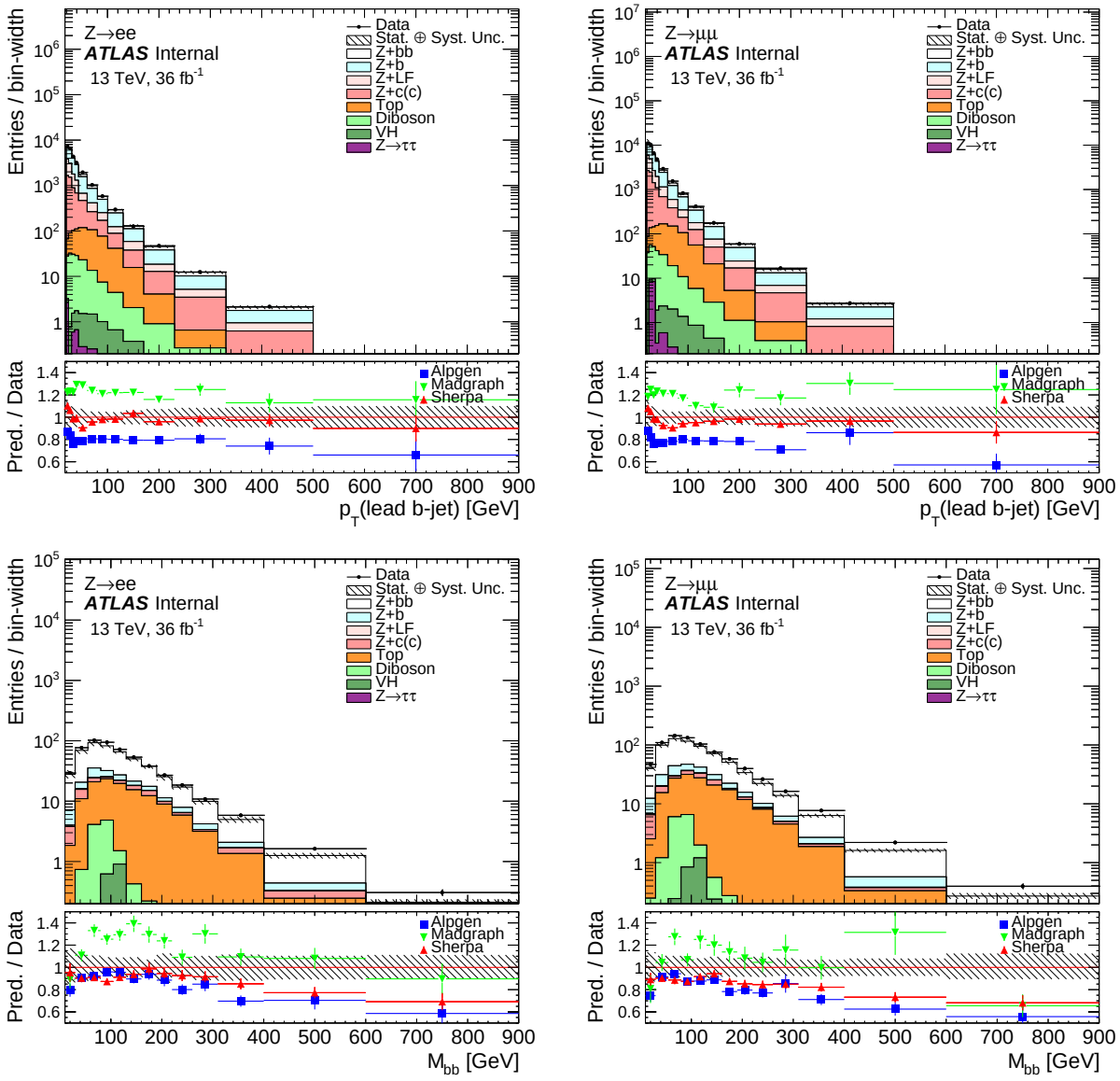

Figure 11.1: Comparison of Data and Monte Carlo predictions for the leading b-jet p_T in the $\geq 1b$-jet signal region (top) and the invariant mass of the 2 leading b-jets in the $\geq 2b$-jets signal region (bottom) for the electron channel (left) and muon channel (right). The comparison to data in the top part of the plots is to the Sherpa samples while ratio of predicted over data in the bottom part of the plots shows the comparison to data for all three generators (Sherpa, Alpgen, and Madgraph).

Sample	Sherpa	Alpgen	MadGraph
single top Wt-channel	596.9 ± 13.7		
single top t-channel	6.4 ± 1.5		
single top s-channel	0.3 ± 0.1		
ttbar	7615.2 ± 51.2		
VH	101.2 ± 0.3		
diboson	1650.2 ± 12.6		
W+Jets Background	0.9 ± 2.3	9.3 ± 6.1	9.8 ± 2.8
Z+c(c)	37751.3 ± 611.1	44327.3 ± 651.9	45759.0 ± 619.0
Z+L	38651.3 ± 1532.3	24940.2 ± 463.7	28483.6 ± 1104.3
Z+1b	96211.3 ± 529.6	64951.5 ± 373.9	137746.7 ± 933.8
Z+≥2b	17288.4 ± 143.3	16895.2 ± 181.6	26127.1 ± 316.8
Z+tau	32.4 ± 7.5	6.3 ± 2.5	32.4 ± 7.5
predicted	199906.4 ± 1739.4	161100.5 ± 903.3	248129.4 ± 1605.7
data	199520.0 ± 446.6		

Table 11.1: Pre-fit event yields of the different processes and data for the three different generators used for Z+jets and W+jets for the electron channel in the Z + $\geq 1b$-jet signal region. A row with only one column indicates that the process does not depend on the generator used for Z+jets.

11.1 Theoretical Fit Model

The binned likelihood function, $L(\mu, \theta)$, that is used to fit the MC to data is defined as:

$$L(\mu, \theta) = \prod_{i=1}^{N} \frac{(\mu s_i + b_i)^{n_i}}{n_i!} e^{-(\mu s_i + b_i)}, \quad (11.1)$$

where N is the number of bins, μ is the signal strength parameter, s_i is the number of signal events in bin i, b_i is the number of background events in bin i, and n_i is the number of measured events in bin i. The nuisance parameters, θ, are used in the fit to describe the normalizations on the different backgrounds as well as the statistical uncertainties on the MC. Both s_i and b_i are functions of the nuisance parameters. All nuisance parameters are treated as being uncorrelated and have a factorized form in the likelihood. More details on the fit can be found in [94].

Sample	Sherpa	Alpgen	MadGraph
single top Wt-channel	800.6 ± 16.3		
single top t-channel	2.7 ± 0.9		
single top s-channel	0.2 ± 0.1		
ttbar	10533.7 ± 61.6		
VH	140.6 ± 0.3		
diboson	2369.2 ± 15.2		
W+Jets Background	1.1 ± 1.1	1.0 ± 0.6	4.8 ± 1.4
Z+c(c)	59105.0 ± 788.5	65880.0 ± 832.7	68180.1 ± 1153.8
Z+L	58004.6 ± 1844.2	40387.7 ± 691.0	44636.5 ± 1758.2
Z+1b	141637.8 ± 672.9	95652.9 ± 459.6	199489.9 ± 1605.3
Z+≥2b	24240.6 ± 198.4	23644.3 ± 226.5	35840.1 ± 769.1
Z+tau	121.8 ± 61.7	36.2 ± 10.9	121.8 ± 61.7
predicted	296958.4 ± 2126.8	239449.7 ± 1199.1	362120.7 ± 2756.7
data	300125.0 ± 547.8		

Table 11.2: Pre-fit event yields of the different processes and data for the three different generators used for Z+jets and W+jets for the muon channel in the Z + ≥ 1b-jet signal region. A row with only one column indicates that the process does not depend on the generator used for Z+jets.

Sample	Sherpa	Alpgen	MadGraph
single top Wt-channel	101.6 ± 6.0		
single top t-channel	0.2 ± 0.2		
single top s-channel	0.0 ± 0.0		
ttbar	3159.7 ± 33.4		
VH	38.6 ± 0.1		
diboson	266.9 ± 4.8		
W+Jets Background	0.2 ± 0.1	0.3 ± 0.3	0.4 ± 0.2
Z+c(c)	609.2 ± 79.3	723.9 ± 79.6	539.2 ± 54.8
Z+L	53.5 ± 0.1	26.5 ± 0.0	28.5 ± 0.1
Z+1b	1109.2 ± 61.9	775.3 ± 55.0	975.0 ± 92.0
Z+≥2b	8323.7 ± 95.4	8382.7 ± 130.3	13463.5 ± 231.1
Z+tau	1.2 ± 0.7	0.0 ± 0.0	1.2 ± 0.7
predicted	13664.7 ± 142.9	13476.2 ± 165.9	18575.4 ± 257.0
data	15017.0 ± 122.5		

Table 11.3: Pre-fit event yields of the different processes and data for the three different generators used for Z+jets and W+jets for the electron channel in the Z + ≥ 2b-jet signal region. A row with only one column indicates that the process does not depend on the generator used for Z+jets.

Sample	Sherpa	Alpgen	MadGraph
single top Wt-channel	123.3 ± 6.4		
single top t-channel	0.3 ± 0.3		
single top s-channel	0.0 ± 0.0		
ttbar	4314.6 ± 40.0		
VH	53.3 ± 0.2		
diboson	377.3 ± 5.5		
W+Jets Background	0.1 ± 0.1	0.0 ± 0.0	0.2 ± 0.2
Z+c(c)	766.9 ± 118.4	849.8 ± 100.2	893.7 ± 148.1
Z+L	82.4 ± 0.2	40.9 ± 0.0	44.0 ± 0.1
Z+1b	1795.2 ± 79.3	1082.3 ± 66.1	1746.2 ± 205.1
Z+≥2b	11507.2 ± 124.2	11595.8 ± 151.5	16826.3 ± 498.9
Z+tau	0.1 ± 1.4	3.5 ± 2.1	0.1 ± 1.4
predicted	19021.2 ± 193.4	18441.6 ± 197.6	24379.8 ± 560.8
data	21531.0 ± 146.7		

Table 11.4: Pre-fit event yields of the different processes and data for the three different generators used for Z+jets and W+jets for the muon channel in the Z + $\geq$ 2b-jet signal region. A row with only one column indicates that the process does not depend on the generator used for Z+jets.

11.2 Choice of Discriminant Variable

In order to extract the normalizations of the flavor composition of the Z+jets samples the fit needs to be performed on a variable that can discriminate between the flavor composition. The obvious choice is to use the output of the b-tagging algorithm described in section 6.4, the MV2c10 weight. The definition of the different working points are given in table 6.1. The binning of the MV2c10 is done to coincide with the fixed cut work points. Each bin will be referred to as a quantile. For example, the 70% quantile bin would contain events with 0.8244 <MV2c10< .9349, where as the 50% quantile bin would contain events with 0.9769 <MV2c10<1.

For the Z1B signal region there are three quantile bins: 70, 60 and 50. The quantiles use the MV2c10 weight of the leading b-tagged jet. In fig. 11.2 the distribution of MV2c10 is shown in these quantiles for both the electron and muon channel. Here it can be seen how well the MV2c10 weight is at discriminating between the flavor composition of the Z+jet

sample.

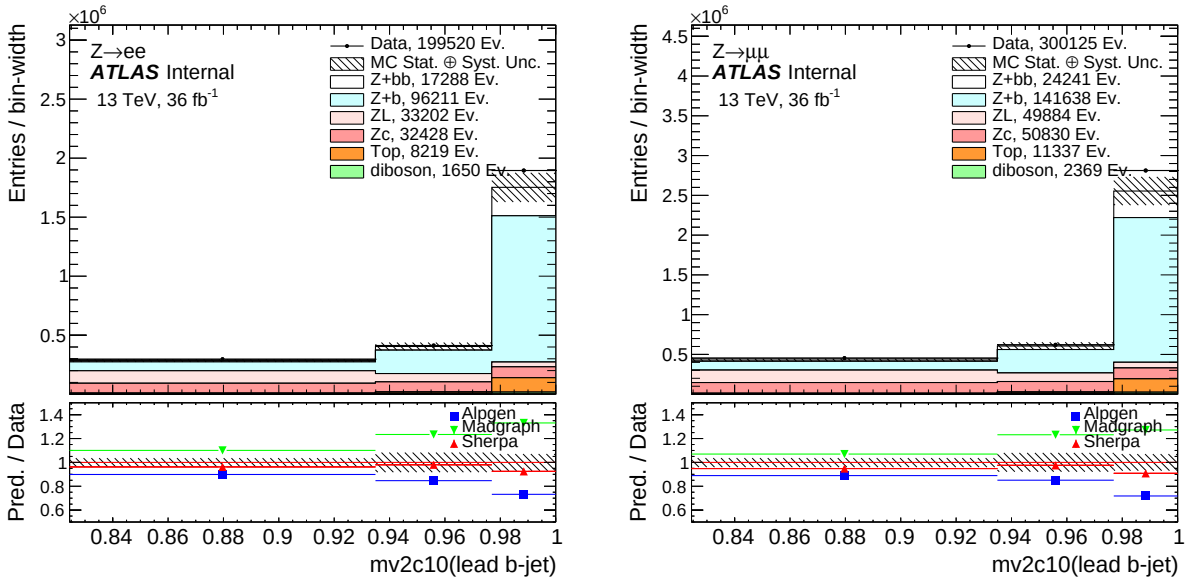

Figure 11.2: MV2c10 weight distribution in the quantile binning for the leading b-tagged jet in the $\geq 1b$-jet signal region for the electron channel (left) and muon channel (right). The comparison to data in the top part of the plots is to the Sherpa samples while ratio of predicted over data in the bottom part of the plots shows the comparison to data for all three generators (Sherpa, Alpgen, and Madgraph).

In the Z2B signal region there are two jets that pass the 70% working point selection. The discriminating variable is still constructed from the MV2c10 quantiles, however it uses the 6 different possible permutations of these quantiles without distinguishing between which is the leading or sub-leading b-jet. The 6 bins are labeled according to there quantile permutation : 70-70, 70-60, 60-60, 70-50, 60-50, and 50-50. So for example, the 70-70 bin will contain all events in which both the leading and sub-leading b-jet fall into the 70% quantile, where as the 70-60 bin will contain all events in which the leading b-jet is in the 70% quantile and the sub-leading b-jet is in the 60% quantile as well as all events in which the leading b-jet is in the 60% quantile and the sub-leading b-jet is in the 70% quantile. This is illustrated in fig. 11.3 for the muon channel using sherpa as the generator. The resulting distribution for these quantiles is shown in fig. 11.4 for both the electron and muon channel. For the Z + light flavor jets truth tagging has been used as is described in Appendix C. Similarly

to what was shown in Z1B signal region the discrimination between signal and background using this variable is quite good.

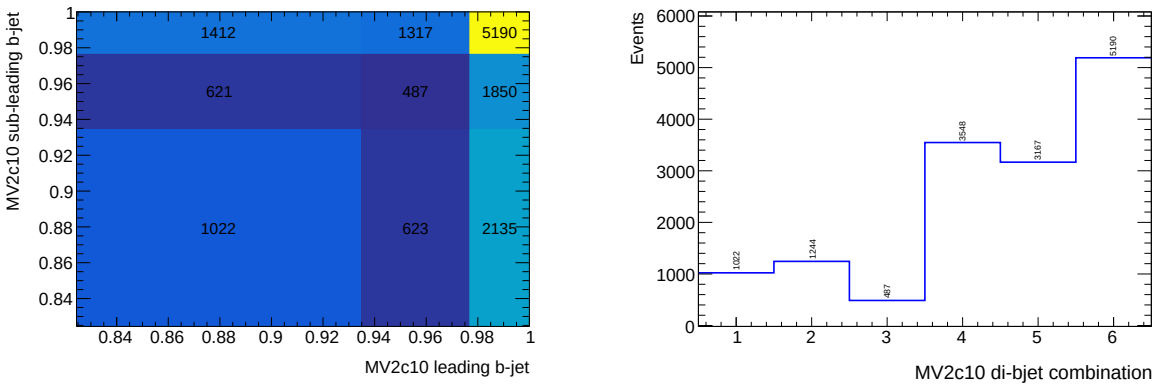

Figure 11.3: Example of combination of the quantile distribution of the two tagged jets in the $\geq$ 2b-tag signal region for the muon channel using Sherpa as generator. The left plot shows the MV2c10 score of the leading b-tagged jet on the x-axis and of the sub-leading b-tagged jet on the y-axis. The right plot shows the same events in a one-dimensional distribution after combining the appropriate permutations. The bin numbering scheme corresponds to the following quantile permutations: bin-1 = 70 − 70, bin-2 = 70 − 60, bin-3 = 60 − 60, bin-4 = 70 − 50, bin-5 = 60 − 50, bin-6 = 50 − 50.

11.3 Fit in the Z+ $\geq 1b$-jet Signal Region

The fit in the Z1B region is performed with two floating parameters. The normalizations of the signal and background components of the Z+jets processes. The five components that Z+jets are broken into was described in section 7.3.2. The signal component, referred to as Z + b-jets, is composed of the sum of the two components Z + b and Z + bb. The background component, referred to as Z + j, is composed of the sum of the remaining three components, Z + c,Z + cc and Z + l. The fit is performed separately for each of the three generators used to generate the Z+jets samples (Sherpa, Alpgen, and Madgraph). This allows for the closure of the scale factors that are obtained from the fits to be tested by comparing the resulting yields coming from the fitted distributions.

The shape of the different background components as well as their sum is shown in

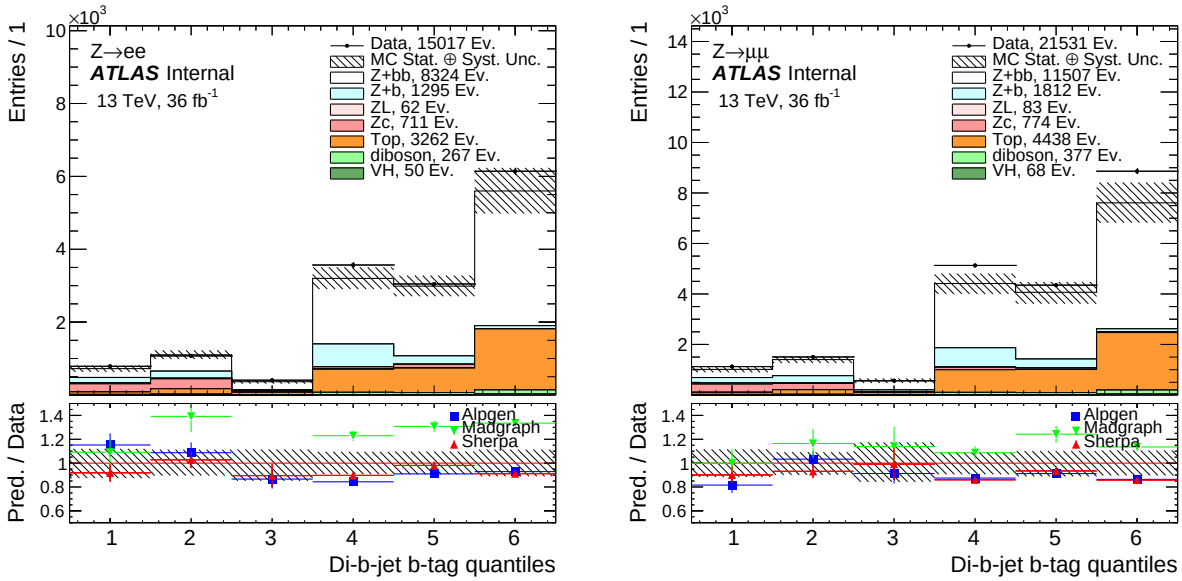

Figure 11.4: Distribution of the combined MV2c10 quantile permutations of the two b-tagged jets in the $\geq$ 2b-tag signal region for the electron channel (left) and muon channel (right). The comparison to data in the top part of the plots is to the Sherpa samples while ratio of predicted over data in the bottom part of the plots shows the comparison to data for all three generators (Sherpa, Alpgen, and Madgraph)

figs. 11.5 and 11.6 comparing them to the signal component for Sherpa. The similar plots for Alpgen and Madgraph can be found in Appendix B.1. The plots show that the shapes are comparable between the two lepton channels for the different background components. The plots also show that shapes of the different background components with respect to each other are very similar. This supports the choice in using there sum as the template in the fit.

The MV2c10 weight distribution in the quantile binning for the Z1B signal region is shown in fig. 11.7 after the fit has been performed. As expected the agreement between data and MC is improved for all three generators used to produce the Z+jets samples. The resulting scale factors extracted from the flavor fit are shown in table 11.5 for the fits performed separately for the electron and muon channel. The combined electron and muon channel flavor fit scale factors are shown in section 11.3. For both tables the uncertainties shown are from the statistical error of the fit. The tables show compatibility of the scale

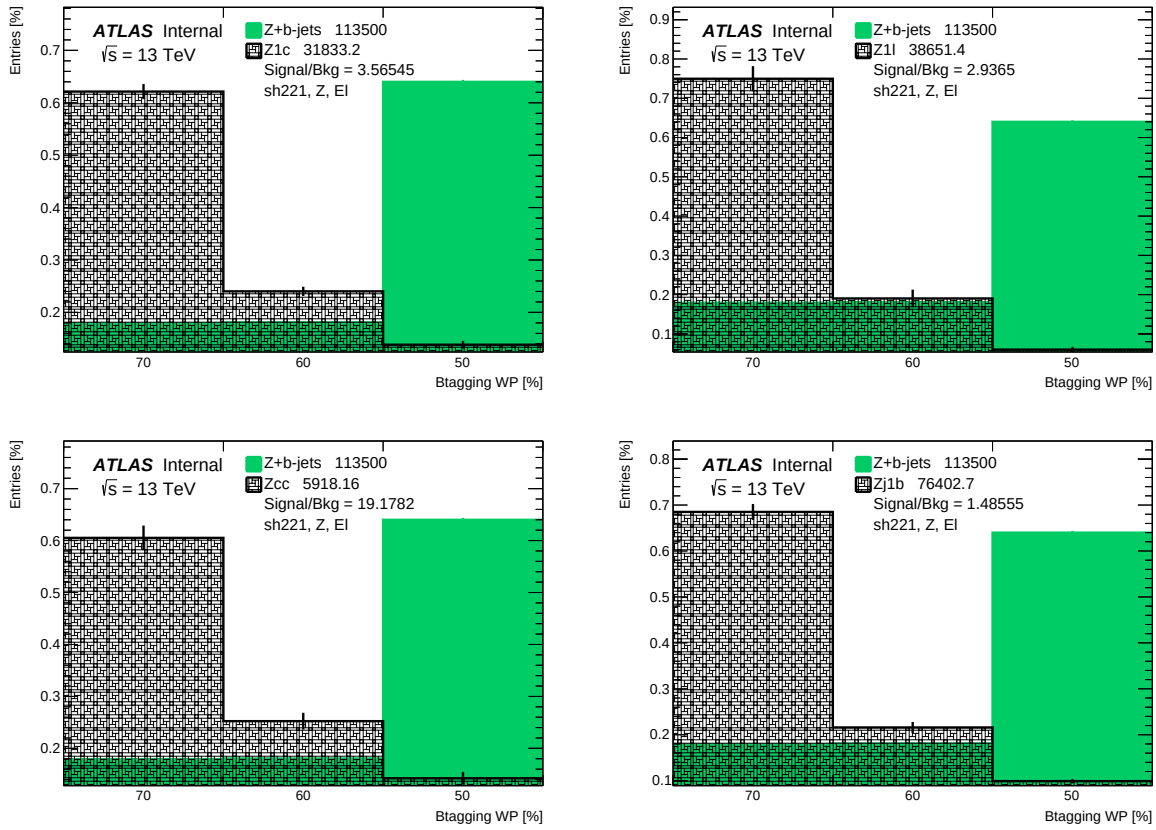

Figure 11.5: Shape comparison of the signal component, Z + b-jets, to the background components Z + c (top left), Z + cc (bottom left), Z + l (top right), and to their sum (bottom right) for the Sherpa generator in the Z1B signal region for the electron channel.

factors between lepton channels for the Z + j component for all three generators. However, for the Z + b-jets component, the difference between the electron and muon scale factors is not within the statistical uncertainty of the fit. They are found to be compatible once systematic uncertainties are considered.

Process	Sherpa		Alpgen		Madgraph	
	el	mu	el	mu	el	mu
Z + j	0.859 ± 0.0219	0.86 ± 0.0179	1.01 ± 0.0145	1.02 ± 0.0127	0.97 ± 0.0202	0.963 ± 0.0211
Z + b-jets	1.1 ± 0.007	1.12 ± 0.00599	1.46 ± 0.0085	1.5 ± 0.00778	0.715 ± 0.00543	0.754 ± 0.00621

Table 11.5: Nominal Scale factors from the flavor fit in the $\geq 1b$-jet signal region for the three different possible generator choices for the Z + jets samples. The uncertainties quoted are only the statistical errors from the fit.

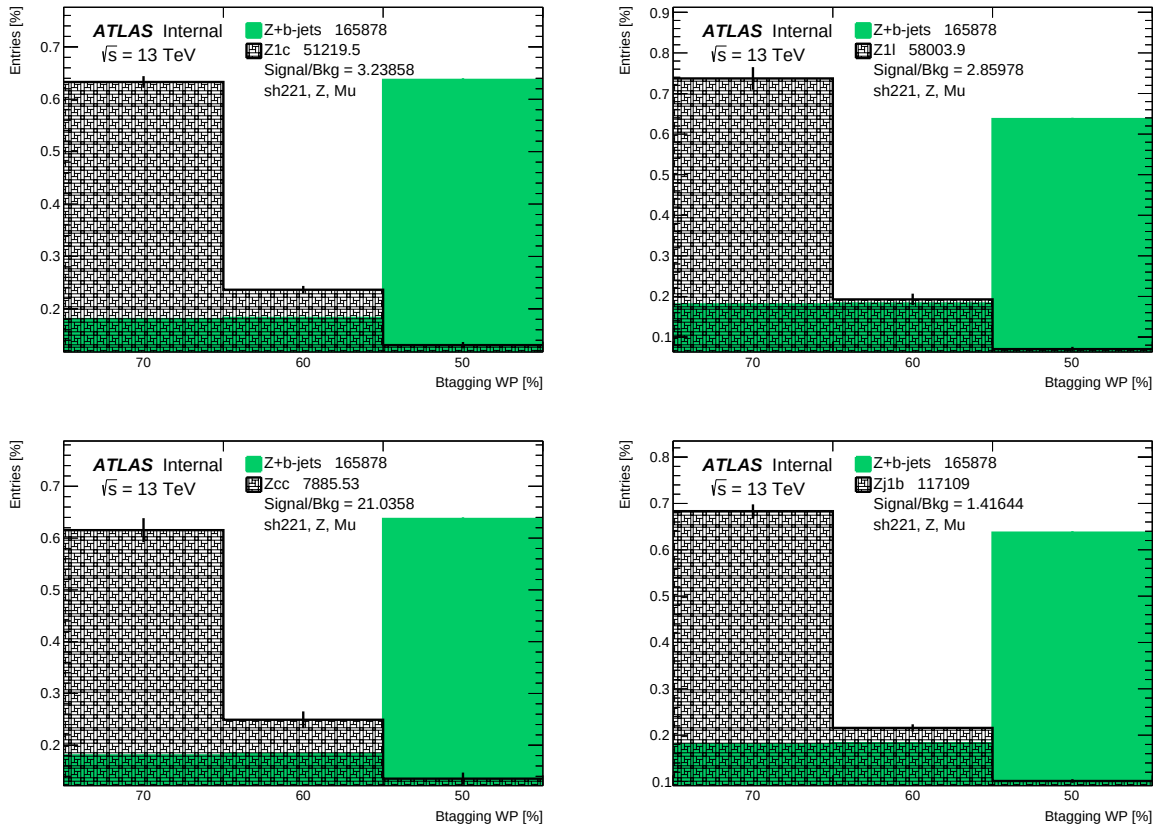

Figure 11.6: Shape comparison of the signal component, Z + b-jets, to the background components Z + c (top left), Z + cc (bottom left), Z + l (top right), and to their sum (bottom right) for the Sherpa generator in the Z1B signal region for the muon channel.

Process	Sherpa	Alpgen	Madgraph
	ele+mu	ele+mu	ele+mu
Z + j	0.8610 ± 0.0139	1.0148 ± 0.0095	0.9711 ± 0.0147
Z + b-jets	1.1085 ± 0.0046	1.4799 ± 0.0057	0.7297 ± 0.0041

Table 11.6: Nominal Scale factors from the combined electron and muon channel flavor fit in the $\geq 1b$-jet signal region for the three different possible generator choices for the Z + jets samples. The uncertainties quoted are only the statistical errors from the fit.

As mentioned earlier, the offset method is used to propagate the detector level systematics through the fit. The resulting scale factors for all the different systematic variations are shown in figs. 11.8 to 11.11 for the Sherpa generator. Similar plots for Alpgen can be found in Appendix B.2. Also shown in these plots is the scale factor obtained from the nominal fit.

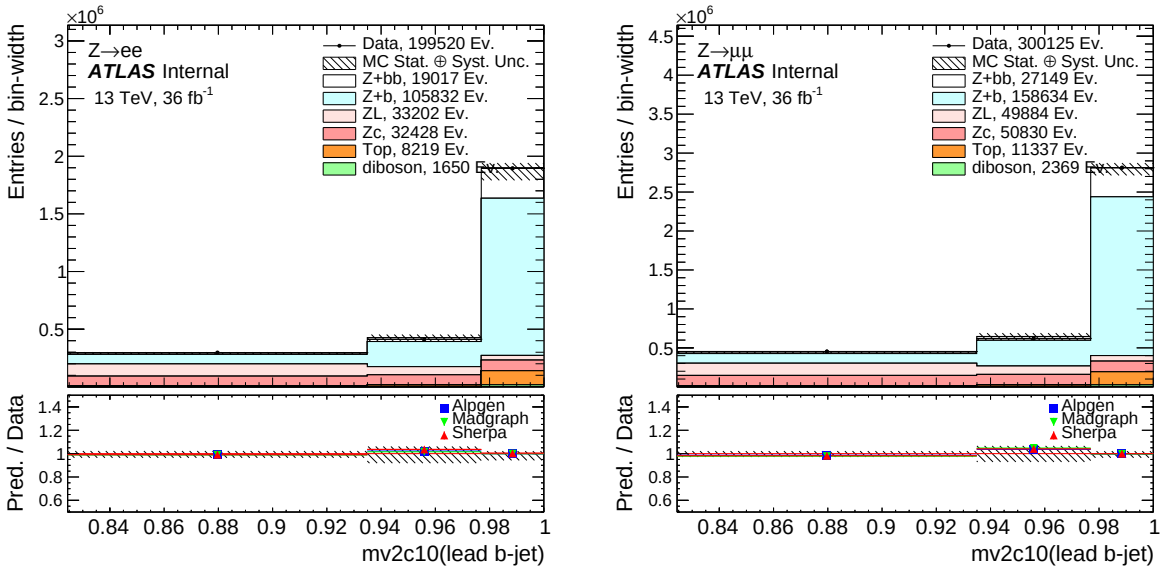

Figure 11.7: Post-fit MV2c10 weight distribution in the quantile binning for the leading b-tagged jet in the $\geq 1b$-jet signal region for the electron channel (left) and muon channel (right). The comparison to data in the top part of the plots is to the Sherpa samples while ratio of Predicted over data in the bottom part of the plots shows the comparison to data for all three generators (Sherpa, Alpgen, and Madgraph).

This is represented by the red horizontal line, while the two yellow horizontal lines in the plots represent the statistical errors from the fit on the nominal scale factor. By looking at the scale factors that come from the systematic variations describing the uncorrelated lepton uncertainties, the difference between the electron and muon channel nominal scale factors for the Z + b-jets component in table 11.5 is covered. For example, the scale factor corresponding to the electron identification efficiency ("EL_EFF_ID_TOTAL_1NPCOR_PLUS_UNCOR" in figs. 11.8 to 11.11), alone is enough to cover the difference. In the muon channel this scale factor is equal to the nominal value scale factor, however, in the electron channel it is approximately 2% different then the nominal scale factor, which covers the difference between the nominal muon and electron channel scale factor.

As expected, both fitted components, Z + j and Z + b-jets, are affected by the flavor tagging parameters. For the Z + b-jets component, the largest deviation from the nominal scale factor is the B_0 component, "FT_EFF_Eigen_B_0_AntiKt4EMTopoJets". The other

significant deviations come from more flavor tagging parameters, the jet energy resolution, the pileup reweighting scale factor uncertainty, and the pileup ρ component of the jet energy scale uncertainty. While for the $Z + j$ component the most significant deviations are observed in two of the light flavor tagging parameters (L_0 and L_1). Other significant deviations also come more of the flavor tagging parameters, flavor composition term of the jet energy scale, as well as the deviations seen for the $Z + b$-jets. While these mentioned variations, have an effect on the scale factors, the majority of the systematic variations have almost no effect on the scale factors. Also the ones that do result in large variations of the scale factors are in general consistent when comparing the electron and muon channels, as well as when comparing generators.

The resulting post-fit yields for the nominal scale factors for all three generators are shown in table 11.7 for the separate electron and muon channel fits and in table 11.8 for the combined lepton channel fit. As one would expect, the results from the combined fit are consistent with the results from the separate lepton channel fits. One would also expect for the post-fit yields to be consistent between generator used. When comparing Sherpa and Alpgen, there is approximately a 5% difference between the yields for the signal components and approximately a 7% difference between the yields for the background components. The uncertainties on the post field yields shown only include the statistical uncertainty, which is not enough to account for the differences between the generators. Plots similar to the ones used to show the effects of the systematics variations on the scale factors are included in Appendix B.3, which shows the resulting post-fit yields that results from the shifted scale factors. For the signal component the largest deviation in the yield compared to nominal is approximately 3% for each generator, which is larger than the observed discrepancy. For the background component, the largest deviation in the yield from nominal is not enough to account for the discrepancy, however, the quadratic sum of the largest deviations from nominal is approximately 5%, and this is enough to account for the discrepancy. This means

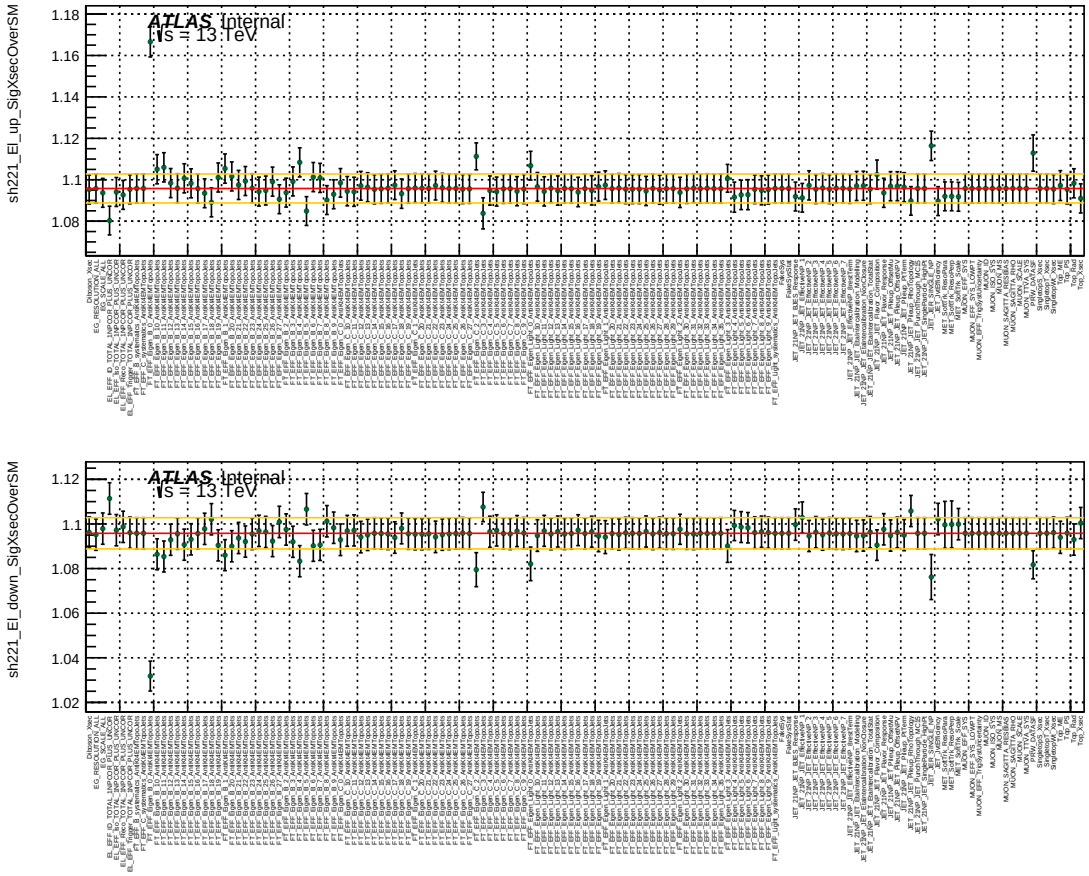

Figure 11.8: Summary of scale factor obtained for the Z + b-jets component in the electron channel fit using Sherpa as the generator for the Z+jets processes, for all the up (left figure) and down (right figure) components of the systematic variations. The horizontal lines represents the fitted SF for the nominal case, i.e. no systematic applied, and the corresponding up and down variation from the statistical error of the fit. Each SF obtained for the different systematic variations is displayed by a point and its corresponding statistical error bar from the fit.

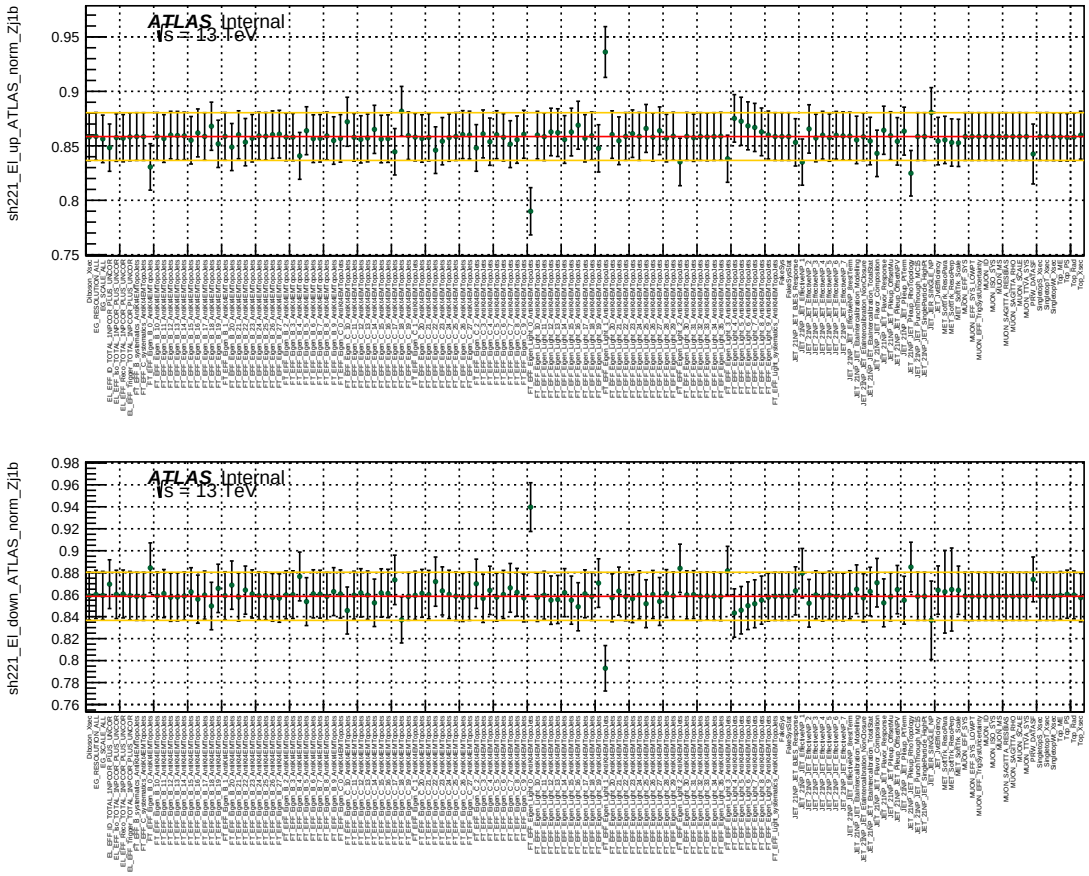

Figure 11.9: Summary of scale factor obtained for the Z + j component in the electron channel fit using Sherpa as the generator for the Z+jets processes, for all the up (left figure) and down (right figure) components of the systematic variations. The horizontal lines represents the fitted SF for the nominal case, i.e. no systematic applied, and the corresponding up and down variation from the statistical error of the fit. Each SF obtained for the different systematic variations is displayed by a point and its corresponding statistical error bar from the fit.

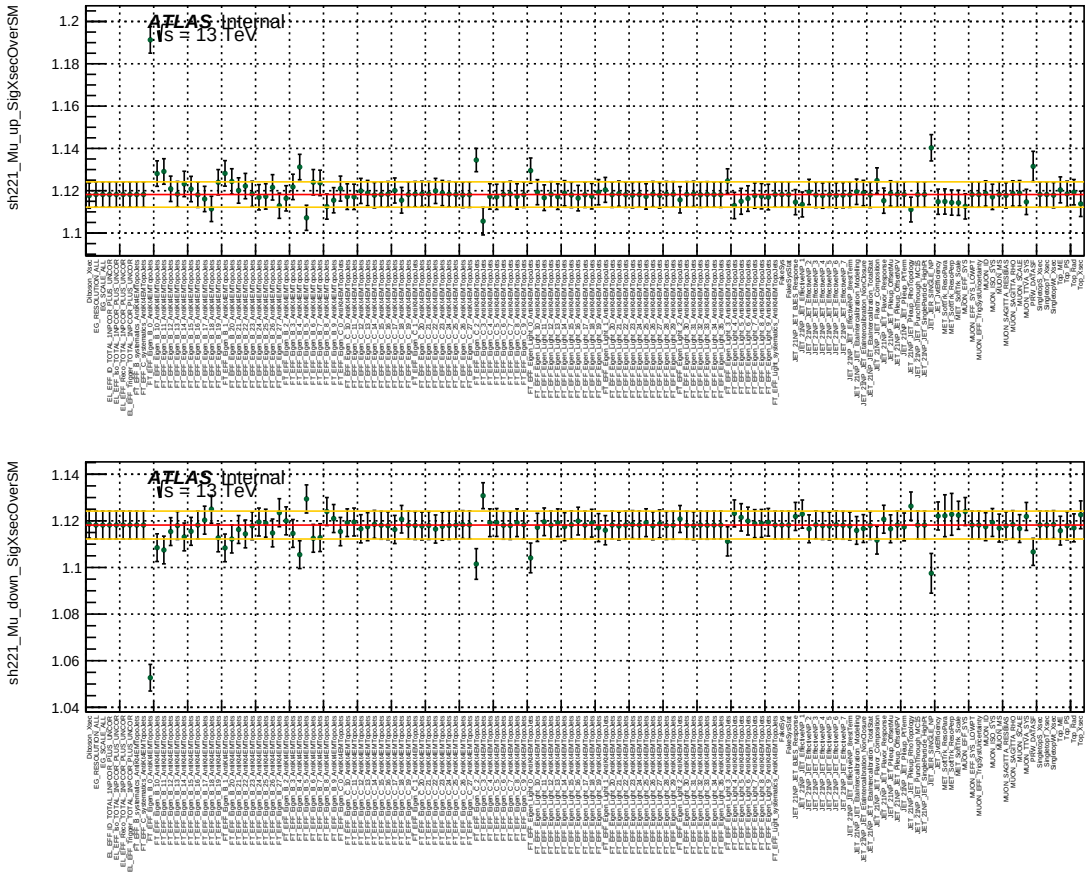

Figure 11.10: Summary of scale factor obtained for the Z + b-jets component in the muon channel fit using Sherpa as the generator for the Z+jets processes, for all the up (left figure) and down (right figure) components of the systematic variations. The horizontal lines represents the fitted SF for the nominal case, i.e. no systematic applied, and the corresponding up and down variation from the statistical error of the fit. Each SF obtained for the different systematic variations is displayed by a point and its corresponding statistical error bar from the fit.

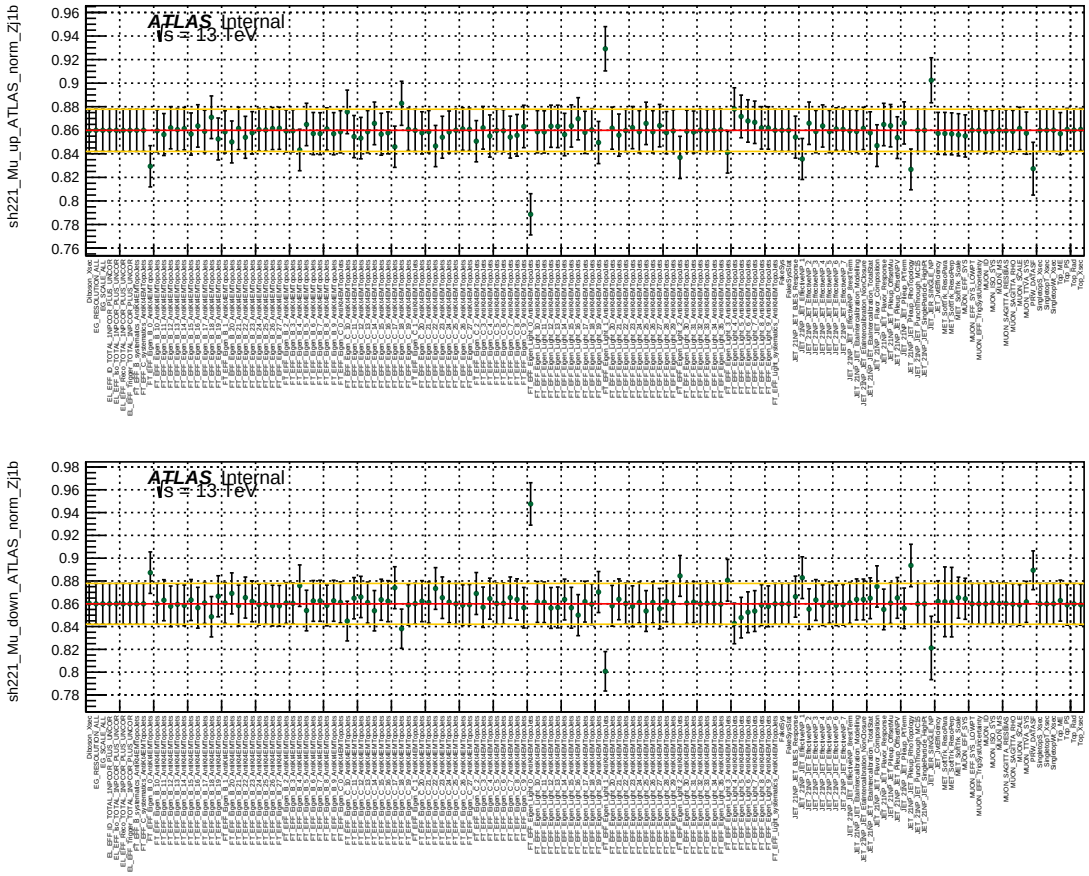

Figure 11.11: Summary of scale factor obtained for the Z + j component in the muon channel fit using Sherpa as the generator for the Z+jets processes, for all the up (left figure) and down (right figure) components of the systematic variations. The horizontal lines represents the fitted SF for the nominal case, i.e. no systematic applied, and the corresponding up and down variation from the statistical error of the fit. Each SF obtained for the different systematic variations is displayed by a point and its corresponding statistical error bar from the fit.

that the systematics uncertainties that are considered are larger than discrepancies between which generator is used for the Z+jet samples, at least in terms of normalization. There could still be shape differences for different distributions that are not covered by the systematic uncertainties. A shape systematic is estimated and described more in section 13.7.

Process	Sherpa		Alpgen		Madgraph	
	ele	mu	ele	mu	ele	mu
Z + j	65600 ± 700	101000 ± 1000	70000 ± 600	108000 ± 1000	72000 ± 700	109000 ± 1000
Z + b-jets	125000 ± 1000	186000 ± 1000	119000 ± 1000	179000 ± 1000	117000 ± 1000	177000 ± 1000

Table 11.7: Post-fit yields for the electron and muon channel fit of the signal component and background component for the nominal Sherpa, Alpgen and Madgraph fits, shown alongside with the statistical error from the fit. The yields have been rounded to 1% precision.

Process	Sherpa	Alpgen	Madgraph
	ele+mu	ele+mu	ele+mu
	166600 ± 2700	178100 ± 1700	181600 ± 2750
	309700 ± 1300	297700 ± 1150	291200 ± 1700

Table 11.8: Post-fit yields for combined electron and muon channels fit of the signal component and background component for the nominal Sherpa, Alpgen and Madgraph fits, shown alongside with the statistical error from the fit.

11.3.1 Estimate of the Flavor Fit Method Uncertainty

An uncertainty is estimated for the flavor fit method used. One option would be to vary the binning used for the fit, however, this is not possible because the flavor tagging calibration factors are only available for the quantile binning that is used. The next option naturally then would be to loosen the MV2c10 cut to include the looser working points, however, this would then introduce an extrapolation uncertainty since we would now be fitting outside the signal region. Therefore the choice to estimate the fit method uncertainty is to perform the fit while treating Z + c and Z + l as separate background components. In the nominal case they were combined and there overall normalization is a free floating parameter. In the modified fit their normalizations are floated separately. The resulting post-fit yields on the combined Z + j background from this configuration differ from the nominal configuration by approximately 5%. The difference is taken as the systematic uncertainty on the flavor fit method.

11.4 Fit in the Z+ $\geq 2b$-jets Signal Region

The fit in the Z2B region is also performed with two floating parameters: the normalizations of the signal and background components of the Z+jets processes. The grouping of the five components of the Z+jets is similar to that in the Z1B fit, except now the component Z + b is part of the background component, therefore the signal component only consists of Z + bb, while the background component consists of the sum of the remaining four, Z + b,Z + c,Z + cc and Z + l. The signal component will be referred to as Z + bb and the background component is referred to as Z + jj. For the Z + light flavor jets truth tagging has been used as is described in Appendix C. The fit is performed separately for each of the three generators used to generate the Z+jets samples (Sherpa, Alpgen, and Madgraph).

The shape of the different background components, as well as their sum, is shown in-figs. 11.12 and 11.13 comparing them to the signal component for Sherpa. The similar plots

for Alpgen and Madgraph can be found in Appendix B.1. The large uncertainties for many of the bins, as well as the large fluctuations show the effects of the low statistics. The Z + l component has very small statistical uncertainties due to the truth tagging method that is used. The Z + b component which benefits from higher statistics than the other background components has a very similar shape between lepton channels, as well as, between the Sherpa and Alpgen generators. For the other two components, Z + c and Z + cc, large fluctuations can be seen between lepton flavors. The sum of the different background components, Z + jj, shows that these fluctuations in the individual components get flattened out and good agreement of it can be seen both between the lepton channels as well as between the two generators Sherpa and Alpgen. The differences with Madgraph can be associated with the lower statistics of those samples compared to the other two generators[1].

The MV2c10 weight distribution in the quantile permutations binning, described earlier, for the Z2B signal region is shown in fig. 11.14 after the fit has been performed and can be compared to the pre-fit distributions in fig. 11.4. As expected, the agreement between data and MC is improved for all three generators used to produce the Z+jets samples. The resulting scale factors extracted from the flavor fit are shown in table 11.9 for the fits performed separately for the electron and muon channel. The combined electron and muon channel flavor fit scale factors are shown in table 11.10. The uncertainties quoted in the tables are from the statistical error of the fit. The tables show compatibility of the scale factors between lepton channels for the Z + jj component for both Sherpa and Alpgen. However, for the Z + bb the difference between the electron and muon scale factors is not within the statistical uncertainty of the fit. They are found to be compatible once systematic uncertainties are considered.

The scale factors obtained by performing the fit using each of the systematic variations are shown in figs. 11.15 to 11.18 for the Sherpa generator along with the nominal scale

1. Appendix A list all samples used as well as the initial number of events for each sample

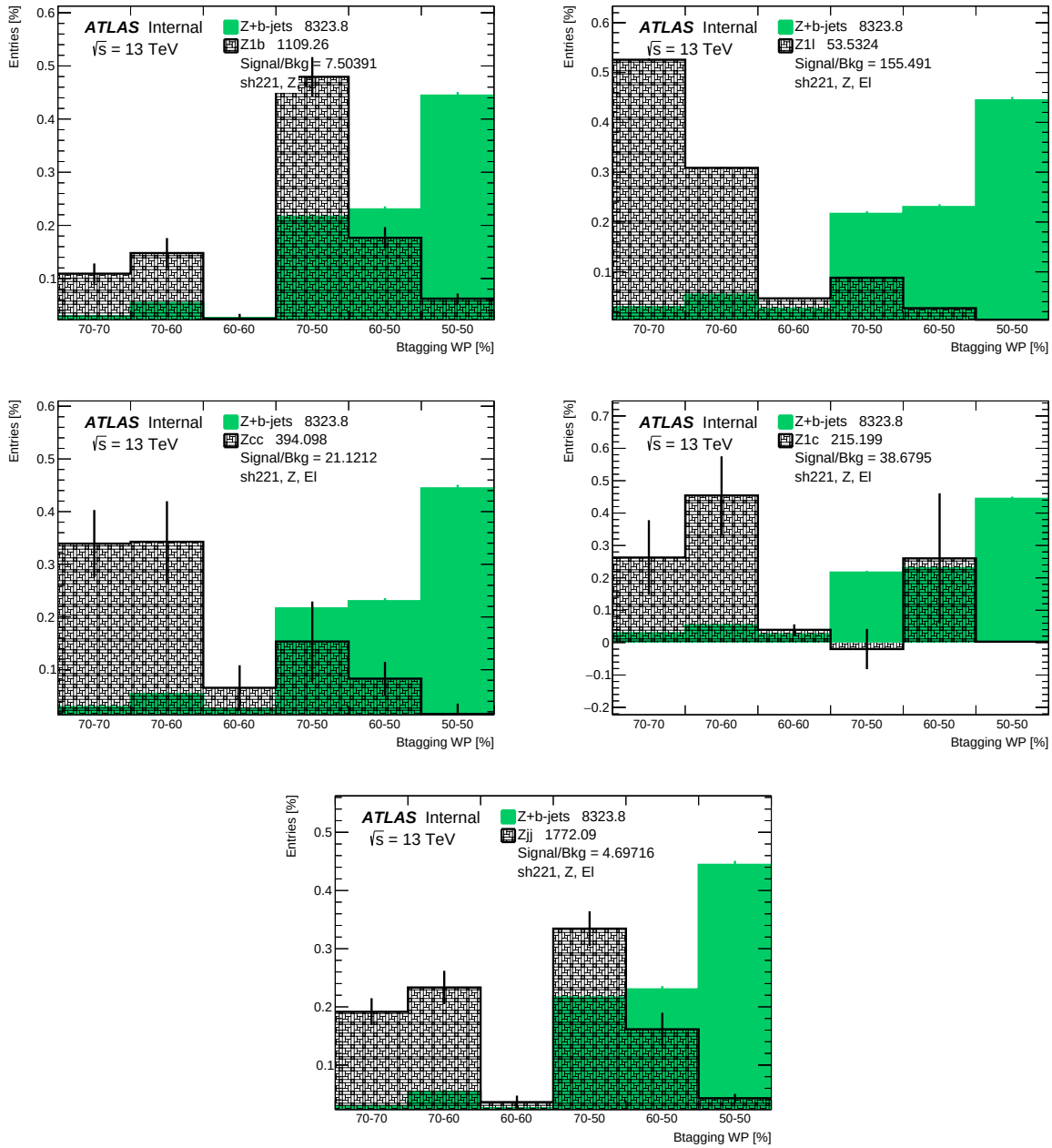

Figure 11.12: Shape comparison of the signal component, Z + bb, to the background components Z + b (top left), Z + cc (middle left), Z + l (top right), Z + c (middle right), and to their sum (bottom) for the Sherpa generator in the Z2B signal region for the electron channel.

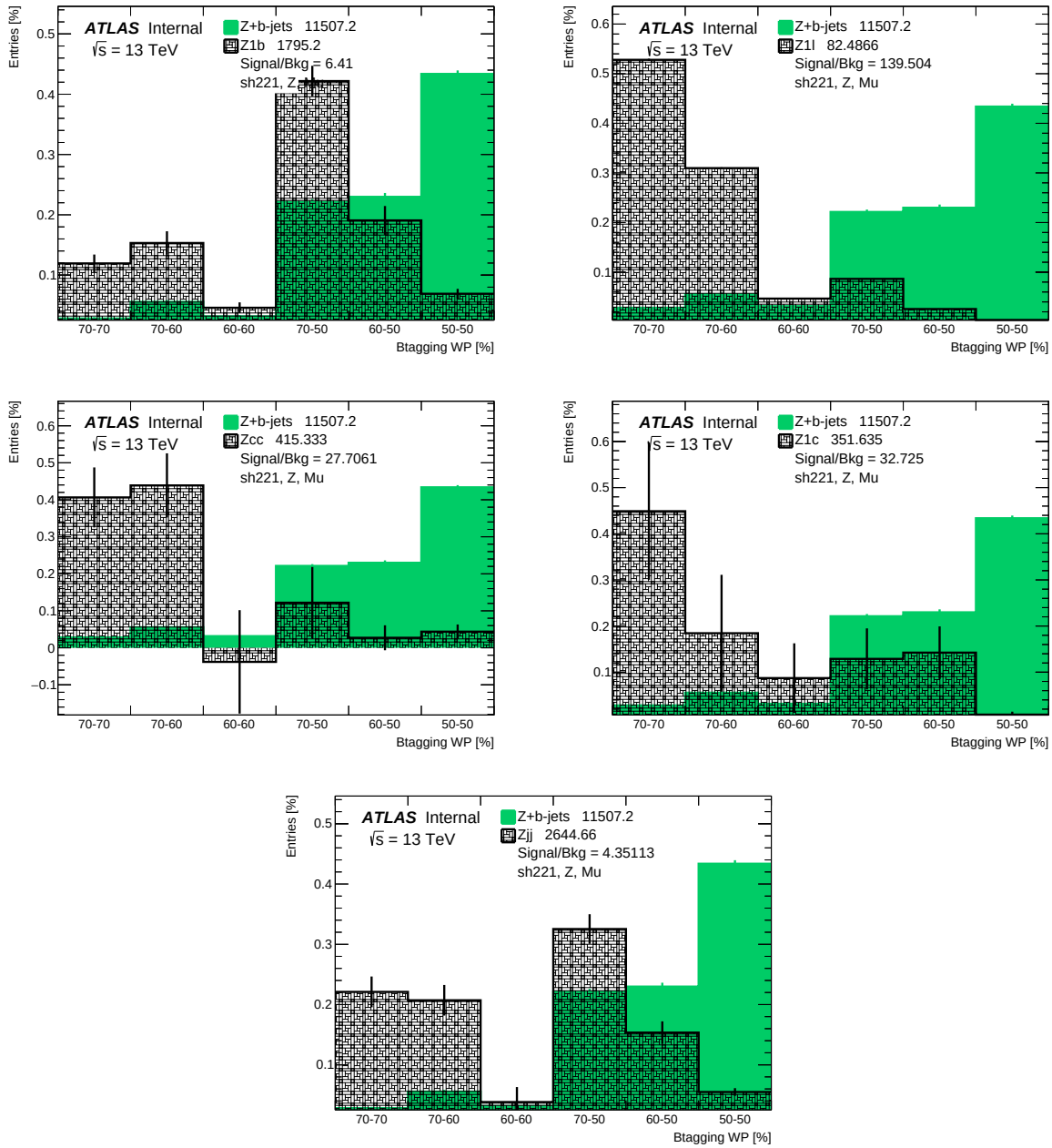

Figure 11.13: Shape comparison of the signal component, Z + bb, to the background components Z + b (top left), Z + cc (middle left), Z + l (top right), Z + c (middle right), and to their sum (bottom) for the Sherpa generator in the Z2B signal region for the muon channel.

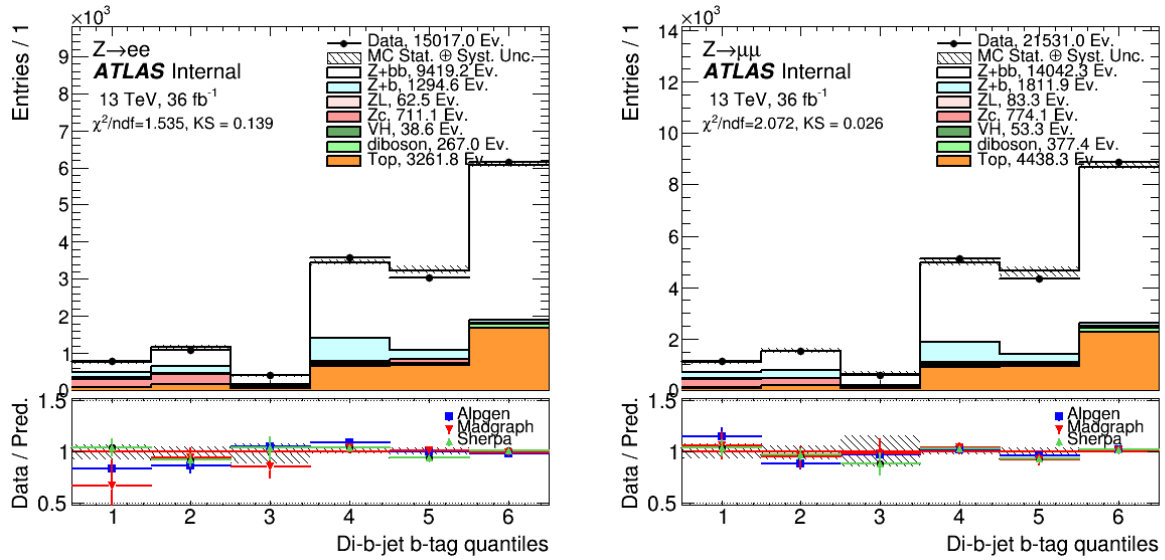

Figure 11.14: Post-fit MV2c10 weight distribution in the quantile permutations binning for the two b-tagged jets in the $\geq$ 2b-tags signal region for the electron channel (left) and muon channel (right). The comparison to data in the top part of the plots is to the Sherpa samples while ratio of predicted over data in the bottom part of the plots shows the comparison to data for all three generators (Sherpa, Alpgen, and Madgraph).

Process	Sherpa		Alpgen		Madgraph	
	ele	mu	ele	mu	ele	mu
Z + jj	1.17 ± 0.10	1.01 ± 0.08	1.27 ± 0.13	1.32 ± 0.11	1.63 ± 0.14	1.06 ± 0.12
Z + bb	1.13 ± 0.02	1.22 ± 0.02	1.15 ± 0.02	1.21 ± 0.02	0.674 ± 0.013	0.828 ± 0.015

Table 11.9: Nominal Scale factors from the flavor fit in the $\geq 2b$-jets signal region for the three different possible generator choices for the Z + jets samples. The uncertainties quoted are only the statistical errors from the fit.

Process	Sherpa	Alpgen	Madgraph
	ele+mu	ele+mu	ele+mu
Z + jj	1.081 ± 0.063	1.299 ± 0.081	1.347 ± 0.091
Z + bb	1.182 ± 0.014	1.184 ± 0.013	0.738 ± 0.01

Table 11.10: Nominal Scale factors from the combined electron and muon channel flavor fit in the $\geq 2b$-jets signal region for the three different possible generator choices for the Z + jets samples. The uncertainties quoted are only the statistical errors from the fit.

factor. Similar plots for Alpgen can be found in Appendix B.2. The plots show that the signal component scale factor associated with the flavor tagging uncertainty B_0 parameter

varies from the nominal scale factor by over 10% for both the electron and muon channel. This systematic variation on its own is enough to make the signal scale factors for the electron and muon channel to be compatible.

The plots show that the systematic variations that affect the scale factor the most are in general consistent between lepton channels, as well as between Sherpa and Alpgen. In the Z2B signal region $t\bar{t}$ is a more significant background and this is evident by the effect the top modeling systematics have on the extracted scale factors. Most of the systematic variations associated with $t\bar{t}$ modeling result in scale factors outside the statistical uncertainty of the nominal scale factor for the signal component of the flavor fit. The systematic scale factor associated with the flavor tagging parameter B_0 results in the largest deviation from the nominal scale factor for both fitted components,Z + jj and Z + bb. The other significant deviations in the signal component come from the jet energy resolution and the pileup reweighting scale factor uncertainty, while most systematic variations have very little effect on the scale factors.

The resulting post-fit yields from the nominal scale factors for all three generators are shown in table 11.11 for the separate electron and muon channel fits and in table 11.12 for the combined lepton channel fit. As expected, the results from the combined fit are consistent with the results from the separate lepton channel fits. Good closure is seen between Sherpa and Alpgen in both lepton flavors.

Process	Sherpa		Alpgen		Madgraph	
	ele	mu	ele	mu	ele	mu
Z + jj	2070 ± 130	2670 ± 160	1940 ± 130	2610 ± 150	2520 ± 140	2850 ± 200
Z + bb	9420 ± 170	14000 ± 200	9630 ± 170	14000 ± 200	9080 ± 170	13900 ± 200

Table 11.11: Post-fit yields for the electron and muon channel fit of the signal component and background component for the nominal Sherpa, Alpgen and Madgraph fits, shown alongside with the statistical error from the fit. The yields have been rounded to 1% precision.

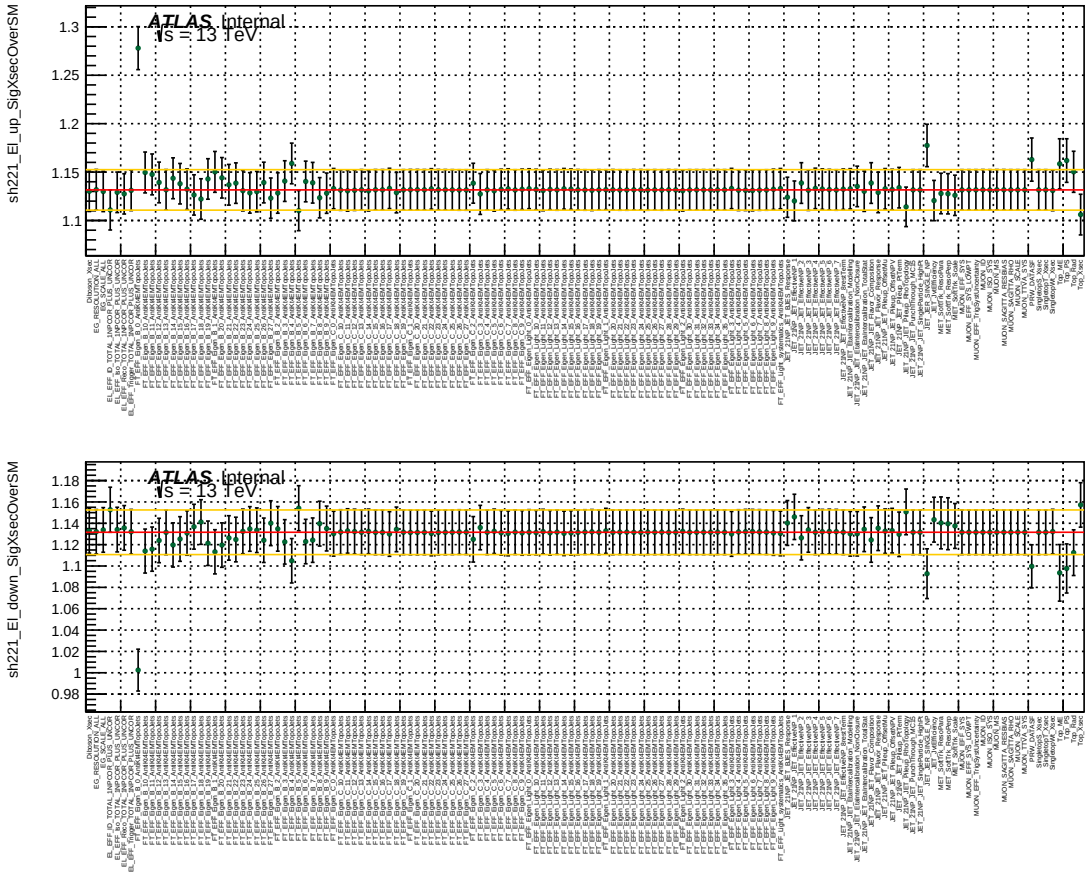

Figure 11.15: Summary of scale factor obtained for the Z + *bb* component in the electron channel fit using Sherpa as the generator for the Z+jets processes, for all the up (left figure) and down (right figure) components of the systematic variations. The horizontal lines represents the fitted SF for the nominal case, i.e. no systematic applied, and the corresponding up and down variation from the statistical error of the fit. Each SF obtained for the different systematic variations is displayed by a point and its corresponding statistical error bar from the fit.

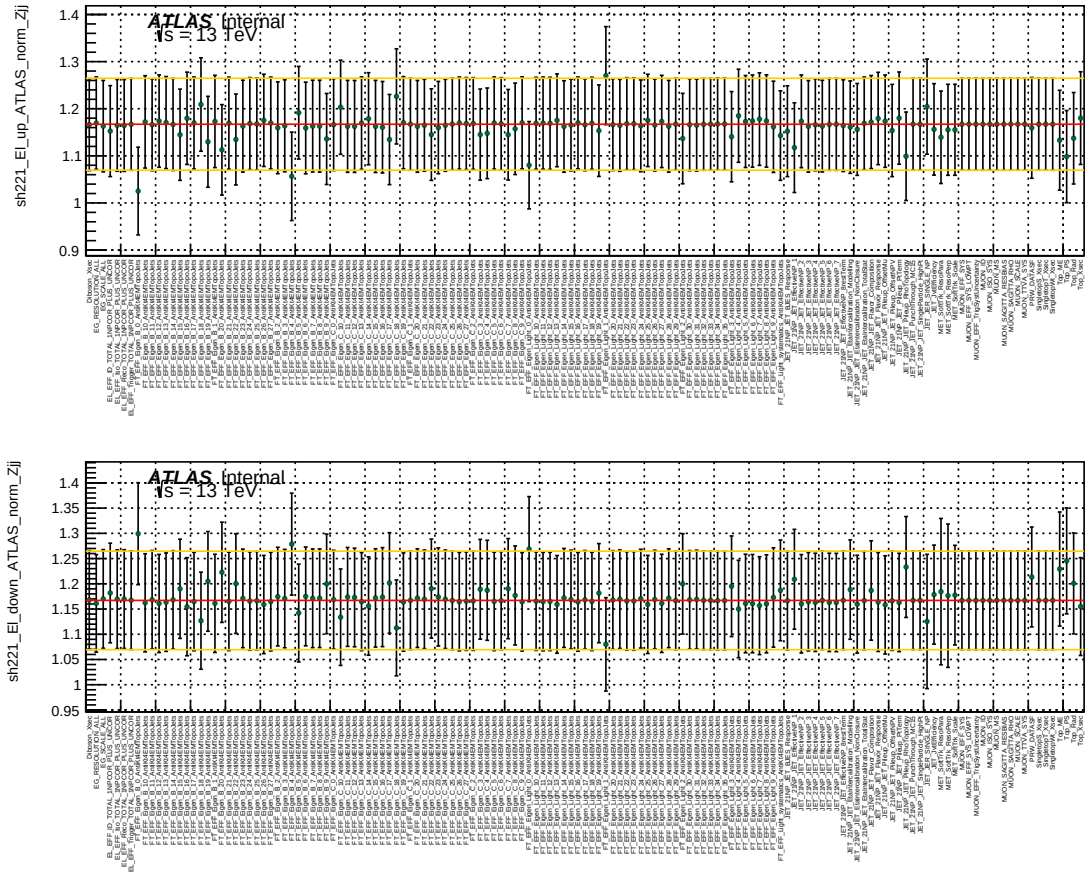

Figure 11.16: Summary of scale factor obtained for the Z + jj component in the electron channel fit using Sherpa as the generator for the Z+jets processes, for all the up (left figure) and down (right figure) components of the systematic variations. The horizontal lines represents the fitted SF for the nominal case, i.e. no systematic applied, and the corresponding up and down variation from the statistical error of the fit. Each SF obtained for the different systematic variations is displayed by a point and its corresponding statistical error bar from the fit.

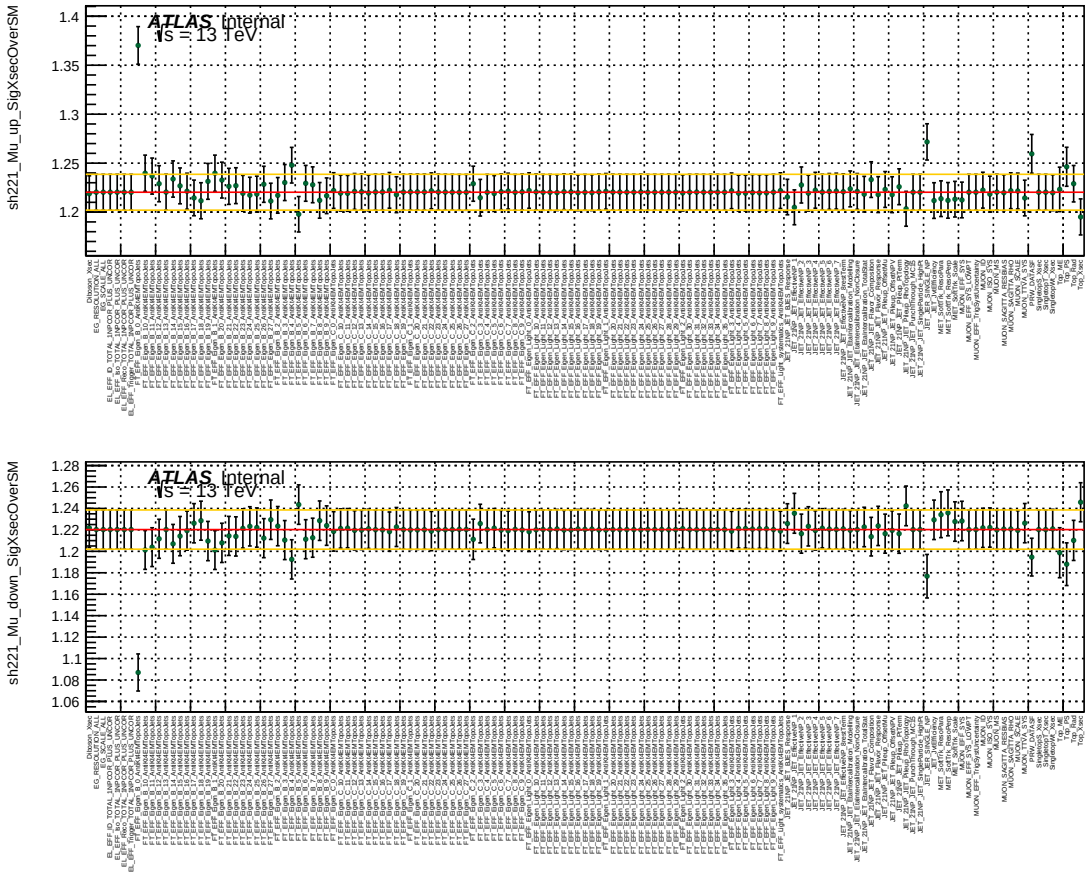

Figure 11.17: Summary of scale factor obtained for the Z + $b\bar{b}$ component in the muon channel fit using Sherpa as the generator for the Z+jets processes, for all the up (left figure) and down (right figure) components of the systematic variations. The horizontal lines represents the fitted SF for the nominal case, i.e. no systematic applied, and the corresponding up and down variation from the statistical error of the fit. Each SF obtained for the different systematic variations is displayed by a point and its corresponding statistical error bar from the fit.

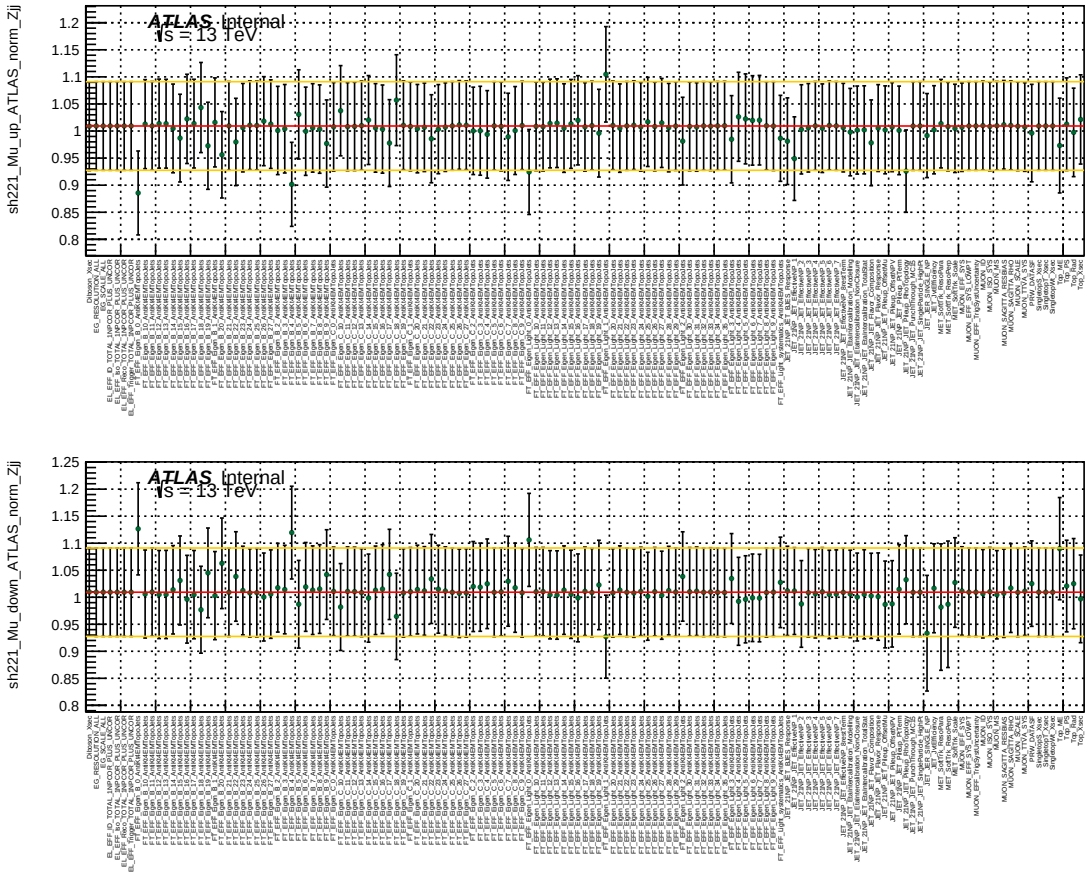

Figure 11.18: Summary of scale factor obtained for the Z + jj component in the muon channel fit using Sherpa as the generator for the Z+jets processes, for all the up (left figure) and down (right figure) components of the systematic variations. The horizontal lines represents the fitted SF for the nominal case, i.e. no systematic applied, and the corresponding up and down variation from the statistical error of the fit. Each SF obtained for the different systematic variations is displayed by a point and its corresponding statistical error bar from the fit.

Process	Sherpa	Alpgen	Madgraph
	ele+mu	ele+mu	ele+mu
Z + jj	4770 ± 280	4540 ± 280	5690 ± 380
Z + bb	23440 ± 280	23650 ± 260	22350 ± 300

Table 11.12: Post-fit yields for combined electron and muon channels fit of the signal component and background component for the nominal Sherpa, Alpgen and Madgraph fits, shown alongside with the statistical error from the fit.

11.4.1 Estimate of the Flavor Fit Method Uncertainty

The uncertainty on the flavor fit method is estimated in the Z2B signal region in a similar approach to that which was done for the Z1B signal region. The fit is redone with a different grouping of the background component. The signal component is left unchanged. The background component is split into two components. The Z + b is separated from the Z + jj component and floated separately. This choice of grouping can be seen by looking at figs. 11.12 and 11.13. In these shape plots it can be seen that the Z + b component tends to peak more in the 70-50 and 60-50 bins where as the other background components, Z + c, Z + cc, and Z + l, tend to peak in 70-70 and 70-60 bins. The resulting post-fit yields on the combined Z + jj background from this configuration differ from the nominal configuration by approximately 3% in the electron channel and less than 1% in the muon channel. The difference is taken as the systematic uncertainty on the flavor fit method.

CHAPTER 12

DETECTOR LEVEL PLOTS

This chapter shows plots at the detector level of some of the main kinematic variables used in the analysis. Only events passing the selections defined in chapter 7 are included in the plots. The first section shows plots in the inclusive Z+jets region. These plots do not apply the b-jet selection and require at least one jet. In the sections showing the detector level plots for the two signal regions each kinematic variable plot is shown three times: once without the flavor fit scale factors; once with the flavor fit scale factor applied to both the signal and background components; and once with the flavor fit scale factors only applied to the background components. The top part of all the plots is comparing Sherpa to data, while the ratio plots of the MC predictions over data show all three generators compared to data. The shaded band in the ratio plot shows the relative size of the detector level systematic uncertainties with respect to the Sherpa generator.

12.1 Inclusive Z+jets Plots

The plots in this section only include events that pass the event selection described in chapter 7 except the b-jet selection is not applied. The event is required to have at least one jet with $p_T > 20$ GeV and $|\eta| < 2.5$. The first few plots show distributions related to the Z boson. Then a few plots are shown showing the kinematics of the jets that are selected. In fig. 12.1 the di-lepton invariant mass associated with the Z boson is shown. fig. 12.2 and fig. 12.3 show the distributions of the rapidity and p_T of the Z boson, respectively. While the rapidity of the Z boson and the di-lepton invariant mass are well described by all three MC generators there are some discrepancies in the p_T of the Z boson.

In fig. 12.4 the inclusive jet multiplicity is shown. The prediction given by Sherpa gives the best results compared to data, while Alpgen and Madgraph show discrepancies that

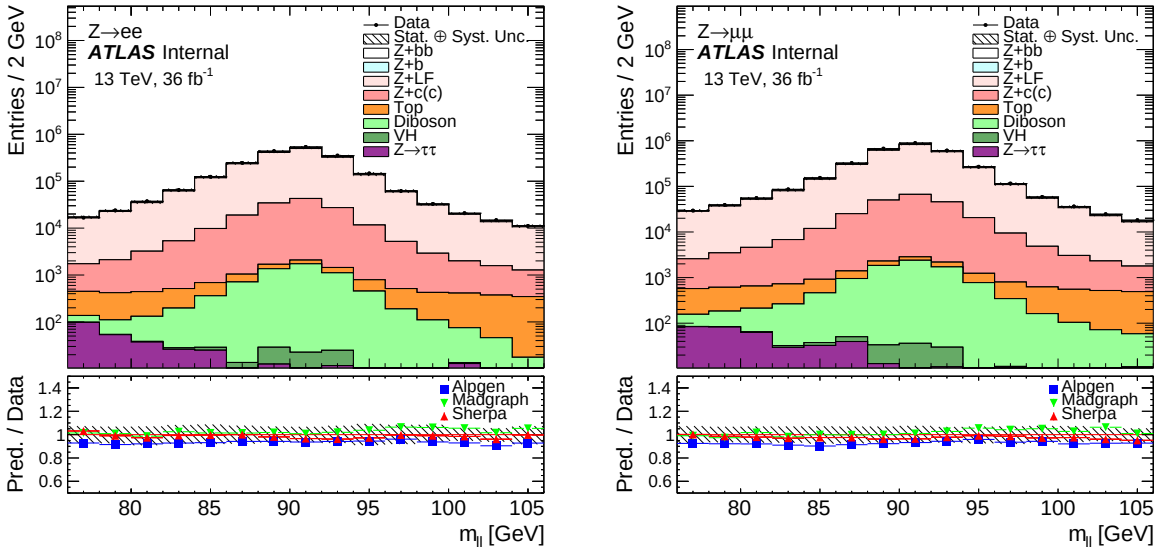

Figure 12.1: Detector level plot of the di-lepton invariant mass in the inclusive region for the electron channel (left) and muon channel (right)

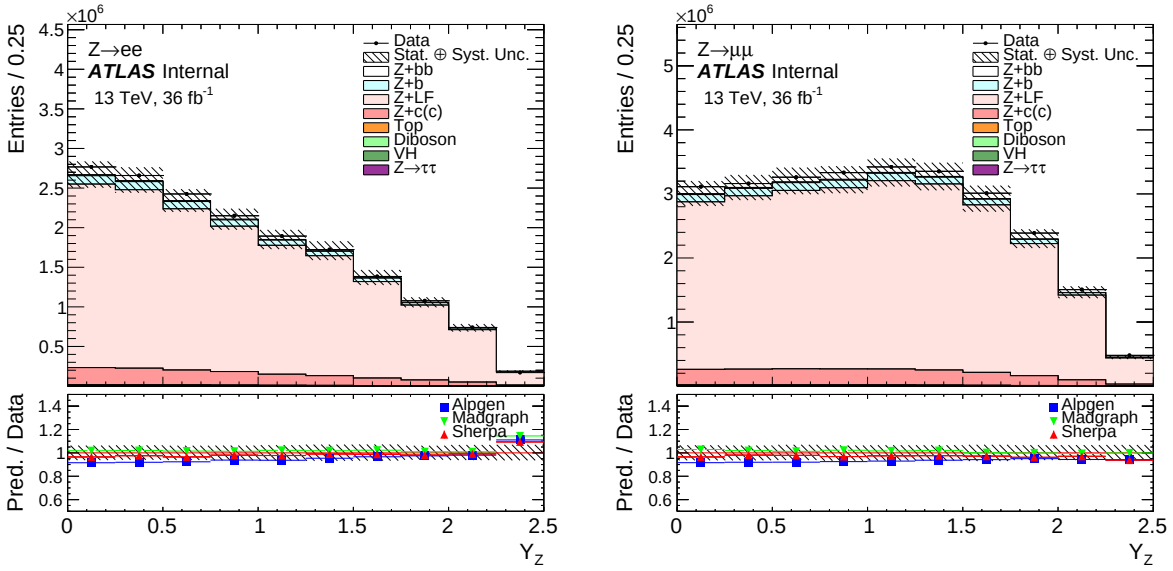

Figure 12.2: Detector level plot of the rapidity of the Z boson in the inclusive region for the electron channel (left) and muon channel (right)

increase with increasing number of jets.

The p_T of the leading jet is shown in fig. 12.5. The discrepancies seen between data and MC are similar to those seen in the p_T of the Z boson observed in fig. 12.3. Finally the rapidity of the leading jet is shown in fig. 12.6.

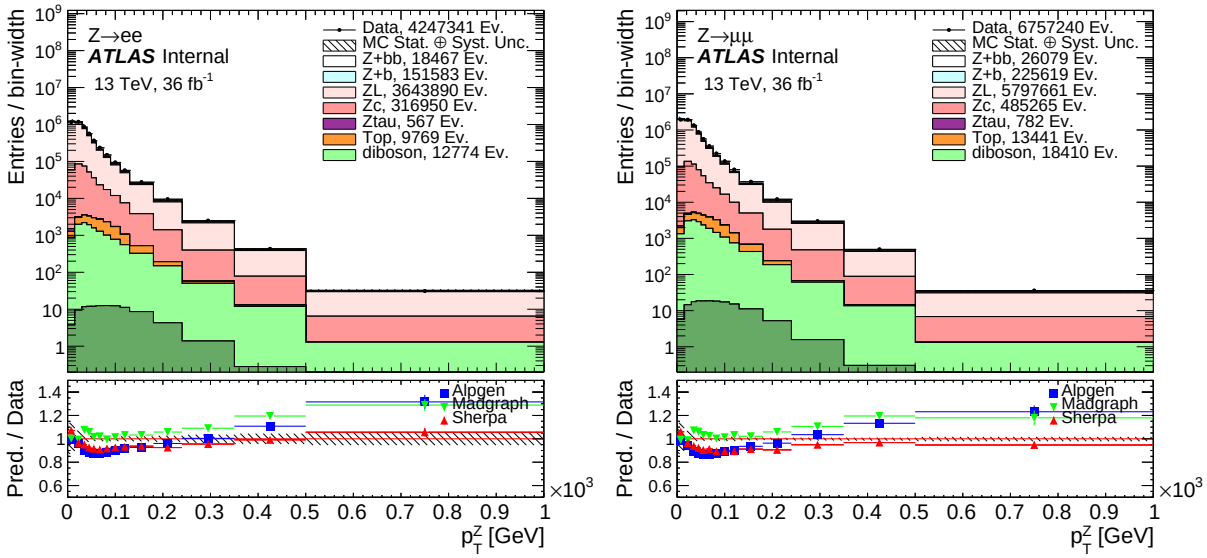

Figure 12.3: Detector level plot of the p_T of the Z boson in the inclusive region for the electron channel (left) and muon channel (right)

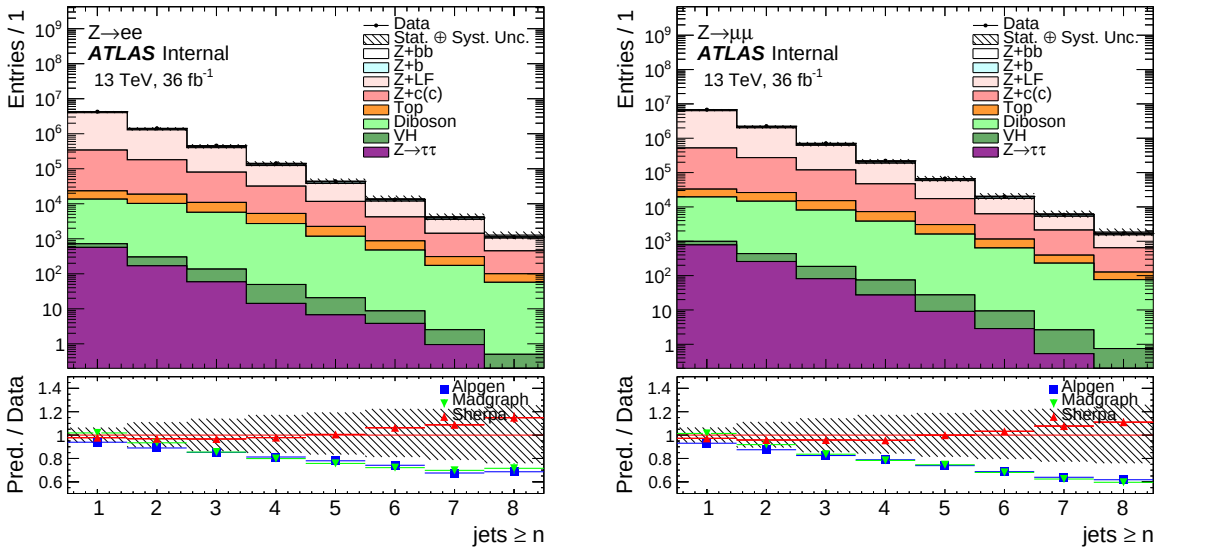

Figure 12.4: Detector level plot of the inclusive jet multiplicity in the inclusive region for the electron channel (left) and muon channel (right)

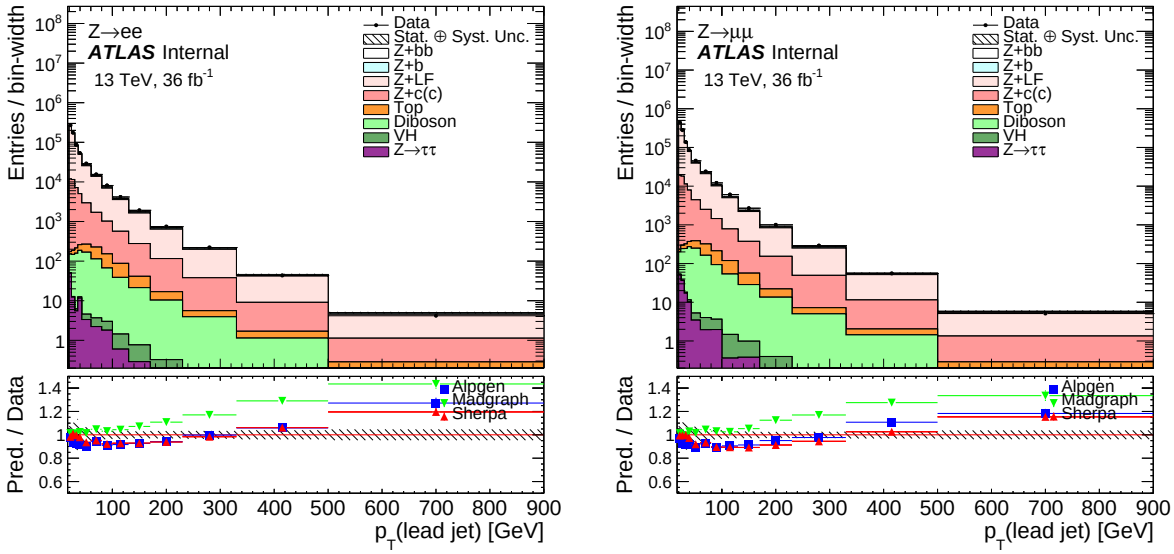

Figure 12.5: Detector level plot of the leading jet p_T in the inclusive region for the electron channel (left) and muon channel (right)

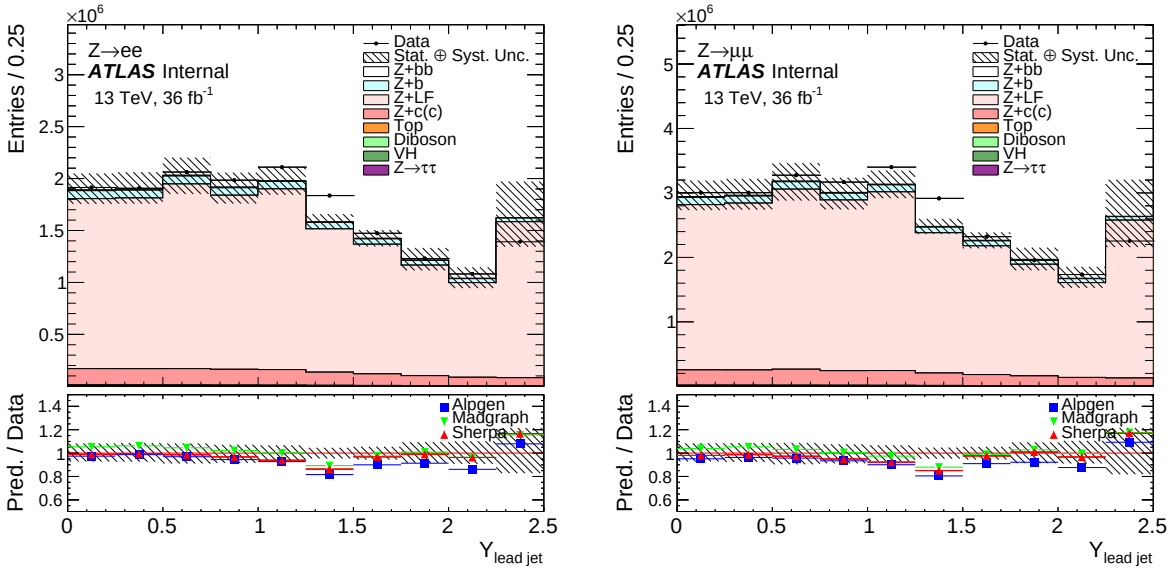

Figure 12.6: Detector level plot of the leading jet rapidity in the inclusive region for the electron channel (left) and muon channel (right)

12.2 Detector Level Plots in the Z+ $\geq 1b$-jet Signal Region

The plots in this section only include events which pass the full event selection, including the b-jet selection requirements. The event yields passing selection can be found in the flavor fit chapter for both the pre-fit yields as well as the post-fit yields. For each plot the distribution is shown without applying the scale factor from the flavor fit, with scale factors applied to both signal and background, and with the scale factors only applied to the background. The latter plots are the ones that are used for inputs in the unfolding, while the ones with both the signal and background scale factors allows for an additional check on the flavor fit.

In fig. 12.7 the inclusive b-jets multiplicity is shown. As is expected from the flavor fit which is fitting the normalizations of the Z+jets components, the MC distributions with the signal and background flavor fit scale factors (middle columns) applied match the data almost perfectly. This means all further distributions with both scale factors applied will have very similar yields/normalizations as data and any discrepancies will be on the shape predicted by MC. The plots also make it clear that the yield of Z+jets is overpredicted by Madgraph, while the yield of Z+jets is underpredicted by Alpgen.

The leading b-jet p_T is shown in fig. 12.8. While fairly good agreement is shown for the three generators in the case of applying both the signal and background scale factors from the flavor fit, there is a discrepancy in the shape for the case of only applying the background scale factors, which appears to be greatest for low p_T.

In fig. 12.9 the rapidity of the leading b-jet is shown. The prediction of the distribution given by Sherpa models data fairly well and all three generators give similar shape predictions. This is similarly seen in the distribution of the rapidity of the Z boson shown in fig. 12.10.

The distribution of the p_T of the Z boson is shown in fig. 12.11. All three generators show large discrepancies in the modeling of the shape of the distribution.

Angular observables between the leading b-jet and the Z boson are shown in figs. 12.12

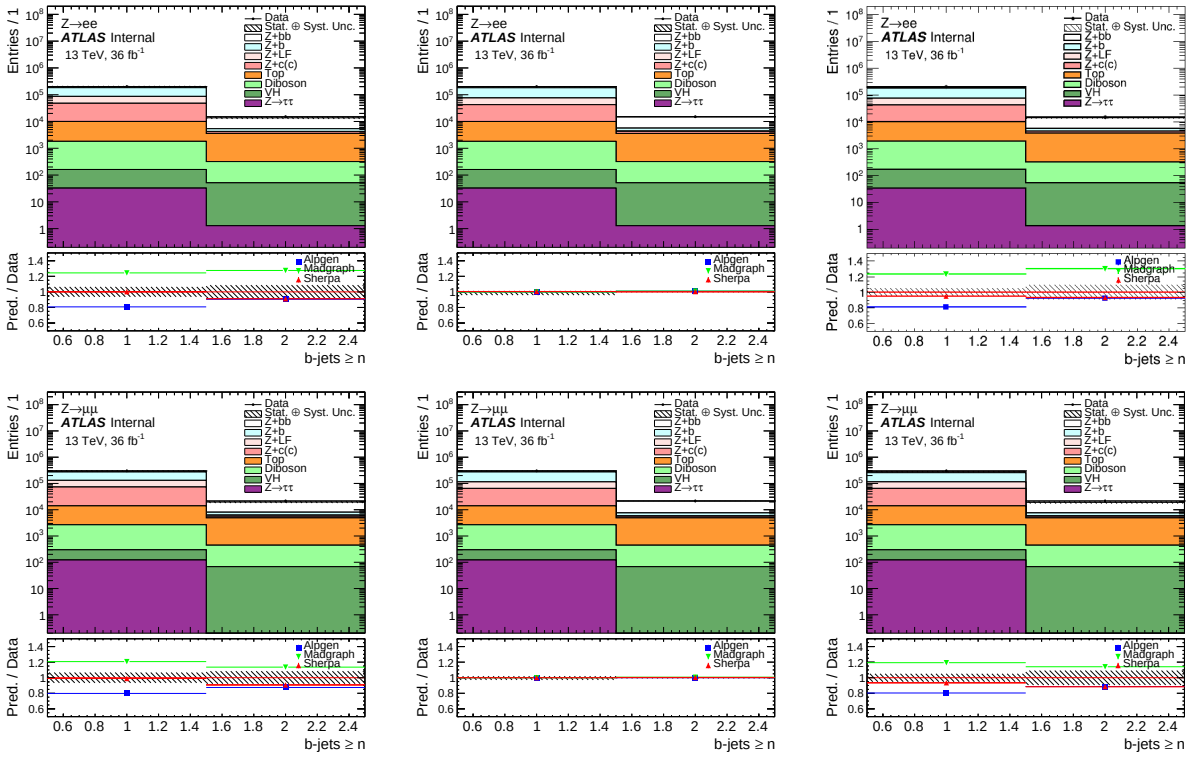

Figure 12.7: Detector level plots of the b-jets multiplicity in the $\geq 1b$-jet signal region for the electron channel (top) and the muon channel (bottom). Left column: Before flavor fit; Middle column: After flavor fit (scaling signal and Z + jets backgrounds); Right column: After flavor fit (scaling only Z + jets backgrounds).

to 12.14. Data is modeled well by Sherpa for these distributions, while Alpgen and Madgraph show large discrepancies.

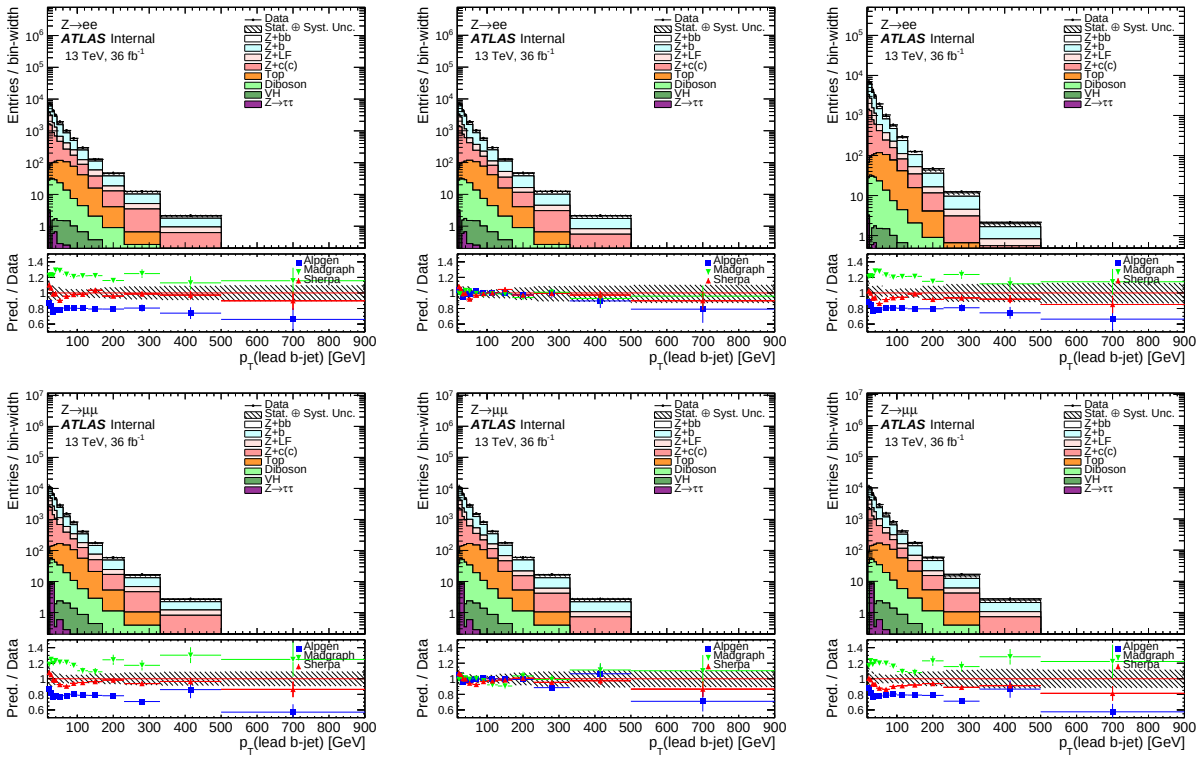

Figure 12.8: Detector level plots of the leading b-jet p_T in the $\geq 1b$-jet signal region for the electron channel (top) and the muon channel (bottom). Left column: Before flavor fit; Middle column: After flavor fit (scaling signal and Z + jets backgrounds); Right column: After flavor fit (scaling only Z + jets backgrounds).

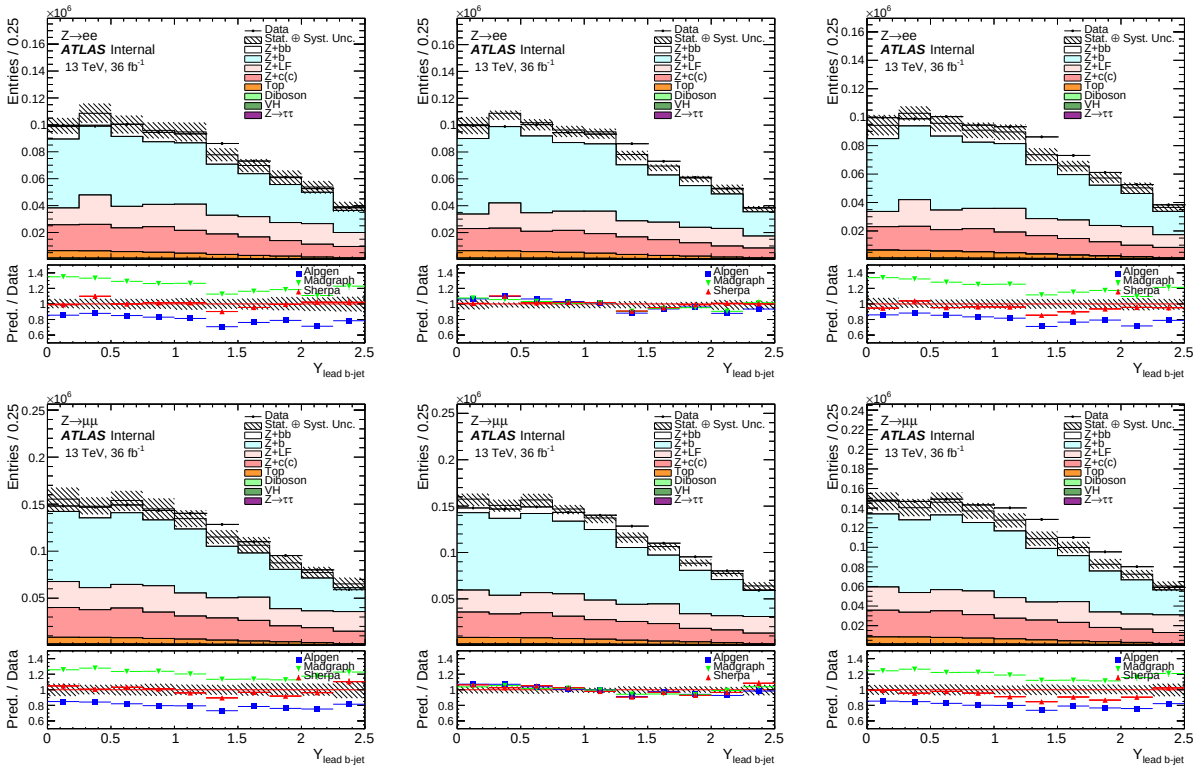

Figure 12.9: Detector level plots of the leading b-jet rapidity in the $\geq 1b$-jet signal region for the electron channel (top) and the muon channel (bottom). Left column: Before flavor fit; Middle column: After flavor fit (scaling signal and Z + jets backgrounds); Right column: After flavor fit (scaling only Z + jets backgrounds).

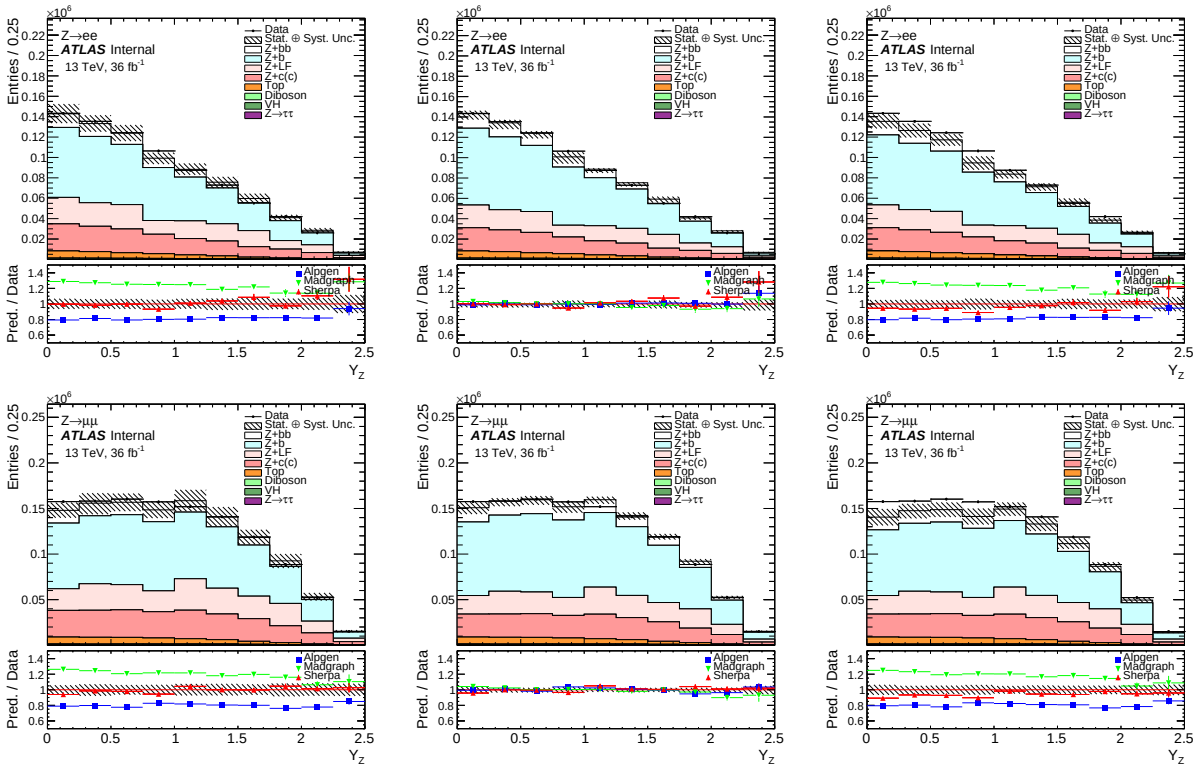

Figure 12.10: Detector level plots of the rapidity of the Z Boson in the $\geq 1b$-jet signal region for the electron channel (top) and the muon channel (bottom). Left column: Before flavor fit; Middle column: After flavor fit (scaling signal and Z + jets backgrounds); Right column: After flavor fit (scaling only Z + jets backgrounds).

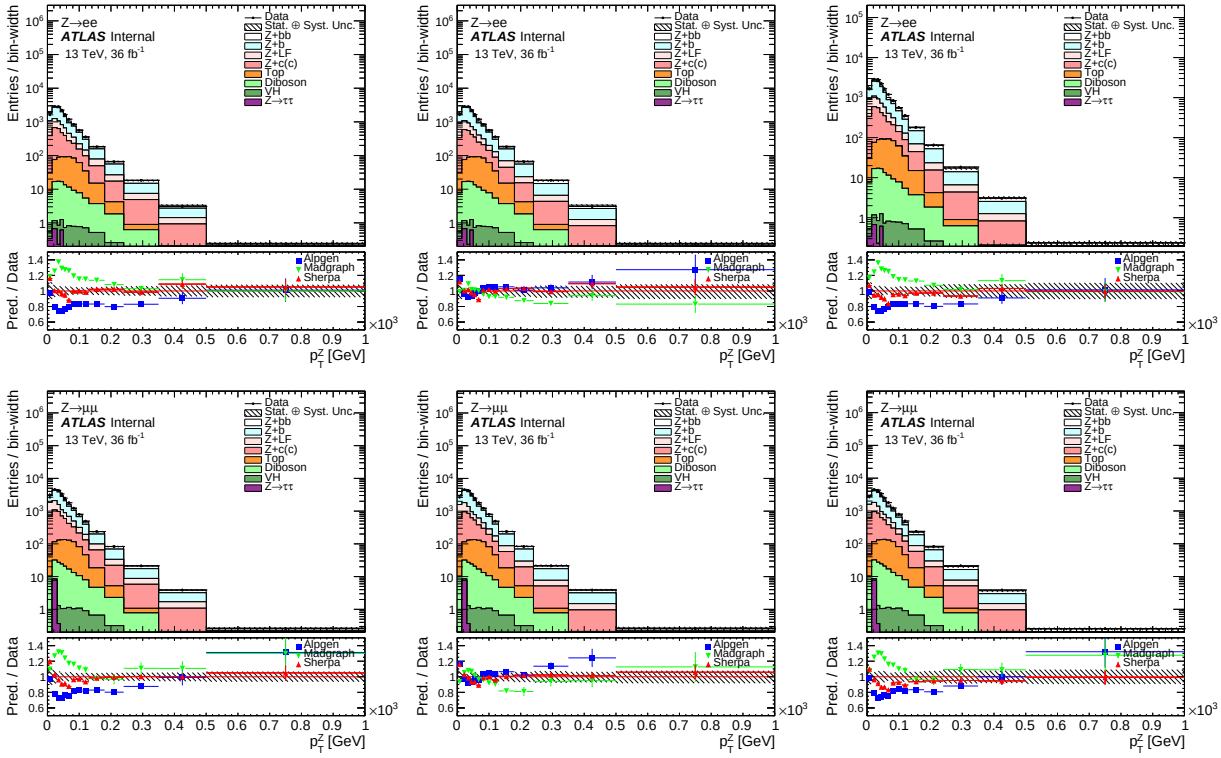

Figure 12.11: Detector level plots of the Z boson p_T in the $\geq 1b$-jet signal region for the electron channel (top) and the muon channel (bottom). Left column: Before flavor fit; Middle column: After flavor fit (scaling signal and Z + jets backgrounds); Right column: After flavor fit (scaling only Z + jets backgrounds).

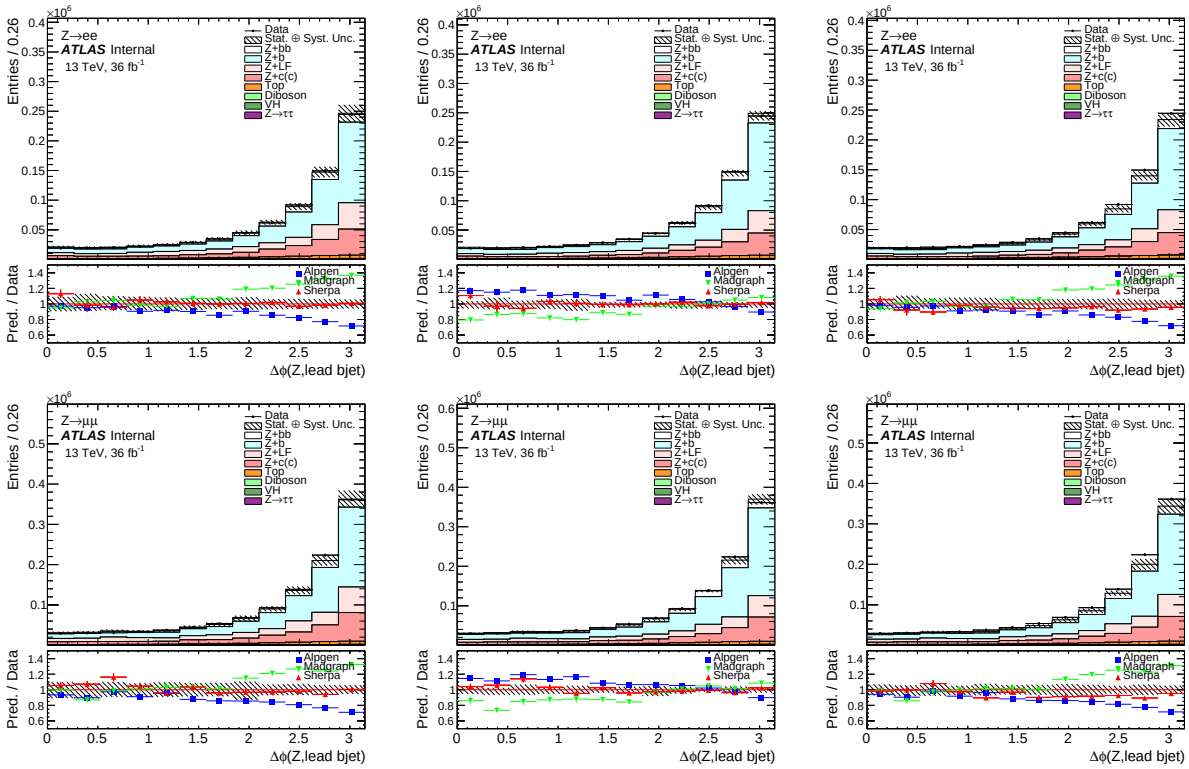

Figure 12.12: Detector level plots of $\Delta\phi$ between the Z boson and the leading b-jet in the $\geq 1b$-jet signal region for the electron channel (top) and the muon channel (bottom). Left column: Before flavor fit; Middle column: After flavor fit (scaling signal and Z + jets backgrounds); Right column: After flavor fit (scaling only Z + jets backgrounds).

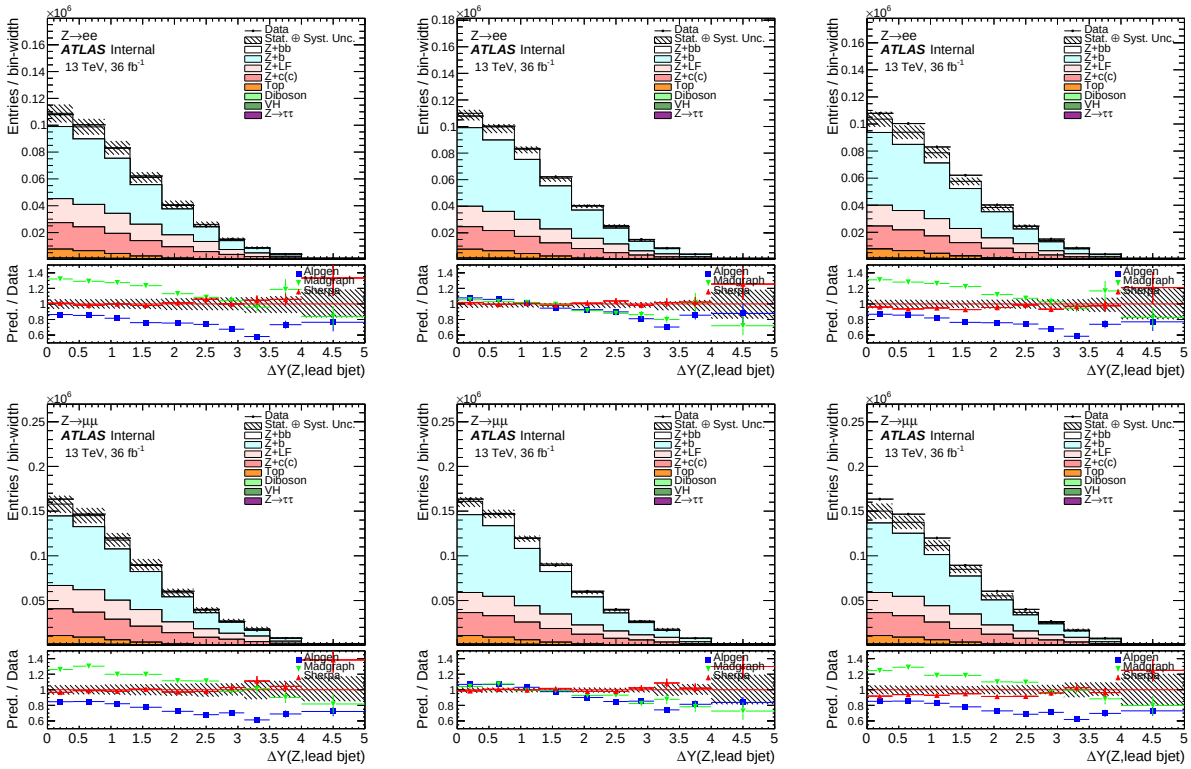

Figure 12.13: Detector level plots of ΔY between the Z boson and the leading b-jet in the $\geq 1b$-jet signal region for the electron channel (top) and the muon channel (bottom). Left column: Before flavor fit; Middle column: After flavor fit (scaling signal and Z + jets backgrounds); Right column: After flavor fit (scaling only Z + jets backgrounds).

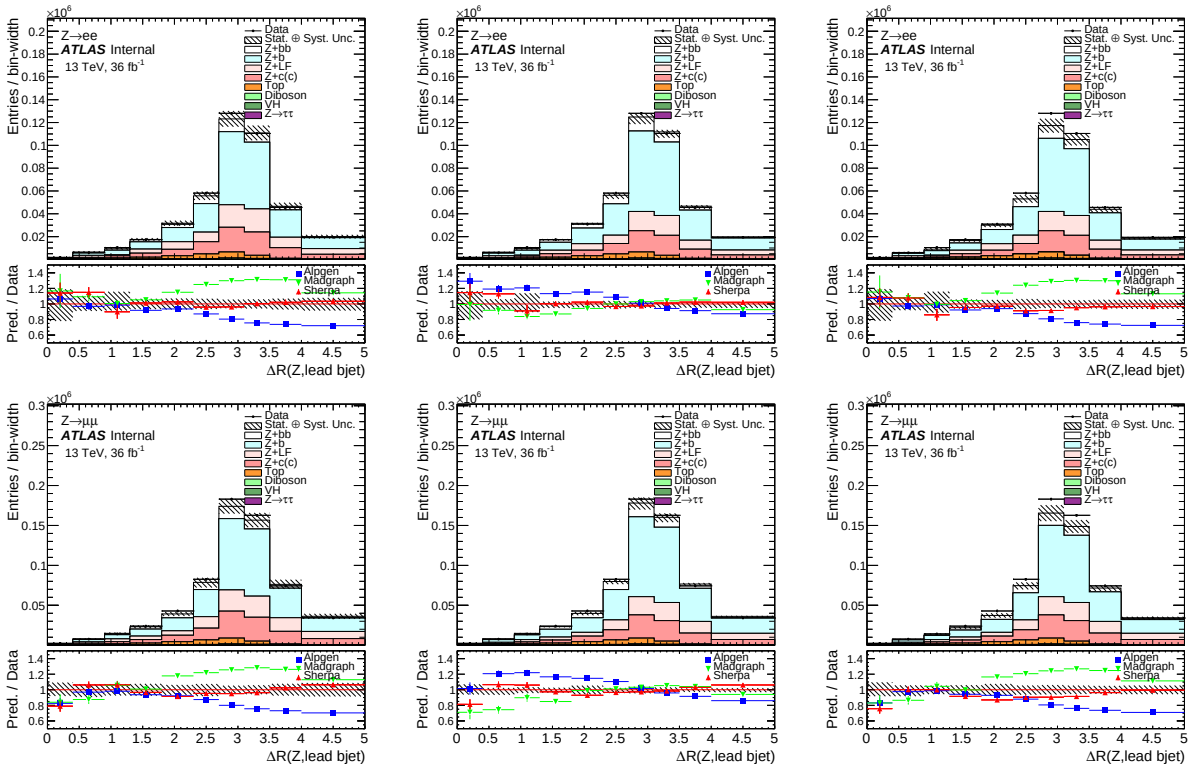

Figure 12.14: Detector level plots of ΔR between the Z boson and the leading b-jet in the $\geq 1b$-jet signal region for the electron channel (top) and the muon channel (bottom). Left column: Before flavor fit; Middle column: After flavor fit (scaling signal and Z + jets backgrounds); Right column: After flavor fit (scaling only Z + jets backgrounds).

12.3 Detector Level Plots in the Z+ $\geq 2b$-jets Signal Region

The plots in this section only include events which pass the full event selection, including the b-jet selection requirements. These events are required to have at least 2 $b-$jets. For each plot the distribution is shown without applying the scale factor from the flavor fit, with scale factors applied to both signal and background, and with the scale factors only applied to the background. The latter plots are the ones that are used for inputs in the unfolding, while the ones with both the signal and background scale factors allows for an additional check on the flavor fit.

Angular observable between the two leading b-jets are shown in figs. 12.15 to 12.17. More specifically in fig. 12.15, the $\Delta\phi$ distribution between the two leading b-jets is shown. It can be seen that all three generators model the data fairly well when both the signal and background scale factors from the flavor fit are applied. When only the background scale factors from the flavor fit are used, both Alpgen and Sherpa underestimate the normalization of the distribution as was anticipated from the plots shown in fig. 12.7. The predictions from Sherpa and Alpgen show similar shape in the distribution and both model the shape of $\Delta\phi$ in data fairly well.

In fig. 12.16 the difference in rapidity, ΔY, between the leading b-jets is shown. Both Sherpa and Alpgen model the shape of this distribution similarly and for the first several bins model the shape seen in data fairly well, however at around ΔY =2.5, discrepancies between the prediction and data can be seen and appear to increase as the number of entries in each bin decrease. These discrepancies carry over to the distributions of Δ between the two leading b-jets shown in fig. 12.17 where both Alpgen and Sherpa model the shape seen in data well for most of the distribution except for the last two bins which also correspond to the two bins with the least number of events.

The p_T of the Z boson is shown in fig. 12.18. Sherpa and Alpgen give very similar predictions for the shape of the distribution.

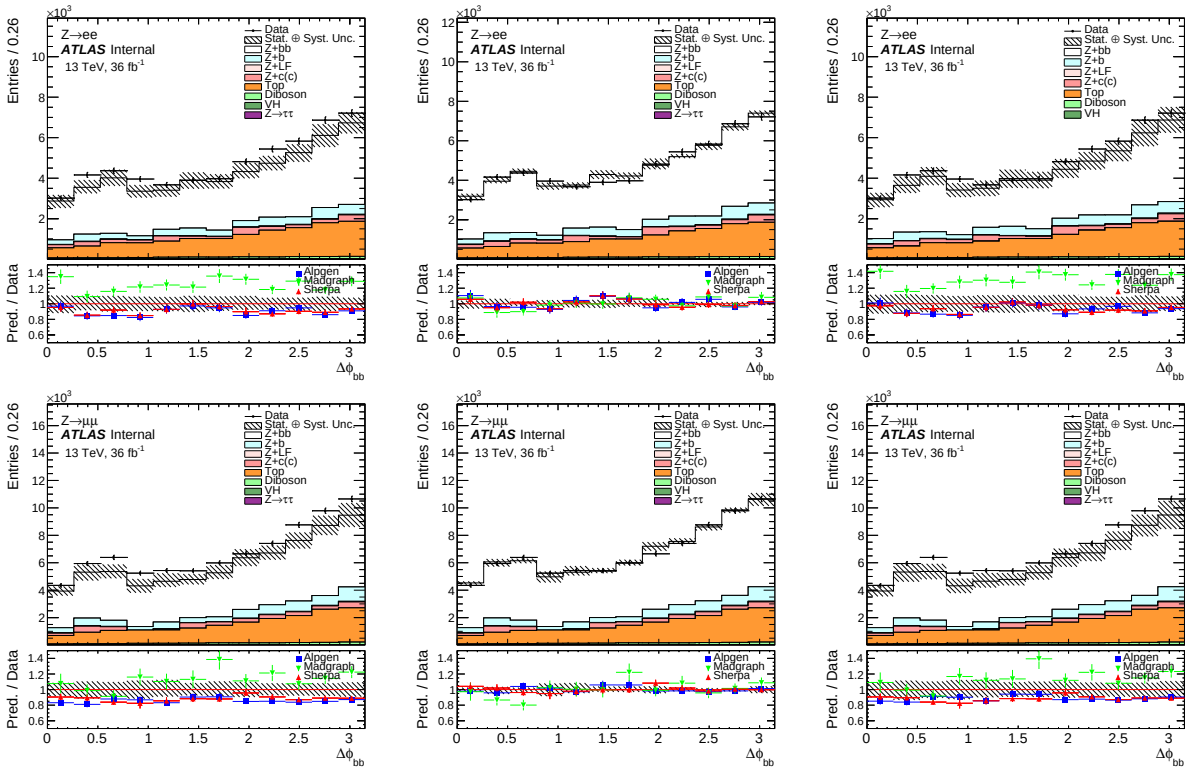

Figure 12.15: Detector level plots of $\Delta\phi$ between the two leading b-jets in the $\geq 2b$-jets signal region for the electron channel (top) and the muon channel (bottom). Left column: Before flavor fit; Middle column: After flavor fit (scaling signal and Z + jets backgrounds); Right column: After flavor fit (scaling only Z + jets backgrounds).

The two leading b-jet pair's p_T, invariant mass, and the ratio of the p_T to the invariant mass are shown in figs. 12.19 to 12.21. Discrepancies can be seen in the modeling of both the p_T and invariant mass which translates to discrepancies seen in their ratio.

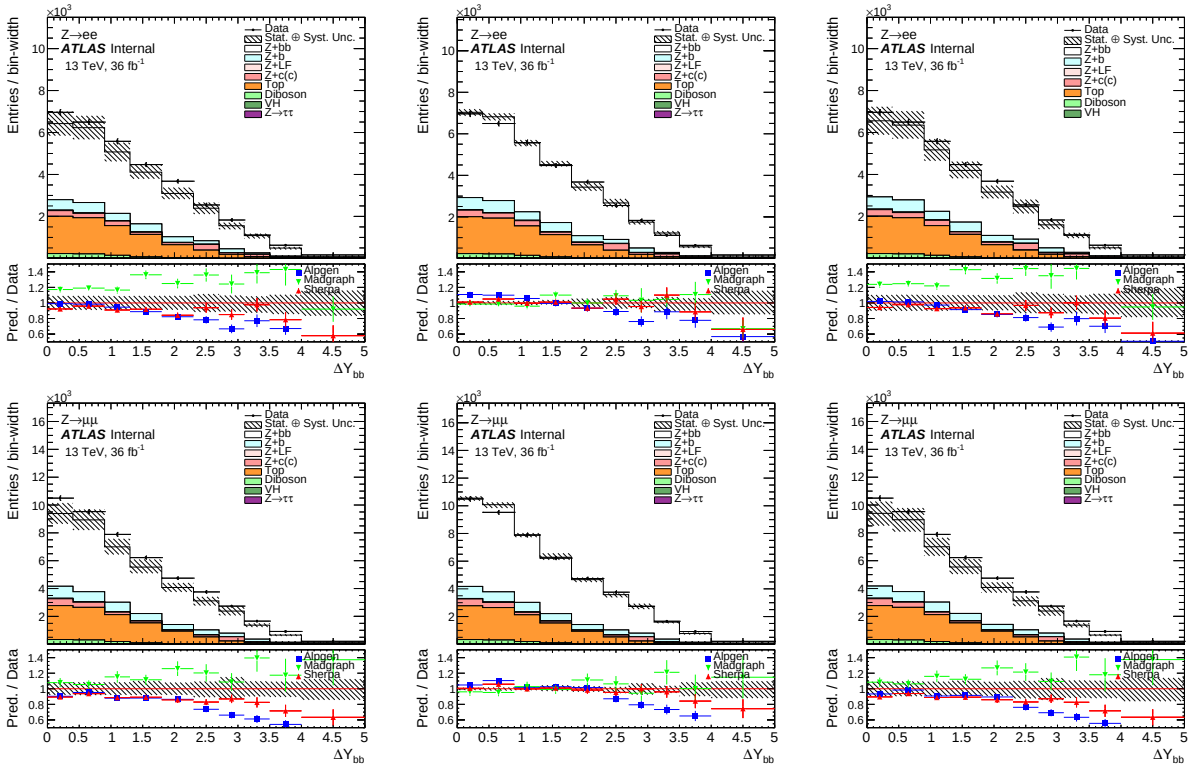

Figure 12.16: Detector level plots of ΔY between the two leading b-jets in the $\geq 2b$-jets signal region for the electron channel (top) and the muon channel (bottom). Left column: Before flavor fit; Middle column: After flavor fit (scaling signal and Z + jets backgrounds); Right column: After flavor fit (scaling only Z + jets backgrounds).

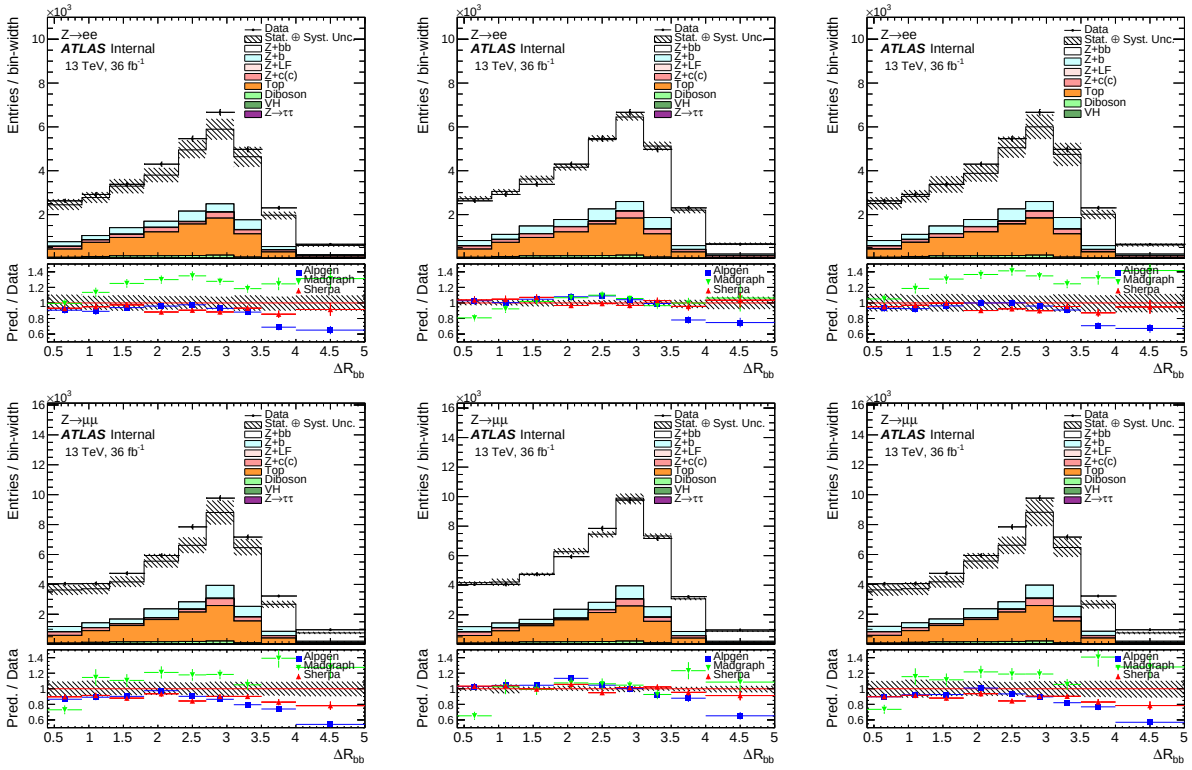

Figure 12.17: Detector level plots of ΔR between the two leading b-jets in the $\geq 2b$-jets signal region for the electron channel (top) and the muon channel (bottom). Left column: Before flavor fit; Middle column: After flavor fit (scaling signal and Z + jets backgrounds); Right column: After flavor fit (scaling only Z + jets backgrounds).

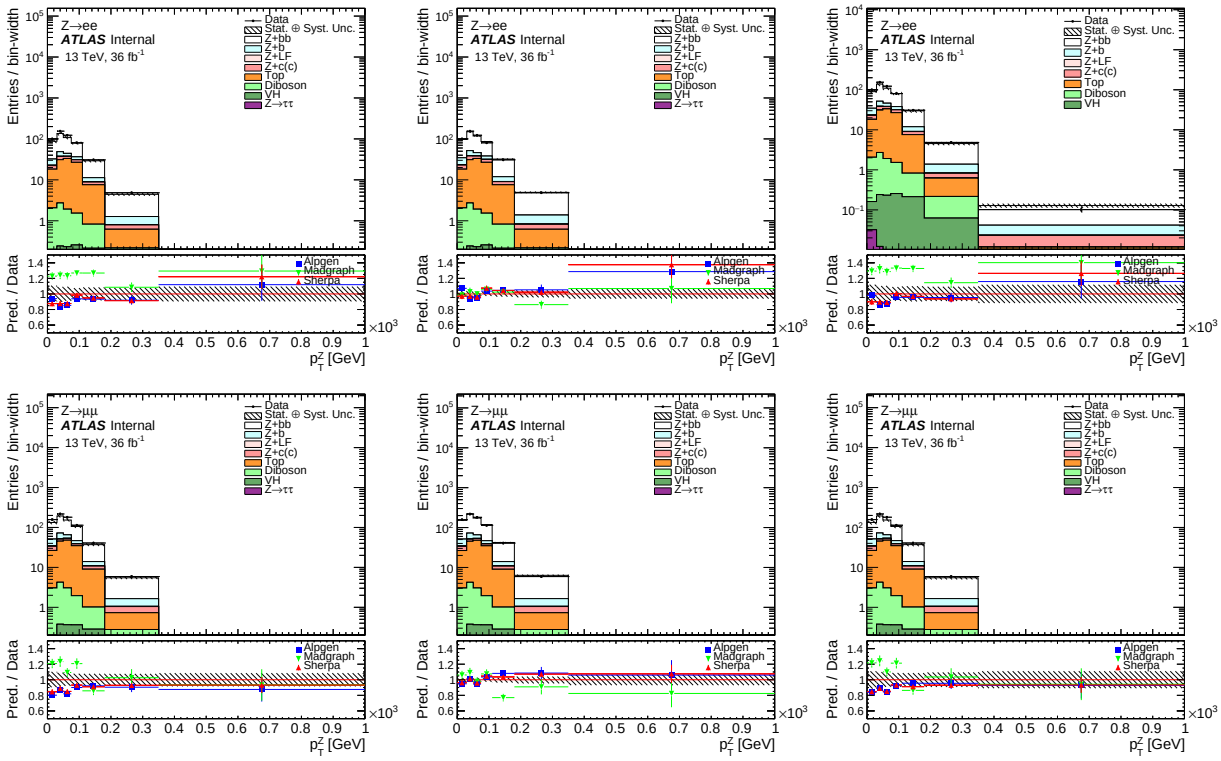

Figure 12.18: Detector level plots of the Z boson p_T in the $\geq 2b$-jets signal region for the electron channel (top) and the muon channel (bottom). Left column: Before flavor fit; Middle column: After flavor fit (scaling signal and Z + jets backgrounds); Right column: After flavor fit (scaling only Z + jets backgrounds).

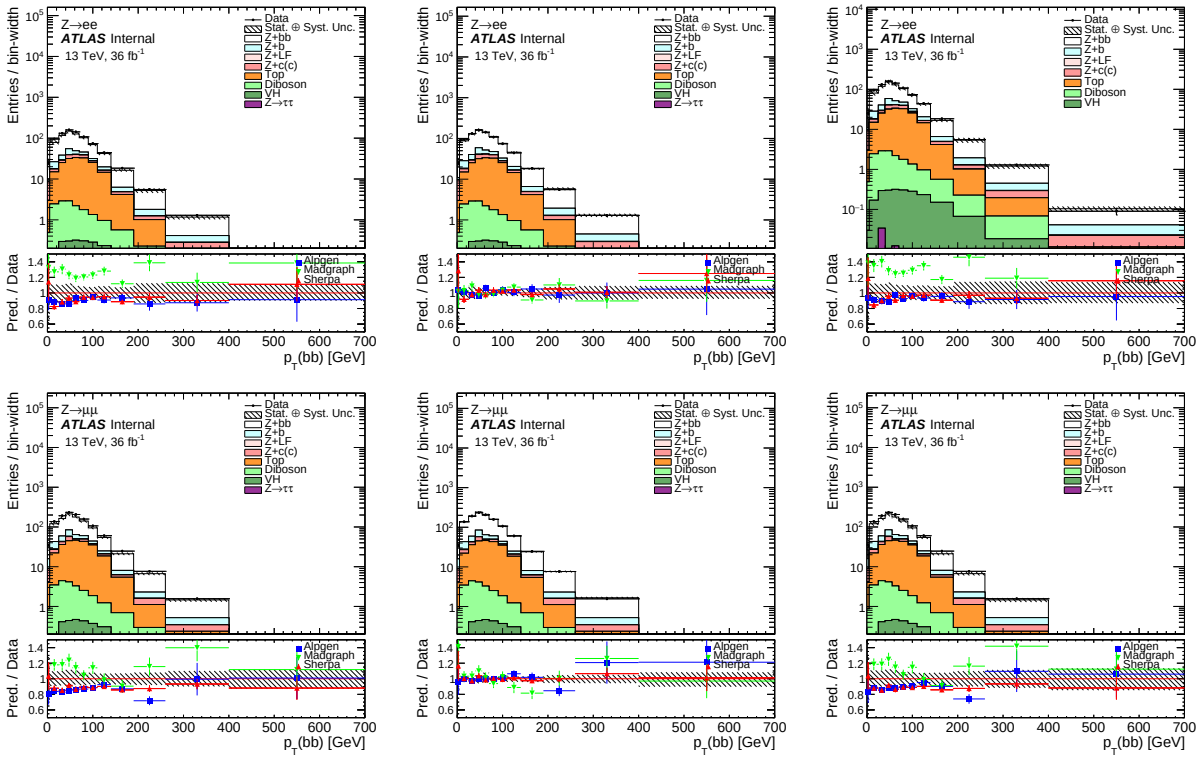

Figure 12.19: Detector level plots of the p_T of the sum of the two leading b-jets four-vectors in the $\geq 2b$-jets signal region for the electron channel (top) and the muon channel (bottom). Left column: Before flavor fit; Middle column: After flavor fit (scaling signal and Z + jets backgrounds); Right column: After flavor fit (scaling only Z + jets backgrounds).

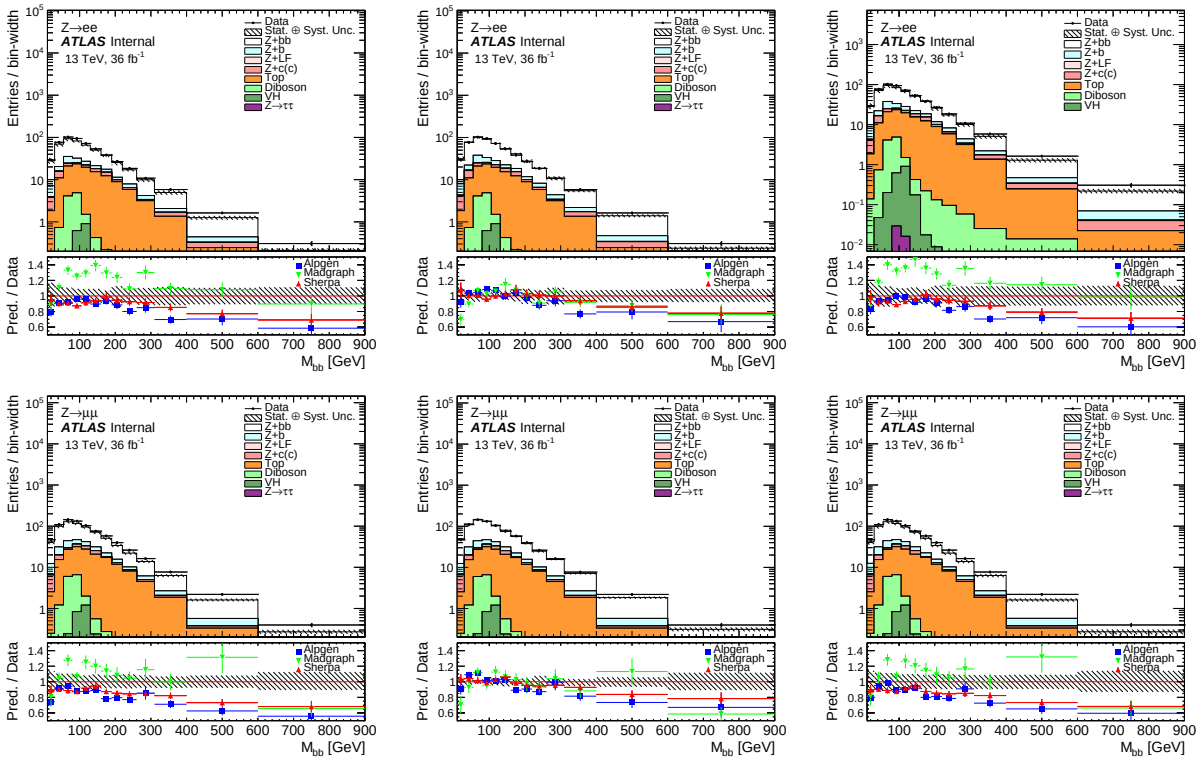

Figure 12.20: Detector level plots of the invariant mass of the two leading b-jets in the $\geq 2b$-jets signal region for the electron channel (top) and the muon channel (bottom). Left column: Before flavor fit; Middle column: After flavor fit (scaling signal and Z + jets backgrounds); Right column: After flavor fit (scaling only Z + jets backgrounds).

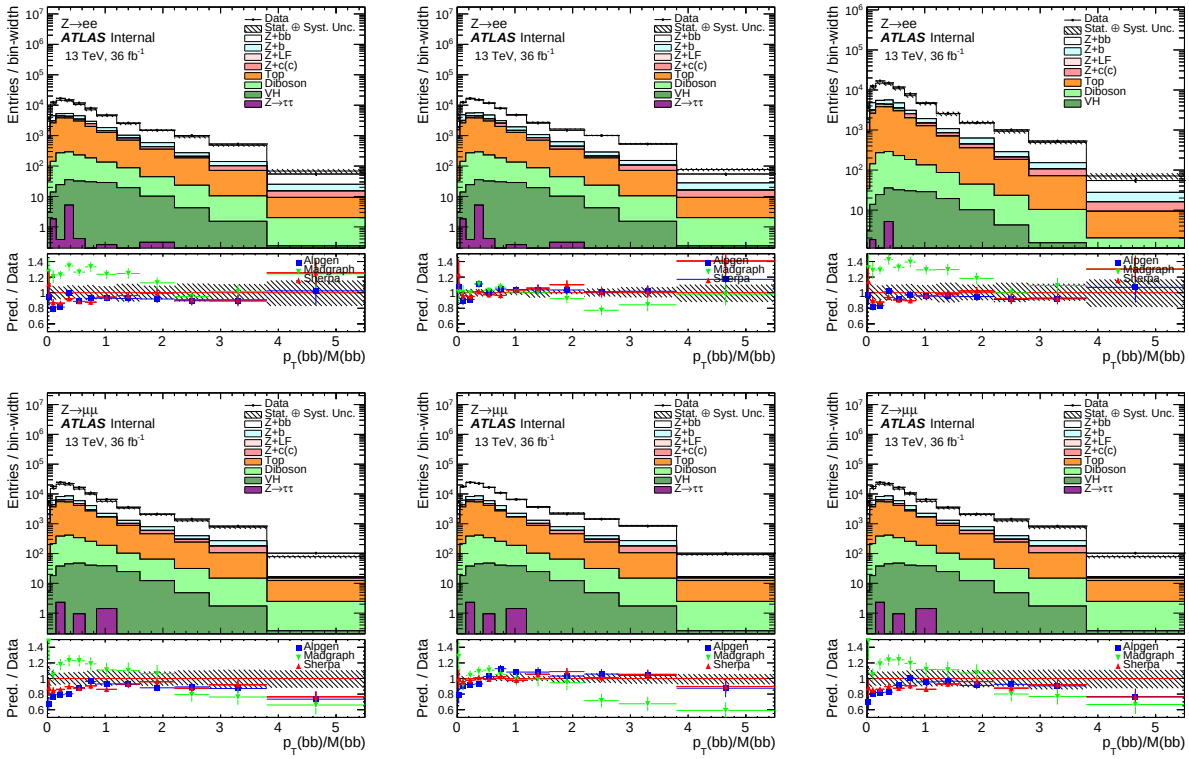

Figure 12.21: Detector level plots of the p_T of the sum of the two leading b-jets four-vectors divided by the invariant mass of them in the $\geq 2b$-jets signal region for the electron channel (top) and the muon channel (bottom). Left column: Before flavor fit; Middle column: After flavor fit (scaling signal and Z + jets backgrounds); Right column: After flavor fit (scaling only Z + jets backgrounds).

CHAPTER 13

UNFOLDING

13.1 Introduction

The distributions so far have been at the detector level. They are distorted due to experimental limitations and are obviously dependent on the performance of the ATLAS detector. We want to make the measurements of the Z boson at the particle level, independent of the detector used, so that it can be easily comparable with theoretical calculations and also comparable to measurements from other experiments. This is done by a procedure known as unfolding. The procedure accounts for the inefficiency and resolution effects in both the jet selection and Z boson selection. It also accounts for differences between the kinematic region identified with detector level selection and the fiducial one defined at the particle level.

The unfolding procedure is performed on data after all backgrounds have been subtracted from it. Backgrounds are estimated according to section 5.2. The scale factors extracted from the flavor fit are applied to the Z+jets background components.

This section will give a brief introduction to unfolding and some of the methods used to unfold.

Suppose we are interested in some variable, y, at the truth level, and that it is distributed according to the pdf $f_{true}(y)$. For example y could be the leading jets p_t. If we don't know the form of the pdf in terms of a finite number of parameters, we can simply represent it as a histogram of y with a finite number of bins. The probability to find y in *bin* i, p_i, is then simply given by

$$\begin{aligned} p_i &= \int_{bin\ i} f_{true}(y)dy \\ &= \frac{\mu_i}{\mu_{tot}}, \end{aligned} \tag{13.1}$$

where μ_i is the expectation value of the number of events in *bin* i of the true histogram.

Simply put, the aim of unfolding is to construct estimators for all the μ_i.

First introduce a few terms, from data we have a sample of measured values of x, which in our case will be a direct measurement of y. So for example x could be the lead jet p_t at the detector level and y could be the lead jet p_t at the particle level. n_i will be the observed number of events of measured value x, in *bin i* of the histogram. ν_i is the expectation value of n_i. From simple probability, we have,

$$\nu_i = \mu_{tot} P(\textit{event is observed in bin } i), \tag{13.2}$$

where μ_{tot} is the expectation value of the total number of events in the true histogram, and P stands for probability. Using the law of total probability, $P(A) = \sum_y P(A|B_y)P(B_y)$, and introducing the efficiency (ie the probability an event is observed), $\varepsilon(y)$, we can rewrite eq. (13.2) as

$$\begin{aligned} \nu_i &= \mu_{tot} \int dy P(A_i|B_y)\varepsilon(y) f_{true}(y), \\ &= \mu_{tot} \int_{bin\ i} dx \int dy P(A_x|B_y)\varepsilon(y) f_{true}(y) \end{aligned} \tag{13.3}$$

where A_x means the observed value is x and B_y means the true value is y and the event is detected. Therefore, $P(A_x|B_y)$ is the conditional probability that the observed value is x given that the true value was y and the event was detected. Expanding out the integral over y in eq. (13.3) as a sum over all bins results in:

$$\nu_i = \sum_{j=1}^{M} \mu_{tot} \int_{bin\ i} dx \int_{bin\ j} dy P(A_x|B_y)\varepsilon(y) f_{true}(y), \tag{13.4}$$

where M, is the number of bins in the true histogram. Multiplying top and bottom of

eq. (13.4) by μ_j we finally arrive at:

$$\begin{aligned} \nu_i &= \sum_{j=1}^{M} R_{ij}\mu_j \\ R_{ij} &= \frac{\int_{bin\ i} dx \int_{bin\ j} dy P(A_x|B_y)\varepsilon(y)f_{true}(y)}{\mu_j/\mu tot}, \end{aligned} \tag{13.5}$$

From eq. (13.5) we can see that the numerator of R_{ij} is just $P(A_i \cap D_j)$, where D_j means the true value y is in *bin* j. The denominator of R_{ij} is just $P(D_j)$. So R_{ij}, which is called the response matrix, can be written as:

$$\begin{aligned} R_{ij} &= \frac{P(A_i \cap D_j)}{P(D_j)} \\ &= P(A_i|D_j). \end{aligned} \tag{13.6}$$

From eq. (13.6) it becomes clear that each element of R_{ij} is just the conditional probability that an observed value will be in *bin* i given that the true value was in *bin* j.

It can be useful to think of the observed bins as "effects" and the true bins as "causes". In this sense the elements of the response matrix represent the conditional probability you will see effect i given that cause j has occurred. Up until now we have assumed that all the effects come from the true causes. But we must also take in account observing a value when there is no true event (ie background). Let β_i be the expectation value for the number of events in *bin* i which come from background processes, then the equation for ν_i in eq. (13.5) becomes:

$$\nu_i = \sum_{j=1}^{M} R_{ij}\mu_j + \beta_i. \tag{13.7}$$

The goal of unfolding is to construct an estimator, $\hat{\mu}$, for μ. The next few sections will go over three methods of unfolding using made up distributions to illustrate the method. The latter two methods are of course the methods used in this analysis.

The true histogram distribution is taken as a double Gaussian and our detector efficiency

is taken as a simple straight line. Both of which are shown in fig. 13.1. The detector resolution is modeled by just a simple Gaussian smear. We generate 10000 truth events from

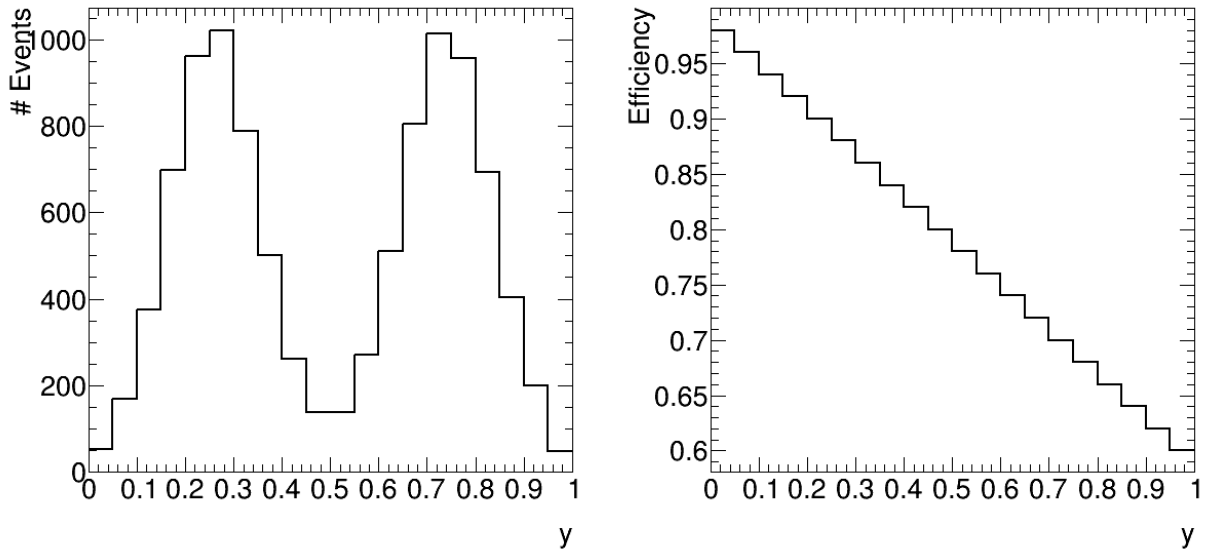

(a) (b)

Figure 13.1: (a) The true histogram distribution of y.(b) The efficiency of detecting an event as a function of the true value y.

the distribution given in fig. 13.1a. For each event a random number between 0 and 1 is generated and if this number is greater then the efficiency given in fig. 13.1b corresponding to the truth bin this event falls into, then the event is not observed in our MC measured. Otherwise, the event is Gaussian smeared and put into the appropriate bin of MC measured, as well as filled in the response matrix. To get our observed "data" we take the MC measured histogram and for each bin we take a random number from a Poisson distribution with expectation value equal to the number of events in the MC measured histogram bin. The resulting histograms are shown in fig. 13.2.

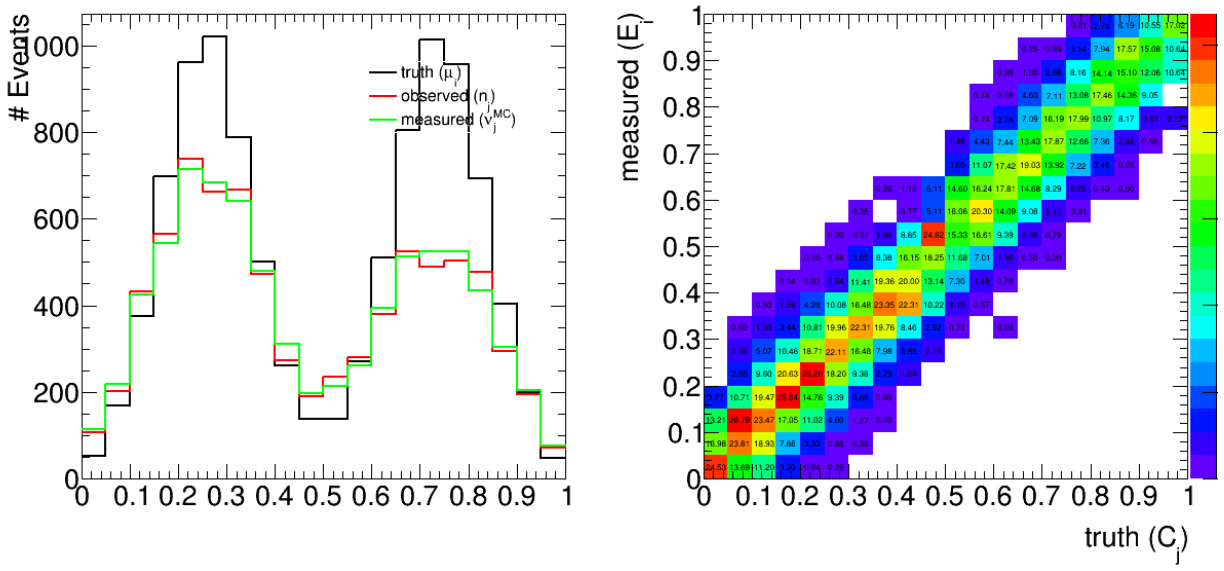

(a) (b)

Figure 13.2: (a) Black is the true histogram μ_i. Red is the observed histogram n_j. Green is the expecation value of the observed measurement ν_j.(b) The response matrix R_{ij}.

13.1.1 Method 1: Inverting Response Matrix

In general we can invert the response matrix. The result is:

$$\mu = \mathbf{R^{-1}}(\nu - \beta). \tag{13.8}$$

A simple choice for our estimator would then be:

$$\hat{\mu} = \mathbf{R^{-1}}(\mathbf{n} - \beta). \tag{13.9}$$

Using this estimator in our example from the previous section gives us the result shown in fig. 13.3. It is easy to see that this is not a very good choice of estimator. The unfolded result shows large fluctuations and large errors. The problem is that we are using n and not ν. The qualitative effect of applying the response matrix, R, is that it smears out some of the fine structure in the expectation values, but they are still there. Upon applying the

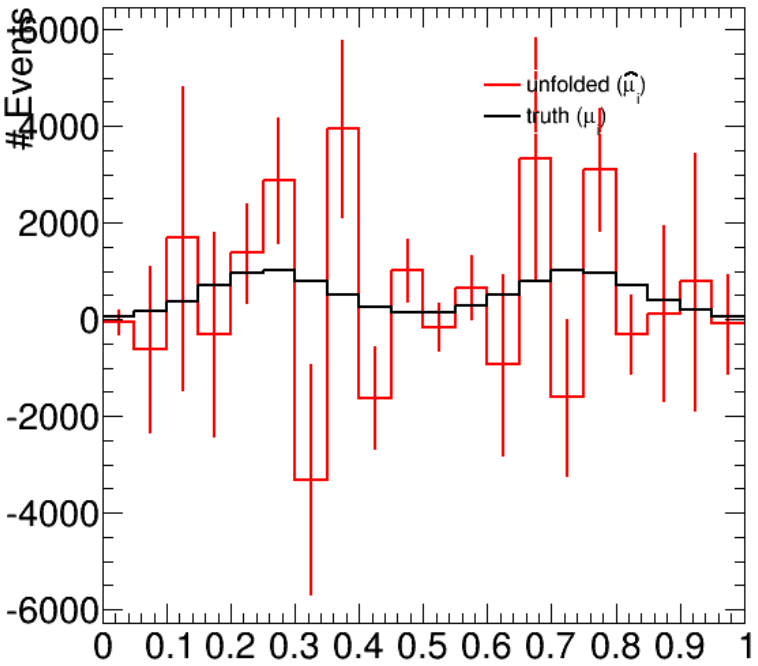

Figure 13.3: The truth histogram distribution along with the unfolded distribution using the inverted response matrix method.

inverse of the response matrix this fine structure is restored. However, we are using n, and when applying R^{-1} the statistical fluctuations of it are seen as small bumps resulting from initial fine structure that isn't actually there. However, there is something important to see in this choice of estimator. Look at the bias of this estimator. This is shown in eq. (13.10).

$$\begin{aligned} \mathbf{E}[\hat{\mu}] &= \mathbf{E}[\mathbf{R^{-1}}(\mathbf{n} - \beta)] \\ &= \mathbf{R^{-1}}(\mathbf{E}[\mathbf{n}] - \beta) \\ &= \mathbf{R^{-1}}(\nu - \beta) \\ &= \mu \end{aligned} \tag{13.10}$$

So this estimator has zero bias. In fact it can be shown that this estimator has the smallest possible covariance among all unbiased estimators. However, as is shown the covariance is

rather large for this example. So in order to reduce the variance the estimator constructed will necessarily have a bias. So the goal then becomes to construct an estimator with a small bias but greatly reduced variance. This leads to our next two methods.

13.1.2 Method 2: Bin-by-Bin Unfolding

The bin-by-bin method of unfolding takes as its estimator:

$$\begin{aligned} \hat{\mu_i} &= C_i(n_i - \beta_i) \\ C_i &= \frac{\mu_i^{MC}}{\nu_i^{MC}}, \end{aligned} \tag{13.11}$$

where ν_i^{MC} and μ_i^{MC} are obtained from Monte Carlo simulations for signal only. ν_i^{MC} includes detector simulation. For our analysis this method is used to unfold the b-jet multiplicity, where the unavailability of flavor fit results in the 3 b-jet bin makes impossible more complicated approaches.

Figure 13.4 shows the resulting unfolded result using this estimator on our example histograms. The results look great, and for our example they actually are, and by looking at the bias we can see why this method works well for our example and something important to keep in mind when seeing this method used. Looking at the expectation value of the estimator:

$$\begin{aligned} \mathbf{E}[\hat{\mu_i}] &= \mathbf{E}[C_i(n_i - \beta_i)] \\ &= C_i(\nu_i - \beta_i) \\ &= \frac{\mu_i^{MC}}{\nu_i^{MC}}\nu_i^{sig} \\ &= (\frac{\mu_i^{MC}}{\nu_i^{MC}} - \frac{\mu_i}{\nu_i^{sig}})\nu_i^{sig} + \mu_i \end{aligned} \tag{13.12}$$

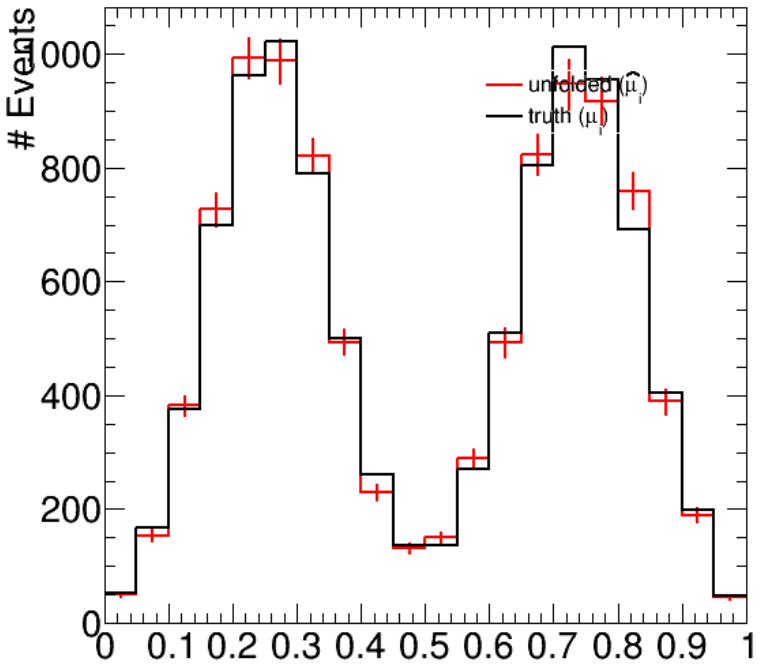

Figure 13.4: The truth histogram distribution along with the unfolded distribution using the bin-by-bin method.

From eq. (13.12) the bias, b_i can easily be seen as,

$$b_i = (\frac{\mu_i^{MC}}{\nu_i^{MC}} - \frac{\mu_i}{\nu_i^{sig}})\nu_i^{sig} \tag{13.13}$$

Using eq. (13.13) we can see that the method will have zero bias if the ratios from the Monte Carlo model are the same as those in the real experiment. In our simple example the Monte Carlo model and the real experiment are the same thing so there is no bias. The examples observed data was generated from the Monte Carlo model, where as in an actual experiment observed data obviously comes from a physical measurement. One of the dangers of this method is that the bias tends to pull the estimates of the true values, $\hat{\mu}_i$, towards the ones predicted by the MC, μ_i^{MC}. As such it is important to include in the estimated systematic errors an estimate of the bias, that is, the model dependence on the correction factors.

13.1.3 Method 3: Iterative Bayesian Unfolding

To motivate this method we will return to our response matrix and its description using "effect" and "cause". So just relabel eq. (13.6) as follows:

$$R_{ij} = P(E_i|C_j), \tag{13.14}$$

where E_i is the measured value, x, is in *bin* i and C_i is the true value, y, is in *bin* j. Again using lead jet p_t as an example then each element in eq. (13.14) would represent the probably the measured lead jet p_t was in *bin* i given that true lead jet p_t was in *bin* j. Use the following as an estimator:

$$\hat{\mu_j} = \frac{1}{\varepsilon_j} \sum_{i=1}^{N} n_i P(C_j|E_i). \tag{13.15}$$

The motivation behind this estimator is fairly straightforward. Each effect, E_i, had to come from some cause, C_j, and a certain percentage, $P(C_j|E_i)$, of the effect E_i came from the cause C_j. So we are just simply summing up the number of events in each effect bin that came from cause C_j. We also need to divide by the efficiency of detecting cause C_j to account for the events that didn't result in any effect.

The strategy of this method is coming up with an estimate for $P(C_j|E_i)$. Remember the response matrix gives us $P(E_i|C_j)$. Using Bayes Theorem:

$$\begin{aligned} P(C_j|E_i) &= \frac{P(E_i|C_j)P(C_j)}{P(E_i)} \\ &= \frac{P(E_i|C_j)P(C_j)}{\sum_{k=1}^{M} P(E_i|C_k)P(C_k)}. \end{aligned} \tag{13.16}$$

Substituting eq. (13.16) into eq. (13.15) gives us the following equation for our estimator:

$$\begin{aligned}\hat{\mu_j} &= \frac{1}{\varepsilon_j}\sum_{i=1}^{N} n_i \frac{P(E_i|C_j)P(C_j)}{\sum_{k=1}^{M} P(E_i|C_k)P(C_k)} \\ &= \frac{1}{\varepsilon_j}\sum_{i=1}^{N} n_i \frac{R_{ij}P(C_j)}{\sum_{k=1}^{M} R_{ik}P(C_k)}.\end{aligned} \tag{13.17}$$

In eq. (13.17) one still has to choose what to use for $P(C_j)$. This is where the iterations come in. After choosing starting values for $P_0(C_j)$, after each iteration $P(C_j)$ is update with the value from the previous iteration:

$$P_1(C_j) = \frac{\hat{\mu_j}}{\sum_{k=1}^{M} \hat{\mu_k}}. \tag{13.18}$$

For this analysis we use truth MC for $P_0(C_j)$. The more iterations that are performed, the less the dependence on the MC truth distribution. However, each iteration increases the variance and to many iterations results in bin-by-bin fluctuations similar to what one gets in method 1. Figure 13.5 shows this method applied to our simple example for different number of iterations used. As this is the method of unfolding used in our analysis a separate section is devoted to discussing estimating the systematics associated with using this method to unfold the data.

13.2 Particle Level

The fiducial region in which the cross-section measurements are made correspond to a similar phase space of the detector level distributions. Selection in the fiducial region is performed at the particle level. The selection of physics objects in the fiducial region is given in table 13.1.

The reconstruction of the particle level objects follows the description given in [95]. The four-momentum vector of particle level leptons are corrected for final state photon radiation.

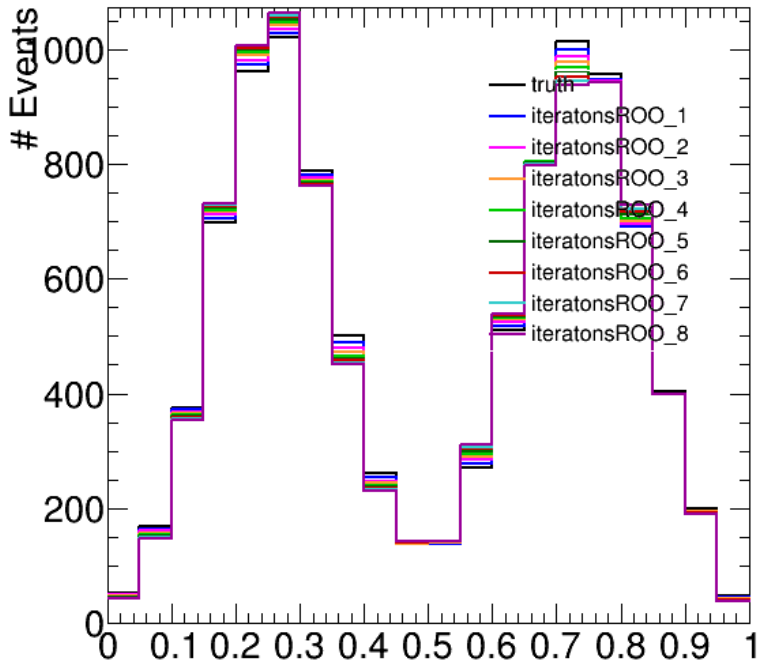

Figure 13.5: The truth histogram distribution along with the unfolded distribution using the iterative Bayesian method with various number of iterations applied.

Object Selection	Acceptance cuts
leptons	$p_T > 27$ GeV and $\|\eta\| < 2.5$
Z Boson	2 same flavor and oppositely charged leptons 76 GeV $< m_{ll} <$ 106 GeV
b-jets	matched with a b-hadron $p_T > 20$ GeV and $\|y\| < 2.5$ ΔR(b-jets, l) >0.4

Table 13.1: Object Selection in fiducial region.

This is done by summing the four-momentum vector of all photons that are contained in a cone of ΔR$<$ 0.1 around the final state lepton and adding it to the lepton's four-momentum. The resulting leptons are often referred to as dressed leptons.

Particle level jets are constructed from all stable final-state particles, excluding the dressed leptons, using the anti-kt algorithm with radius parameter R=0.4. This is the same

algorithm that was used to construct the detector level jets. Jets are classified as b-jets using the same hadron cone matching that was used in section 7.3.2. If a b-hadron is contained in a cone of ΔR$<$ 0.3 around the jet then the jet is considered a b-jet.

13.3 Response Matrices

The response matrices used in the unfolding are constructed by first constructing migration matrices. A migration matrix is produced for each distribution that is unfolded. They are a two-dimensional square matrix with bins of the particle-level distribution along the x-axis and bins of the detector level distribution along the y-axis. The migration matrices are filled using "matched" events in the signal MC. Matched events are events which pass both the detector level selection and the truth(particle) level selections[1]. The response matrix is then obtained from the migration matrix by dividing each entry in it by the number of events in the bin of the truth distribution corresponding to the column that entry is in[2].

The response matrices for the leading b-jet p_T and rapidity are shown in figs. 13.6 and 13.7 for the Z + $\geq 1b$-jet signal region using Sherpa as the signal MC. The response matrices for the other distributions that are unfolded can be found in Appendix D.1. The sum of the entries in any given column of the response matrix gives the efficiency of reconstructing an event corresponding to that truth bin. That is, the probability that an event in any given truth bin is reconstructed at the detector level is equal to the sum of the corresponding column in the response matrix. It can be seen in the response matrices that entries in the muon channel are typically higher than in the electron channel reflecting that the efficiency of reconstructing muons is higher than the efficiency of reconstructing electrons for the

1. This means the projections of the migration matrix along the x-axis or y-axis do not give the full truth level distribution or reconstruction level distribution but instead give subsets of the corresponding distributions.

2. If M_{ij} is the migration matrix and μ_j is the number of events in bin j of the truth distribution, then $R_{ij} = \frac{M_{ij}}{\mu_j}$

selections used.

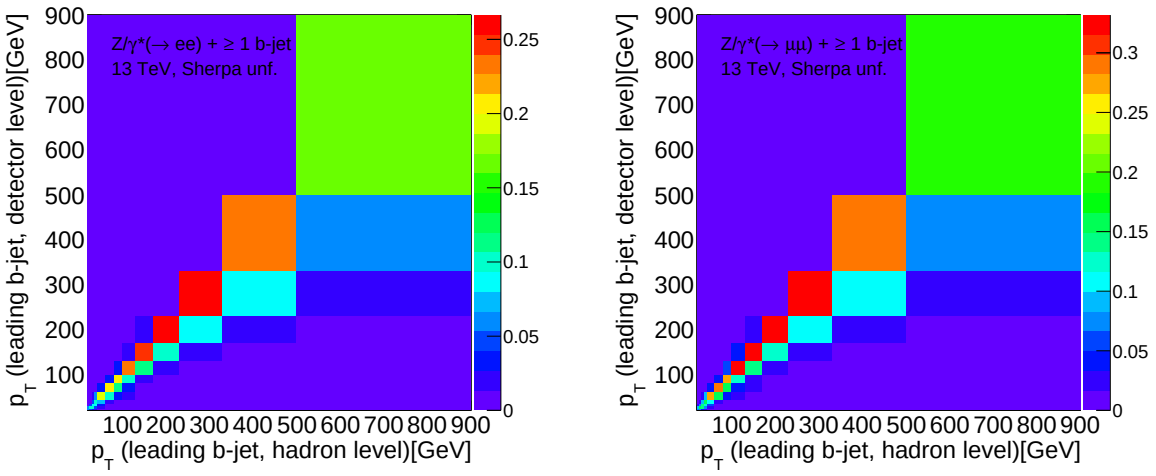

Figure 13.6: Response matrix for the leading b-jet p_T for the Z + $\geq 1b$-jet signal region in the electron channel (left) and muon channel (right) using Sherpa.

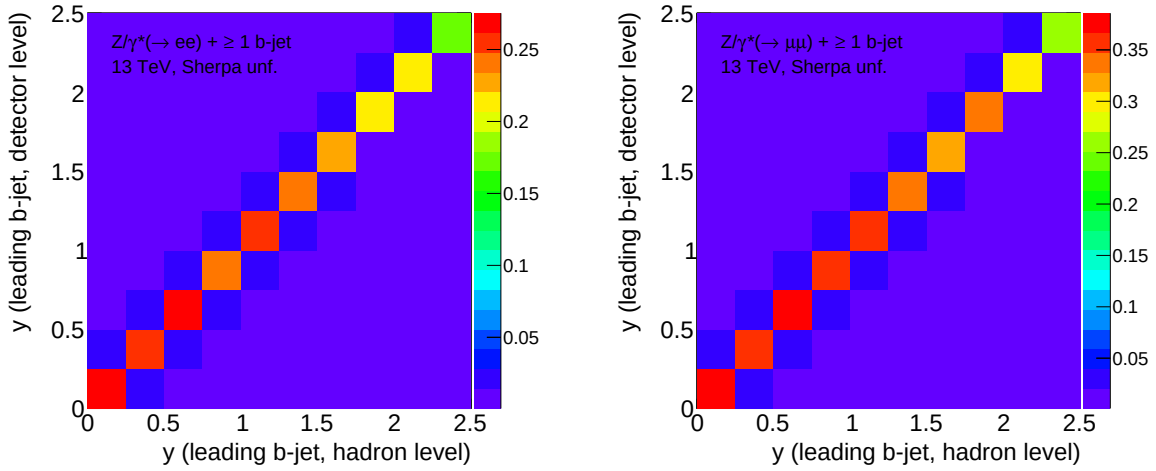

Figure 13.7: Response matrix for the leading b-jet rapidity for the Z + $\geq 1b$-jet signal region in the electron channel (left) and muon channel (right) using Sherpa.

There are several sources of the inefficiency of an event passing the truth level selection but failing the detector level selection. For example, the lepton identification inefficiencies, the trigger inefficiencies, or the b-tag inefficiencies. There are also small differences in the phase space of the two regions. For example, there is a difference in η for the electron

selection in the truth selection and detector level selection (the detector level selection does not include electrons in the crack region of the calorimeter). The reconstruction efficiency for the leading b-jet p_T and rapidity are shown in figs. 13.8 and 13.9 for the Z + $\geq 1b$-jet signal region for all three generators. The reconstruction efficiencies of the other distributions that are unfolded are included in Appendix D.2.

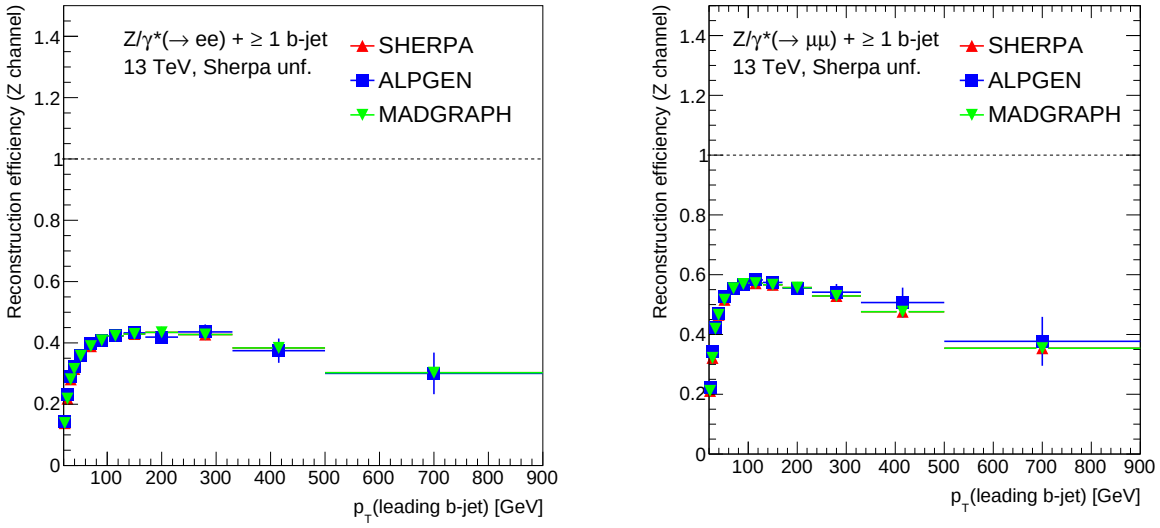

Figure 13.8: Reconstruction efficiency of the leading b-jet p_T for the Z + $\geq 1b$-jet signal region in the electron channel (left) and muon channel (right) using Sherpa.

13.4 Fake Corrections

A correction is made prior to unfolding to account for events which pass the detector level selection but fail the particle level selection. When thinking of the response matrix in terms of cause and effect this type of event would be an effect with no corresponding cause. An example of a cause of this, would be a jet reconstructed with a p_T above the selection threshold at the detector level but below the threshold at the truth level. To account for this effect a fake correction is applied to both the background-subtracted data and to the reconstructed MC signal sample. It is a bin-by-bin correction defined by the ratio of the

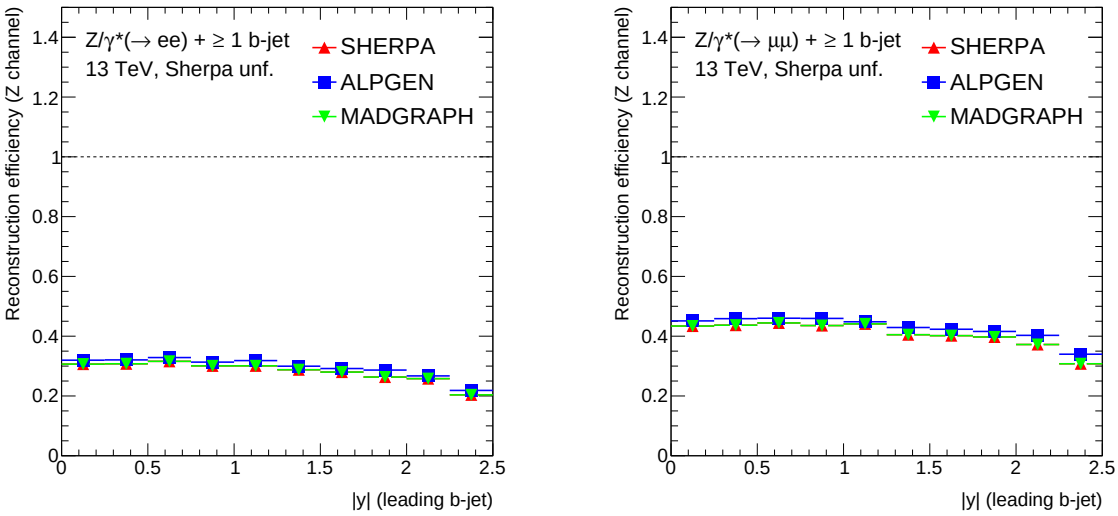

Figure 13.9: Reconstruction efficiency of the leading b-jet rapidity for the Z + $\geq 1b$-jet signal region in the electron channel (left) and muon channel (right) using Sherpa.

detector level distribution of matched events divided by the detector level distribution of all events passing detector level selection (ie events in the denominator do not have truth selection applied to them). The fake corrections applied to the leading b-jet p_T and rapidity distributions are shown in figs. 13.10 and 13.11 for the Z + $\geq 1b$-jet signal region. The fake corrections for the other distributions that are unfolded are shown in Appendix D.3. The plots show that there is good agreement in the fake corrections obtained for the three different generator choices.

13.5 Closure Test

A simple closure test is performed to validate the consistency in the unfolding procedure. This is done using Sherpa as both pseudo-data and simulated signal MC. Roughly half of the events generated by Sherpa are used as pseudo-data and the other half are used to correct for the detector level effects (ie fake correction, response matrix, etc.). The Sherpa events are divided into the two categories according to their event number. Even events are used as

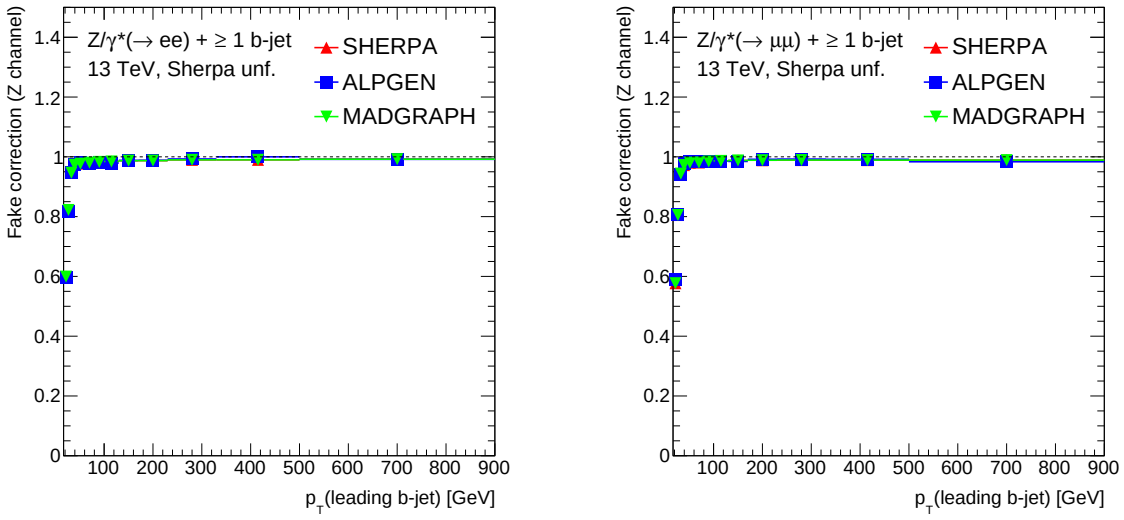

Figure 13.10: Fake correction of the leading b-jet p_T for the Z + $\geq 1b$-jet signal region in the electron channel (left) and muon channel (right) using Sherpa.

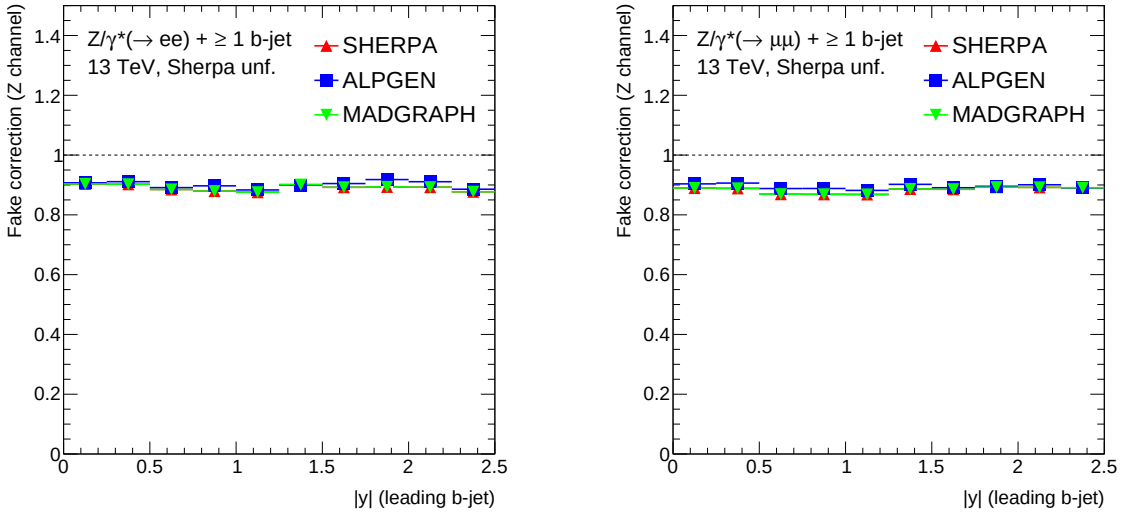

Figure 13.11: Fake correction of the leading b-jet rapidity for the Z + $\geq 1b$-jet signal region in the electron channel (left) and muon channel (right) using Sherpa.

pseudo data and odd numbered events are used for modeling. The results of this test for the leading b-jet p_T and rapidity are shown in figs. 13.12 and 13.13 for the Z + $\geq 1b$-jet signal region. The plots show closure of the unfolding procedure.

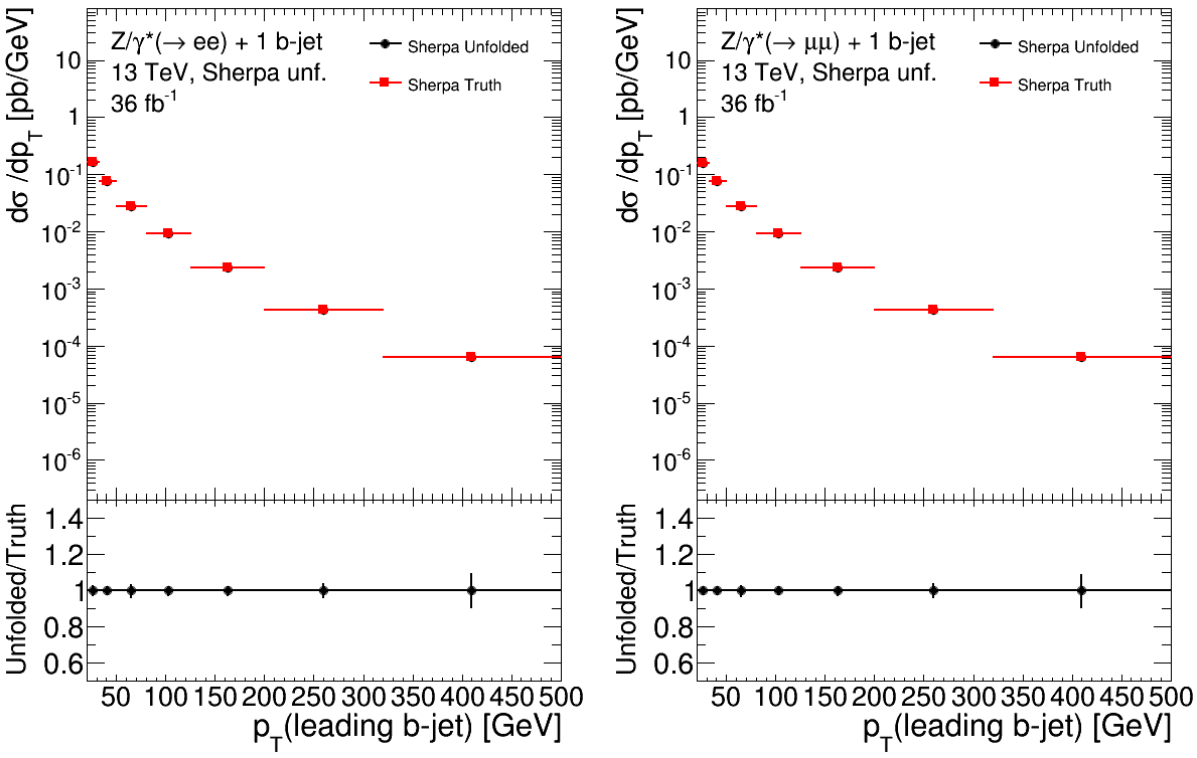

Figure 13.12: Closure test of the unfolding procedure using half of the Sherpa events as pseudo-data and other half to unfold the pseudo-data. Unfolding of the leading b-jet p_T for the Z + $\geq 1b$-jet signal region in the electron channel (left) and muon channel (right).

13.6 Integrated Cross Section

To determine the integrated cross section in the Z + $\geq 1b$-jet and Z + $\geq 2b$-jets signal regions the inclusive b-jet multiplicity distribution is unfolded. The bin-to-bin migrations are assumed to be small and this distribution is unfolded using the bin-by-bin method described in section 13.1.2. Using the iterative method would of required estimating the background in both the inclusive three b-jets bin and zero b-jets bin. The bin-by-bin scale factors, C_i in eq. (13.11), are defined as the number of MC events that pass the particle level selection divided by the number of MC events that pass the detector level selection. The resulting scale factors, $1/C_i$, are shown in table 13.2 for both Sherpa and Alpgen. The scale factors from Alpgen are used to define a modeling uncertainty which will be described more in section 13.7.1.

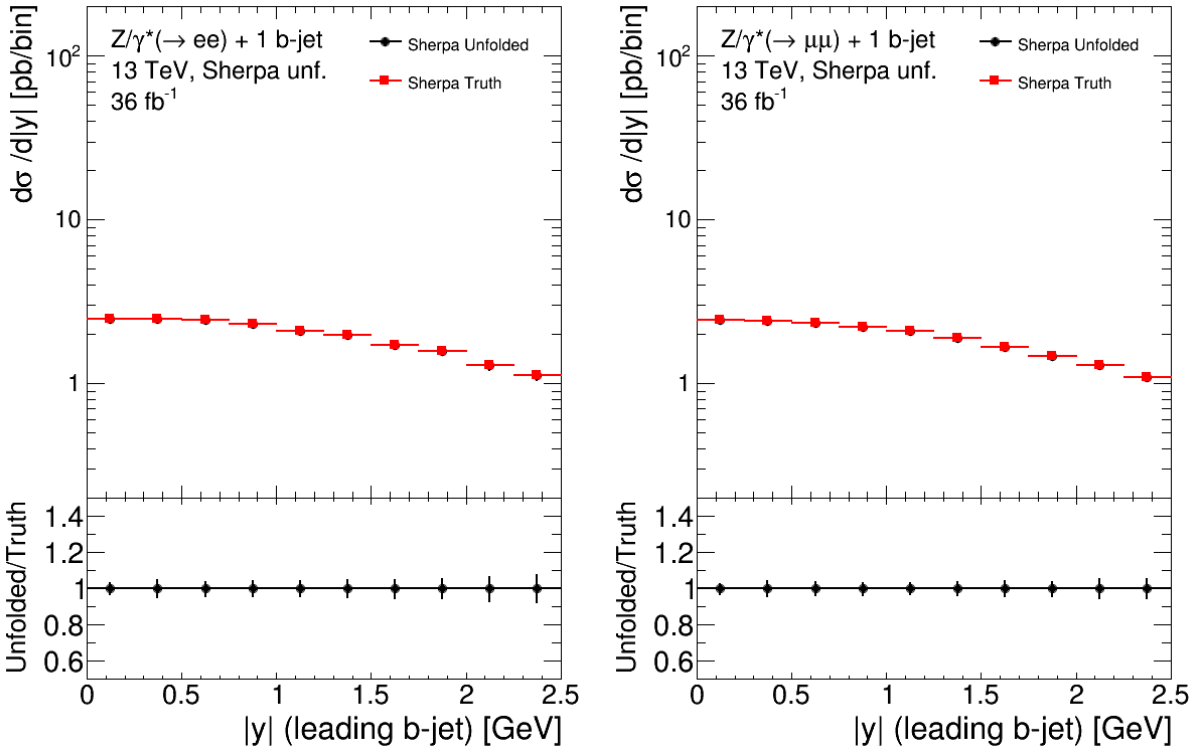

Figure 13.13: Closure test of the unfolding procedure using half of the Sherpa events as pseudo-data and other half to unfold the pseudo-data. Unfolding of the leading b-jet rapidity for the Z + $\geq 1b$-jet signal region in the electron channel (left) and muon channel (right).

13.7 Systematic Uncertainties

This section will describe how the different systematic sources are propagated to the cross-section measurement. As mentioned in chapter 10 for each detector level systematic there is an up and down variation corresponding to a shift of $\pm 1\sigma$ of the considered systematic uncertainty. For each systematic variation the flavor fit is redone using the varied distributions. The data is then unfolded using the results from the flavor fit of the systematic variation. Which components of the unfolding inputs are modified will depend on the systematic source being considered.

The systematic uncertainties associated with detector performance will result in shifts in both the signal and background MC predictions. These include the JES, JER, lepton, missing transverse energy, and b-tagging efficiency uncertainties. Since these sources affect

Channels	Muon	Electron
	Sherpa Unfolding Factors (Stat. err)	
$\geq 1b$-jet	0.4723 ± 0.0008	0.3251 ± 0.0008
$\geq 2b$-jets	0.289 ± 0.002	0.208 ± 0.002
	Alpgen Unfolding Factors (Stat. err)	
$\geq 1b$-jet	0.489 ± 0.001	0.338 ± 0.001
$\geq 2b$-jets	0.299 ± 0.002	0.217 ± 0.002

Table 13.2: Unfolding bin-by-bin scale factors for b-jet multiplicity derived separately from both Sherpa and Alpgen for the Z+$\geq 1b$-jet and Z+$\geq 2b$-jets signal regions. The errors shown are statistical only.

both the signal and background MC, the background subtracted data, migration matrices, and fake corrections will be modified by these sources.

The scale factors from the flavor fit for the signal component of the Z+jets is not applied to the inputs of the unfolding. This means uncertainties specifically associated with a background source will not result in modified migration matrices or fake corrections and instead will only modify the background distribution that is subtracted from data. For example, for the $t\bar{t}$ systematic variations that are considered and described in section 10.3, the only sample that is shifted from nominal prior to the flavor fit is the $t\bar{t}$ distribution itself. The background components of the Z+jets samples, Z + L and Z + c, will be shifted from nominal after the flavor fit is redone with the shifted $t\bar{t}$ sample, however, no other components of the inputs to the unfolding will be effected by these types of systematics. The systematic uncertainties considered for the top samples were described in section 10.3. For the other minor background process, diboson, VH, etc, only a 5% uncertainty coming from the theoretical uncertainty on their higher order cross-section used for their normalization is considered.

An uncertainty on the background component of the Z+jets samples is estimated by using Alpgen. The background components are the Z+L and Z+c component in the Z+$\geq 1b$-jet signal region and the Z+L,Z+c, and Z+b components in the Z+$\geq 2b$-jets signal region as described in chapter 11. The uncertainty is estimated by replacing the Sherpa background components with the Alpgen background components. The flavor fit is done using both the

signal and background component of Alpgen, however only the background component is propagated to the unfolding. This means the migration matrices and fake corrections are produced using Sherpa (the same ones that are used in the nominal unfolding) and Alpgen is only used in the background subtraction. This uncertainty component is referred to as '"VjBkg" in the tables and plots that follow.

In the nominal flavor fit the normalization of the background component of the Z+jets samples (chapter 11) is a single free floating parameter. An uncertainty on the flavor fit method used is estimated by performing the fit by breaking up the background component into two separate components and allowing their normalizations to each float independently in the fit (section 11.3.1 and section 11.4.1). The resulting uncertainty is referred to as the "FlavFit" uncertainty in the following plots and tables.

For all of the above uncertainties mentioned the relative difference between the result obtained by unfolding with the nominal distributions and the result obtained by unfolding with the varied samples is taken as the systematic uncertainty on the cross-section measurement. The up and down variation of each systematic uncertainty is averaged and their quadratic sum is taken as the total systematic uncertainty on the measurement.

13.7.1 Uncertainty on Unfolding Method

The uncertainties associated with the unfolding method used comes mainly from two sources. The modeling of the MC used for unfolding and the statistical fluctuations of the MC samples used to unfold. This section describes how these uncertainties are estimated.

The finite statistics of the Sherpa MC samples used can cause fluctuations in the detector response and the fake corrections. The effect this has on the unfolding method is studied using toy MC. The various unfolding inputs are fluctuated independently according to Gaussian distributions. The fluctuated unfolding inputs are then used to unfold the data. This is performed for 100 pseudo-experiments and the RMS of each bin of the unfolded distribution

is taken as the systematic uncertainty on the MC statistics.

As was shown in the detector level plots of the distributions that are to be unfolded, the MC does not perfectly model the data. The bias this introduces in the unfolding procedure needs to estimated. This is done using a data-driven closure test. The Z+jets Sherpa samples are reweighted at the particle level using a smooth function such that the detector level distribution better matches that of the background subtracted data. This reweighting is done separately for each distribution that is unfolded. The weights are determined by taking the background subtracted data distribution and dividing it by the detector level Sherpa MC signal distribution. This gives the weights at the centers of each bin in the distribution. To obtain a smooth function across the distribution a cubic spline interpolation is applied. An example of these smooth reweighting functions is shown in fig. 13.14 for the leading b-jet p_T and rapidity in the Z+1b-jet signal region for the electron channel.

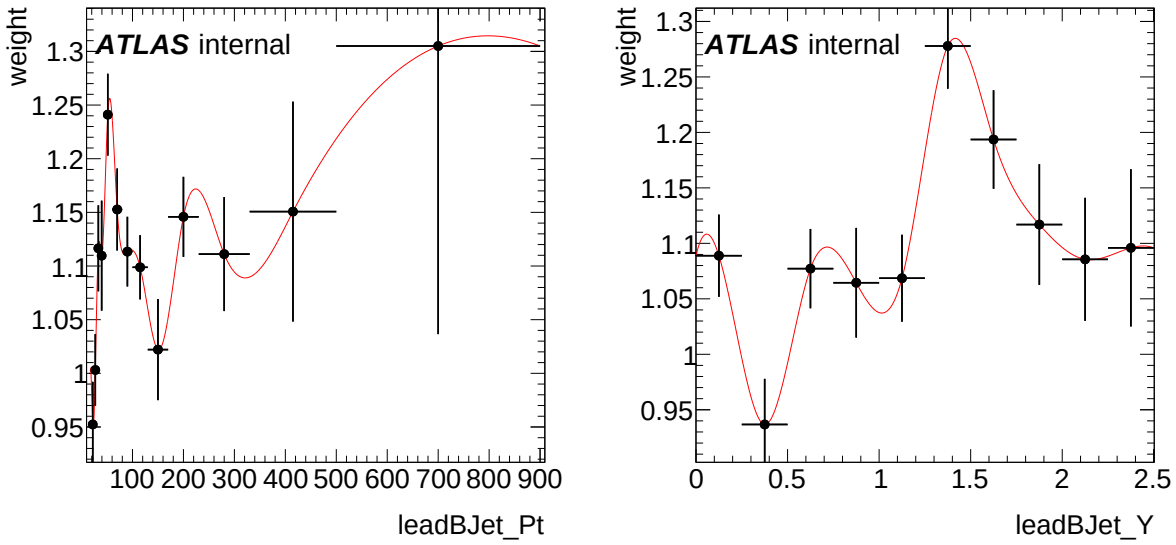

Figure 13.14: The ratio of background subtracted data to Sherpa MC signal at the detector level in the Z+1b-jet signal region for the electron channel for the leading b-jet p_T (left) and rapidity (right). Shown also is the spline function used to interpolate between points.

The spline function is then used to reweight the Sherpa MC signal samples at the truth level. The resulting reweighted reconstruction level distribution along with unweighted dis-

tribution are shown in fig. 13.15 and can be compared to the background subtracted data. The agreement between the signal MC and the data distribution is improved by the reweighting. The reweighted Sherpa signal samples are then used as pseodo-data and unfolded using the nominal Sherpa samples (ie nominal response matrix, truth level distribution and detector level distributions). The unfolded reweighted Sherpa sample is then compared to the reweighted truth level distribution. The non-closure of the two distributions is taken as the systematics uncertainty on the modeling dependency on the initial signal distribution that is being unfolded.

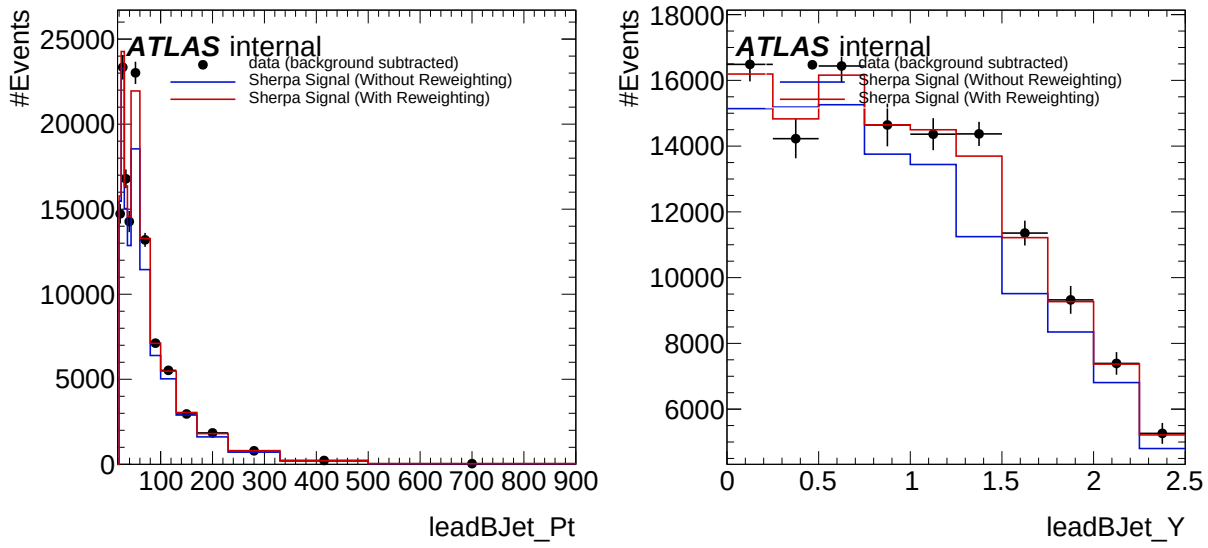

Figure 13.15: The detector level distributions of the leading b-jet p_T (left) and rapidity (right) with and without truth level reweighting as well as the background subtracted data distribution for the electron channel in the Z+1b-jet signal region.

Another unfolding uncertainty considers the effects from shape differences of a variable between data and MC that is not one of the variables that is unfolded. The p_T of the leading lepton was chosen as the variable to use to examine this effect. The uncertainty is determined using a similar data-driven closure test as is done for the shape difference on the unfolding variable. The Sherpa MC are reweighted at the truth level such that the detector level distributions of the leading lepton p_T of MC and data agree. The weights are

derived by taking the ratio of the background-subtracted data distribution to the Sherpa signal distribution. The reweighted Sherpa samples are then used to unfold the data. The difference between the nominal unfolded data and the data unfolded with the reweighted distribution are taken as the systematic uncertainty.

In fig. 13.16 the unfolded Sherpa reweighted distributions are shown as well as the truth reweighted particle level distributions for the leading b-jet p_T and rapidity in the Z+1b-jet signal region for the electron channel. The difference between the two distributions is used to derive the systematic uncertainty on the shape differences. The relative difference is shown in the bottom of the figure along with the sytematic uncertainty derived from the shape difference from the leading lepton p_T and from the MC statistics. The breakdown of these three systematics for all other variables that are unfolded are shown in Appendix D.4. The general observation is that the uncertainty from the mismodeling of the lepton p_T is negligible for all variables and that the modeling uncertainty is dominated by the shape differences on the unfolded observables.

The uncertainties on the unfolding for the bin-by-bin method used to unfold the inclusive b-jet multiplicity is determined differently than what was just described for the iterative unfolding method. The statistical uncertainty associated with the MC statistics is taken as the statistical uncertainty on the unfolding factors of Sherpa. These were included in table 13.2. The modeling uncertainty is taken as the relative difference of the unfolding factors between Sherpa and Alpgen.

13.7.2 Summary of Systematic Uncertainties

This section shows the breakdown of the systematic uncertainties on the measured cross sections.

The breakdown of the systematics for the inclusive cross section is shown in table 13.3 and table 13.4 for the Z + $\geq$ 1b-jet (Z1B) and the Z + $\geq$ 2b-jets (Z2B) signal regions,

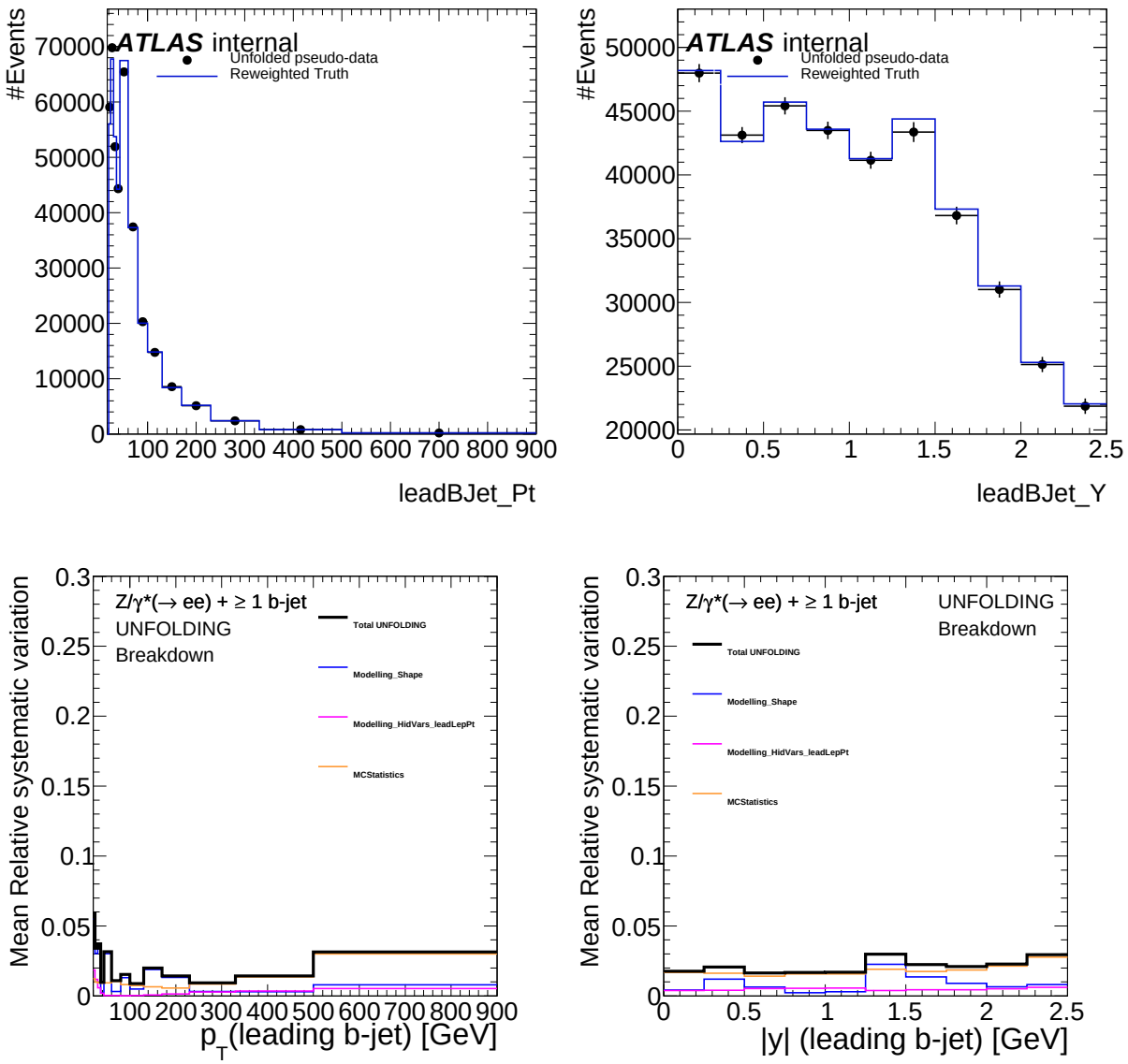

Figure 13.16: The unfolded reweighted detector level distribution along with corresponding truth reweighted particle level distribution (top) for the leading b-jet p_T (left) and rapidity (right) in the Z+1b-jet signal region for the electron channel. The difference between the two distributions is used to determine the unfolding modeling shape systematic uncertainty (bottom). Also shown are the systematic uncertainties determined using the lepton p_T truth reweighting and from the MC statistics.

respectively. Within signal regions the systematics are very similar between the electron and muon channel. For both signal regions the dominant source comes from the b-tagging systematic. In the Z1B signal region top is a relatively small background and as a result its contribution to the total systematic is also small. In contrast, in the Z2B signal region, top is a much more significant background and this is reflected in the size of its systematic uncertainty in the Z2B signal region. The smaller systematic uncertainty coming from the "VjBkg" component in the Z2B signal region compared to the Z1B signal region is easily seen from the yields shown in chapter 11 where in the Z2B signal region Sherpa and Alpgen give very similar predictions for the number of background events.

Systematic source	$Z \to e^+e^- + \geq 1b$-jet relative uncertainty (%)	$Z \to \mu^+\mu^- + \geq 1b$-jet relative uncertainty (%)
BTagging	±7.31	±7.55
JES	±1.44	±1.11
JER	±2.07	±1.97
JVT	±0.63	±0.39
MUON	±0.05	±0.68
ELECTRON	±1.51	±0.04
MET	±0.62	±0.73
PRW	±1.54	±1.19
Top	±0.59	±0.48
FlavFit	±1.89	±2.78
VjBkg	±3.54	±3.87
TTLFNorm	-	-
Unfolding (modelling)	±4.03	±3.62
Unfolding (MC stat)	±0.24	±0.18
Total (%)	±9.95	±10.09

Table 13.3: Breakdown of systematic uncertainties on unfolded b-jet multiplicity for the Z $+ \geq 1b$-jet signal region.

In fig. 13.17 to fig. 13.30 the breakdown of the systematic uncertainties on the measured differential cross sections are shown. In general the dominant systematic is from the b-tagging uncertainty. In fig. 13.17 and fig. 13.18 the breakdown is shown for the leading b-jet p_T and rapidity. The b-tagging systematic can be seen to be the dominant systematic in most bins. In the first few bins of the b-jet p_T the JER and JES also contribute significantly to the total systematic uncertainty.

The kinematics of the Z boson are shown in fig. 13.19 and fig. 13.20 for the Z1B signal region. Again for all bins the b-tagging systematic contributes significantly. The flavor fit systematic is over 20% in the first bin of the p_T of Z boson. The large fluctuations seen in last few bins correspond to bins with low statistics.

The breakdown of the systematics for the angular observables between the Z boson and leading b-jet are shown in figs. 13.21 to 13.23. While the b-tagging uncertainty contributes significantly again in all bins, there are also several bins where the VjBkg component con-

Systematic source	$Z \to e^+e^- + \geq 2b$-jets relative uncertainty (%)	$Z \to \mu^+\mu^- + \geq 2b$-jets relative uncertainty (%)
BTagging	±13.86	±13.26
JES	±2.52	±2.53
JER	±4.06	±4.43
JVT	±1.16	±0.85
MUON	±0.27	±1.02
ELECTRON	±2.09	±0.21
MET	±1.05	±1.80
PRW	±2.33	±3.02
Top	±4.79	±3.19
FlavFit	±0.74	±0.03
VjBkg	±1.35	±0.40
TTLFNorm	±0.04	±0.05
Unfolding (modelling)	±4.62	±3.53
Unfolding (MC stat)	±0.9	±0.798
Total (%)	±16.58	±15.47

Table 13.4: Breakdown of systematic uncertainties on unfolded b-jet multiplicity for the Z $+ \geq 2b$-jets signal region.

tributes significantly, especially in the rapidity distribution between the Z boson and the leading b-jet.

In the Z2B signal the contribution to the total uncertainty from the btagging systematic is in general larger then than it is in the Z1B signal region. It also tends be much larger than the relative uncertainty from all other sources. The breakdown for the Z boson p_T is shown in fig. 13.24 for the Z2B signal region. Except for a few bins in the electron channel, the btagging uncertainty is the primary source of uncertainty contributing to the total uncertainty. The last bin in the electron channel where the relative uncertainty from the VjBkg is approximately the same as that of the btagging uncertainty also corresponds to the bin where the statistics are lowest.

The breakdown of the systematics for the angular observables between the two leading b-jets are shown in figs. 13.25 to 13.27. For $\Delta\phi_{bb}$ the largest relative uncertainty in each bin is from the b-tagging uncertainty. The next largest sources of uncertainty comes from the unfolding uncertainty, JER, JES, and ttbar systematics. This is similarly seen in the

plots ΔY and ΔR between the two leading b-jets except for some distributions there are bins where there are sources larger than the b-tagging uncertainty. The two large unfolding uncertainties in the last bins of both ΔY and ΔR come from the MC statistics component of the unfolding uncertainty, while the large relative unfolding uncertainty in the first bin of ΔR in muon channel distribution is coming mostly from the shape modeling component.

The invariant mass of the two leading b-jets is shown in fig. 13.28. The b-tagging systematic is once again the larger source of uncertainty, however in the electron channel many of the other uncertainty source are relatively larger than in the muon channel. These include the uncertainty from the VjBkg component, ttbar component and the JER component. For the p_T of the sum of the two leading b-jets four-vectors, shown in fig. 13.29, the JER and unfolding uncertainty contribute significantly to the total relative uncertainty in the first bin which carries over to the the ratio of the p_T over the invariant mass, shown in fig. 13.30. The ttbar uncertainty also is a major component for a few of the bins in both distributions for the electron channel.

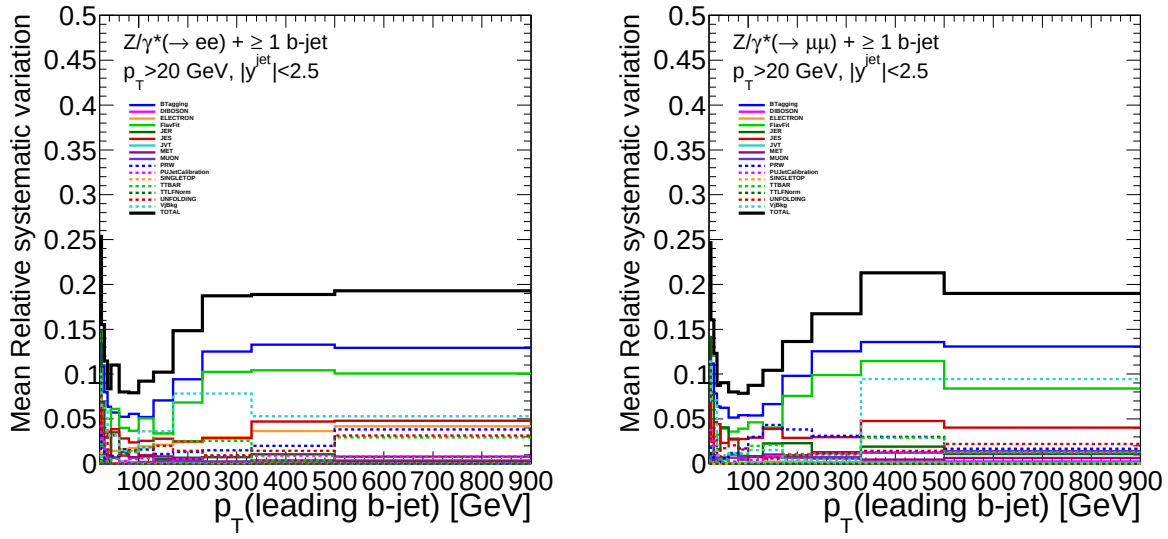

Figure 13.17: Breakdown of the systematic uncertainties on the unfolded measurement for the leading b-jet p_T for the electron channel (left) and muon channel (right) in the Z + 1b-jet signal region.

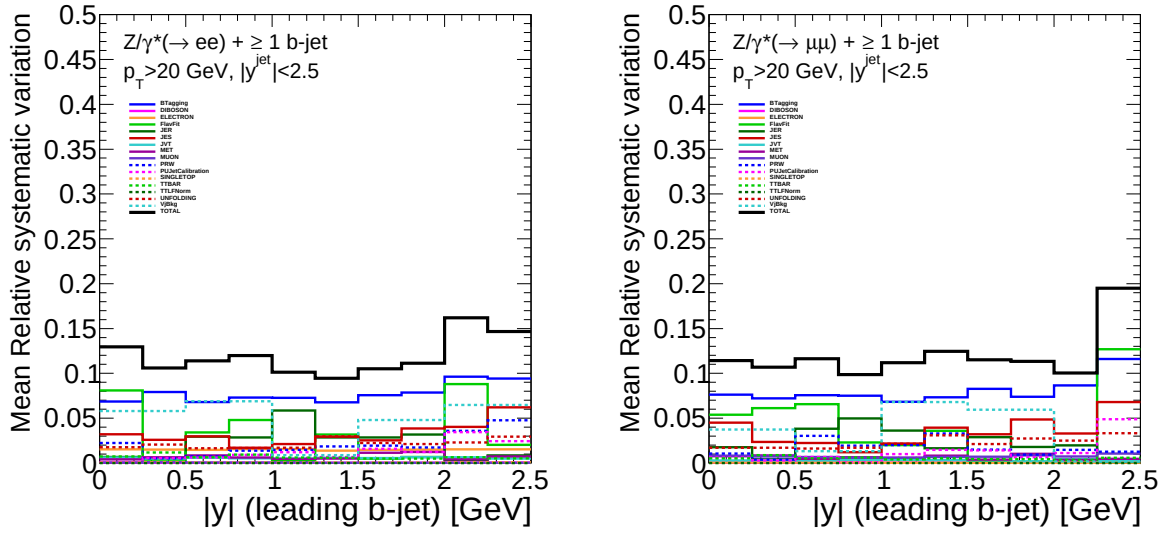

Figure 13.18: Breakdown of the systematic uncertainties on the unfolded measurement for the leading b-jet rapidity for the electron channel (left) and muon channel (right) in the Z + 1b-jet signal region.

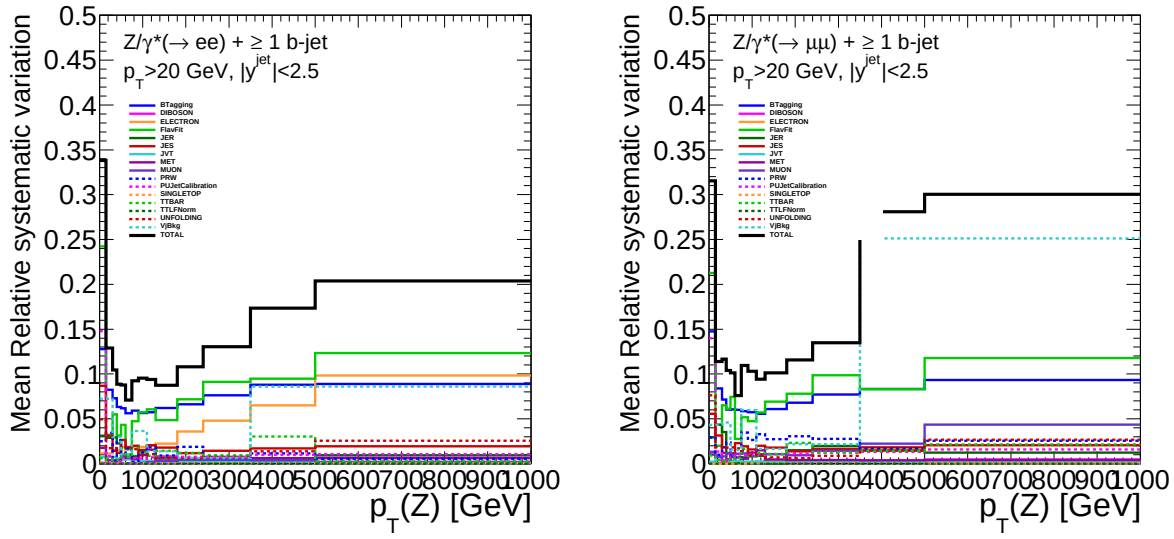

Figure 13.19: Breakdown of the systematic uncertainties on the unfolded measurement for the Z boson p_T for the electron channel (left) and muon channel (right) in the Z + 1b-jet signal region.

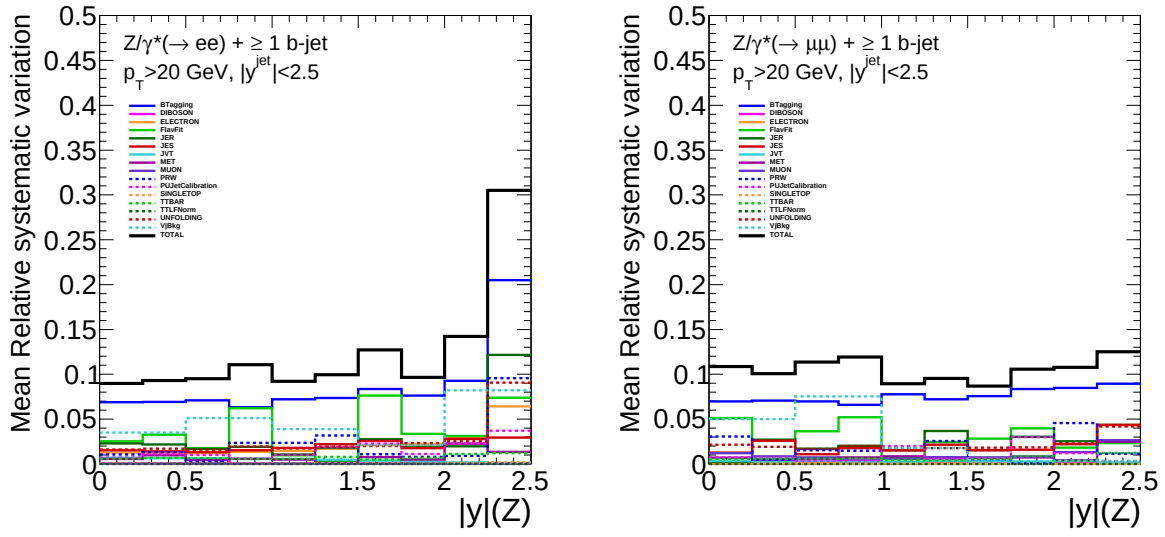

Figure 13.20: Breakdown of the systematic uncertainties on the unfolded measurement for the Z boson rapidity for the electron channel (left) and muon channel (right) in the Z + 1b-jet signal region.

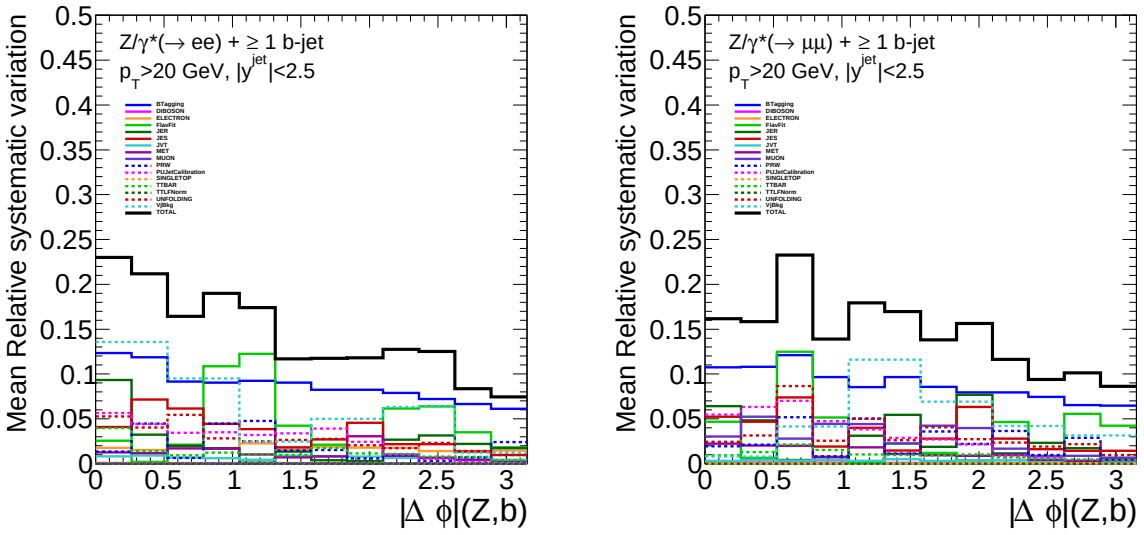

Figure 13.21: Breakdown of the systematic uncertainties on the unfolded measurement for the $\Delta\phi$ between the leading b-jet and Z boson for the electron channel (left) and muon channel (right) in the Z + 1b-jet signal region.

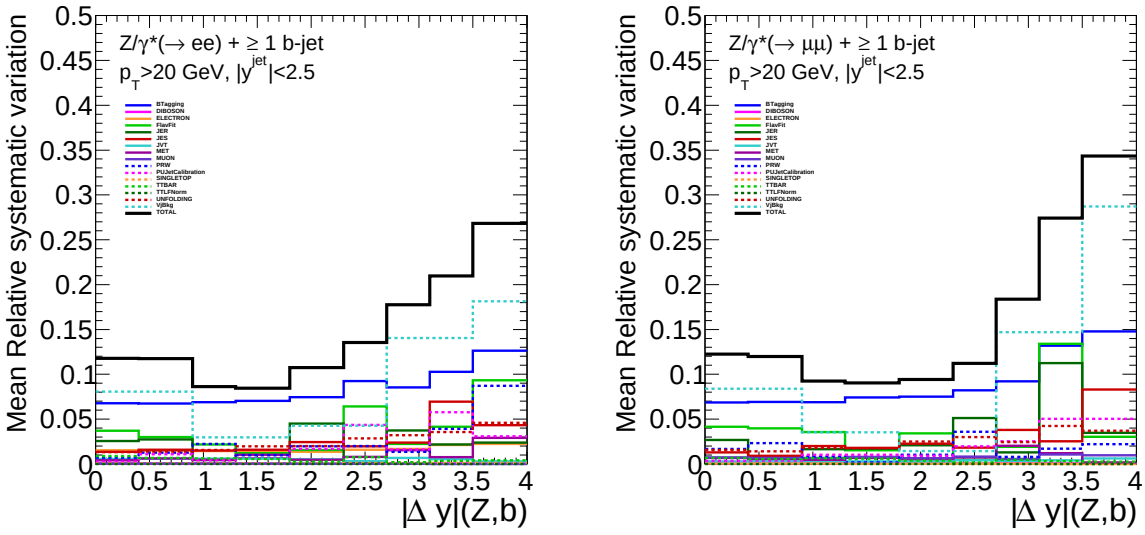

Figure 13.22: Breakdown of the systematic uncertainties on the unfolded measurement for the ΔY between the leading b-jet and Z boson for the electron channel (left) and muon channel (right) in the Z + 1b-jet signal region.

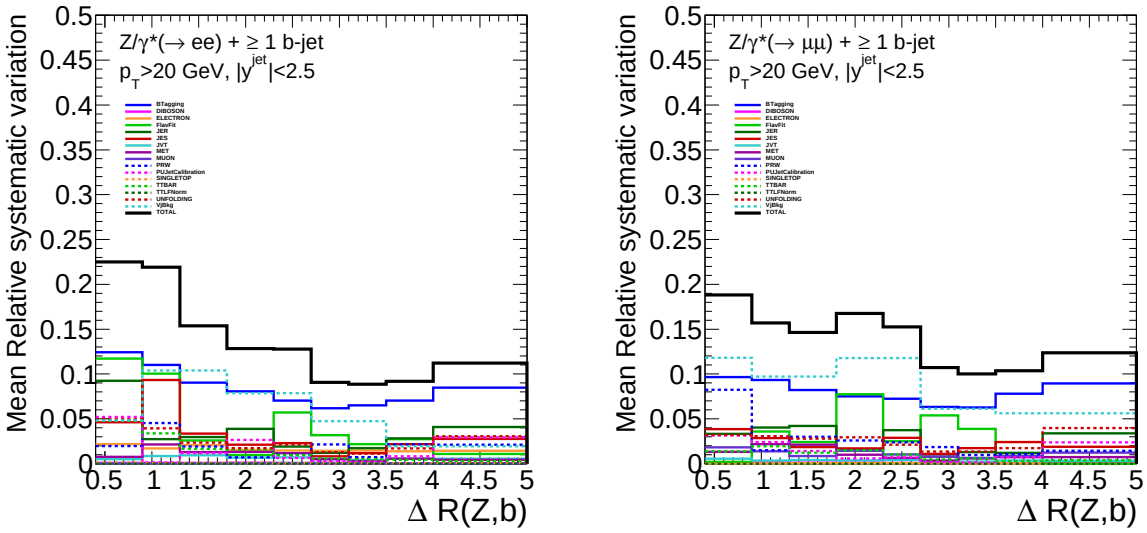

Figure 13.23: Breakdown of the systematic uncertainties on the unfolded measurement for the ΔR between the leading b-jet and Z boson for the electron channel (left) and muon channel (right) in the Z + 1b-jet signal region.

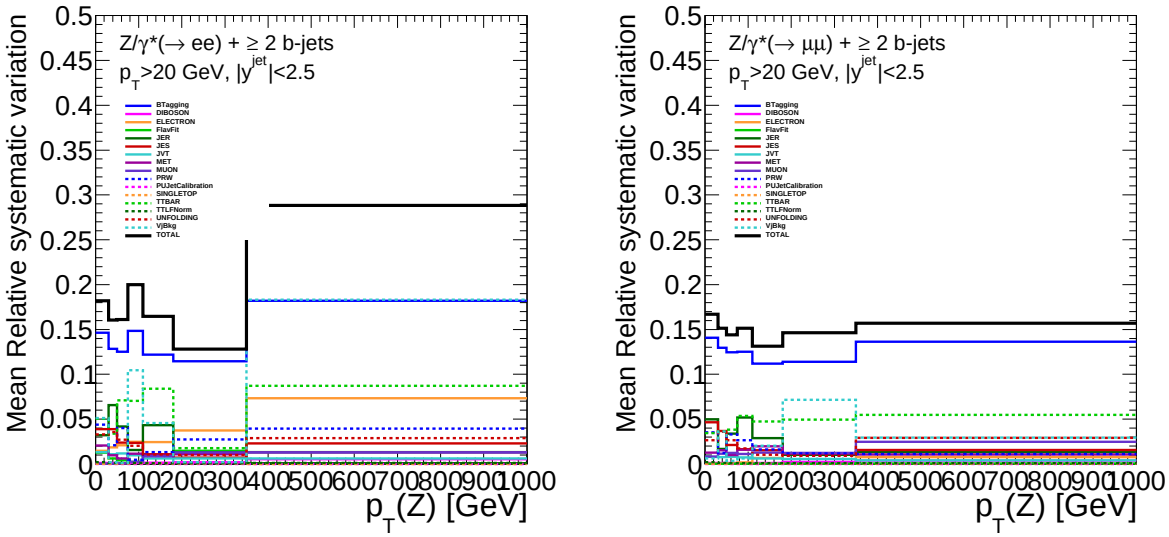

Figure 13.24: Breakdown of the systematic uncertainties on the unfolded measurement for the Z boson p_T for the electron channel (left) and muon channel (right) in the Z + 2b-jets signal region.

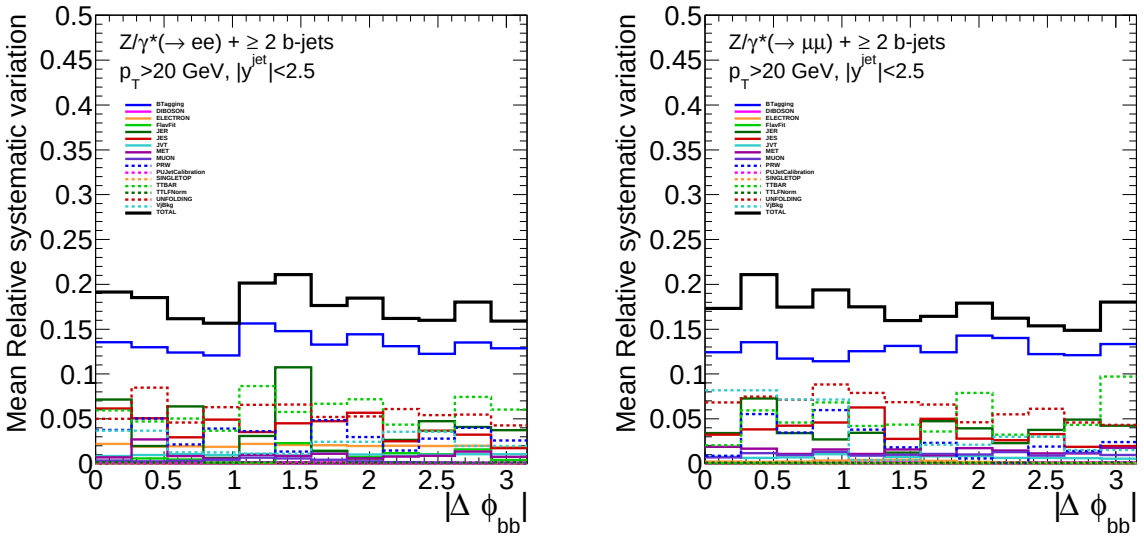

Figure 13.25: Breakdown of the systematic uncertainties on the unfolded measurement for the $\Delta\phi$ between the two leading b-jets for the electron channel (left) and muon channel (right) in the Z + 2b-jets signal region.

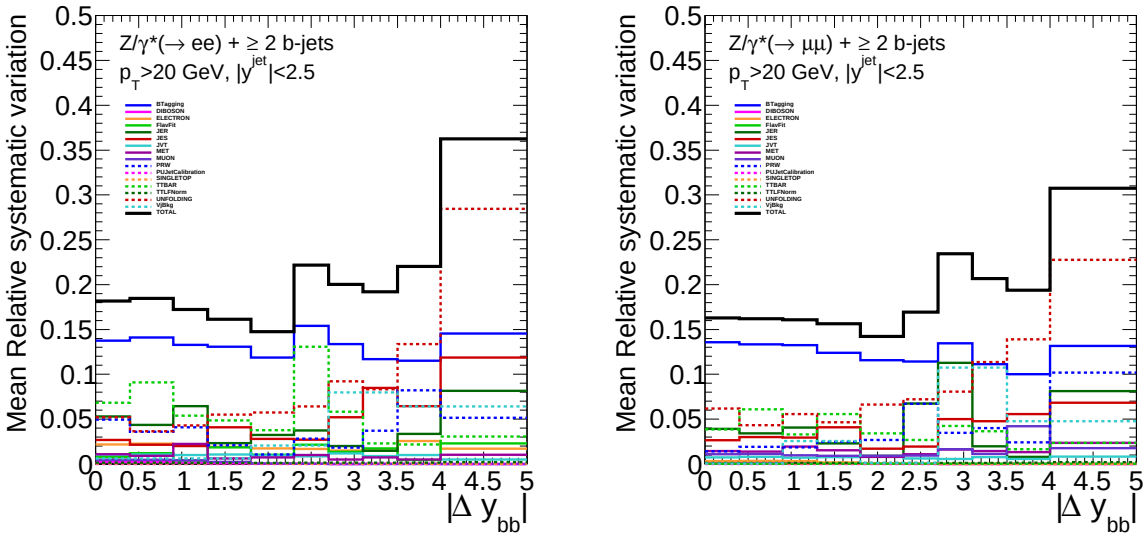

Figure 13.26: Breakdown of the systematic uncertainties on the unfolded measurement for the ΔY between the two leading b-jets for the electron channel (left) and muon channel (right) in the Z + 2b-jets signal region.

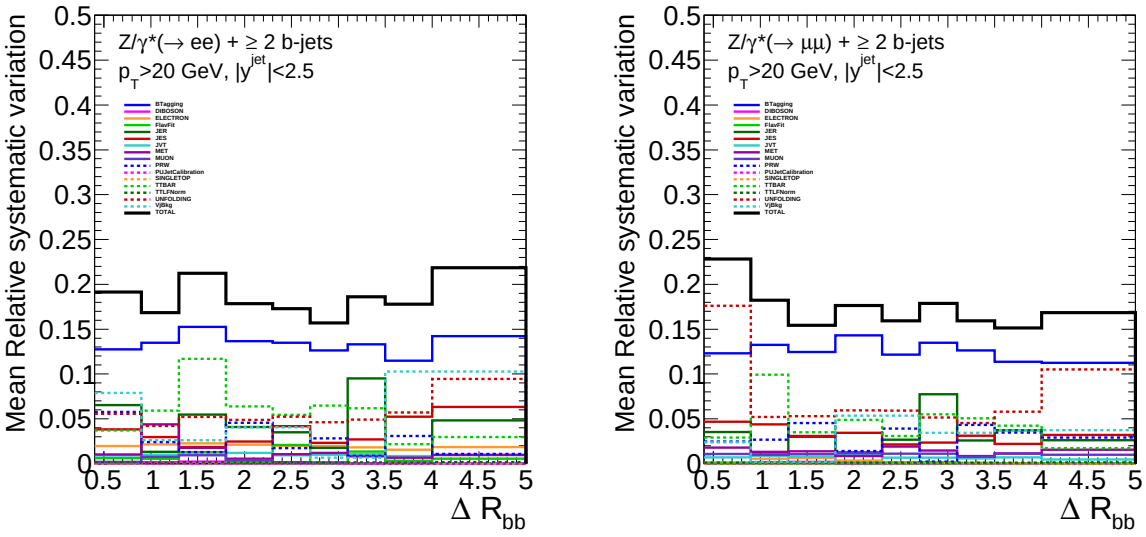

Figure 13.27: Breakdown of the systematic uncertainties on the unfolded measurement for the ΔR between the two leading b-jets for the electron channel (left) and muon channel (right) in the Z + 2b-jets signal region.

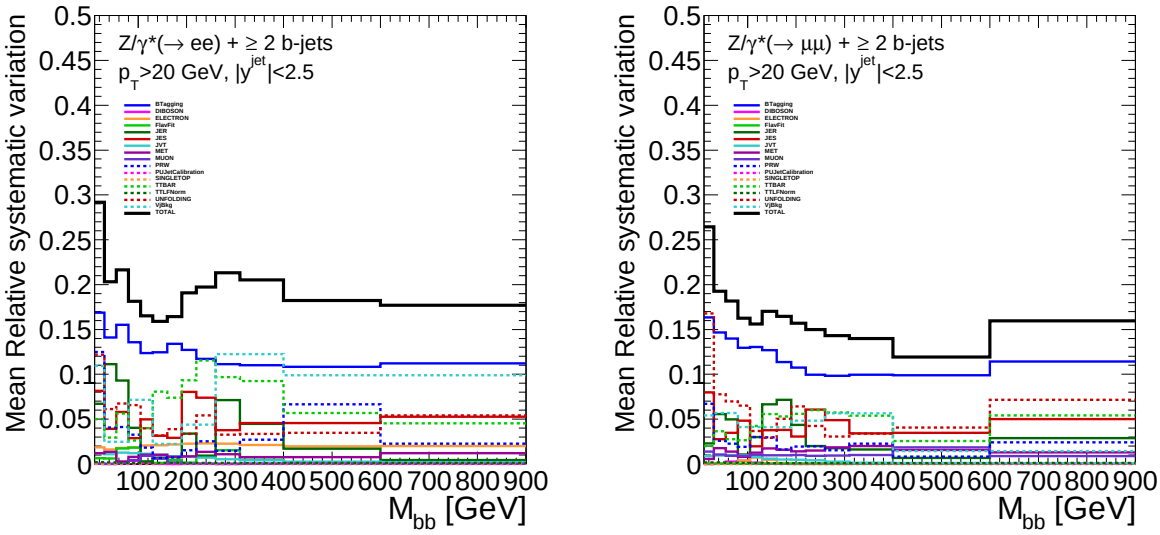

Figure 13.28: Breakdown of the systematic uncertainties on the unfolded measurement for the invariant mass of the two leading b-jets for the electron channel (left) and muon channel (right) in the Z + 2b-jets signal region.

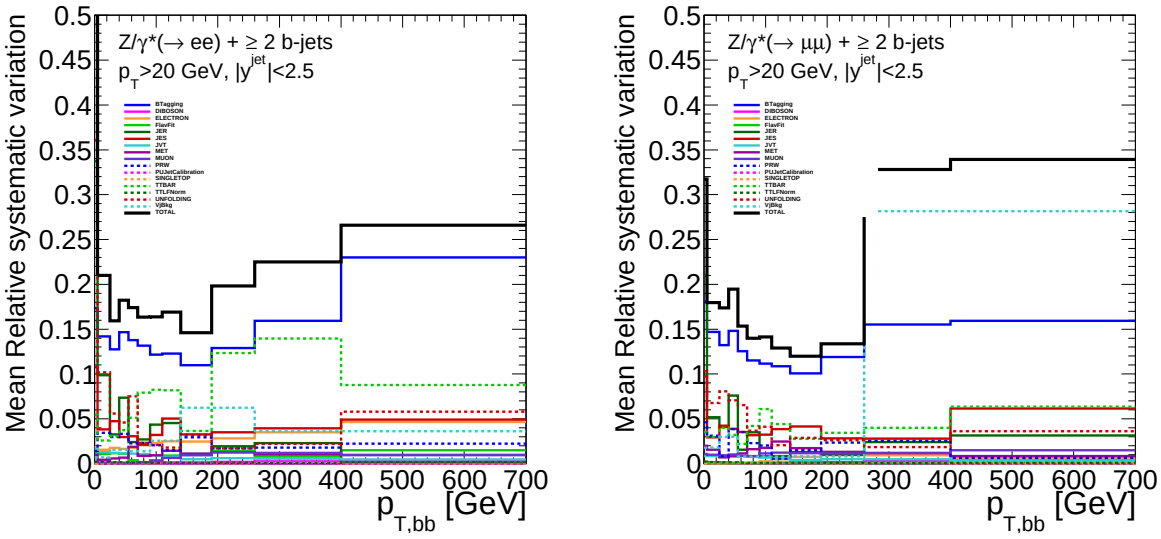

Figure 13.29: Breakdown of the systematic uncertainties on the unfolded measurement for the p_T of the sum of the two leading b-jets four-vectors for the electron channel (left) and muon channel (right) in the Z + 2b-jets signal region.

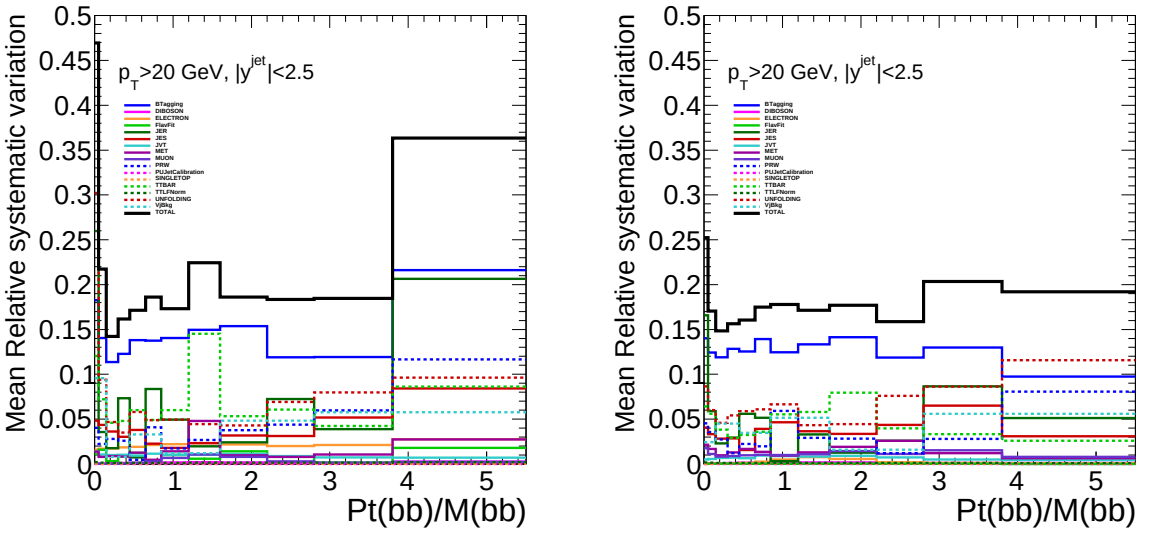

Figure 13.30: Breakdown of the systematic uncertainties on the unfolded measurement for the p_T of the sum of the two leading b-jets four-vectors divided by the invariant mass of them for the electron channel (left) and muon channel (right) in the Z + 2b-jets signal region.

13.7.3 Statistical Uncertainty on Unfolded Data

The effect of the statistical uncertainty on data needs to be accounted for. Statistical fluctuations of the data would effect both the flavor fit and the unfolding, therefore they need to be accounted for simultaneously in both. A statistical fluctuation on the flavor fit discriminant variable would result in a correlated statistical fluctuation in the distribution of the variables being unfolded. This is accounted for by using the Bootstrap method in which a series of pseudo-experiments is performed which fluctuates the data in a way that maintains correlations between variables. This is done by constructing each pseudo-experiment from data by refilling all histograms after each event has been fluctuated by a random weight taken from a Poisson distribution with a mean of one. A thousand such pseudo-experiments are produced.

A new flavor fit is performed for each pseudo-experiment and the resulting scale factors from the flavor fit are applied to the Z+jets background components. Each bootstrap replica is then unfolded using the scale factors from the new the flavor fit to obtain the background-subtracted pseudo-data. Besides the background-subtracted pseudo-data, all other inputs used in the unfolding are the nominal samples. The results of the unfolded distributions of the one thousand pseudo-experiments are then averaged over each bin of the distribution that was unfolded, taking the root-mean-squared spread of each bin as the statistical uncertainty due to the number of events in data. Examples of the resulting unfolded measurements of the one thousand replicas are shown in fig. 13.31 for the inclusive b-jet multiplicity in the electron channel. Gaussian fits are included to show the statistical behavior of the replicas and can be compared to the values shown in tables 14.1 and 14.2.

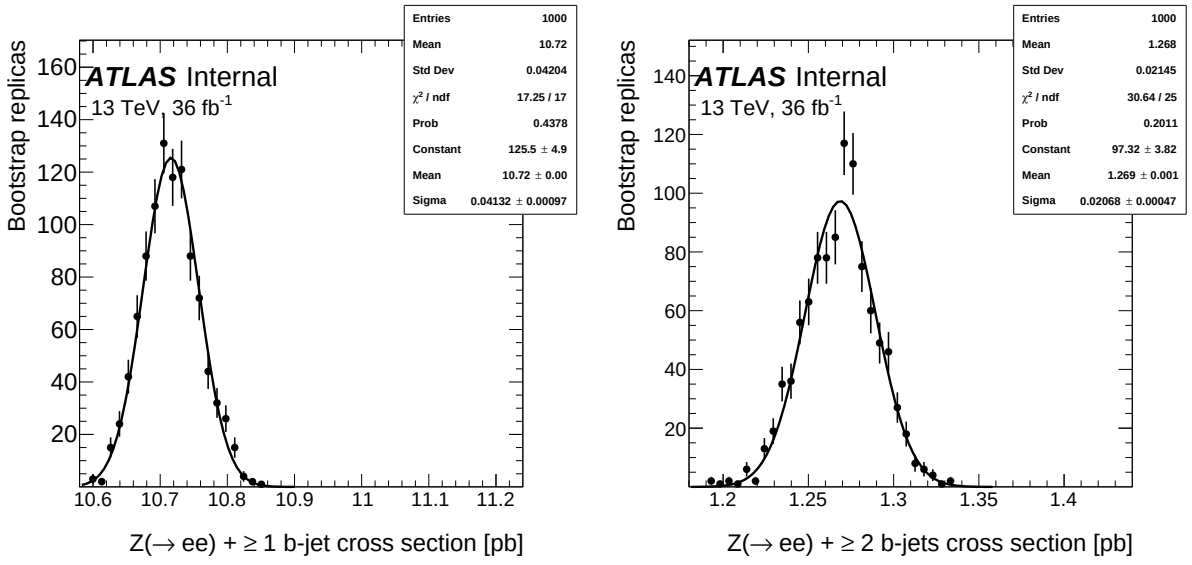

Figure 13.31: Cross-section measurement of inclusive b-jet multiplicity from unfolding one thousand bootstrap replicas in the Z + $\geq 1b$-jet (left) and Z + $\geq 2b$-jets (right) signal regions for the electron channel. The Gaussian fit is included only to show the statistical behavior of the replicas.

CHAPTER 14

RESULTS

This chapter shows the fiducial cross-sections at the particle level. Events are selected according to chapter 7. The different background components are predicted using MC and were described in section 5.2. The background component of the Z+jets samples are extracted using a flavor fit of the b-tagging algorithm discriminant, MV2c10 (chapter 11). The predicted background distributions are then subtracted from the measured data distributions. Unfolding is then used to take the background-subtracted data from the detector level to the fiducial truth level cross-section. The fiducial definition was given in section 13.2.

The integrated cross-sections for the production of Z + 1b-jet and Z + 2b-jets is measured by unfolding the inclusive b-jet multiplicity using the bin-by-bin method (section 13.1.2). The differential cross-sections are measured in the two different inclusive b-jet regions using an iterative unfolding method (section 13.1.3). In both methods Sherpa is used to unfold the data and the unfolded data is compared to predictions given by Sherpa, Algpen, and Madgraph.

14.1 Integrated Cross-sections

The integrated cross-section results are shown in table 14.1 and table 14.2 for the Z + $\geq$ 1b-jet and Z + $\geq$ 2b-jets signal regions, respectively. Also included are the predictions from the three different MC generators considered in this thesis. The MC predictions only include statistical uncertainties. The measured result includes the statistical (section 13.7.3), systematic (section 13.7), and luminosity uncertainties (section 10.2). A breakdown of the systematic uncertainties was given in section 13.7.2. The total systematic uncertainty is taken as the quadratic sum of the different components listed in the corresponding tables in section 13.7.2. The uncertainty on the measurement is dominated by the systematic

uncertainty, with which the component contributing the most to the systematic uncertainty is the b-tagging uncertainties.

$\sigma(Z \to + \geq 1b\text{-jet})$ [pb]		
	Electron Channel	Muon Channel
Sample	value ± stat. ± syst. ± lumi.	value ± stat. ± syst. ± lumi.
Data	10.715 ±0.042 ±1.066 ±0.225	11.040 ±0.038 ±1.113 ±0.232
Monte Carlo	value ± stat.	value ± stat.
Sherpa	9.819 ±0.030	9.877 ±0.030
Alpgen	6.806 ±0.021	6.856 ±0.021
Madgraph	13.401 ±0.051	13.336 ±0.073

Table 14.1: Integrated cross-section of Z boson production in association with at least 1 b-jet in the electron and muon channel. Monte Carlo predictions only include statistical uncertainties.

$\sigma(Z \to + \geq 2b\text{-jets})$ [pb]		
	Electron Channel	Muon Channel
Sample	value ± stat. ± syst. ± lumi.	value ± stat. ± syst. ± lumi.
Data	1.269 ±0.021 ±0.210 ±0.027	1.359 ±0.019 ±0.210 ±0.029
Monte Carlo	value ± stat.	value ± stat.
Sherpa	1.128 ± 0.007	1.119 ±0.007
Alpgen	1.085 ± 0.008	1.089 ±0.008
Madgraph	1.651 ± 0.015	1.591 ±0.028

Table 14.2: Integrated cross-section of Z boson production in association with at least 2 b-jets in the electron and muon channel. Monte Carlo predictions only include statistical uncertainties.

The three generators were described in chapter 5. Sherpa calculates the matrix elements to NLO using the 5FNS. Madgraph calculates the matrix elements to LO and also used the 5FNS for the samples used. Alpgen on the other hand uses the 4FNS and also calculates the matrix elements to LO. The results are fairly consistent between lepton flavors. For the measured result in both the Z1B and Z2B signal regions the two lepton flavors are within one sigma of each other. This is also true for the predicted values from Sherpa. The differences between lepton flavors for both Madgraph and Alpgen are just slightly larger than one sigma.

In the Z + $\geq 1b$-jet signal region the data is best described by the NLO 5FNS Sherpa

prediction and is compatible within one sigma. The Sherpa prediction underestimates the data by approximately 10%. The LO 5FNS Madgraph prediction overestimates the measured cross-section by approximately 20%, slightly larger than being within one sigma. The prediction given by the LO 4FNS Alpgen prediction is much lower than the measured cross-section.

In the Z + $\geq 2b$-jets signal region the measured result has a total uncertainty of $\sim$16% in both lepton channels. A somewhat similar trend is seen in the predictions. Sherpa once again best describes the data and is within one sigma while again predicting a slightly smaller cross-section. Alpgen again underestimates the measured cross-section, however, in this signal region the prediction is compatible with the measured result and within one sigma in the electron channel and only slightly larger than one sigma from the measured result in the muon channel. In contrast, the Madgraph prediction is within one sigma of data in the muon channel and just over one sigma in the electron channel. Similar to Z1B signal region Alpgen underestimates the measured results and Madgraph overestimates the prediction.

This is in general in agreement with the results from the Run 1 analysis [96] which was performed at a center of mass energy, $\sqrt{s}$, of 7 TeV. A few of the major differences between the analysis are the predictions used. For example, the Run 1 paper used a different parton shower generator for Alpgen as well as a different PDF for Sherpa. The analysis also used a different parton shower generator for the aMC@NLO generator, as well as a different PDF. The analysis also had a prediction from aMC@NLO using both a NLO 4FNS and a LO 5FNS. The Run 1 analysis saw the best compatibility of data with the NLO 5FNS in the Z1B signal region, however in the Z2B signal region, the NLO 4FNS showed the best compatibility with data. The analysis results in these Run 2 results show that both signal regions are best modeled by the Sherpa NLO 5FNS, however other theoretical predictions were not yet available.

14.2 Differential Cross-section Measurements in the Z + $\geq 1b$-jet Signal Region

This section shows the results of the differential cross-sections at the particle level of the production of a Z boson along with at least one b-jet. The data has been taken to the particle level by unfolding it with Sherpa samples and is compared to the predictions from Sherpa, Alpgen and Madgraph. The error bands include both the statistical uncertainty on data and the total systematic uncertainties. A breakdown of the latter was shown in section 13.7.2. The uncertainties on the predictions include only the statistical uncertainty. The differences in the overall normalizations on the cross section was already observed in section 14.1 so this section will focus more on the shape differences/agreement.

The differential cross section as a function of the leading b-jet p_T and rapidity are shown in fig. 14.1 and fig. 14.2, respectively. The shapes predicted for the electron and muon channel are very similar for all three predictions. Madgraph and Sherpa predict similar shapes for the p_T of the leading b-jet, both predicting softer jets compared to the unfolded data. The shape of the p_T predicted by Alpgen shows the best agreement with the shape of the unfolded data. All three generators predict a similar shape for the rapidity of the leading b-jet and the shape is fairly well modeled when compared to that of data.

The differential cross section as a function of the Z boson p_T and rapidity are shown in fig. 14.3 and fig. 14.4. All three generators predict different shapes for the p_T of the Z boson and each prediction shows significant mismodeling of the p_T compared to data. This significant mismodeling of the Z boson p_T is not seen in the rapidity of the Z boson. The shape of the rapidity of the Z boson compared to data is fairly well modeled by all three predictions.

The differential cross section as a function of the the angular observables between the Z boson and leading b-jet are shown in figs. 14.5 to 14.7. The predictions from Madgraph and Alpgen show significant mismodeling in the shape of all three observables. Sherpa shows the

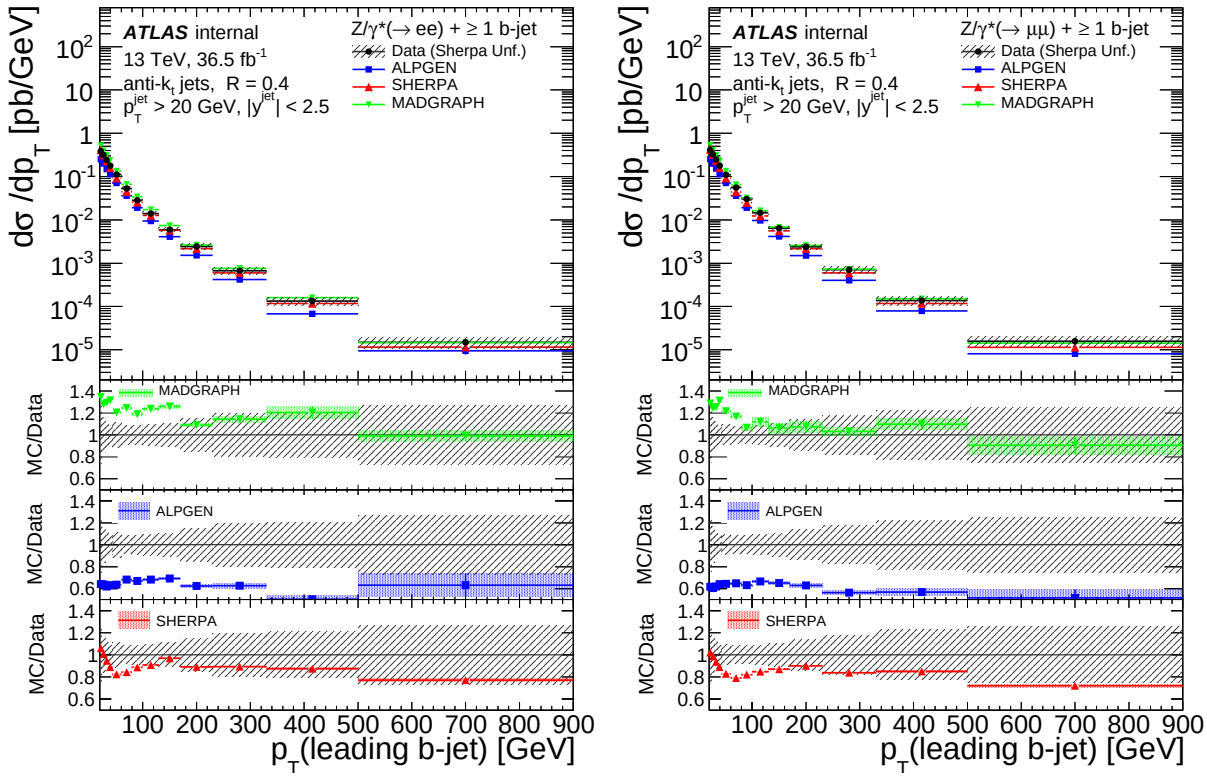

Figure 14.1: Differential cross section for the production of a Z boson with at least one b-jet as a function of leading b-jet p_T for the electron channel (left) and muon channel (right).

best modeling of the shape seen in data for all three observables.

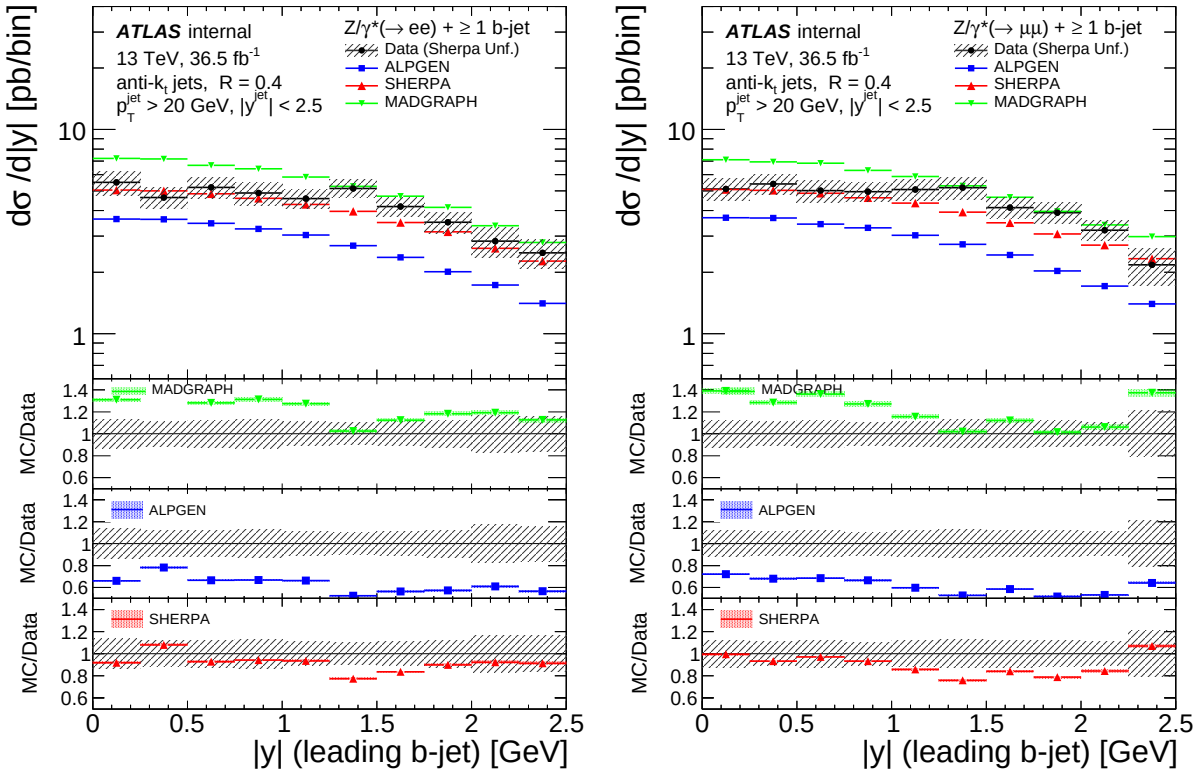

Figure 14.2: Differential cross section for the production of a Z boson with at least one b-jet as a function of leading b-jet rapidity for the electron channel (left) and muon channel (right).

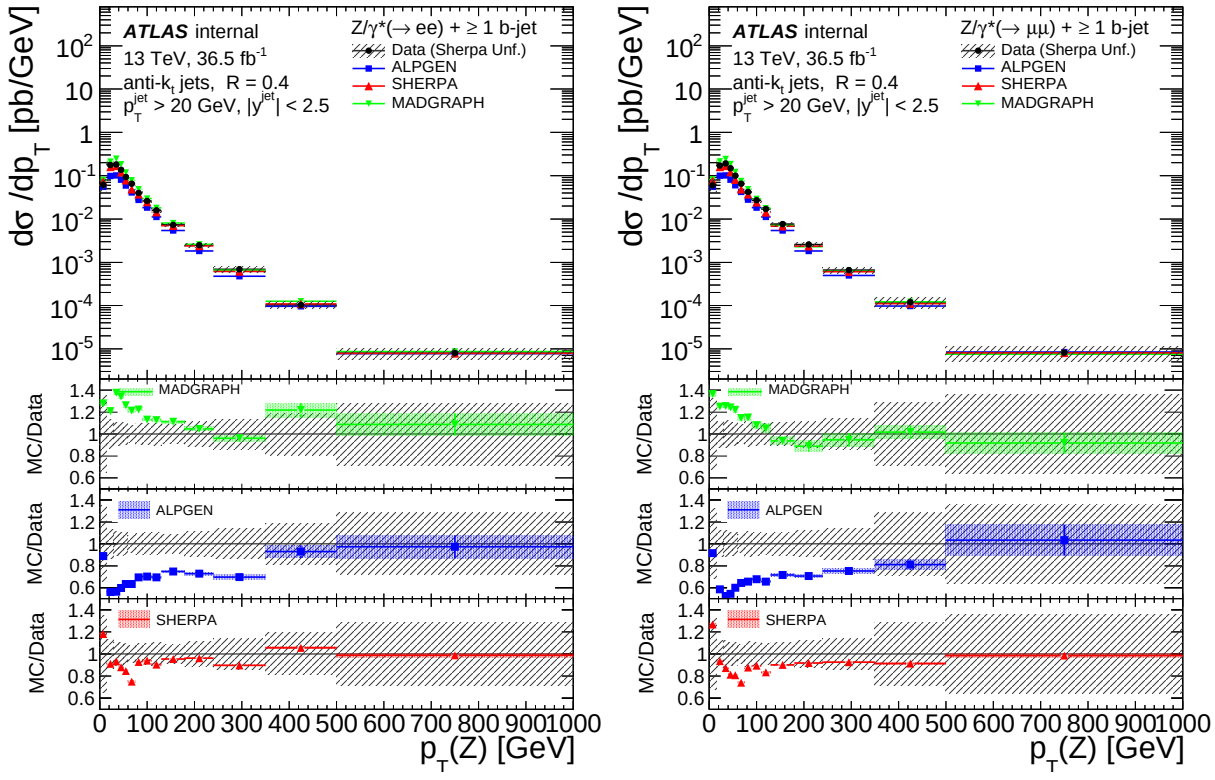

Figure 14.3: Differential cross section for the production of a Z boson with at least one b-jet as a function of Z boson p_T for the electron channel (left) and muon channel (right).

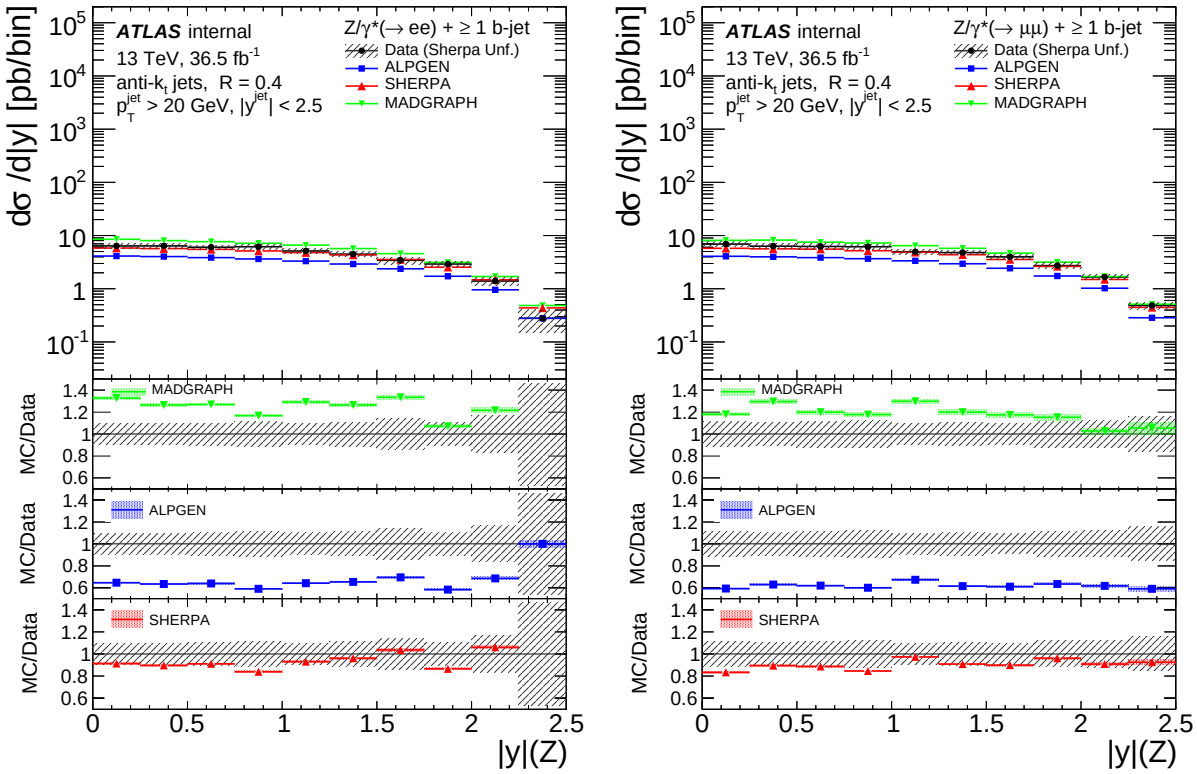

Figure 14.4: Differential cross section for the production of a Z boson with at least one b-jet as a function of Z boson rapidity for the electron channel (left) and muon channel (right).

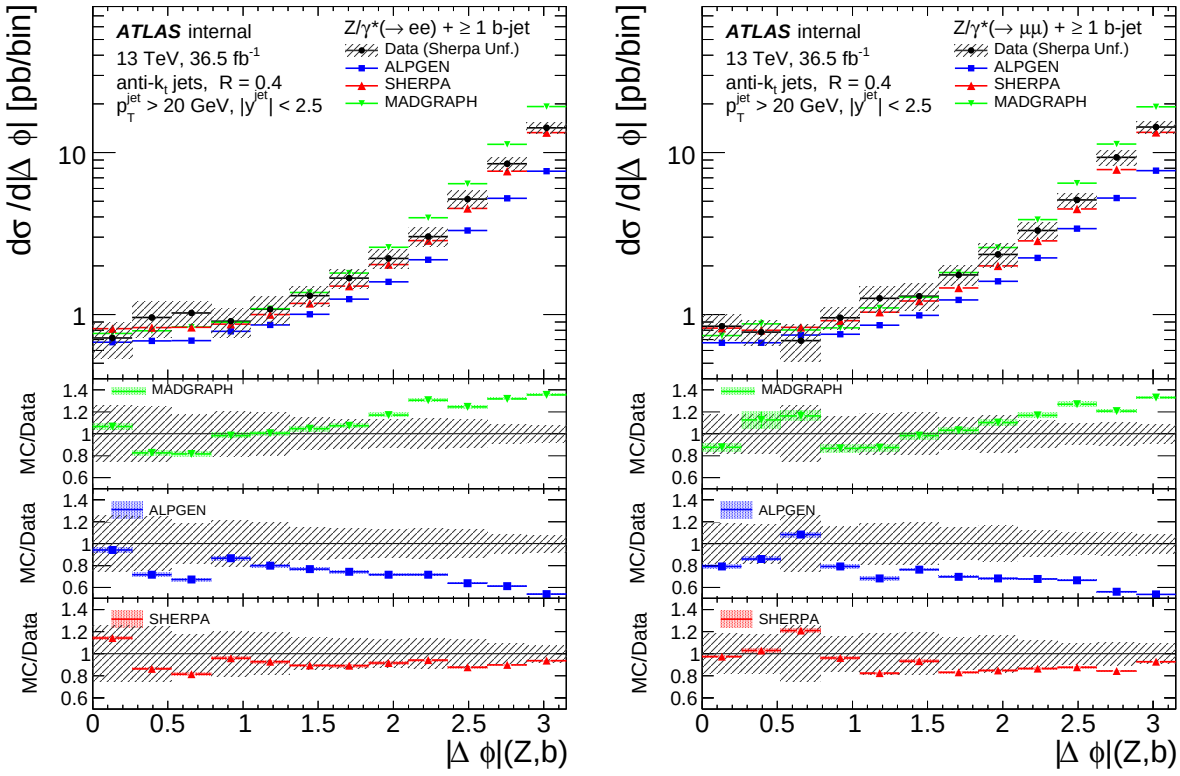

Figure 14.5: Differential cross section for the production of a Z boson with at least one b-jet as a function of $\Delta\phi$ between the leading b-jet and Z boson for the electron channel (left) and muon channel (right).

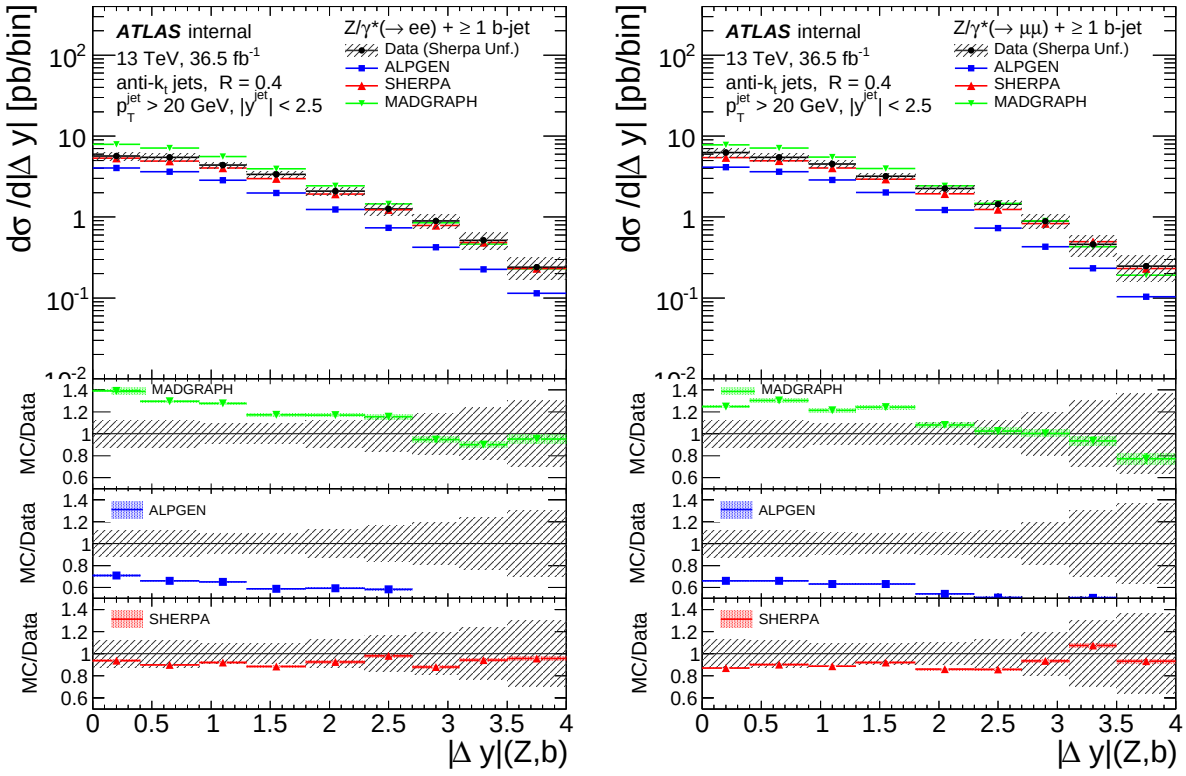

Figure 14.6: Differential cross section for the production of a Z boson with at least one b-jet as a function of ΔY between the leading b-jet and Z boson for the electron channel (left) and muon channel (right).

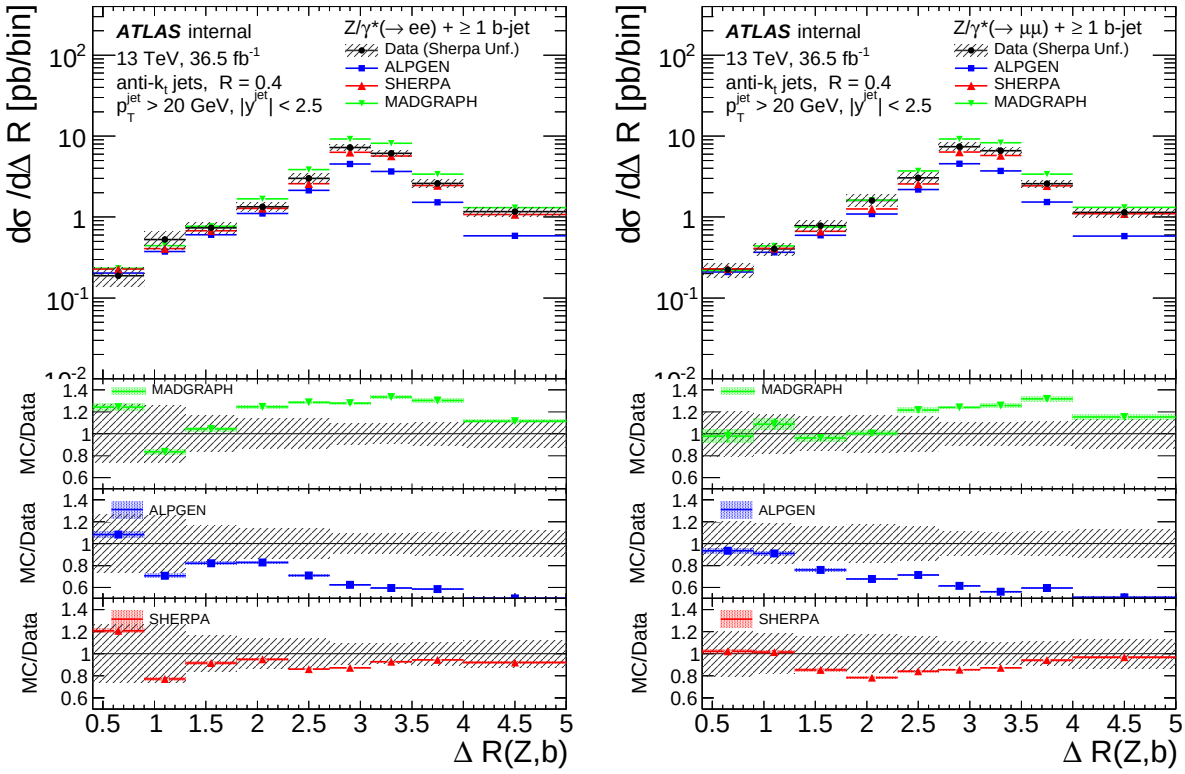

Figure 14.7: Differential cross section for the production of a Z boson with at least one b-jet as a function of ΔR between the leading b-jet and Z boson for the electron channel (left) and muon channel (right).

14.3 Differential Cross-section Measurements in the Z + $\geq 2b$-jets Signal Region

This section shows the results of the differential cross-sections at the particle level of the production of a Z boson along with at least two b-jets. The differential cross-section as a function of the p_T of the Z boson is shown in fig. 14.8. Sherpa and Alpgen predict similar shapes when compared to data. The shape differences between the MC predictions and data are within the uncertainties shown.

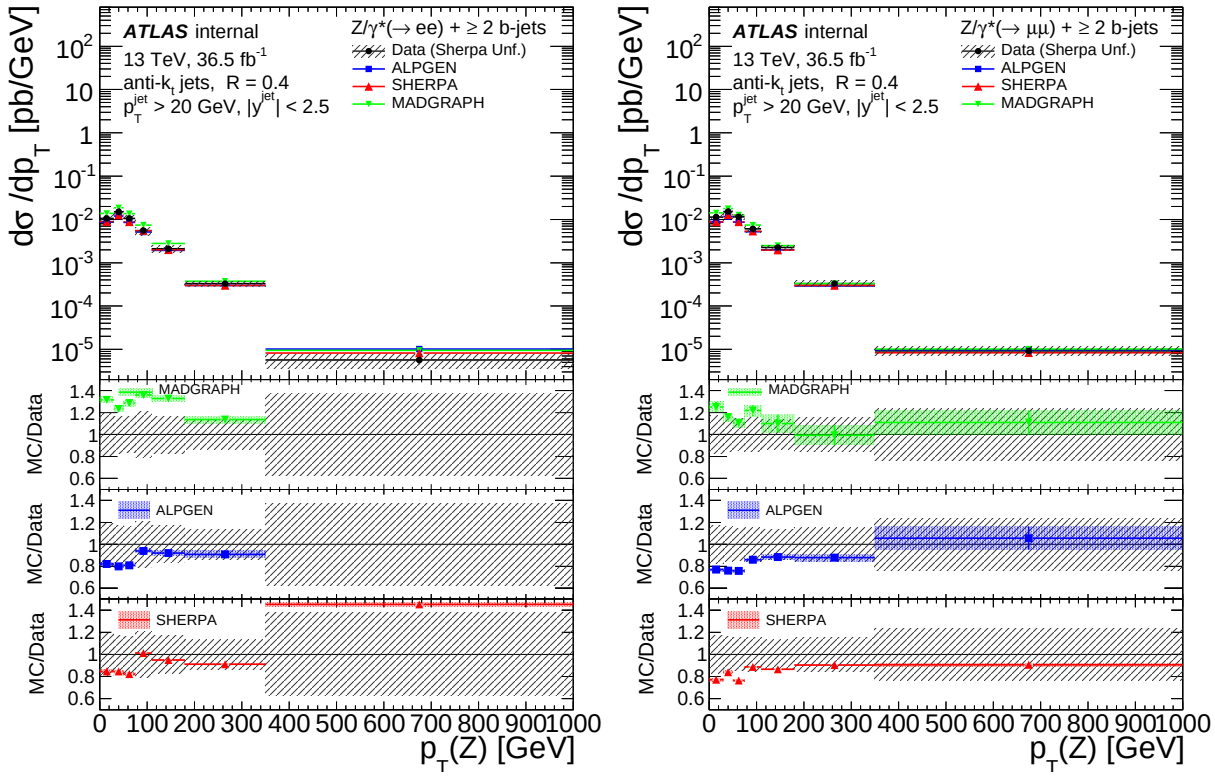

Figure 14.8: Differential cross section for the production of a Z boson with at least two b-jets as a function of Z boson p_T for the electron channel (left) and muon channel (right).

The differential cross-section as a function of the angular observables between the two leading b-jets are shown in figs. 14.9 to 14.11. The distribution of $\Delta\phi$ between the two leading b-jets is modeled similarly well by both Sherpa and Alpgen where the predictions are within the uncertainties shown for most bins. For ΔY between the two leading b-jets the

difference between the prediction and data tends to be smallest for smaller values of ΔY and increase as ΔY increases. The difference is seen to grow more rapidly for Alpgen compared to Sherpa. This trend in $\Delta\phi$ and ΔY carries over somewhat to the distribution of ΔR. The predictions of ΔR are similar for Algen and Sherpa for $\Delta R < 3.5$. For values larger than this Alpgen predicts a noticeably smaller cross section.

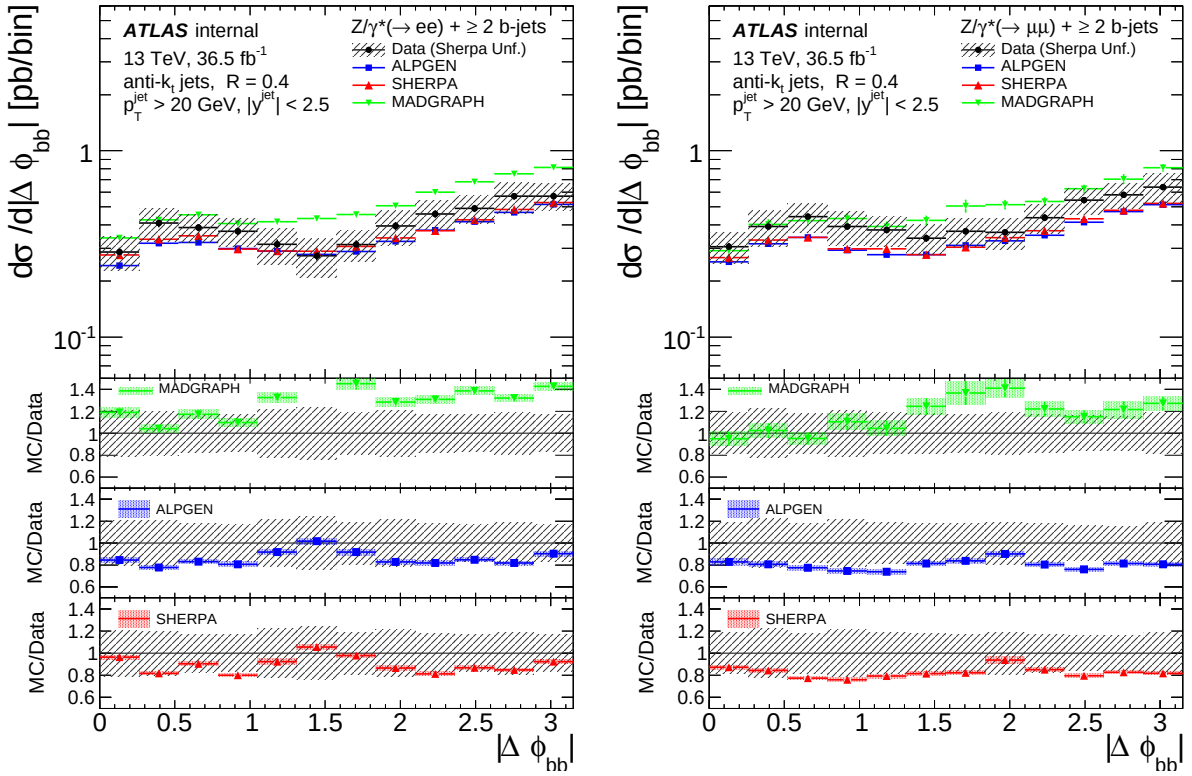

Figure 14.9: Differential cross section for the production of a Z boson with at least two b-jets as a function of $\Delta\phi$ between the two leading b-jets for the electron channel (left) and muon channel (right).

The differential cross-section as a function of the invariant mass of the two leading b-jets is shown in fig. 14.12. The predictions from Alpgen and Sherpa agree with the data within the uncertainties for the lower values of the invariant mass. For larger values of the invariant mass discrepancies in the shape with respect to data are seen that are not within the uncertainties. For larger values of the invariant mass the difference between the prediction and data tends to be larger for Alpgen compared to Sherpa. The unfolded distribution for the

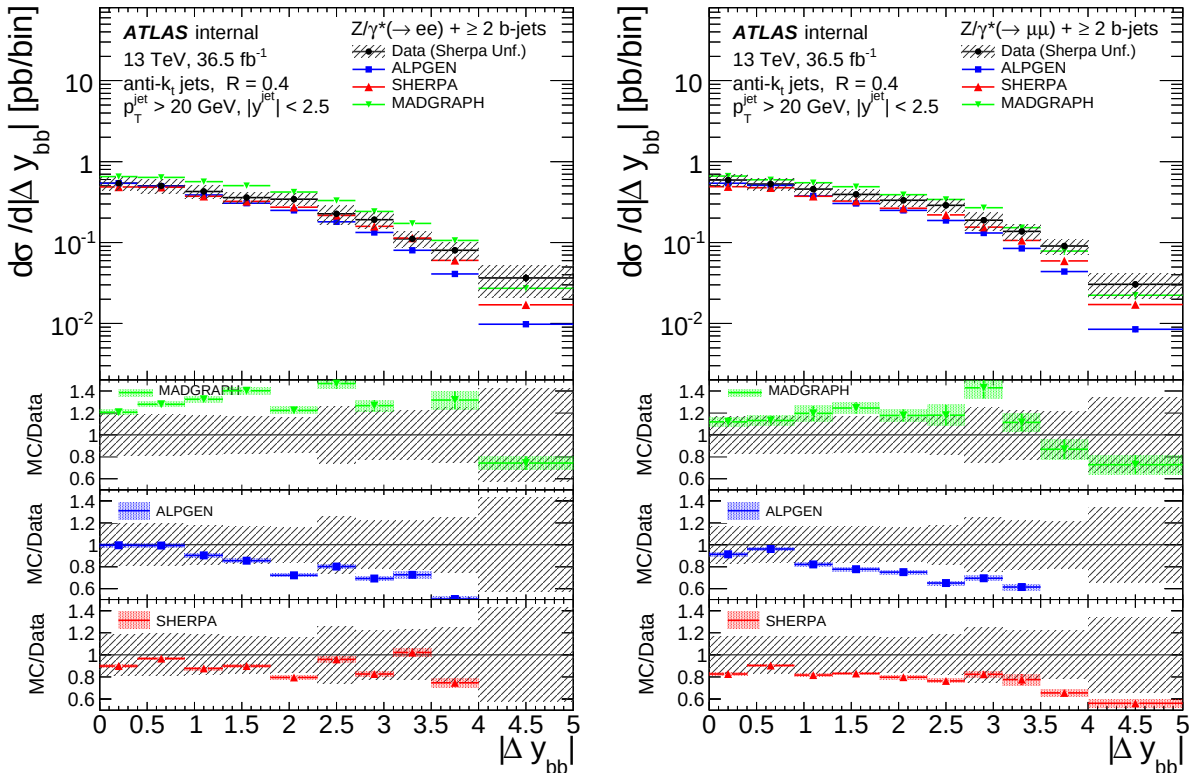

Figure 14.10: Differential cross section for the production of a Z boson with at least two b-jets as a function of ΔY between the two leading b-jets for the electron channel (left) and muon channel (right).

p_T of the sum of the two leading b-jets four-vectors is shown in fig. 14.13. The modeling of the shape, in general, shows better agreement with data than is seen for the invariant mass. The discrepancies between the predictions and data for the p_T are within the uncertainties across the full spectrum shown. This is also seen in the unfolded distribution of the ratio of these two variables which is shown in fig. 14.14.

14.4 Summary

The unfolded data is compared to the predictions from three different generators. The predictions from the NLO 5FNS Sherpa, LO 5FNS Madgraph, and LO 4FNS Alpgen. In the measurement of the inclusive cross-section the data is best described by the prediction given by Sherpa in both the Z + 1b-jet and Z + 2b-jets signal regions. In both signal regions

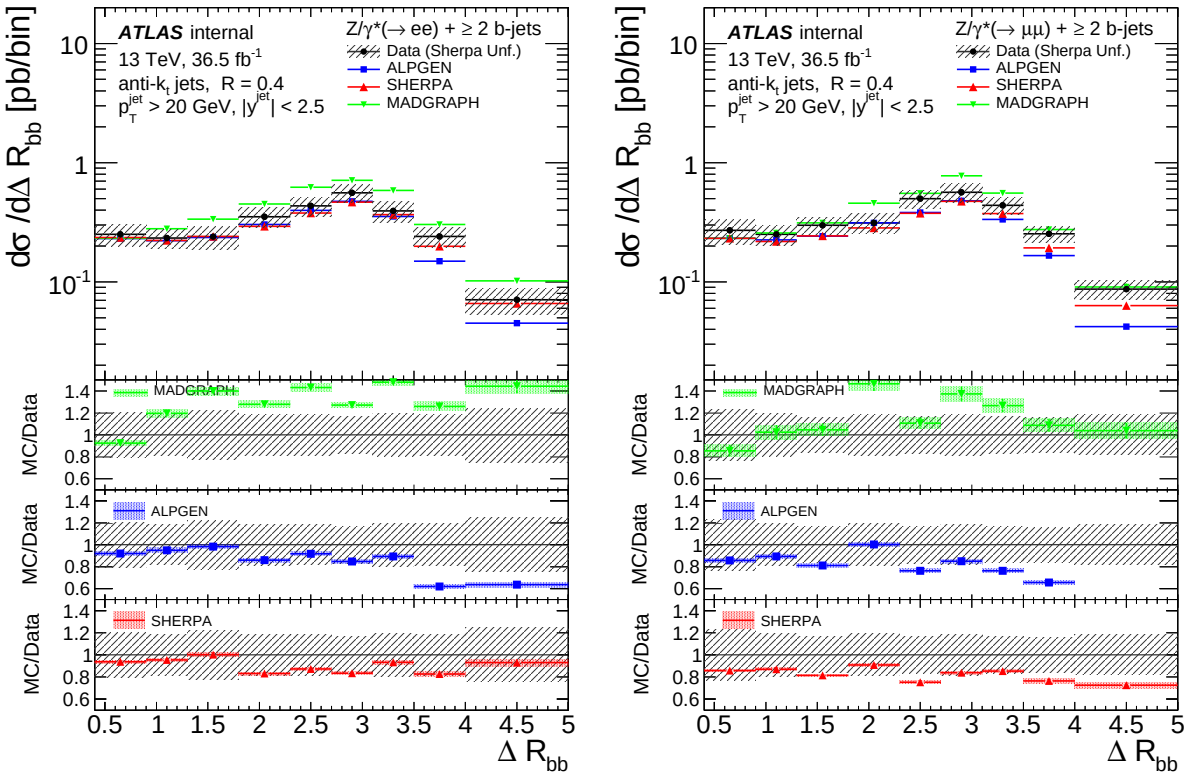

Figure 14.11: Differential cross section for the production of a Z boson with at least two b-jets as a function of ΔR between the two leading b-jets for the electron channel (left) and muon channel (right).

Sherpa underestimates the data. The prediction from Alpgen also underestimates the data in both signal regions, especially in the Z + 1b-jet signal region. Madgraph overestimates the data in both signal regions.

In the Z + 1b-jet signal region the inclusive cross-section measured in both lepton channels are better predicted by both 5FNS predictions then the 4FNS. In the Z + 2b-jets signal region Madgraph is closer to the measured result in the muon channel than Alpgen, however Alpgen is closer to the measured result in the electron channel than Madgraph.

The predicted differential cross-section shapes do not show a clear preference for one generator over the others. For example, in the Z1B signal region all three generators predict different shapes from each other as well as from the measured data for the p_T of the Z boson, however in the Z2B signal region the shape predicted is similar for Alpgen and Sherpa. The

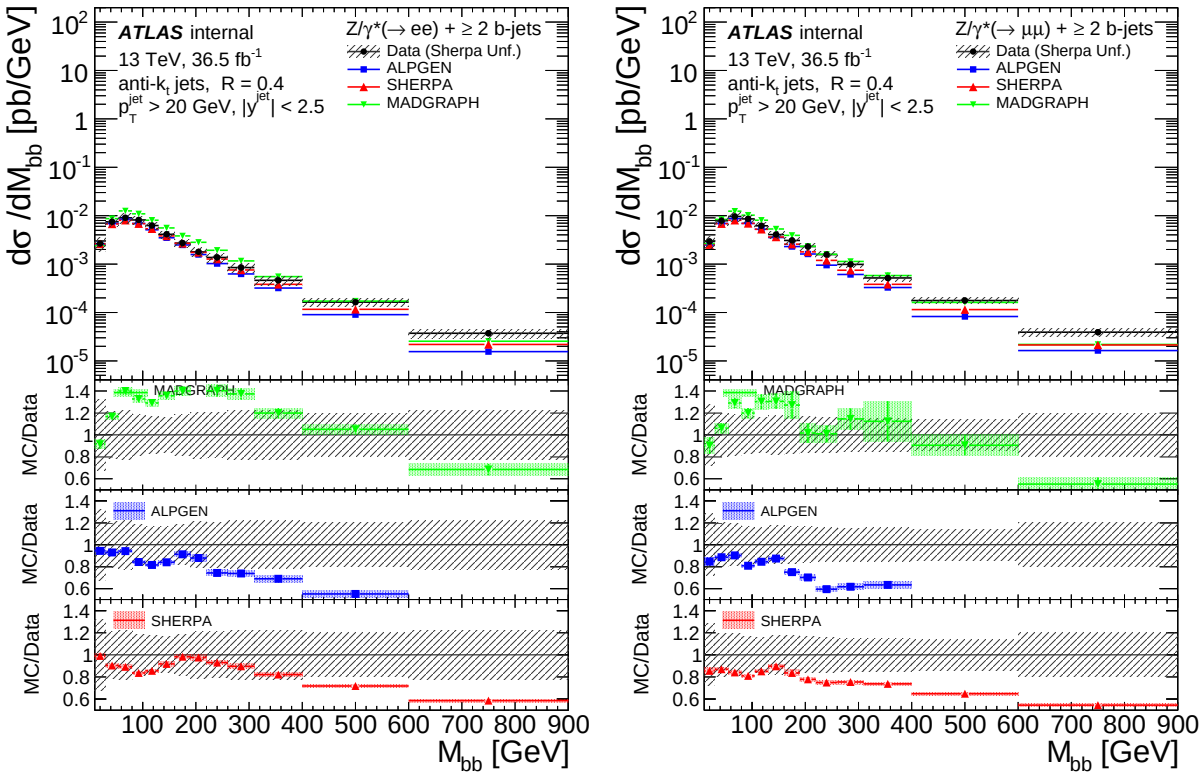

Figure 14.12: Differential cross section for the production of a Z boson with at least two *b*-jets as a function of invariant mass of the two leading b-jets for the electron channel (left) and muon channel (right).

predicted shape of the rapidity of the Z boson in the Z1B signal region, however, is similar among all three predictions and is compatible with the shape of the unfolded data.

In the future NLO predictions will be available for both the 4FNS and 5FNS allowing further investigation into the differences between the two schemes.

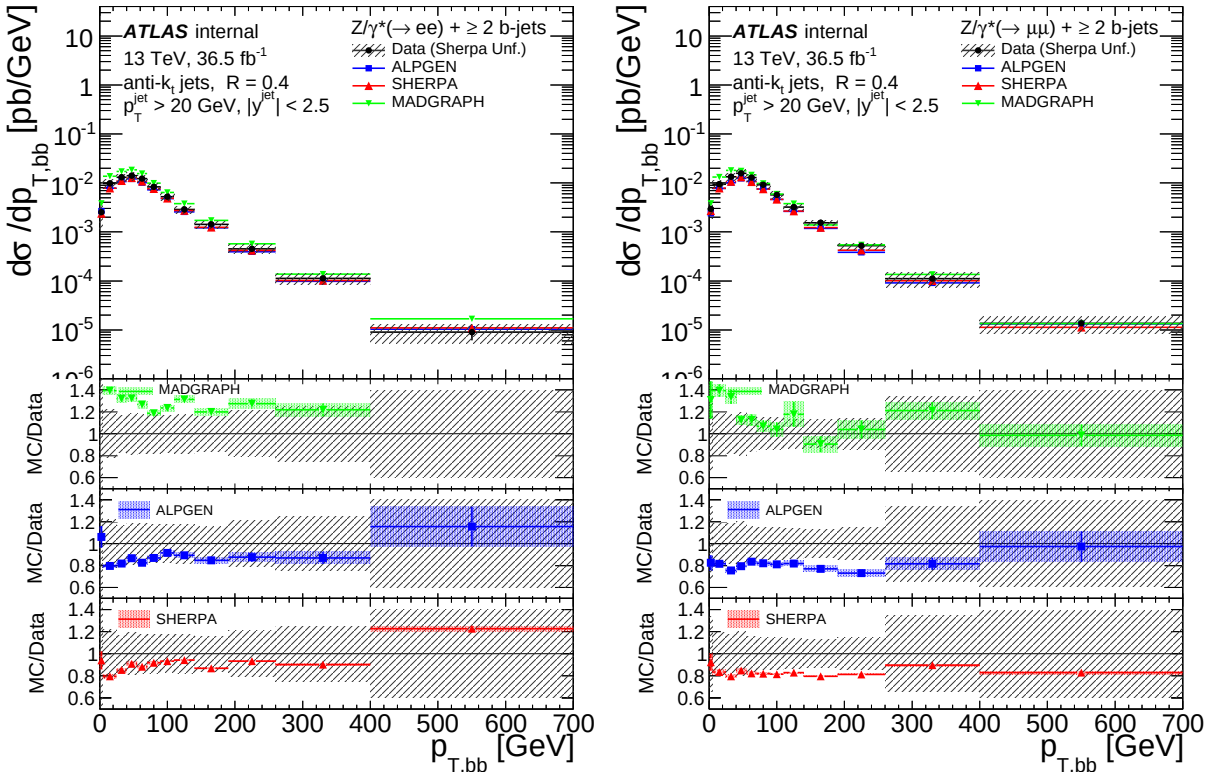

Figure 14.13: Differential cross section for the production of a Z boson with at least two b-jets as a function of p_T of the sum of the two leading b-jets four-vectors for the electron channel (left) and muon channel (right).

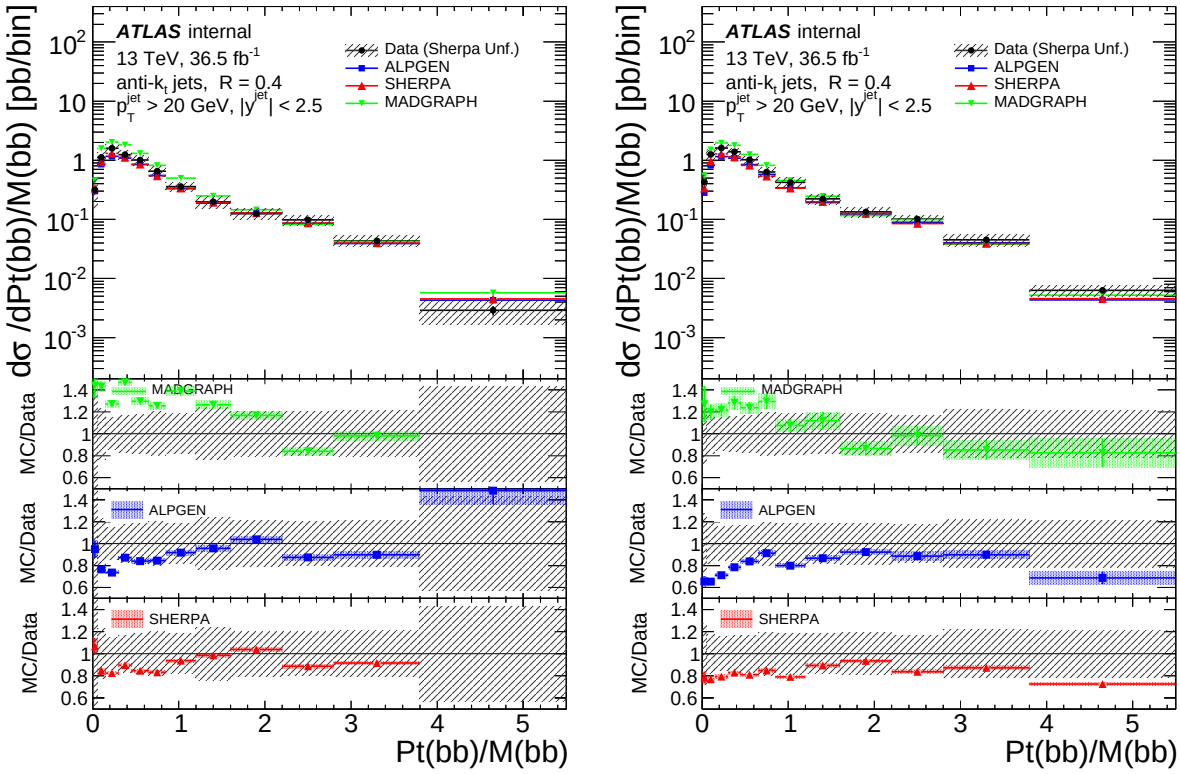

Figure 14.14: Differential cross section for the production of a Z boson with at least two b-jets as a function of p_T of the sum of the two leading b-jets four-vectors divided by the invariant mass of them for the electron channel (left) and muon channel (right).

CHAPTER 15

CONCLUSION

The production cross-section of a Z boson in association with at least one or two b-jets is measured. The measurement is done separately for the electron and muon decay channel. It is done using data recorded by the ATLAS detector in proton-proton collisions at a center of mass energy ($\sqrt{s}$) of 13 TeV. The data used corresponds to an integrated luminosity of 35.6 fb^{-1}. The inclusive cross-section is measured for events with at least one b-jet and for events with at least two b-jets. The differential cross-section is measured as a function of various variables. The measured results are compared to predictions given by three different generators: Sherpa, Algpen, and Madgraph.

The prediction given by Sherpa is within the uncertainties of the prediction and the measurement for the inclusive cross-section for both signal regions and lepton flavors. All three generators show varying levels agreement at modeling the different differential cross-sections.

Bibliography

[1] Fabio Maltoni, Giovanni Ridolfi, and Maria Ubiali. "b-initiated processes at the LHC: a reappraisal". In: *JHEP* 07 (2012). [Erratum: JHEP04,095(2013)], p. 022. DOI: 10.1007/JHEP04(2013)095,10.1007/JHEP07(2012)022. arXiv: 1203.6393 [hep-ph] (cit. on p. 1).

[2] Fernando Febres Cordero, L. Reina, and D. Wackeroth. "W- and Z-boson production with a massive bottom-quark pair at the Large Hadron Collider". In: *Phys. Rev.* D80 (2009), p. 034015. DOI: 10.1103/PhysRevD.80.034015. arXiv: 0906.1923 [hep-ph] (cit. on p. 1).

[3] A. D. Martin et al. "Parton distributions for the LHC". In: *Eur. Phys. J.* C63 (2009), pp. 189–285. DOI: 10.1140/epjc/s10052-009-1072-5. arXiv: 0901.0002 [hep-ph] (cit. on p. 1).

[4] T. Aaltonen et al. "Measurement of Cross Sections for b Jet Production in Events with a Z Boson in p^- anti-p Collisions at $\sqrt{s}$ = 1.96-TeV". In: *Phys. Rev.* D79 (2009), p. 052008. DOI: 10.1103/PhysRevD.79.052008. arXiv: 0812.4458 [hep-ex] (cit. on p. 1).

[5] Victor Mukhamedovich Abazov et al. "Measurement of the ratio of differential cross sections $\sigma(p\bar{p} \to Z + bjet)/\sigma(p\bar{p} \to Z + jet)$ in $p\bar{p}$ collisions at $\sqrt(s)$ = 1.96 TeV". In: *Phys. Rev.* D87.9 (2013), p. 092010. DOI: 10.1103/PhysRevD.87.092010. arXiv: 1301.2233 [hep-ex] (cit. on p. 1).

[6] Georges Aad et al. "Measurement of the cross-section for b-jets produced in association with a Z boson at $\sqrt{s} = 7$ TeV with the ATLAS detector". In: *Phys. Lett.* B706 (2012), pp. 295–313. DOI: 10.1016/j.physletb.2011.11.059. arXiv: 1109.1403 [hep-ex] (cit. on p. 2).

[7] Serguei Chatrchyan et al. "Measurement of the production cross sections for a Z boson and one or more b jets in pp collisions at sqrt(s) = 7 TeV". In: *JHEP* 06 (2014), p. 120. DOI: 10.1007/JHEP06(2014)120. arXiv: 1402.1521 [hep-ex] (cit. on p. 2).

[8] S. L. Glashow. "Partial Symmetries of Weak Interactions". In: *Nucl. Phys.* 22 (1961), pp. 579–588. DOI: 10.1016/0029-5582(61)90469-2 (cit. on p. 5).

[9] Steven Weinberg. "A Model of Leptons". In: *Phys. Rev. Lett.* 19 (21 Nov. 1967), pp. 1264–1266. DOI: 10.1103/PhysRevLett.19.1264. URL: https://link.aps.org/doi/10.1103/PhysRevLett.19.1264 (cit. on p. 5).

[10] Steven Weinberg. "A Model of Leptons". In: *Phys. Rev. Lett.* 19 (1967), pp. 1264–1266. DOI: 10.1103/PhysRevLett.19.1264 (cit. on p. 5).

[11] G. Arnison et al. "Experimental Observation of Lepton Pairs of Invariant Mass Around 95-GeV/c**2 at the CERN SPS Collider". In: *Phys. Lett.* B126 (1983). [,7.55(1983)], pp. 398–410. DOI: 10.1016/0370-2693(83)90188-0 (cit. on p. 5).

[12] G. Arnison et al. "Experimental Observation of Isolated Large Transverse Energy Electrons with Associated Missing Energy at s**(1/2) = 540-GeV". In: *Phys. Lett.* B122 (1983). [,611(1983)], pp. 103–116. DOI: 10.1016/0370-2693(83)91177-2 (cit. on p. 5).

[13] Peter W. Higgs. "Broken Symmetries and the Masses of Gauge Bosons". In: *Phys. Rev. Lett.* 13 (1964). [,160(1964)], pp. 508–509. DOI: 10.1103/PhysRevLett.13.508 (cit. on p. 5).

[14] Serguei Chatrchyan et al. "Observation of a new boson at a mass of 125 GeV with the CMS experiment at the LHC". In: *Phys. Lett.* B716 (2012), pp. 30–61. DOI: 10.1016/j.physletb.2012.08.021. arXiv: 1207.7235 [hep-ex] (cit. on p. 5).

[15] Georges Aad et al. "Observation of a new particle in the search for the Standard Model Higgs boson with the ATLAS detector at the LHC". In: *Phys. Lett.* B716 (2012), pp. 1–29. DOI: 10.1016/j.physletb.2012.08.020. arXiv: 1207.7214 [hep-ex] (cit. on p. 5).

[16] ATLAS Collaboration. *Summary plots from the ATLAS Standard Model physics group.* https://atlas.web.cern.ch/Atlas/GROUPS/PHYSICS/CombinedSummaryPlots/SM/. [Online; accessed 24-March-2018]. 2018 (cit. on p. 6).

[17] V. C. Rubin, N. Thonnard, and W. K. Ford Jr. "Rotational properties of 21 SC galaxies with a large range of luminosities and radii, from NGC 4605 /R = 4kpc/ to UGC 2885 /R = 122 kpc/". In: *Astrophys. J.* 238 (1980), p. 471. DOI: 10.1086/158003 (cit. on p. 5).

[18] G. Paal, I. Horvath, and B. Lukacs. "Inflation and compactification from galaxy redshifts?" In: 191 (May 1992), pp. 107–124. DOI: 10.1007/BF00644200 (cit. on p. 6).

[19] Andrew Purcell. "Go on a particle quest at the first CERN webfest. Le premier webfest du CERN se lance à la conquête des particules". In: BUL-NA-2012-269. 35/2012 (Aug. 2012), p. 10. URL: https://cds.cern.ch/record/1473657 (cit. on p. 7).

[20] John M. Campbell, J. W. Huston, and W. J. Stirling. "Hard Interactions of Quarks and Gluons: A Primer for LHC Physics". In: *Rept. Prog. Phys.* 70 (2007), p. 89. DOI: 10.1088/0034-4885/70/1/R02. arXiv: hep-ph/0611148 [hep-ph] (cit. on p. 8).

[21] John C. Collins, Davison E. Soper, and George F. Sterman. "Factorization of Hard Processes in QCD". In: *Adv. Ser. Direct. High Energy Phys.* 5 (1989), pp. 1–91. DOI: 10.1142/9789814503266_0001. arXiv: hep-ph/0409313 [hep-ph] (cit. on pp. 9, 10).

[22] F. Halzen and Alan D. Martin. *QUARKS AND LEPTONS: AN INTRODUCTORY COURSE IN MODERN PARTICLE PHYSICS*. 1984. ISBN: 0471887412, 9780471887416 (cit. on p. 10).

[23] A. D. Martin et al. "Parton distributions for the LHC". In: *Eur. Phys. J.* C63 (2009), pp. 189–285. DOI: 10.1140/epjc/s10052-009-1072-5. arXiv: 0901.0002 [hep-ph] (cit. on p. 11).

[24] G. Altarelli and G. Parisi. "Asymptotic freedom in parton language". In: *Nuclear Physics B* 126.2 (1977), pp. 298–318. ISSN: 0550-3213. DOI: https://doi.org/10.1016/0550-3213(77)90384-4. URL: http://www.sciencedirect.com/science/article/pii/0550321377903844 (cit. on p. 11).

[25] Richard D. Ball. "Global Parton Distributions for the LHC Run II". In: *Nuovo Cim.* C38.4 (2016), p. 127. DOI: 10.1393/ncc/i2015-15127-9. arXiv: 1507.07891 [hep-ph] (cit. on p. 11).

[26] L. A. Harland-Lang et al. "Parton distributions in the LHC era: MMHT 2014 PDFs". In: *Eur. Phys. J.* C75.5 (2015), p. 204. DOI: 10.1140/epjc/s10052-015-3397-6. arXiv: 1412.3989 [hep-ph] (cit. on p. 11).

[27] Stefan Höche. "Introduction to parton-shower event generators". In: *Proceedings, Theoretical Advanced Study Institute in Elementary Particle Physics: Journeys Through the Precision Frontier: Amplitudes for Colliders (TASI 2014): Boulder, Colorado, June 2-27, 2014*. 2015, pp. 235–295. DOI: 10.1142/9789814678766_0005. arXiv: 1411.4085 [hep-ph] (cit. on p. 13).

[28] B. R. Webber. "Fragmentation and hadronization". In: *Int. J. Mod. Phys.* A15S1 (2000). [eConfC990809,577(2000)], pp. 577–606. DOI: 10.1142/S0217751X00005334. arXiv: hep-ph/9912292 [hep-ph] (cit. on p. 12).

[29] B. R. Webber. "Fragmentation and hadronization". In: *Int. J. Mod. Phys.* A15S1 (2000). [eConfC990809,577(2000)], pp. 577–606. DOI: 10.1142/S0217751X00005334. arXiv: hep-ph/9912292 [hep-ph] (cit. on p. 14).

[30] Lyndon Evans and Philip Bryant. "LHC Machine". In: *JINST* 3 (2008), S08001. DOI: 10.1088/1748-0221/3/08/S08001 (cit. on p. 15).

[31] Albert Mollén and R Erlandsson. "Investigation of Ageing effects and Image stability in Hybrid Photon Pixel detectors at the LHCb experiment CERN". In: (Jan. 2010) (cit. on p. 15).

[32] CERN Christiane Lefèvre. "The CERN accelerator complex". Dec. 2008. URL: https://cds.cern.ch/record/1260465 (cit. on p. 17).

[33] ATLAS Collaboration. *ATLAS Luminosity Public Results Run 2*. https://twiki.cern.ch/twiki/bin/view/AtlasPublic/LuminosityPublicResultsRun2. [Online; accessed 12-April-2018]. 2016 (cit. on pp. 18, 19).

[34] ATLAS Collaboration. "The ATLAS Experiment at the CERN Large Hadron Collider". In: *JINST* 3 (2008), S08003. DOI: 10.1088/1748-0221/3/08/S08003 (cit. on pp. 18, 20, 22, 23, 25–29).

[35] CERN Joao Pequenao. "Computer generated image of the whole ATLAS detector". Mar. 2008. URL: https://cds.cern.ch/record/1095924 (cit. on p. 20).

[36] Till Tantau. "Graph Drawing in TikZ". In: *Proceedings of the 20th International Conference on Graph Drawing*. GD'12. Redmond, WA: Springer-Verlag, 2013, pp. 517–528. ISBN: 978-3-642-36762-5. DOI: 10.1007/978-3-642-36763-2_46 (cit. on p. 21).

[37] S Haywood et al. *ATLAS inner detector: Technical Design Report, 2*. Technical Design Report ATLAS. Geneva: CERN, 1997. URL: http://cds.cern.ch/record/331064 (cit. on p. 21).

[38] *ATLAS liquid-argon calorimeter: Technical Design Report*. Technical Design Report ATLAS. Geneva: CERN, 1996. URL: https://cds.cern.ch/record/331061 (cit. on p. 24).

[39] *ATLAS tile calorimeter: Technical Design Report*. Technical Design Report ATLAS. Geneva: CERN, 1996. URL: https://cds.cern.ch/record/331062 (cit. on p. 26).

[40] *ATLAS muon spectrometer: Technical Design Report*. Technical Design Report ATLAS. Geneva: CERN, 1997. URL: https://cds.cern.ch/record/331068 (cit. on p. 28).

[41] ATLAS Collaboration. "Performance of the ATLAS trigger system in 2015". In: *The European Physical Journal C* 77.5 (May 2017), p. 317. ISSN: 1434-6052. DOI: 10.1140/epjc/s10052-017-4852-3. URL: https://doi.org/10.1140/epjc/s10052-017-4852-3 (cit. on pp. 29, 71).

[42] Aranzazu Ruiz-Martinez and ATLAS Collaboration. *The Run-2 ATLAS Trigger System*. Tech. rep. ATL-DAQ-PROC-2016-003. Geneva: CERN, Feb. 2016. URL: https://cds.cern.ch/record/2133909 (cit. on p. 29).

[43] Stefan Weinzierl. "Introduction to Monte Carlo methods". In: (2000). arXiv: hep-ph/0006269 [hep-ph] (cit. on p. 33).

[44] M. A. Dobbs et al. "Les Houches guidebook to Monte Carlo generators for hadron collider physics". In: *Physics at TeV colliders. Proceedings, Workshop, Les Houches, France, May 26-June 3, 2003*. 2004, pp. 411–459. arXiv: hep-ph/0403045 [hep-ph]. URL: http://lss.fnal.gov/cgi-bin/find_paper.pl?conf-04-183 (cit. on p. 33).

[45] *Summary of ATLAS Pythia 8 tunes*. Tech. rep. ATL-PHYS-PUB-2012-003. Geneva: CERN, Aug. 2012. URL: https://cds.cern.ch/record/1474107 (cit. on p. 33).

[46] A. D. Martin et al. "Parton distributions for the LHC". In: *Eur. Phys. J.* C63 (2009), pp. 189–285. DOI: 10.1140/epjc/s10052-009-1072-5. arXiv: 0901.0002 [hep-ph] (cit. on p. 33).

[47] S. Agostinelli et al. "Geant4—a simulation toolkit". In: *Nuclear Instruments and Methods in Physics Research Section A: Accelerators, Spectrometers, Detectors and Associated Equipment* 506.3 (2003), pp. 250–303. ISSN: 0168-9002. DOI: https://doi.org/10.1016/S0168-9002(03)01368-8. URL: http://www.sciencedirect.com/science/article/pii/S0168900203013688 (cit. on p. 34).

[48] Charalampos Anastasiou et al. "High precision QCD at hadron colliders: Electroweak gauge boson rapidity distributions at NNLO". In: *Phys. Rev.* D69 (2004), p. 094008. DOI: 10.1103/PhysRevD.69.094008. arXiv: hep-ph/0312266 [hep-ph] (cit. on p. 35).

[49] J Butterworth et al. *Single Boson and Diboson Production Cross Sections in pp Collisions at sqrts=7 TeV*. Tech. rep. ATL-COM-PHYS-2010-695. Geneva: CERN, Aug. 2010. URL: https://cds.cern.ch/record/1287902 (cit. on p. 35).

[50] T. Gleisberg et al. "Event generation with SHERPA 1.1". In: *JHEP* 02 (2009), p. 007. DOI: 10.1088/1126-6708/2009/02/007. arXiv: 0811.4622 [hep-ph] (cit. on p. 35).

[51] Stefan Höche et al. "QCD matrix elements + parton showers. The NLO case". In: *Journal of High Energy Physics* 2013.4 (Apr. 2013), p. 27. ISSN: 1029-8479. DOI: 10.1007/JHEP04(2013)027. URL: https://doi.org/10.1007/JHEP04(2013)027 (cit. on p. 35).

[52] Richard D. Ball et al. "Parton distributions for the LHC Run II". In: *JHEP* 04 (2015), p. 040. DOI: 10.1007/JHEP04(2015)040. arXiv: 1410.8849 [hep-ph] (cit. on pp. 35, 38).

[53] Michelangelo L. Mangano et al. "ALPGEN, a generator for hard multiparton processes in hadronic collisions". In: *JHEP* 07 (2003), p. 001. DOI: 10.1088/1126-6708/2003/07/001. arXiv: hep-ph/0206293 [hep-ph] (cit. on p. 36).

[54] Torbjorn Sjostrand, Stephen Mrenna, and Peter Z. Skands. "PYTHIA 6.4 Physics and Manual". In: *JHEP* 05 (2006), p. 026. DOI: 10.1088/1126-6708/2006/05/026. arXiv: hep-ph/0603175 [hep-ph] (cit. on p. 36).

[55] Peter Zeiler Skands. "Tuning Monte Carlo Generators: The Perugia Tunes". In: *Phys. Rev.* D82 (2010), p. 074018. DOI: 10.1103/PhysRevD.82.074018. arXiv: 1005.3457 [hep-ph] (cit. on p. 36).

[56] J. Pumplin et al. "New generation of parton distributions with uncertainties from global QCD analysis". In: *JHEP* 07 (2002), p. 012. DOI: 10.1088/1126-6708/2002/07/012. arXiv: hep-ph/0201195 [hep-ph] (cit. on p. 36).

[57] J. Alwall et al. "The automated computation of tree-level and next-to-leading order differential cross sections, and their matching to parton shower simulations". In: *JHEP* 07 (2014), p. 079. DOI: 10.1007/JHEP07(2014)079. arXiv: 1405.0301 [hep-ph] (cit. on p. 37).

[58] Torbjorn Sjostrand, Stephen Mrenna, and Peter Z. Skands. "A Brief Introduction to PYTHIA 8.1". In: *Comput. Phys. Commun.* 178 (2008), pp. 852–867. DOI: 10.1016/j.cpc.2008.01.036. arXiv: 0710.3820 [hep-ph] (cit. on p. 37).

[59] *ATLAS Run 1 Pythia8 tunes*. Tech. rep. ATL-PHYS-PUB-2014-021. Geneva: CERN, Nov. 2014. URL: https://cds.cern.ch/record/1966419 (cit. on p. 37).

[60] Simone Alioli et al. "A general framework for implementing NLO calculations in shower Monte Carlo programs: the POWHEG BOX". In: *JHEP* 06 (2010), p. 043. DOI: 10.1007/JHEP06(2010)043. arXiv: 1002.2581 [hep-ph] (cit. on p. 39).

[61] Keith Hamilton, Paolo Nason, and Giulia Zanderighi. "MINLO: Multi-Scale Improved NLO". In: *JHEP* 10 (2012), p. 155. DOI: 10.1007/JHEP10(2012)155. arXiv: 1206.3572 [hep-ph] (cit. on p. 39).

[62] *Studies on top-quark Monte Carlo modelling for Top2016*. Tech. rep. ATL-PHYS-PUB-2016-020. Geneva: CERN, Sept. 2016. URL: http://cds.cern.ch/record/2216168 (cit. on p. 39).

[63] Michal Czakon and Alexander Mitov. "Top++: A Program for the Calculation of the Top-Pair Cross-Section at Hadron Colliders". In: *Comput. Phys. Commun.* 185 (2014), p. 2930. DOI: 10.1016/j.cpc.2014.06.021. arXiv: 1112.5675 [hep-ph] (cit. on p. 39).

[64] E. Boos and L. Dudko. "The Single Top Quark Physics". In: *Int. J. Mod. Phys.* A27 (2012), p. 1230026. DOI: 10.1142/S0217751X12300268. arXiv: 1211.7146 [hep-ph] (cit. on p. 40).

[65] *Electron efficiency measurements with the ATLAS detector using the 2015 LHC proton-proton collision data*. Tech. rep. ATLAS-CONF-2016-024. Geneva: CERN, June 2016. URL: https://cds.cern.ch/record/2157687 (cit. on pp. 41, 71, 88).

[66] W Lampl et al. *Calorimeter Clustering Algorithms: Description and Performance*. Tech. rep. ATL-LARG-PUB-2008-002. ATL-COM-LARG-2008-003. Geneva: CERN, Apr. 2008. URL: https://cds.cern.ch/record/1099735 (cit. on p. 41).

[67] M. Aaboud et al. "Performance of the ATLAS Track Reconstruction Algorithms in Dense Environments in LHC Run 2". In: *Eur. Phys. J.* C77.10 (2017), p. 673. DOI: 10.1140/epjc/s10052-017-5225-7. arXiv: 1704.07983 [hep-ex] (cit. on p. 41).

[68] T G Cornelissen et al. "The global 2track fitter in ATLAS". In: *Journal of Physics: Conference Series* 119.3 (July 2008), p. 032013. DOI: 10.1088/1742-6596/119/3/032013. URL: https://doi.org/10.1088%2F1742-6596%2F119%2F3%2F032013 (cit. on p. 42).

[69] "Improved electron reconstruction in ATLAS using the Gaussian Sum Filter-based model for bremsstrahlung". In: (2012) (cit. on p. 42).

[70] Morad Aaboud et al. "Electron and photon energy calibration with the ATLAS detector using 2015-2016 LHC proton-proton collision data". In: *Submitted to: JINST* (2018). arXiv: 1812.03848 [hep-ex] (cit. on pp. 42, 65, 66, 88).

[71] Georges Aad et al. "Muon reconstruction performance of the ATLAS detector in proton–proton collision data at $\sqrt{s}$ =13 TeV". In: *Eur. Phys. J.* C76.5 (2016), p. 292. DOI: 10.1140/epjc/s10052-016-4120-y. arXiv: 1603.05598 [hep-ex] (cit. on pp. 44, 46, 66, 71).

[72] *Performance of the ATLAS Inner Detector Track and Vertex Reconstruction in the High Pile-Up LHC Environment*. Tech. rep. ATLAS-CONF-2012-042. Geneva: CERN, Mar. 2012. URL: https://cds.cern.ch/record/1435196 (cit. on p. 44).

[73] S. Hassani et al. "A muon identification and combined reconstruction procedure for the ATLAS detector at the LHC using the (MUONBOY, STACO, MuTag) reconstruction packages". In: *Nuclear Instruments and Methods in Physics Research Section A: Accelerators, Spectrometers, Detectors and Associated Equipment* 572.1 (2007). Frontier Detectors for Frontier Physics, pp. 77–79. ISSN: 0168-9002. DOI: https://doi.org/10.1016/j.nima.2006.10.340. URL: http://www.sciencedirect.com/science/article/pii/S0168900206019863 (cit. on p. 44).

[74] Gavin P. Salam. "Towards Jetography". In: *Eur. Phys. J.* C67 (2010), pp. 637–686. DOI: 10.1140/epjc/s10052-010-1314-6. arXiv: 0906.1833 [hep-ph] (cit. on p. 47).

[75] Matteo Cacciari, Gavin P. Salam, and Gregory Soyez. "The anti-k_t jet clustering algorithm". In: *JHEP* 04 (2008), p. 063. DOI: 10.1088/1126-6708/2008/04/063. arXiv: 0802.1189 [hep-ph] (cit. on p. 47).

[76] Matteo Cacciari, Gavin P. Salam, and Gregory Soyez. "FastJet User Manual". In: *Eur. Phys. J.* C72 (2012), p. 1896. DOI: 10.1140/epjc/s10052-012-1896-2. arXiv: 1111.6097 [hep-ph] (cit. on p. 47).

[77] Georges Aad et al. "Topological cell clustering in the ATLAS calorimeters and its performance in LHC Run 1". In: *Eur. Phys. J.* C77 (2017), p. 490. DOI: 10.1140/epjc/s10052-017-5004-5. arXiv: 1603.02934 [hep-ex] (cit. on pp. 47, 51).

[78] Matteo Cacciari, Gavin P Salam, and Gregory Soyez. "The anti-ktjet clustering algorithm". In: *Journal of High Energy Physics* 2008.04 (Apr. 2008), pp. 063–063. DOI: 10.1088/1126-6708/2008/04/063. URL: https://doi.org/10.1088%2F1126-6708%2F2008%2F04%2F063 (cit. on p. 50).

[79] M. Aaboud et al. "Jet energy scale measurements and their systematic uncertainties in proton-proton collisions at $\sqrt{s} = 13$ TeV with the ATLAS detector". In: *Phys. Rev.* D96.7 (2017), p. 072002. DOI: 10.1103/PhysRevD.96.072002. arXiv: 1703.09665 [hep-ex] (cit. on pp. 51, 53–55, 57).

[80] Georges Aad et al. "Jet energy measurement with the ATLAS detector in proton-proton collisions at $\sqrt{s} = 7$ TeV". In: *Eur. Phys. J.* C73.3 (2013), p. 2304. DOI: 10.1140/epjc/s10052-013-2304-2. arXiv: 1112.6426 [hep-ex] (cit. on p. 56).

[81] *Jet global sequential corrections with the ATLAS detector in proton-proton collisions at sqrt(s) = 8 TeV*. Tech. rep. ATLAS-CONF-2015-002. Geneva: CERN, Mar. 2015. URL: https://cds.cern.ch/record/2001682 (cit. on p. 56).

[82] *Optimisation of the ATLAS b-tagging performance for the 2016 LHC Run*. Tech. rep. ATL-PHYS-PUB-2016-012. Geneva: CERN, June 2016. URL: https://cds.cern.ch/record/2160731 (cit. on pp. 57–60, 63).

[83] *Expected performance of the ATLAS b-tagging algorithms in Run-2*. Tech. rep. ATL-PHYS-PUB-2015-022. Geneva: CERN, July 2015. URL: https://cds.cern.ch/record/2037697 (cit. on pp. 57, 61, 62).

[84] G Piacquadio and C Weiser. "A new inclusive secondary vertex algorithm for b-jet tagging in ATLAS". In: *Journal of Physics: Conference Series* 119.3 (July 2008), p. 032032. DOI: 10.1088/1742-6596/119/3/032032. URL: https://doi.org/10.1088%2F1742-6596%2F119%2F3%2F032032 (cit. on p. 60).

[85] The ATLAS collaboration. "$E_{\mathrm{T}}^{\mathrm{miss}}$ performance in the ATLAS detector using 2015-2016 LHC p-p collisions". In: (2018) (cit. on pp. 64, 89).

[86] *Selection of jets produced in 13TeV proton-proton collisions with the ATLAS detector*. Tech. rep. ATLAS-CONF-2015-029. Geneva: CERN, July 2015. URL: http://cds.cern.ch/record/2037702 (cit. on p. 67).

[87] *Tagging and suppression of pileup jets with the ATLAS detector*. Tech. rep. ATLAS-CONF-2014-018. Geneva: CERN, May 2014. URL: https://cds.cern.ch/record/1700870 (cit. on pp. 67, 71).

[88] E Le Menedeu et al. *Continuous b-tagging for the ATLAS experiment*. Tech. rep. ATL-COM-PHYS-2014-035. Geneva: CERN, Jan. 2014. URL: https://cds.cern.ch/record/1644430 (cit. on p. 71).

[89] Georges Aad et al. "Performance of b-Jet Identification in the ATLAS Experiment". In: *JINST* 11.04 (2016), P04008. DOI: 10.1088/1748-0221/11/04/P04008. arXiv: 1512.01094 [hep-ex] (cit. on pp. 72, 87).

[90] M. Aaboud et al. "Jet energy scale measurements and their systematic uncertainties in proton-proton collisions at $\sqrt{s} = 13$ TeV with the ATLAS detector". In: *Phys. Rev.* D96.7 (2017), p. 072002. DOI: 10.1103/PhysRevD.96.072002. arXiv: 1703.09665 [hep-ex] (cit. on p. 86).

[91] Georges Aad et al. "Jet energy measurement and its systematic uncertainty in proton-proton collisions at $\sqrt{s} = 7$ TeV with the ATLAS detector". In: *Eur. Phys. J.* C75 (2015), p. 17. DOI: 10.1140/epjc/s10052-014-3190-y. arXiv: 1406.0076 [hep-ex] (cit. on p. 87).

[92] Luigi Marchese. *Muon reconstruction performance of the ATLAS detector in 2016*. Tech. rep. ATL-PHYS-PROC-2017-246. Geneva: CERN, Nov. 2017. DOI: 10.1051/epjconf/201818203008. URL: https://cds.cern.ch/record/2292925 (cit. on p. 89).

[93] *Luminosity determination in pp collisions at $\sqrt{s} = 13$ TeV using the ATLAS detector at the LHC*. Tech. rep. ATLAS-CONF-2019-021. Geneva: CERN, June 2019. URL: http://cds.cern.ch/record/2677054 (cit. on p. 89).

[94] Glen Cowan et al. "Asymptotic formulae for likelihood-based tests of new physics". In: *Eur. Phys. J.* C71 (2011). [Erratum: Eur. Phys. J.C73,2501(2013)], p. 1554. DOI: 10.1140/epjc/s10052-011-1554-0,10.1140/epjc/s10052-013-2501-z. arXiv: 1007.1727 [physics.data-an] (cit. on p. 97).

[95] *Proposal for truth particle observable definitions in physics measurements*. Tech. rep. ATL-PHYS-PUB-2015-013. Geneva: CERN, June 2015. URL: https://cds.cern.ch/record/2022743 (cit. on p. 154).

[96] Georges Aad et al. “Measurement of differential production cross-sections for a Z boson in association with b-jets in 7 TeV proton-proton collisions with the ATLAS detector”. In: *JHEP* 10 (2014), p. 141. DOI: 10.1007/JHEP10(2014)141. arXiv: 1407.3643 [hep-ex] (cit. on p. 184).

Appendices

APPENDIX A

SUMMARY OF SAMPLES USED

This chapter contains tables summarizing the nominal samples used in this analysis.

Process	Summary Name	DSID	$\sigma \cdot$ BR [pb]	k-factor	ϵ_{filter}	# init. ev.
$W^- \to \ell\nu + H \to b\bar{b}$	PwPy8EG_NNPDF3_AZNLO_WmH125J_MINLO_lvbb_VpT	345053	0.17949	0.582	1	975900
$W^+ \to \ell\nu + H \to b\bar{b}$	PwPy8EG_NNPDF3_AZNLO_WpH125J_MINLO_lvbb_VpT	345054	0.28278	0.582	1	1979950
$Z^+ \to \ell\nu + H \to b\bar{b}$	PwPy8EG_NNPDF3_AZNLO_ZH125J_MINLO_llbb_VpT	345055	0.07704	0.582	1	2928500
$Z \to \ell\ell + Z \to qq$	Sh_221_NNPDF30NNLO_ZqqZll	363356	15.563	1.0	0.1396	5317000
$W^- \to \ell\nu + W^+ \to qq$	Sh_221_NNPDF30NNLO_WpqqWmlv	363359	24.717	1.0	1.0	6733000
$W^+ \to \ell\nu + W^- \to qq$	Sh_221_NNPDF30NNLO_WplvWmqq	363360	24.725	1.0	1.0	7115000
$Z \to \ell\ell + W \to qq$	Sh_221_NNPDF30NNLO_WqqZll	363358	3.437	1.0	1.0	5124000
$W \to \ell\nu + Z \to qqZ$	Sh_221_NNPDF30NNLO_WlvZqq	363489	11.413	1.0	1.0	7100000
$t\bar{t}$, lep-jets	PwPy8EG_A14_ttbar_hdamp258p75_nonallhad	410501	831.76	0.543	1.0	58829000
top t-channel	PowhegPythiaEvtGen_P2012_singletop_tchan_lept_top	410011	43.739	1.0094	1.0	2992600
anti-top t-channel	PowhegPythiaEvtGen_P2012_singletop_tchan_lept_antitop	410012	25.778	1.0193	1.0	4989800
top Wt-channel	PowhegPythiaEvtGen_P2012_Wt_inclusive_top	410013	34.009	1.054	1.0	4865800
anti-top Wt-channel	PowhegPythiaEvtGen_P2012_Wt_inclusive_antitop	410014	33.989	1.054	1.0	4945600
top s-channel	PowhegPythiaEvtGen_P2012_SingleTopSchan_noAllHad_top	410025	2.0517	1.0046	1.0	997800
anti-top s-channel	PowhegPythiaEvtGen_P2012_SingleTopSchan_noAllHad_antitop	410026	1.2615	1.0215	1.0	995400

Table A.1: Simulated background samples

Process	Summary Name	DSID	$\sigma \cdot$ BR [pb]	ϵ_{filter}	k-factor	# init. ev.
$W(e\nu)$+jets	Sherpa_221_NNPDF30NNLO_Wenu_MAXHTPTV0_70_CVetoBVeto	364170	19127.0	8.2447E-01	0.9702	24740000
Sherpa 2.2.1	Sherpa_221_NNPDF30NNLO_Wenu_MAXHTPTV0_70_CFilterBVeto	364171	19130.0	1.3030E-01	0.9702	9853500
	Sherpa_221_NNPDF30NNLO_Wenu_MAXHTPTV0_70_BFilter	364172	19135.0	4.4141E-02	0.9702	17242400
	Sherpa_221_NNPDF30NNLO_Wenu_MAXHTPTV70_140_CVetoBVeto	364173	942.58	6.6872E-01	0.9702	14660500
	Sherpa_221_NNPDF30NNLO_Wenu_MAXHTPTV70_140_CFilterBVeto	364174	945.67	2.2787E-01	0.9702	9818400
	Sherpa_221_NNPDF30NNLO_Wenu_MAXHTPTV70_140_BFilter	364175	945.15	1.0341E-01	0.9702	9801900
	Sherpa_221_NNPDF30NNLO_Wenu_MAXHTPTV140_280_CVetoBVeto	364176	339.81	5.9691E-01	0.9702	9879000
	Sherpa_221_NNPDF30NNLO_Wenu_MAXHTPTV140_280_CFilterBVeto	364177	339.87	2.8965E-01	0.9702	7410000
	Sherpa_221_NNPDF30NNLO_Wenu_MAXHTPTV140_280_BFilter	364178	339.48	1.0898E-01	0.9702	24677800
	Sherpa_221_NNPDF30NNLO_Wenu_MAXHTPTV280_500_CVetoBVeto	364179	72.084	5.4441E-01	0.9702	4923800
	Sherpa_221_NNPDF30NNLO_Wenu_MAXHTPTV280_500_CFilterBVeto	364180	72.128	3.1675E-01	0.9702	2963400
	Sherpa_221_NNPDF30NNLO_Wenu_MAXHTPTV280_500_BFilter	364181	72.113	1.3391E-01	0.9702	2958000
	Sherpa_221_NNPDF30NNLO_Wenu_MAXHTPTV500_1000	364182	15.224	1.0	0.9702	5916800
	Sherpa_221_NNPDF30NNLO_Wenu_MAXHTPTV1000_E_CMS	364183	1.2334	1.0	0.9702	3947000
$W(\mu\nu)$+jets	Sherpa_221_NNPDF30NNLO_Wmunu_MAXHTPTV0_70_CVetoBVeto	364156	19143.0	8.2447E-01	0.9702	24723000
Sherpa 2.2.1	Sherpa_221_NNPDF30NNLO_Wmunu_MAXHTPTV0_70_CFilterBVeto	364157	19121.0	1.3030E-01	0.9702	9847000
	Sherpa_221_NNPDF30NNLO_Wmunu_MAXHTPTV0_70_BFilter	364158	19135.0	4.4141E-02	0.9702	17226200
	Sherpa_221_NNPDF30NNLO_Wmunu_MAXHTPTV70_140_CVetoBVeto	364159	944.85	6.6872E-01	0.9702	14788000
	Sherpa_221_NNPDF30NNLO_Wmunu_MAXHTPTV70_140_CFilterBVeto	364160	937.78	2.2787E-01	0.9702	9853800
	Sherpa_221_NNPDF30NNLO_Wmunu_MAXHTPTV70_140_BFilter	364161	944.63	1.0341E-01	0.9702	19639000
	Sherpa_221_NNPDF30NNLO_Wmunu_MAXHTPTV140_280_CVetoBVeto	364162	339.54	5.9691E-01	0.9702	9882000
	Sherpa_221_NNPDF30NNLO_Wmunu_MAXHTPTV140_280_CFilterBVeto	364163	340.06	2.8965E-01	0.9702	7408000
	Sherpa_221_NNPDF30NNLO_Wmunu_MAXHTPTV140_280_BFilter	364164	339.54	1.0898E-01	0.9702	24585000
	Sherpa_221_NNPDF30NNLO_Wmunu_MAXHTPTV280_500_CVetoBVeto	364165	72.067	5.4441E-01	0.9702	4940000
	Sherpa_221_NNPDF30NNLO_Wmunu_MAXHTPTV280_500_CFilterBVeto	364166	72.198	3.1675E-01	0.9702	2958000
	Sherpa_221_NNPDF30NNLO_Wmunu_MAXHTPTV280_500_BFilter	364167	72.045	1.3391E-01	0.9702	2959500
	Sherpa_221_NNPDF30NNLO_Wmunu_MAXHTPTV500_1000	364168	15.01	1.0	0.9702	5910500
	Sherpa_221_NNPDF30NNLO_Wmunu_MAXHTPTV1000_E_CMS	364169	1.2344	1.0	0.9702	3919000

Table A.2: Simulated Sherpa samples for W+jets where $W \to e\nu$ and $W \to \mu\nu$.

Process	Summary Name	DSID	$\sigma \cdot$ BR [pb]	ϵ_{filter}	k-factor	# init. ev.
$W(e\nu)$+jets	AlpgenPythiaEvtGen_P2012_WenuNp0	361800	14322	1.0	1.1109	14813000
ALPGEN	AlpgenPythiaEvtGen_P2012_WenuNp1	361801	3042.3	1.0	1.1109	29614000
+Pythia6	AlpgenPythiaEvtGen_P2012_WenuNp2	361802	858.06	1.0	1.1109	9804000
	AlpgenPythiaEvtGen_P2012_WenuNp3	361803	251.95	1.0	1.1109	15729000
	AlpgenPythiaEvtGen_P2012_WenuNp4	361804	77.439	1.0	1.1109	4670000
	AlpgenPythiaEvtGen_P2012_WenuNp5	361805	33.371	1.0	1.1109	5000
	AlpgenPythiaEvtGen_P2012_WenucNp0	361860	597.55	1.0	1.1109	2968000
	AlpgenPythiaEvtGen_P2012_WenucNp1	361861	188.43	1.0	1.1109	1476000
	AlpgenPythiaEvtGen_P2012_WenucNp2	361862	50.904	1.0	1.1109	590000
	AlpgenPythiaEvtGen_P2012_WenucNp3	361863	13.913	1.0	1.1109	149000
	AlpgenPythiaEvtGen_P2012_WenucNp4	361864	5.7192	1.0	1.1109	48000
	AlpgenPythiaEvtGen_P2012_WenuccNp0	361850	85.913	1.0	1.1109	1140000
	AlpgenPythiaEvtGen_P2012_WenuccNp1	361851	106.24	1.0	1.1109	1136000
	AlpgenPythiaEvtGen_P2012_WenuccNp2	361852	68.43	1.0	1.1109	196000
	AlpgenPythiaEvtGen_P2012_WenuccNp3	361853	38.212	1.0	1.1109	113000
	AlpgenPythiaEvtGen_P2012_WenubbNp0	361830	31.741	1.0	1.1109	3858000
	AlpgenPythiaEvtGen_P2012_WenubbNp1	361831	33.675	1.0	1.1109	3547000
	AlpgenPythiaEvtGen_P2012_WenubbNp2	361832	18.645	1.0	1.1109	1773000
	AlpgenPythiaEvtGen_P2012_WenubbNp3	361833	12.617	1.0	1.1109	1028000
$W(\mu\nu)$+jets	AlpgenPythiaEvtGen_P2012_WmunuNp0	361810	14323	1.0	1.1109	14824000
ALPGEN	AlpgenPythiaEvtGen_P2012_WmunuNp1	361811	3041.4	1.0	1.1109	29605000
+Pythia6	AlpgenPythiaEvtGen_P2012_WmunuNp2	361812	858.11	1.0	1.1109	9857000
	AlpgenPythiaEvtGen_P2012_WmunuNp3	361813	252.01	1.0	1.1109	7898000
	AlpgenPythiaEvtGen_P2012_WmunuNp4	361814	77.496	1.0	1.1109	4921000
	AlpgenPythiaEvtGen_P2012_WmunuNp5	361815	33.341	1.0	1.1109	1976000
	AlpgenPythiaEvtGen_P2012_WmunucNp0	361865	597.71	1.0	1.1109	2971000
	AlpgenPythiaEvtGen_P2012_WmunucNp1	361866	188.2	1.0	1.1109	1477000
	AlpgenPythiaEvtGen_P2012_WmunucNp2	361867	50.728	1.0	1.1109	590000
	AlpgenPythiaEvtGen_P2012_WmunucNp3	361868	13.954	1.0	1.1109	150000
	AlpgenPythiaEvtGen_P2012_WmunucNp4	361869	5.7551	1.0	1.1109	47000
	AlpgenPythiaEvtGen_P2012_WmunuccNp0	361850	85.852	1.0	1.1109	1142000
	AlpgenPythiaEvtGen_P2012_WmunuccNp1	361851	106.27	1.0	1.1109	1137000
	AlpgenPythiaEvtGen_P2012_WmunuccNp2	361852	68.429	1.0	1.1109	199000
	AlpgenPythiaEvtGen_P2012_WmunuccNp3	361853	38.236	1.0	1.1109	113000
	AlpgenPythiaEvtGen_P2012_WmunubbNp0	361830	31.731	1.0	1.1109	3860000
	AlpgenPythiaEvtGen_P2012_WmunubbNp1	361831	33.677	1.0	1.1109	3565000
	AlpgenPythiaEvtGen_P2012_WmunubbNp2	361832	18.624	1.0	1.1109	1776000
	AlpgenPythiaEvtGen_P2012_WmunubbNp3	361833	12.674	1.0	1.1109	1036000

Table A.3: Simulated Alpgen samples for W+jets where $W \to e\nu$ and $W \to \mu\nu$.

Process	Summary Name	DSID	$\sigma \cdot$ BR [pb]	ϵ_{filter}	k-factor	# init. ev.
$W(e\nu)$+jets	MGPy8EG_N30NLO_Wenu_Ht0_70_CVetoBVeto	363600	16719.0	8.3756E-01	1.12	24472000
Madgraph	MGPy8EG_N30NLO_Wenu_Ht0_70_CFilterBVeto	363601	16720.0	1.3829E-01	1.12	15847800
+Pythia8	MGPy8EG_N30NLO_Wenu_Ht0_70_BFilter	363602	16717.0	2.4191E-02	1.12	8782750
	MGPy8EG_N30NLO_Wenu_Ht70_140_CVetoBVeto	363603	755.1	7.1172E-01	1.12	4733500
	MGPy8EG_N30NLO_Wenu_Ht70_140_CFilterBVeto	363604	755.77	2.3976E-01	1.12	4417600
	MGPy8EG_N30NLO_Wenu_Ht70_140_BFilter	363605	755.73	4.8330E-02	1.12	4787025
	MGPy8EG_N30NLO_Wenu_Ht140_280_CVetoBVeto	363606	318.96	6.6554E-01	1.12	4782500
	MGPy8EG_N30NLO_Wenu_Ht140_280_CFilterBVeto	363607	319.93	2.6354E-01	1.12	3808450
	MGPy8EG_N30NLO_Wenu_Ht140_280_BFilter	363608	319.45	6.9423E-02	1.12	3984560
	MGPy8EG_N30NLO_Wenu_Ht280_500_CVetoBVeto	363609	73.528	6.1903E-01	1.12	1784000
	MGPy8EG_N30NLO_Wenu_Ht280_500_CFilterBVeto	363610	73.562	2.8524E-01	1.12	1868600
	MGPy8EG_N30NLO_Wenu_Ht280_500_BFilter	363611	73.556	9.5211E-02	1.12	1966050
	MGPy8EG_N30NLO_Wenu_Ht500_700_CVetoBVeto	363612	11.529	5.8680E-01	1.12	969000
	MGPy8EG_N30NLO_Wenu_Ht500_700_CFilterBVeto	363613	11.517	2.9823E-01	1.12	302000
	MGPy8EG_N30NLO_Wenu_Ht500_700_BFilter	363614	11.51	1.1526E-01	1.12	285500
	MGPy8EG_N30NLO_Wenu_Ht700_1000_CVetoBVeto	363615	4.0158	5.6645E-01	1.12	361000
	MGPy8EG_N30NLO_Wenu_Ht700_1000_CFilterBVeto	363616	4.014	3.0425E-01	1.12	173600
	MGPy8EG_N30NLO_Wenu_Ht700_1000_BFilter	363617	4.0123	1.2837E-01	1.12	95000
	MGPy8EG_N30NLO_Wenu_Ht1000_2000_CVetoBVeto	363618	1.3243	5.4797E-01	1.12	84000
	MGPy8EG_N30NLO_Wenu_Ht1000_2000_CFilterBVeto	363619	1.3286	3.0760E-01	1.12	51200
	MGPy8EG_N30NLO_Wenu_Ht1000_2000_BFilter	363620	1.326	1.4260E-01	1.12	51200
	MGPy8EG_N30NLO_Wenu_Ht2000_E_CMS_CVetoBVeto	363621	0.04229	5.2445E-01	1.12	7000
	MGPy8EG_N30NLO_Wenu_Ht2000_E_CMS_CFilterBVeto	363622	0.04188	3.1678E-01	1.12	7000
	MGPy8EG_N30NLO_Wenu_Ht2000_E_CMS_BFilter	363623	0.04738	1.5125E-01	1.12	7000
$W(\mu\nu)$+jets	MGPy8EG_N30NLO_Wmunu_Ht0_70_CVetoBVeto	363624	16720.0	8.3755E-01	1.12	24087000
Madgraph	MGPy8EG_N30NLO_Wmunu_Ht0_70_CFilterBVeto	363625	16717.0	1.3835E-01	1.12	9646600
+Pythia8	MGPy8EG_N30NLO_Wmunu_Ht0_70_BFilter	363626	16719.0	2.4199E-02	1.12	8853500
	MGPy8EG_N30NLO_Wmunu_Ht70_140_CVetoBVeto	363627	755.19	7.1182E-01	1.12	4446000
	MGPy8EG_N30NLO_Wmunu_Ht70_140_CFilterBVeto	363628	755.62	2.3986E-01	1.12	4427300
	MGPy8EG_N30NLO_Wmunu_Ht70_140_BFilter	363629	755.77	4.8328E-02	1.12	2134000
	MGPy8EG_N30NLO_Wmunu_Ht140_280_CVetoBVeto	363630	318.83	6.6550E-01	1.12	491000
	MGPy8EG_N30NLO_Wmunu_Ht140_280_CFilterBVeto	363631	319.89	2.6394E-01	1.12	3920750
	MGPy8EG_N30NLO_Wmunu_Ht140_280_BFilter	363632	319.41	6.9437E-02	1.12	3633080
	MGPy8EG_N30NLO_Wmunu_Ht280_500_CVetoBVeto	363633	73.585	6.1863E-01	1.12	1928000
	MGPy8EG_N30NLO_Wmunu_Ht280_500_CFilterBVeto	363634	73.548	2.8512E-01	1.12	1853400
	MGPy8EG_N30NLO_Wmunu_Ht280_500_BFilter	363635	73.569	9.5191E-02	1.12	1777800
	MGPy8EG_N30NLO_Wmunu_Ht500_700_CVetoBVeto	363636	11.522	5.8643E-01	1.12	1063000
	MGPy8EG_N30NLO_Wmunu_Ht500_700_CFilterBVeto	363637	11.524	2.9645E-01	1.12	291000
	MGPy8EG_N30NLO_Wmunu_Ht500_700_BFilter	363638	11.522	1.1565E-01	1.12	552000
	MGPy8EG_N30NLO_Wmunu_Ht700_1000_CVetoBVeto	363639	4.0194	5.6682E-01	1.12	352000
	MGPy8EG_N30NLO_Wmunu_Ht700_1000_CFilterBVeto	363640	4.0252	3.0485E-01	1.12	95200
	MGPy8EG_N30NLO_Wmunu_Ht700_1000_BFilter	363641	4.0139	1.2845E-01	1.12	95000
	MGPy8EG_N30NLO_Wmunu_Ht1000_2000_CVetoBVeto	363642	1.3262	5.4537E-01	1.12	40500
	MGPy8EG_N30NLO_Wmunu_Ht1000_2000_CFilterBVeto	363643	1.3215	3.0792E-01	1.12	51200
	MGPy8EG_N30NLO_Wmunu_Ht1000_2000_BFilter	363644	1.3287	1.4358E-01	1.12	76000
	MGPy8EG_N30NLO_Wmunu_Ht2000_E_CMS_CVetoBVeto	363645	0.041697	5.1966E-01	1.12	5800
	MGPy8EG_N30NLO_Wmunu_Ht2000_E_CMS_CFilterBVeto	363646	0.042199	3.1695E-01	1.12	7000
	MGPy8EG_N30NLO_Wmunu_Ht2000_E_CMS_BFilter	363647	0.042049	1.5886E-01	1.12	6700

Table A.4: Simulated MadGraph samples for W+jets where $W \to e\nu$ and $W \to \mu\nu$.

Process	Summary Name	DSID	$\sigma \cdot$ BR [pb]	ϵ_{filter}	k-factor	# init. ev.
$W(\tau\nu)$+jets	Sherpa_221_NNPDF30NNLO_Wtaunu_MAXHTPTV0_70_CVetoBVeto	364184	19152.0	8.2495E-01	0.9702	24740000
Sherpa 2.2.1	Sherpa_221_NNPDF30NNLO_Wtaunu_MAXHTPTV0_70_CFilterBVeto	364185	19153.0	1.2934E-01	0.9702	9865600
	Sherpa_221_NNPDF30NNLO_Wtaunu_MAXHTPTV0_70_BFilter	364186	19163.0	4.4594E-02	0.9702	17273200
	Sherpa_221_NNPDF30NNLO_Wtaunu_MAXHTPTV70_140_CVetoBVeto	364187	947.65	6.7382E-01	0.9702	14808500
	Sherpa_221_NNPDF30NNLO_Wtaunu_MAXHTPTV70_140_CFilterBVeto	364188	946.73	2.2222E-01	0.9702	9860000
	Sherpa_221_NNPDF30NNLO_Wtaunu_MAXHTPTV70_140_BFilter	364189	943.3	1.0391E-01	0.9702	9857000
	Sherpa_221_NNPDF30NNLO_Wtaunu_MAXHTPTV140_280_CVetoBVeto	364190	339.36	5.9622E-01	0.9702	9899000
	Sherpa_221_NNPDF30NNLO_Wtaunu_MAXHTPTV140_280_CFilterBVeto	364191	339.63	2.9025E-01	0.9702	7365000
	Sherpa_221_NNPDF30NNLO_Wtaunu_MAXHTPTV140_280_BFilter	364192	339.54	1.1799EE-01	0.9702	9834000
	Sherpa_221_NNPDF30NNLO_Wtaunu_MAXHTPTV280_500_CVetoBVeto	364193	72.065	5.4569E-01	0.9702	4931200
	Sherpa_221_NNPDF30NNLO_Wtaunu_MAXHTPTV280_500_CFilterBVeto	364194	71.972	3.1648E-01	0.9702	2956400
	Sherpa_221_NNPDF30NNLO_Wtaunu_MAXHTPTV280_500_BFilter	364195	72.026	1.3426E-01	0.9702	2954100
	Sherpa_221_NNPDF30NNLO_Wtaunu_MAXHTPTV500_1000	364196	15.046	1.0	0.9702	5945000
	Sherpa_221_NNPDF30NNLO_Wtaunu_MAXHTPTV1000_E_CMS	364197	1.2339	1.0	0.9702	3946000
$W(\tau\nu)$+jets	AlpgenPythiaEvtGen_P2012_WtaunuNp0	361820	14322	1.0	1.1109	14809000
ALPGEN	AlpgenPythiaEvtGen_P2012_WtaunuNp1	361821	3041.8	1.0	1.1109	29342000
+Pythia6	AlpgenPythiaEvtGen_P2012_WtaunuNp2	361822	858.14	1.0	1.1109	9759000
	AlpgenPythiaEvtGen_P2012_WtaunuNp3	361823	252.16	1.0	1.1109	7903000
	AlpgenPythiaEvtGen_P2012_WtaunuNp4	361824	77.496	1.0	1.1109	4837000
	AlpgenPythiaEvtGen_P2012_WtaunuNp5	361825	33.279	1.0	1.1109	1976000
	AlpgenPythiaEvtGen_P2012_WtaunucNp0	361870	597.34	1.0	1.1109	2968000
	AlpgenPythiaEvtGen_P2012_WtaunucNp1	361871	188.47	1.0	1.1109	1488000
	AlpgenPythiaEvtGen_P2012_WtaunucNp2	361872	50.769	1.0	1.1109	589000
	AlpgenPythiaEvtGen_P2012_WtaunucNp3	361873	13.901	1.0	1.1109	147000
	AlpgenPythiaEvtGen_P2012_WtaunucNp4	361874	5.7584	1.0	1.1109	50000
	AlpgenPythiaEvtGen_P2012_WtaunuccNp0	361855	85.86	1.0	1.1109	1134000
	AlpgenPythiaEvtGen_P2012_WtaunuccNp1	361856	106.18	1.0	1.1109	1134000
	AlpgenPythiaEvtGen_P2012_WtaunuccNp2	361857	68.147	1.0	1.1109	195000
	AlpgenPythiaEvtGen_P2012_WtaunuccNp3	361858	38.236	1.0	1.1109	115000
	AlpgenPythiaEvtGen_P2012_WtaunubbNp0	361840	31.739	1.0	1.1109	3855000
	AlpgenPythiaEvtGen_P2012_WtaunubbNp1	361841	33.64	1.0	1.1109	3566000
	AlpgenPythiaEvtGen_P2012_WtaunubbNp2	361842	18.636	1.0	1.1109	1781000
	AlpgenPythiaEvtGen_P2012_WtaunubbNp3	361843	12.67	1.0	1.1109	1036000

Table A.5: Simulated Sherpa and Alpgen samples for W+jets where $W \to \tau\nu$

Process	Summary Name	DSID	$\sigma \cdot$ BR [pb]	ϵ_{filter}	k-factor	# init. ev.
$Z(ee)$+jets	Sherpa_221_NNPDF30NNLO_Zee_MAXHTPTV0_70_CVetoBVeto	364114	1981.8	8.2106E-01	0.9751	7900000
Sherpa 2.2.1	Sherpa_221_NNPDF30NNLO_Zee_MAXHTPTV0_70_CFilterBVeto	364115	1980.8	1.1295E-01	0.9751	4940500
	Sherpa_221_NNPDF30NNLO_Zee_MAXHTPTV0_70_BFilter	364116	1981.7	6.3809E-02	0.9751	7883600
	Sherpa_221_NNPDF30NNLO_Zee_MAXHTPTV70_140_CVetoBVeto	364117	110.5	6.9043E-01	0.9751	5925000
	Sherpa_221_NNPDF30NNLO_Zee_MAXHTPTV70_140_CFilterBVeto	364118	110.63	1.8382E-01	0.9751	1972600
	Sherpa_221_NNPDF30NNLO_Zee_MAXHTPTV70_140_BFilter	364119	110.31	1.1443E-01	0.9751	5855000
	Sherpa_221_NNPDF30NNLO_Zee_MAXHTPTV140_280_CVetoBVeto	364120	40.731	6.1452E-01	0.9751	4949000
	Sherpa_221_NNPDF30NNLO_Zee_MAXHTPTV140_280_CFilterBVeto	364121	40.67	2.3044E-01	0.9751	2962600
	Sherpa_221_NNPDF30NNLO_Zee_MAXHTPTV140_280_BFilter	364122	40.694	1.4927E-01	0.9751	12010900
	Sherpa_221_NNPDF30NNLO_Zee_MAXHTPTV280_500_CVetoBVeto	364123	8.6743	5.6134E-01	0.9751	1932800
	Sherpa_221_NNPDF30NNLO_Zee_MAXHTPTV280_500_CFilterBVeto	364124	8.6711	2.6294E-01	0.9751	988900
	Sherpa_221_NNPDF30NNLO_Zee_MAXHTPTV280_500_BFilter	364125	8.6766	1.7223E-01	0.9751	1976850
	Sherpa_221_NNPDF30NNLO_Zee_MAXHTPTV500_1000	364126	1.8081	1.0	0.9751	2973000
	Sherpa_221_NNPDF30NNLO_Zee_MAXHTPTV1000_E_CMS	364127	0.14857	1.0	0.9751	988000
$Z(\mu\mu)$+jets	Sherpa_221_NNPDF30NNLO_Zmumu_MAXHTPTV0_70_CVetoBVeto	364100	1983.0	8.2210E-01	0.9751	7891000
Sherpa 2.2.1	Sherpa_221_NNPDF30NNLO_Zmumu_MAXHTPTV0_70_CFilterBVeto	364101	1978.4	1.1308E-01	0.9751	4940500
	Sherpa_221_NNPDF30NNLO_Zmumu_MAXHTPTV0_70_BFilter	364102	1982.2	6.4161E-02	0.9751	7902000
	Sherpa_221_NNPDF30NNLO_Zmumu_MAXHTPTV70_140_CVetoBVeto	364103	108.92	6.8873E-01	0.9751	5917000
	Sherpa_221_NNPDF30NNLO_Zmumu_MAXHTPTV70_140_CFilterBVeto	364104	109.42	1.8596E-01	0.9751	1969800
	Sherpa_221_NNPDF30NNLO_Zmumu_MAXHTPTV70_140_BFilter	364105	108.91	1.1375E-01	0.9751	5900600
	Sherpa_221_NNPDF30NNLO_Zmumu_MAXHTPTV140_280_CVetoBVeto	364106	39.878	6.0899E-01	0.9751	4943000
	Sherpa_221_NNPDF30NNLO_Zmumu_MAXHTPTV140_280_CFilterBVeto	364107	39.795	2.3308E-01	0.9751	2954400
	Sherpa_221_NNPDF30NNLO_Zmumu_MAXHTPTV140_280_BFilter	364108	39.908	1.4618E-01	0.9751	12339300
	Sherpa_221_NNPDF30NNLO_Zmumu_MAXHTPTV280_500_CVetoBVeto	364109	8.5375	5.5906E-01	0.9751	1973000
	Sherpa_221_NNPDF30NNLO_Zmumu_MAXHTPTV280_500_CFilterBVeto	364110	8.5403	2.6528E-01	0.9751	986000
	Sherpa_221_NNPDF30NNLO_Zmumu_MAXHTPTV280_500_BFilter	364111	8.4932	1.7559E-01	0.9751	1971400
	Sherpa_221_NNPDF30NNLO_Zmumu_MAXHTPTV500_1000	364112	1.7881	1.0	0.9751	2960500
	Sherpa_221_NNPDF30NNLO_Zmumu_MAXHTPTV1000_E_CMS	364113	0.14769	1.0	0.9751	988000

Table A.6: Simulated Sherpa samples for Z+jets where $Z \to ee$ and $Z \to \mu\mu$.

Process	Summary Name	DSID	$\sigma \cdot$ BR [pb]	ϵ_{filter}	k-factor	# init. ev.
$Z(ee)$+jets	AlpgenPythiaEvtGen_P2012_ZeeNp0	361700	1283.9	1.0	1.196	7877000
ALPGEN	AlpgenPythiaEvtGen_P2012_ZeeNp1	361701	277.24	1.0	1.196	7682000
+Pythia6	AlpgenPythiaEvtGen_P2012_ZeeNp2	361702	75.799	1.0	1.196	4928000
	AlpgenPythiaEvtGen_P2012_ZeeNp3	361703	21.576	1.0	1.196	1941000
	AlpgenPythiaEvtGen_P2012_ZeeNp4	361704	6.1543	1.0	1.196	986000
	AlpgenPythiaEvtGen_P2012_ZeeNp5	361705	2.4924	1.0	1.196	495000
	AlpgenPythiaEvtGen_P2012_ZeeccNp0	361735	63.35	1.0	1.196	295000
	AlpgenPythiaEvtGen_P2012_ZeeccNp1	361736	28.672	1.0	1.196	198000
	AlpgenPythiaEvtGen_P2012_ZeeccNp2	361737	8.0836	1.0	1.196	99000
	AlpgenPythiaEvtGen_P2012_ZeeccNp3Incl	361738	4.6769	1.0	1.196	40000
	AlpgenPythiaEvtGen_P2012_ZeebbNp0	361730	16.65	1.0	1.196	544000
	AlpgenPythiaEvtGen_P2012_ZeebbNp1	361731	7.6399	1.0	1.196	249000
	AlpgenPythiaEvtGen_P2012_ZeebbNp2	361732	3.0629	1.0	1.196	104000
	AlpgenPythiaEvtGen_P2012_ZeebbNp3Incl	361733	1.7879	1.0	1.196	50000
$Z(\mu\mu)$+jets	AlpgenPythiaEvtGen_P2012_ZmumuNp0	361710	1284.2	1.0	1.196	7924000
ALPGEN	AlpgenPythiaEvtGen_P2012_ZmumuNp1	361711	277.3	1.0	1.196	7880000
+Pythia6	AlpgenPythiaEvtGen_P2012_ZmumuNp2	361712	75.788	1.0	1.196	4851000
	AlpgenPythiaEvtGen_P2012_ZmumuNp3	361713	21.562	1.0	1.196	1980000
	AlpgenPythiaEvtGen_P2012_ZmumuNp4	361714	6.1623	1.0	1.196	988000
	AlpgenPythiaEvtGen_P2012_ZmumuNp5	361715	2.4669	1.0	1.196	490000
	AlpgenPythiaEvtGen_P2012_ZmumuccNp0	361745	62.424	1.0	1.196	298000
	AlpgenPythiaEvtGen_P2012_ZmumuccNp1	361746	28.675	1.0	1.196	197000
	AlpgenPythiaEvtGen_P2012_ZmumuccNp2	361747	8.0972	1.0	1.196	98000
	AlpgenPythiaEvtGen_P2012_ZmumuccNp3Incl	361748	4.6782	1.0	1.196	40000
	AlpgenPythiaEvtGen_P2012_ZmumubbNp0	361740	16.625	1.0	1.196	544000
	AlpgenPythiaEvtGen_P2012_ZmumubbNp1	361741	7.6356	1.0	1.196	248000
	AlpgenPythiaEvtGen_P2012_ZmumubbNp2	361742	3.0646	1.0	1.196	105000
	AlpgenPythiaEvtGen_P2012_ZmumubbNp3Incl	361743	1.7986	1.0	1.196	49000

Table A.7: Simulated Alpgen samples for Z+jets where $Z \to ee$ and $Z \to \mu\mu$.

Process	Summary Name	DSID	$\sigma \cdot$ BR [pb]	ϵ_{filter}	k-factor	# init. ev.
$Z(ee)$+jets	MGPy8EG_N30NLO_Zee_Ht0_70_CVetoBVeto	363147	1719.7	0.83292	1.141	2951000
Madgraph	MGPy8EG_N30NLO_Zee_Ht0_70_CFilterBVeto	363148	1719.4	0.10775	1.141	972900
+Pythia8	MGPy8EG_N30NLO_Zee_Ht0_70_BFilter	363149	1719.4	0.059156	1.141	709950
	MGPy8EG_N30NLO_Zee_Ht70_140_CVetoBVeto	363150	85.105	0.71754	1.141	981200
	MGPy8EG_N30NLO_Zee_Ht70_140_CFilterBVeto	363151	85.041	0.17377	1.141	973200
	MGPy8EG_N30NLO_Zee_Ht70_140_BFilter	363152	85.175	0.10763	1.141	195220
	MGPy8EG_N30NLO_Zee_Ht140_280_CVetoBVeto	363153	36.005	0.67279	1.141	490000
	MGPy8EG_N30NLO_Zee_Ht140_280_CFilterBVeto	363154	36.028	0.19996	1.141	244850
	MGPy8EG_N30NLO_Zee_Ht140_280_BFilter	363155	36.06	0.12486	1.141	193980
	MGPy8EG_N30NLO_Zee_Ht280_500_CVetoBVeto	363156	8.2054	0.62846	1.141	197000
	MGPy8EG_N30NLO_Zee_Ht280_500_CFilterBVeto	363157	8.2126	0.22726	1.141	98000
	MGPy8EG_N30NLO_Zee_Ht280_500_BFilter	363158	8.2474	0.14193	1.141	58000
	MGPy8EG_N30NLO_Zee_Ht500_700_CVetoBVeto	363159	1.2733	0.5966	1.141	49000
	MGPy8EG_N30NLO_Zee_Ht500_700_CFilterBVeto	363160	1.273	0.24847	1.141	50000
	MGPy8EG_N30NLO_Zee_Ht500_700_BFilter	363161	1.2722	0.15256	1.141	6000
	MGPy8EG_N30NLO_Zee_Ht700_1000_CVetoBVeto	363162	0.44546	0.57676	1.141	47900
	MGPy8EG_N30NLO_Zee_Ht700_1000_CFilterBVeto	363163	0.44611	0.26137	1.141	5000
	MGPy8EG_N30NLO_Zee_Ht700_1000_BFilter	363164	0.44603	0.16181	1.141	5000
	MGPy8EG_N30NLO_Zee_Ht1000_2000_CVetoBVeto	363165	0.15208	0.55543	1.141	49000
	MGPy8EG_N30NLO_Zee_Ht1000_2000_CFilterBVeto	363166	0.15248	0.27476	1.141	49000
	MGPy8EG_N30NLO_Zee_Ht1000_2000_BFilter	363167	0.15327	0.16618	1.141	49960
	MGPy8EG_N30NLO_Zee_Ht2000_E_CMS_CVetoBVeto	363168	0.0056989	0.53136	1.141	20000
	MGPy8EG_N30NLO_Zee_Ht2000_E_CMS_CFilterBVeto	363169	0.0057408	0.2923	1.141	20000
	MGPy8EG_N30NLO_Zee_Ht2000_E_CMS_BFilter	363170	0.0057164	0.17489	1.141	5000
$Z(\mu\mu)$+jets	MGPy8EG_N30NLO_Zmumu_Ht0_70_CVetoBVeto	363123	1714.5	0.83157	1.141	1920000
Madgraph	MGPy8EG_N30NLO_Zmumu_Ht0_70_CFilterBVeto	363124	1715.5	0.10835	1.141	555500
+Pythia8	MGPy8EG_N30NLO_Zmumu_Ht0_70_BFilter	363125	1715.7	0.059162	1.141	487000
	MGPy8EG_N30NLO_Zmumu_Ht70_140_CVetoBVeto	363126	84.57	0.71809	1.141	483000
	MGPy8EG_N30NLO_Zmumu_Ht70_140_CFilterBVeto	363127	84.588	0.17404	1.141	138500
	MGPy8EG_N30NLO_Zmumu_Ht70_140_BFilter	363128	84.752	0.10804	1.141	78000
	MGPy8EG_N30NLO_Zmumu_Ht140_280_CVetoBVeto	363129	35.883	0.67432	1.141	69000
	MGPy8EG_N30NLO_Zmumu_Ht140_280_CFilterBVeto	363130	35.908	0.19951	1.141	24000
	MGPy8EG_N30NLO_Zmumu_Ht140_280_BFilter	363131	35.887	0.12607	1.141	8000
	MGPy8EG_N30NLO_Zmumu_Ht280_500_CVetoBVeto	363132	8.1871	0.62802	1.141	99000
	MGPy8EG_N30NLO_Zmumu_Ht280_500_CFilterBVeto	363133	8.1805	0.2282	1.141	45000
	MGPy8EG_N30NLO_Zmumu_Ht280_500_BFilter	363134	8.1705	0.14263	1.141	29000
	MGPy8EG_N30NLO_Zmumu_Ht500_700_CVetoBVeto	363135	1.271	0.59722	1.141	10000
	MGPy8EG_N30NLO_Zmumu_Ht500_700_CFilterBVeto	363136	1.2672	0.24952	1.141	9000
	MGPy8EG_N30NLO_Zmumu_Ht500_700_BFilter	363137	1.2699	0.15292	1.141	10000
	MGPy8EG_N30NLO_Zmumu_Ht700_1000_CVetoBVeto	363138	0.43601	0.57118	1.141	5000
	MGPy8EG_N30NLO_Zmumu_Ht700_1000_CFilterBVeto	363139	0.44623	0.25948	1.141	5000
	MGPy8EG_N30NLO_Zmumu_Ht700_1000_BFilter	363140	0.44567	0.15965	1.141	4500
	MGPy8EG_N30NLO_Zmumu_Ht1000_2000_CVetoBVeto	363141	0.14899	0.54908	1.141	4500
	MGPy8EG_N30NLO_Zmumu_Ht1000_2000_CFilterBVeto	363142	0.14625	0.27164	1.141	1000
	MGPy8EG_N30NLO_Zmumu_Ht1000_2000_BFilter	363143	0.14705	0.17299	1.141	1000
	MGPy8EG_N30NLO_Zmumu_Ht2000_E_CMS_CVetoBVeto	363144	0.005538	0.56337	1.141	1000
	MGPy8EG_N30NLO_Zmumu_Ht2000_E_CMS_CFilterBVeto	363145	0.0055466	0.29294	1.141	1000
	MGPy8EG_N30NLO_Zmumu_Ht2000_E_CMS_BFilter	363146	0.0056422	0.16307	1.141	1000

Table A.8: Simulated MadGraph samples for Z+jets where $Z \to ee$ and $Z \to \mu\mu$.

Process	Summary Name	DSID	$\sigma \cdot$ BR [pb]	ϵ_{filter}	k-factor	# init. ev.
$Z(\tau\tau)$+jets	Sherpa_221_NNPDF30NNLO_Ztautau_MAXHTPTV0_70_CVetoBVeto	364128	1981.6	8.2142E-01	0.9751	7907000
Sherpa 2.2.1	Sherpa_221_NNPDF30NNLO_Ztautau_MAXHTPTV0_70_CFilterBVeto	364129	1978.8	1.1314E-01	0.9751	4941000
	Sherpa_221_NNPDF30NNLO_Ztautau_MAXHTPTV0_70_BFilter	364130	1981.8	6.4453E-02	0.9751	7890600
	Sherpa_221_NNPDF30NNLO_Ztautau_MAXHTPTV70_140_CVetoBVeto	364131	110.37	6.8883E-01	0.9751	5935500
	Sherpa_221_NNPDF30NNLO_Ztautau_MAXHTPTV70_140_CFilterBVeto	364132	110.51	1.8290E-01	0.9751	1961200
	Sherpa_221_NNPDF30NNLO_Ztautau_MAXHTPTV70_140_BFilter	364133	110.87	1.283E-01	0.9751	5912550
	Sherpa_221_NNPDF30NNLO_Ztautau_MAXHTPTV140_280_CVetoBVeto	364134	40.781	6.0821E-01	0.9751	4956000
	Sherpa_221_NNPDF30NNLO_Ztautau_MAXHTPTV140_280_CFilterBVeto	364135	40.74	2.2897E-01	0.9751	2973000
	Sherpa_221_NNPDF30NNLO_Ztautau_MAXHTPTV140_280_BFilter	364136	40.761	1.3442E-01	0.9751	4932950
	Sherpa_221_NNPDF30NNLO_Ztautau_MAXHTPTV280_500_CVetoBVeto	364137	8.5502	5.6036E-01	0.9751	1973000
	Sherpa_221_NNPDF30NNLO_Ztautau_MAXHTPTV280_500_CFilterBVeto	364138	8.6707	2.6245E-01	0.9751	986000
	Sherpa_221_NNPDF30NNLO_Ztautau_MAXHTPTV280_500_BFilter	364139	8.6804	1.7313E-01	0.9751	1974950
	Sherpa_221_NNPDF30NNLO_Ztautau_MAXHTPTV500_1000	364140	1.8096	1.0	0.9751	2744800
	Sherpa_221_NNPDF30NNLO_Ztautau_MAXHTPTV1000_E_CMS	364141	0.14834	1.0	0.9751	980000
$Z(\tau\tau)$+jets	AlpgenPythiaEvtGen_P2012_ZtautauNp0	361720	1283.9	1.0	1.196	7900000
ALPGEN	AlpgenPythiaEvtGen_P2012_ZtautauNp1	361721	277.28	1.0	1.196	7876000
+Pythia6	AlpgenPythiaEvtGen_P2012_ZtautauNp2	361722	75.815	1.0	1.196	4922000
	AlpgenPythiaEvtGen_P2012_ZtautauNp3	361723	21.531	1.0	1.196	1971000
	AlpgenPythiaEvtGen_P2012_ZtautauNp4	361724	6.1591	1.0	1.196	983000
	AlpgenPythiaEvtGen_P2012_ZtautauNp5	361725	2.4558	1.0	1.196	494000
	AlpgenPythiaEvtGen_P2012_ZtautauccNp0	361755	62.452	1.0	1.196	296000
	AlpgenPythiaEvtGen_P2012_ZtautauccNp1	361756	28.642	1.0	1.196	198000
	AlpgenPythiaEvtGen_P2012_ZtautauccNp2	361757	8.0984	1.0	1.196	98000
	AlpgenPythiaEvtGen_P2012_ZtautauccNp3Incl	361758	4.6471	1.0	1.196	39000
	AlpgenPythiaEvtGen_P2012_ZtautaubbNp0	361750	16.633	1.0	1.196	546000
	AlpgenPythiaEvtGen_P2012_ZtautaubbNp1	361751	7.6356	1.0	1.196	246000
	AlpgenPythiaEvtGen_P2012_ZtautaubbNp2	361752	3.0705	1.0	1.196	54000
	AlpgenPythiaEvtGen_P2012_ZtautaubbNp3Incl	361753	1.7937	1.0	1.196	50000

Table A.9: Simulated Sherpa and Alpgen samples for Z+jets where $Z \to \tau\tau$

APPENDIX B

FLAVOR FIT

B.1 Shape Plots of Fit Templates

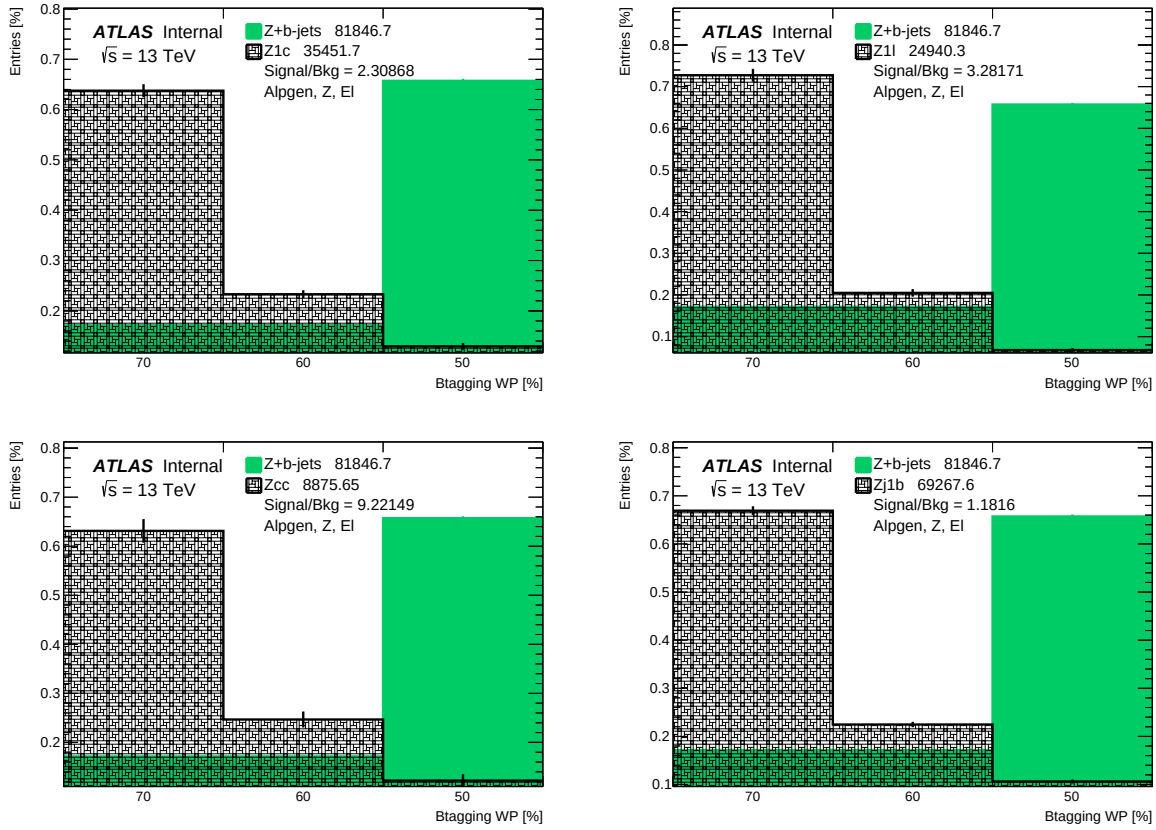

Figure B.1: Shape comparison of the signal component,Z + b-jets, to the background components Z + c (top left), Z + cc (bottom left), Z + l (top right), and to their sum (bottom right) for the Alpgen generator in the Z1B signal region for the electron channel.

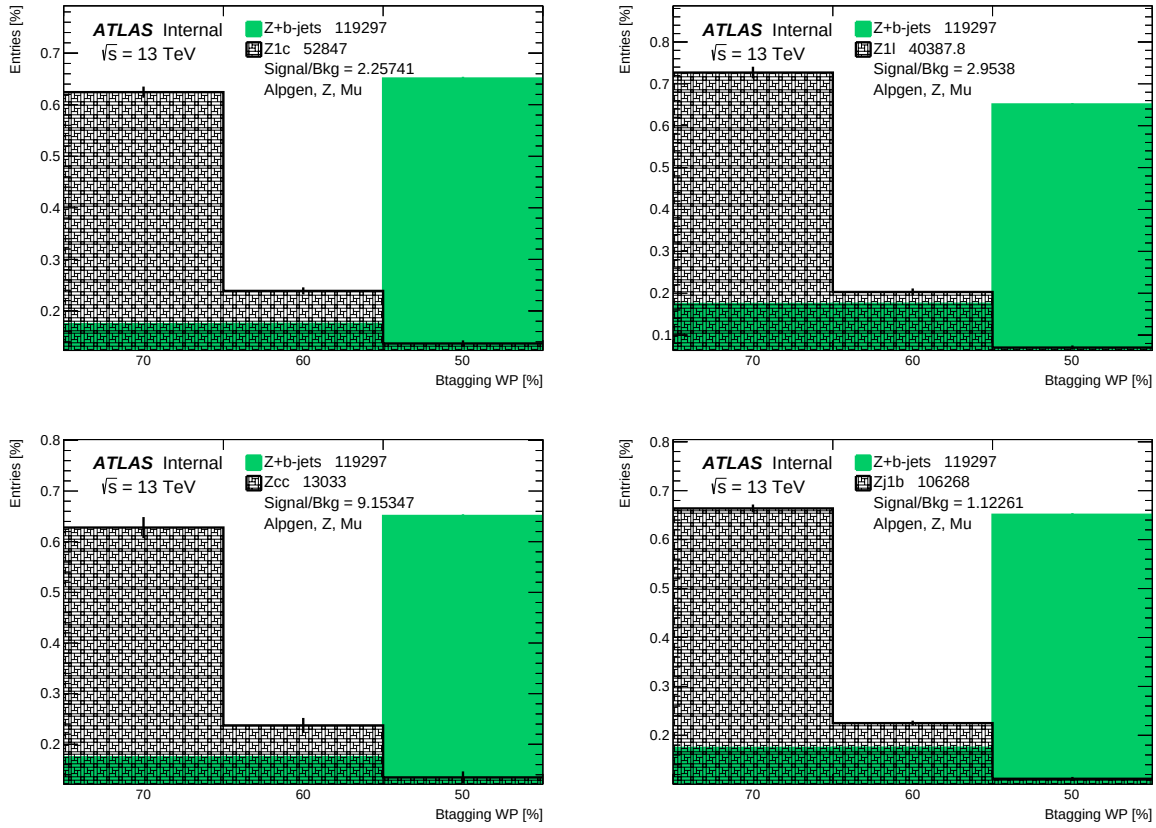

Figure B.2: Shape comparison of the signal component,Z + b-jets, to the background components Z + c (top left), Z + cc (bottom left), Z + l (top right), and to their sum (bottom right) for the Alpgen generator in the Z1B signal region for the muon channel.

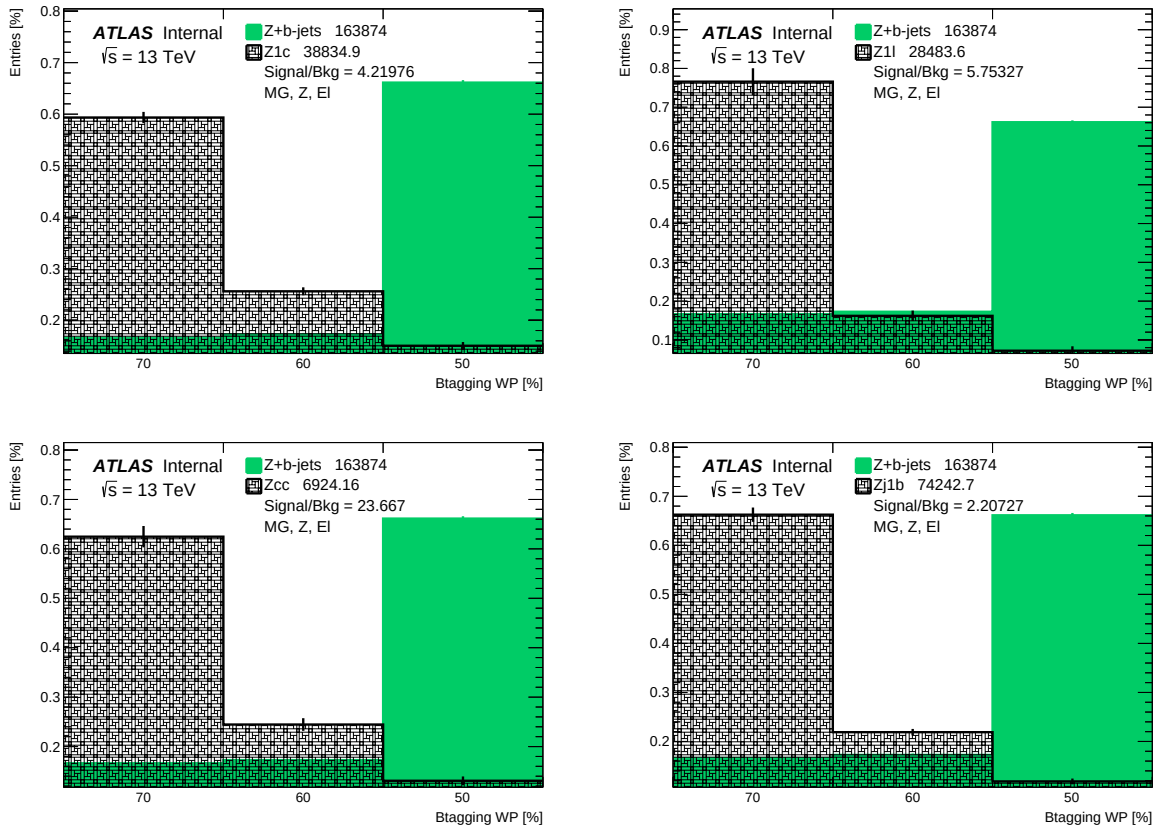

Figure B.3: Shape comparison of the signal component,Z + b-jets, to the background components Z + c (top left), Z + cc (bottom left), Z + l (top right), and to their sum (bottom right) for the Madgraph generator in the Z1B signal region for the electron channel.

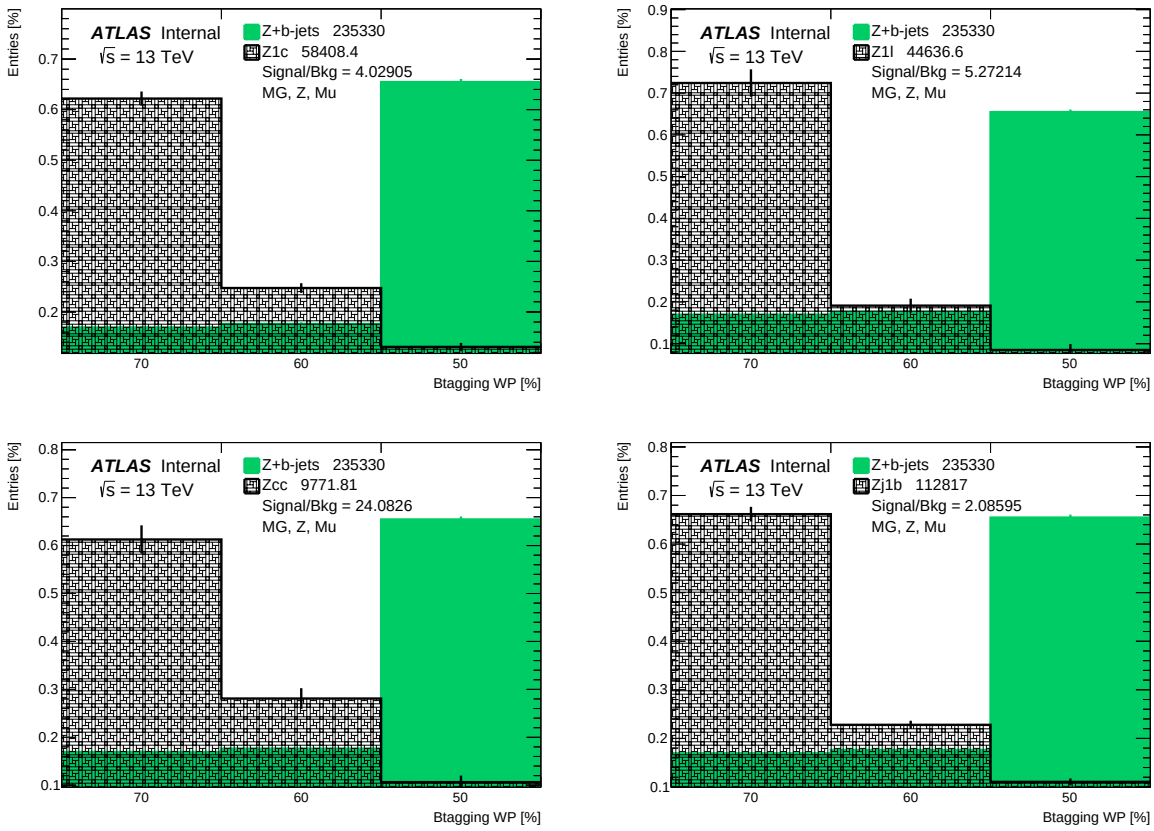

Figure B.4: Shape comparison of the signal component,Z + b-jets, to the background components Z + c (top left), Z + cc (bottom left), Z + l (top right), and to their sum (bottom right) for the Madgraph generator in the Z1B signal region for the muon channel.

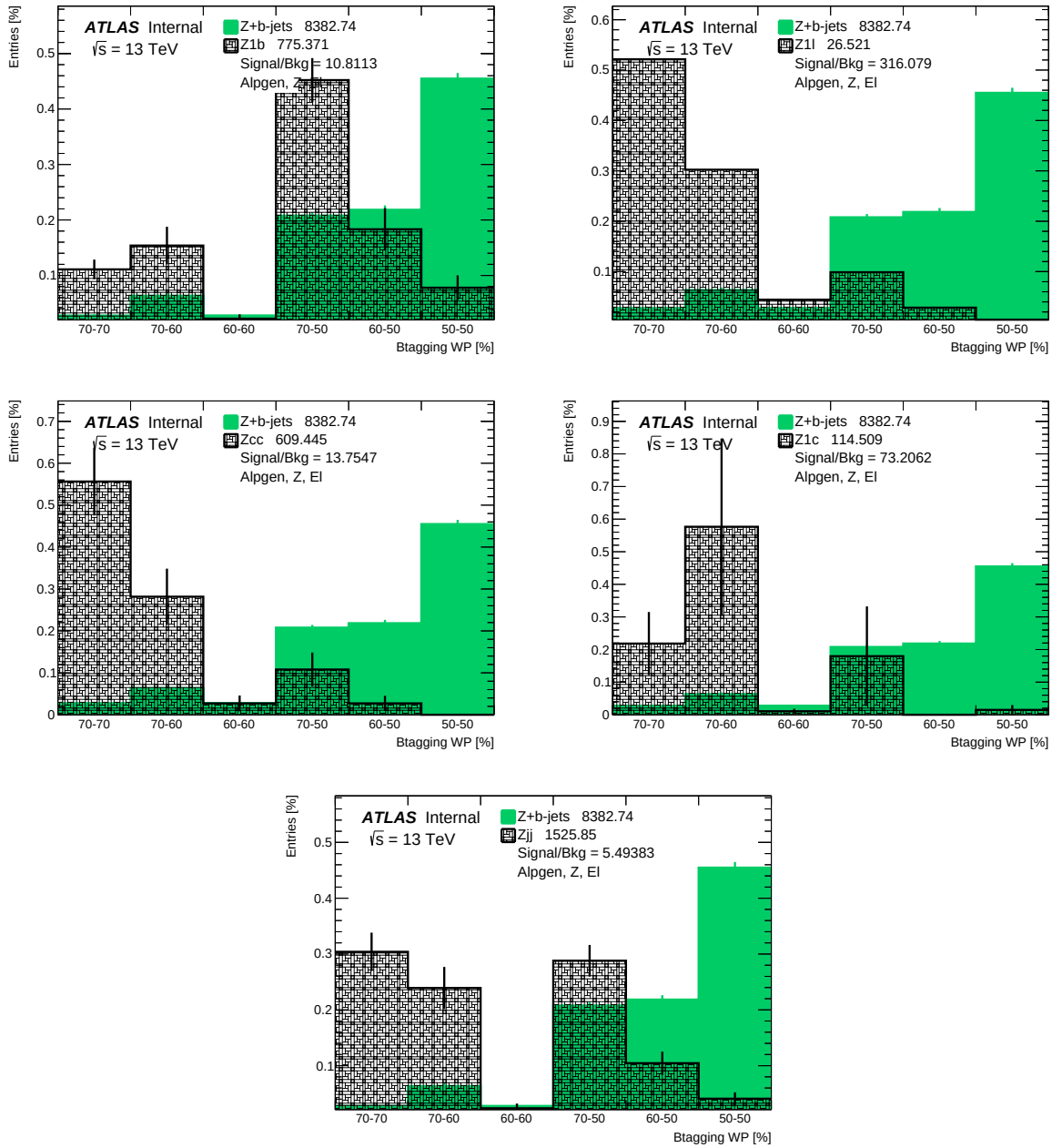

Figure B.5: Shape comparison of the signal component,Z + bb, to the background components Z + b (top left), Z + cc (middle left), Z + l (top right), Z + c (middle right), and to their sum (bottom) for the Alpgen generator in the Z2B signal region for the electron channel.

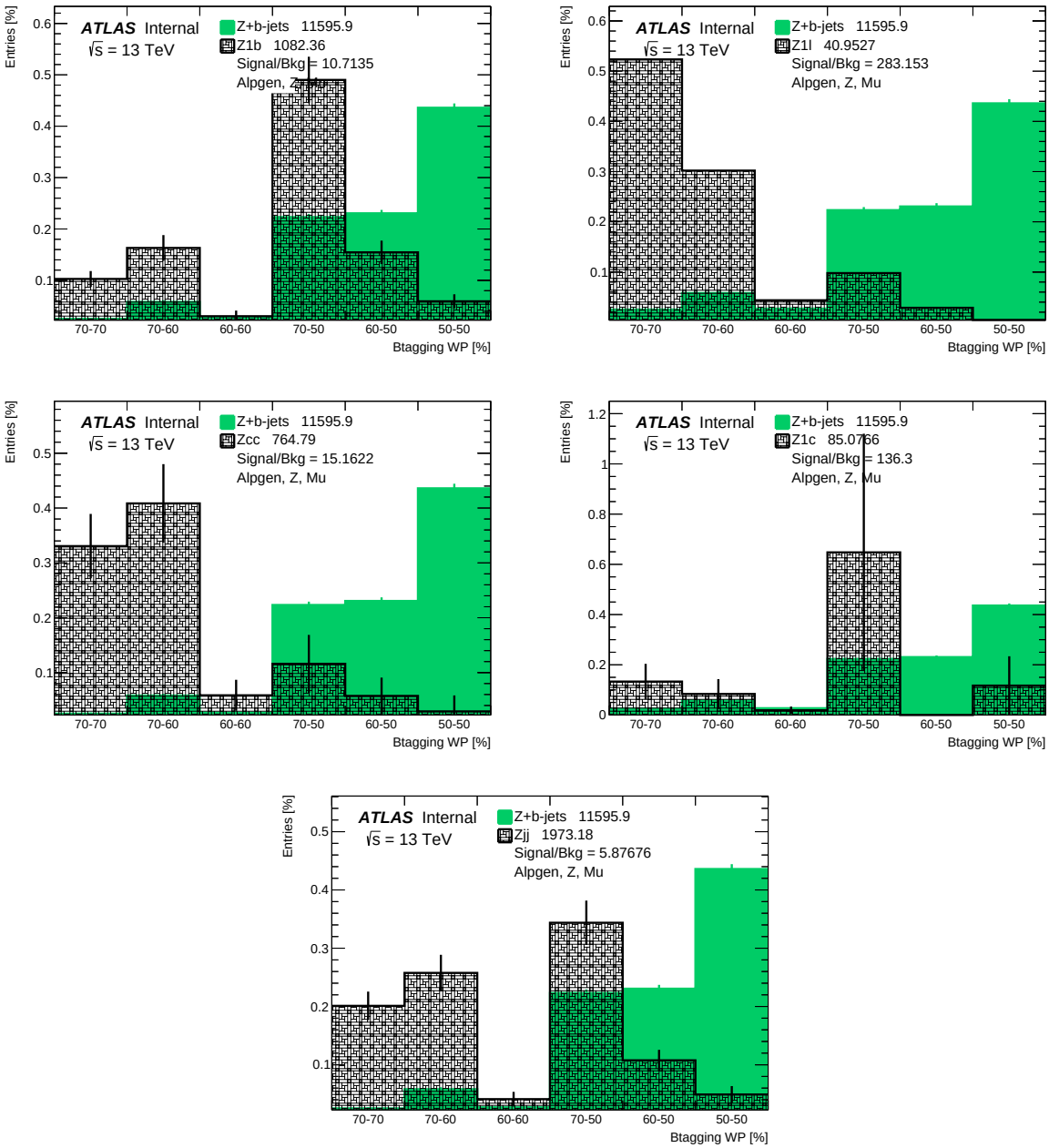

Figure B.6: Shape comparison of the signal component,Z + bb, to the background components Z + b (top left), Z + cc (middle left), Z + l (top right), Z + c (middle right), and to their sum (bottom) for the Alpgen generator in the Z2B signal region for the muon channel.

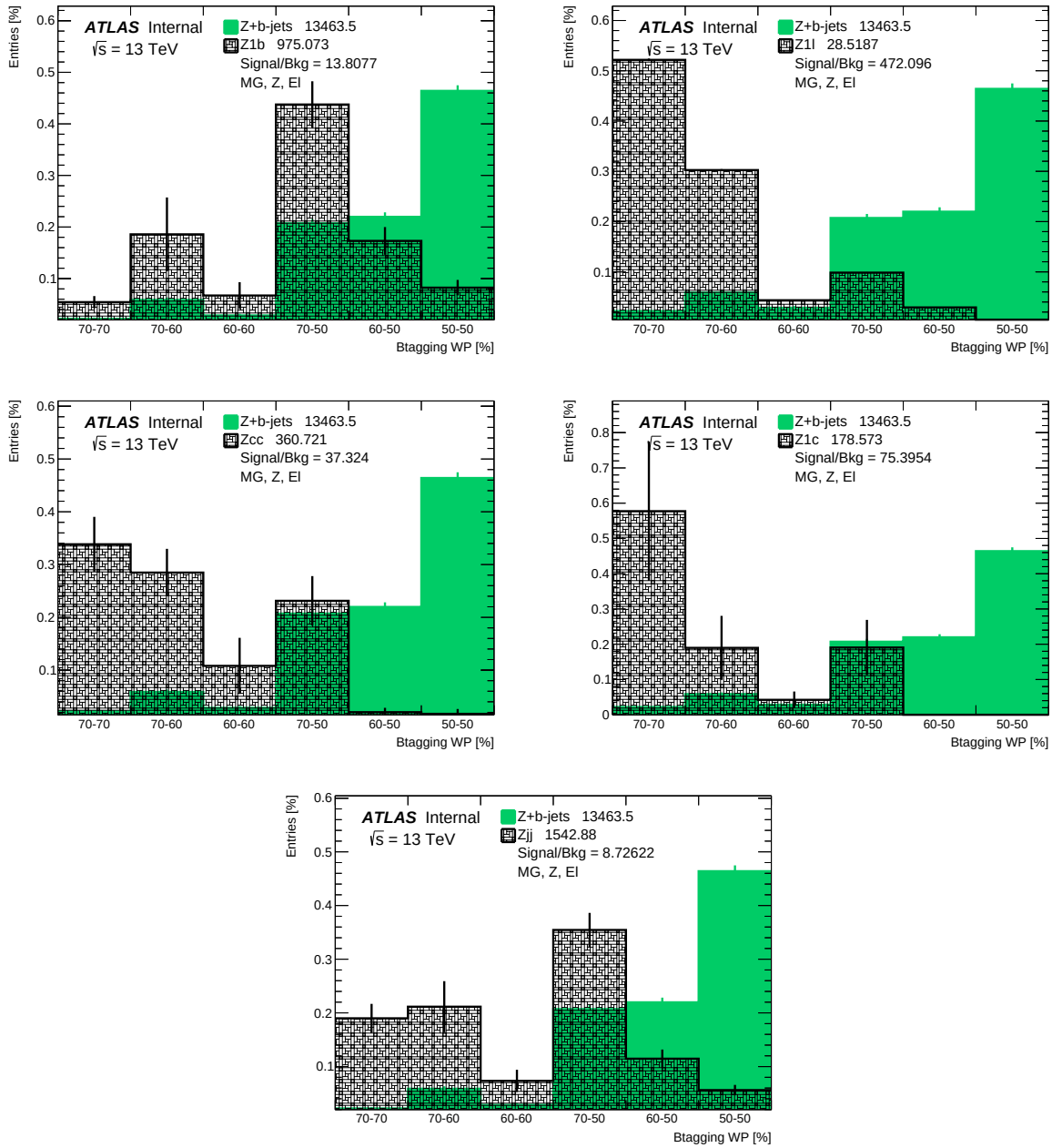

Figure B.7: Shape comparison of the signal component,Z + bb, to the background components Z + b (top left), Z + cc (middle left), Z + l (top right), Z + c (middle right), and to their sum (bottom) for the Madgraph generator in the Z2B signal region for the electron channel.

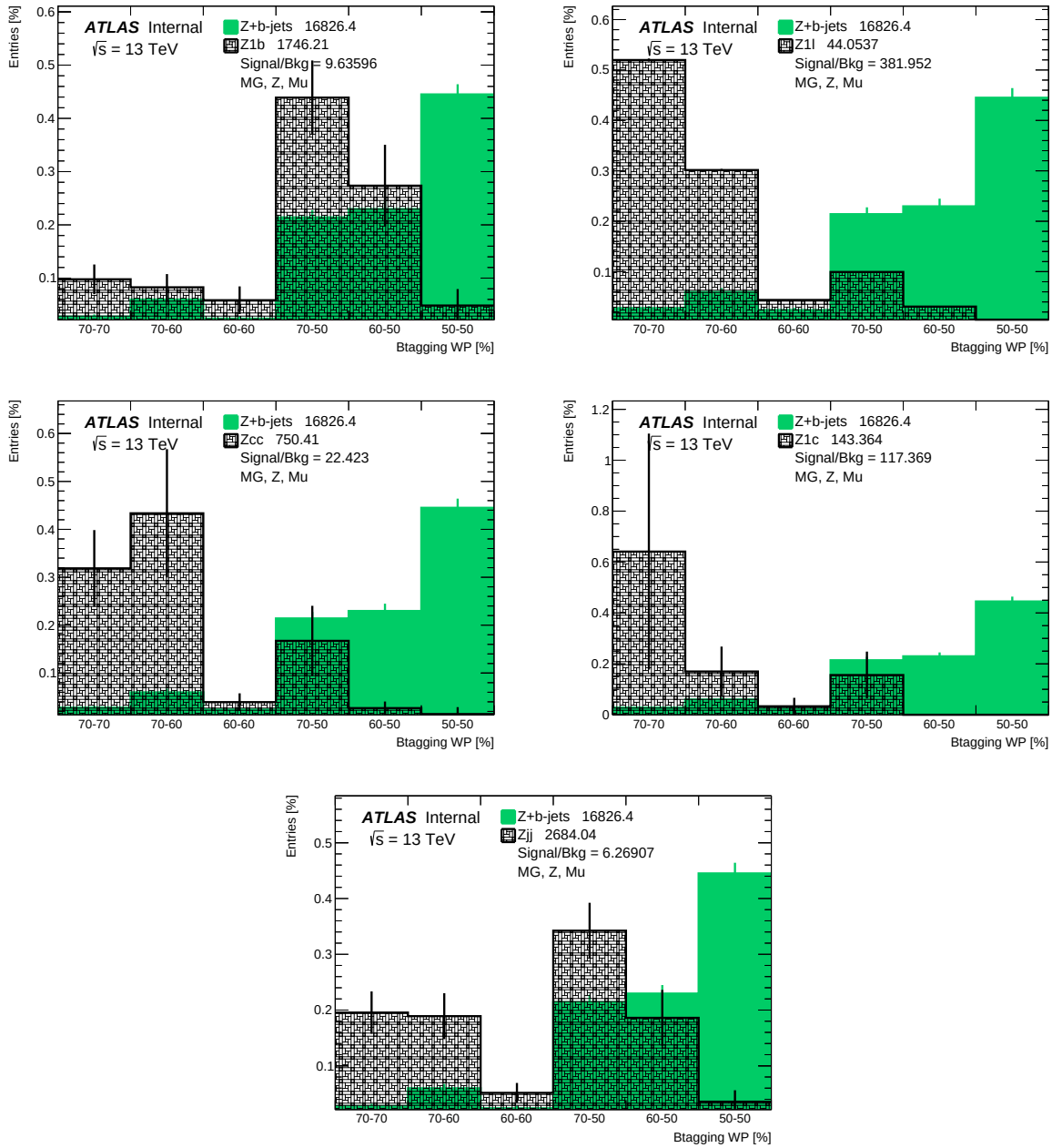

Figure B.8: Shape comparison of the signal component,Z + bb, to the background components Z + b (top left), Z + cc (middle left), Z + l (top right), Z + c (middle right), and to their sum (bottom) for the Madgraph generator in the Z2B signal region for the muon channel.

B.2 Scale Factors from Systematic Variations using Alpgen Generator

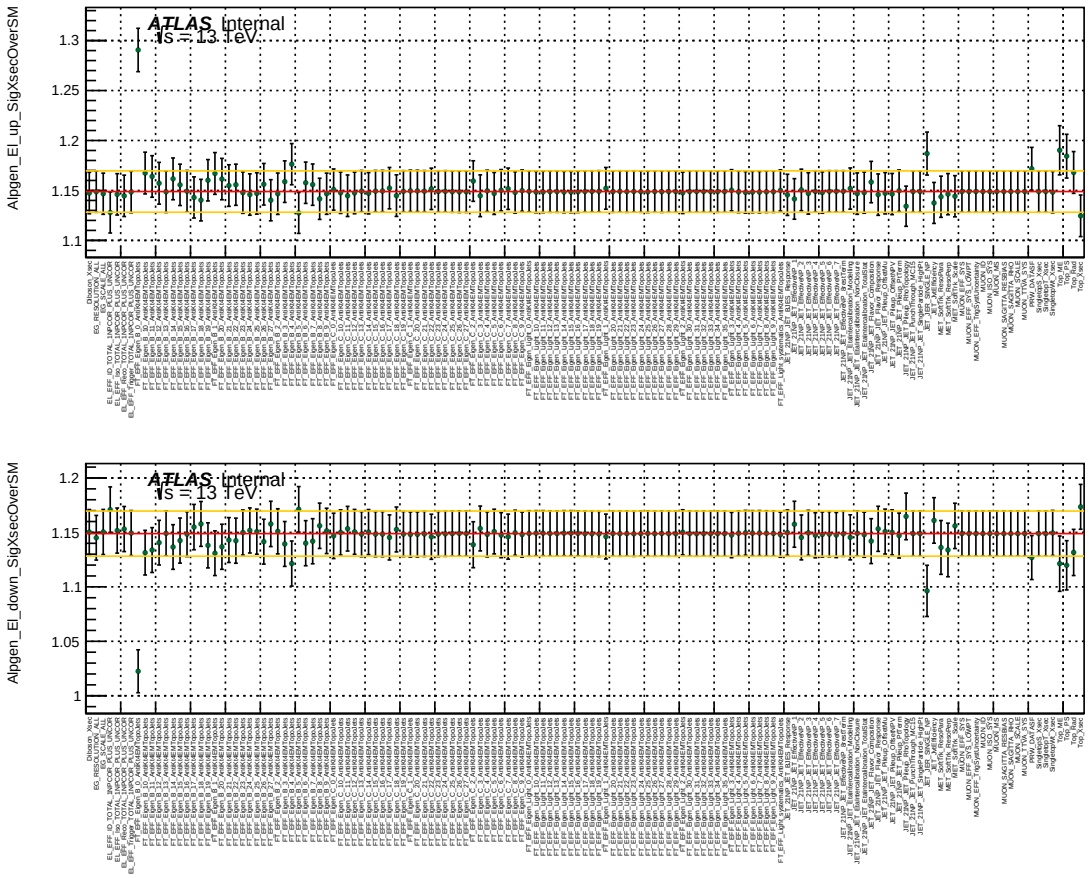

Figure B.9: Summary of scale factor obtained for the Z + b-jets component in the electron channel fit using Alpgen as the generator for the Z+jets processes, for all the up (left figure) and down (right figure) components of the systematic variations. The horizontal lines represents the fitted SF for the nominal case, i.e. no systematic applied, and the corresponding up and down variation from the statistical error of the fit. Each SF obtained for the different systematic variations is displayed by a point and its corresponding statistical error bar from the fit.

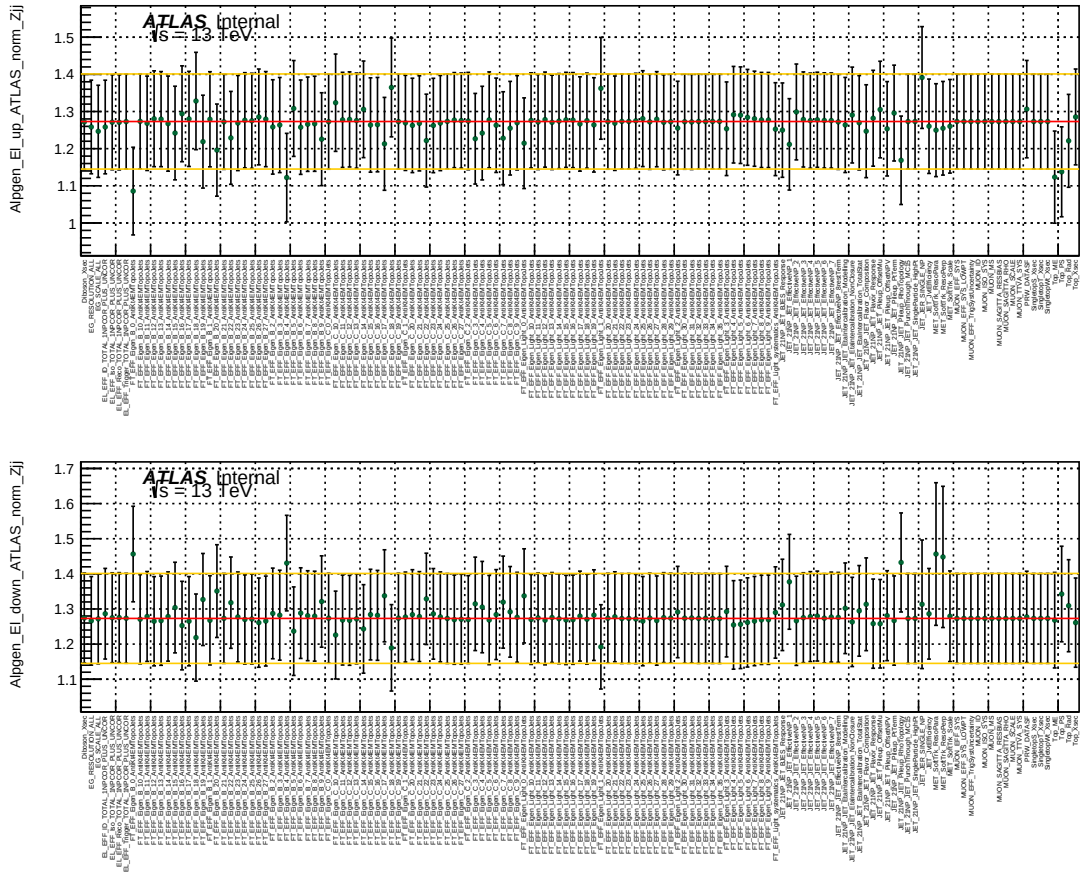

Figure B.10: Summary of scale factor obtained for the Z + j component in the electron channel fit using Alpgen as the generator for the Z+jets processes, for all the up (left figure) and down (right figure) components of the systematic variations. The horizontal lines represents the fitted SF for the nominal case, i.e. no systematic applied, and the corresponding up and down variation from the statistical error of the fit. Each SF obtained for the different systematic variations is displayed by a point and its corresponding statistical error bar from the fit.

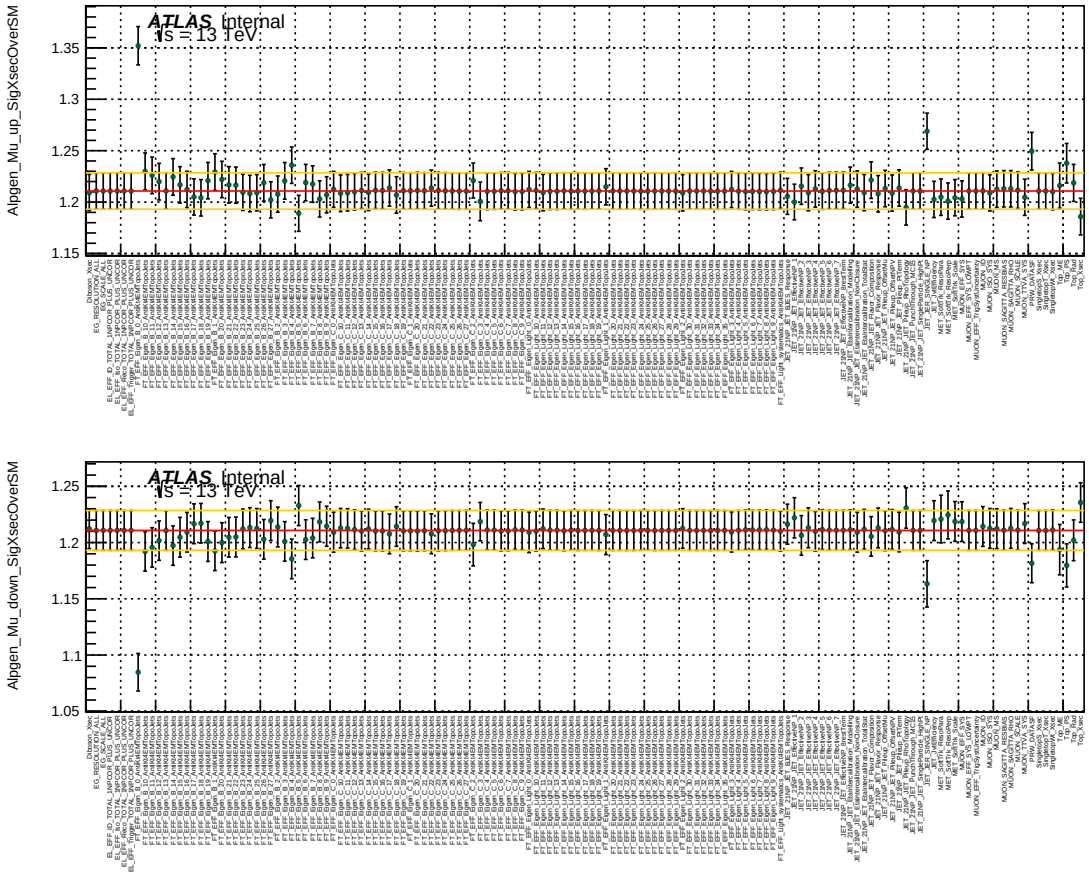

Figure B.11: Summary of scale factor obtained for the Z + b-jets component in the muon channel fit using Alpgen as the generator for the Z+jets processes, for all the up (left figure) and down (right figure) components of the systematic variations. The horizontal lines represents the fitted SF for the nominal case, i.e. no systematic applied, and the corresponding up and down variation from the statistical error of the fit. Each SF obtained for the different systematic variations is displayed by a point and its corresponding statistical error bar from the fit.

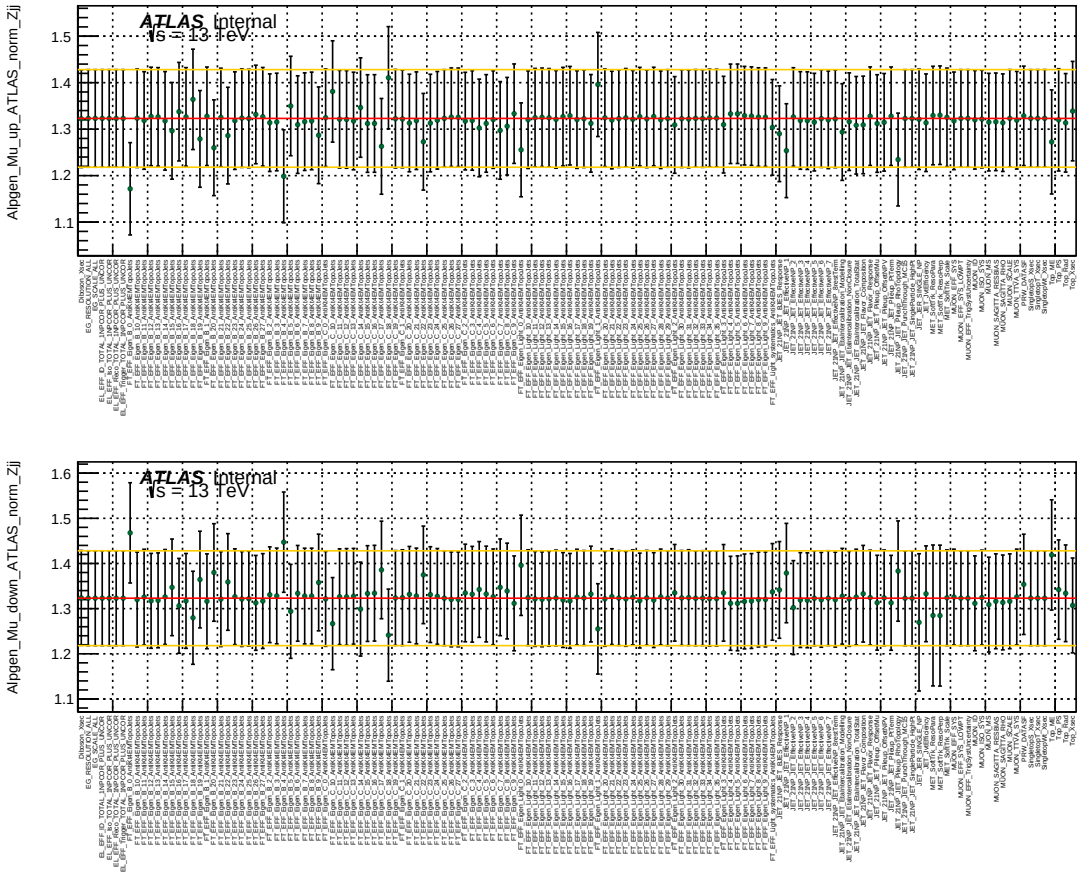

Figure B.12: Summary of scale factor obtained for the Z + j component in the muon channel fit using Alpgen as the generator for the Z+jets processes, for all the up (left figure) and down (right figure) components of the systematic variations. The horizontal lines represents the fitted SF for the nominal case, i.e. no systematic applied, and the corresponding up and down variation from the statistical error of the fit. Each SF obtained for the different systematic variations is displayed by a point and its corresponding statistical error bar from the fit.

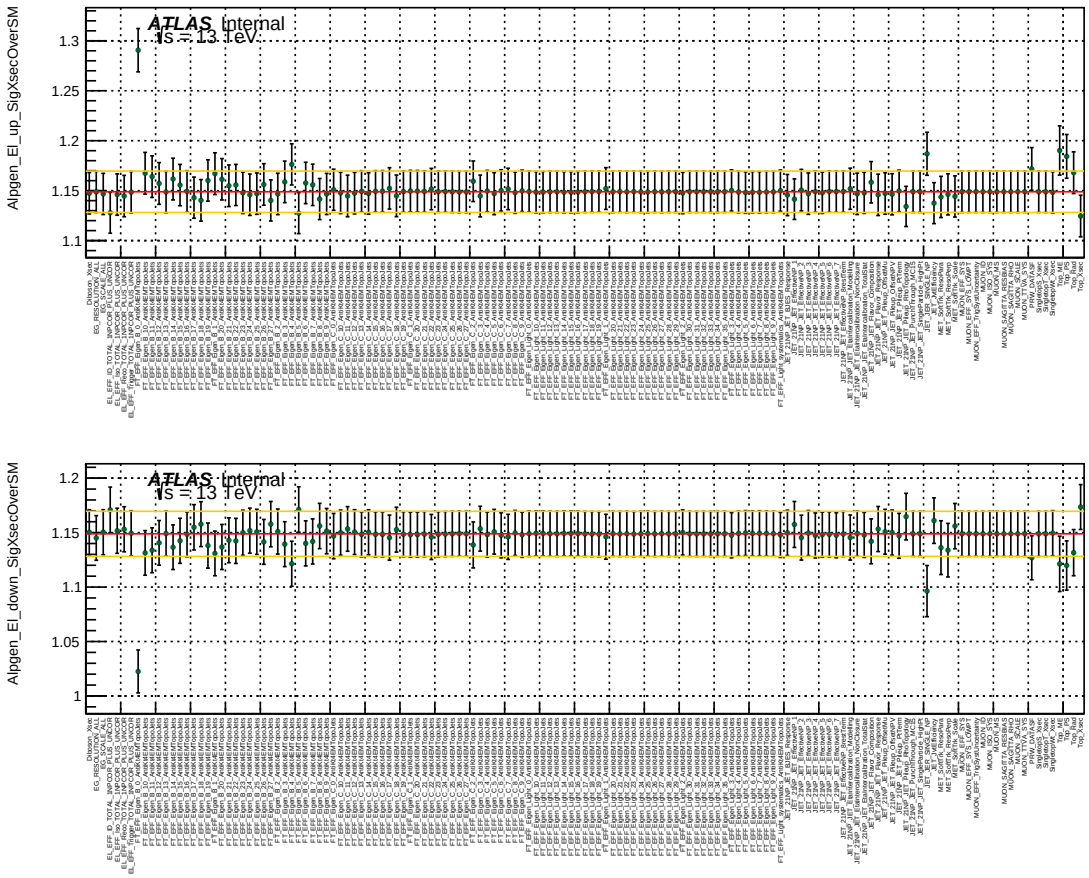

Figure B.13: Summary of scale factor obtained for the Z + *bb* component in the electron channel fit using Alpgen as the generator for the Z+jets processes, for all the up (left figure) and down (right figure) components of the systematic variations. The horizontal lines represents the fitted SF for the nominal case, i.e. no systematic applied, and the corresponding up and down variation from the statistical error of the fit. Each SF obtained for the different systematic variations is displayed by a point and its corresponding statistical error bar from the fit.

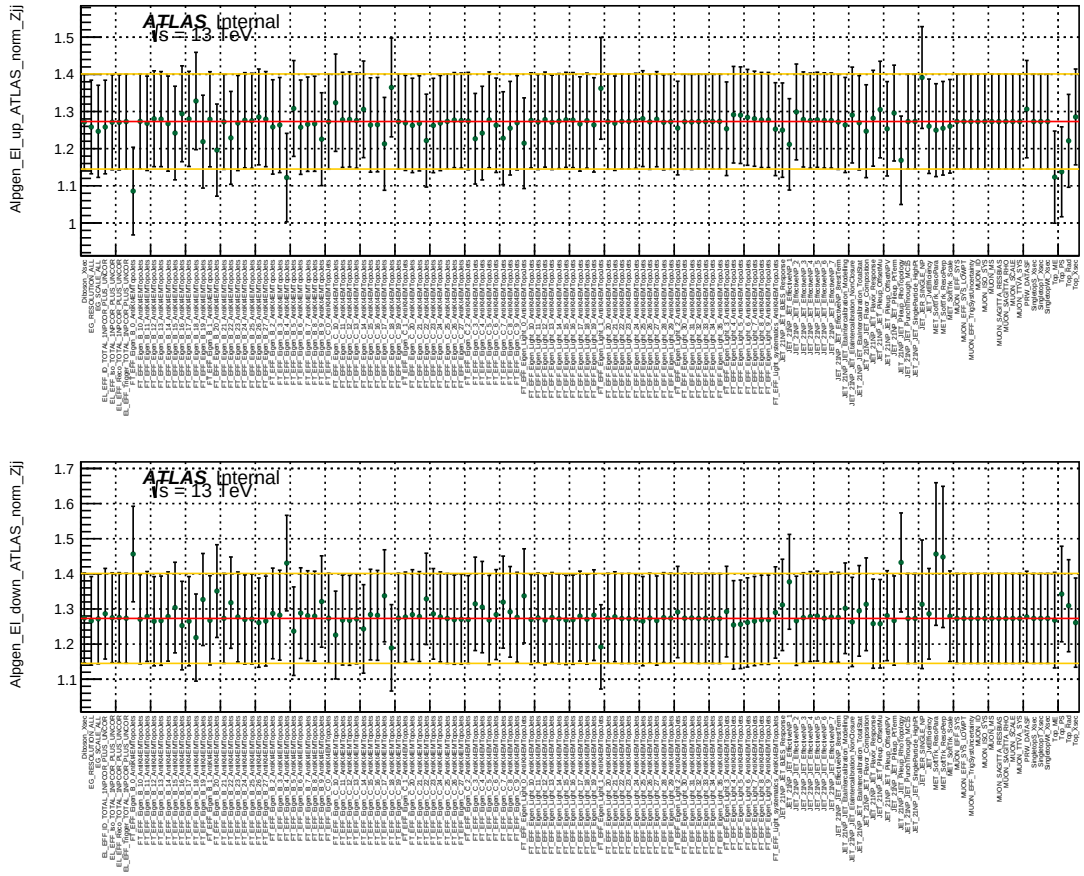

Figure B.14: Summary of scale factor obtained for the Z + jj component in the electron channel fit using Alpgen as the generator for the Z+jets processes, for all the up (left figure) and down (right figure) components of the systematic variations. The horizontal lines represents the fitted SF for the nominal case, i.e. no systematic applied, and the corresponding up and down variation from the statistical error of the fit. Each SF obtained for the different systematic variations is displayed by a point and its corresponding statistical error bar from the fit.

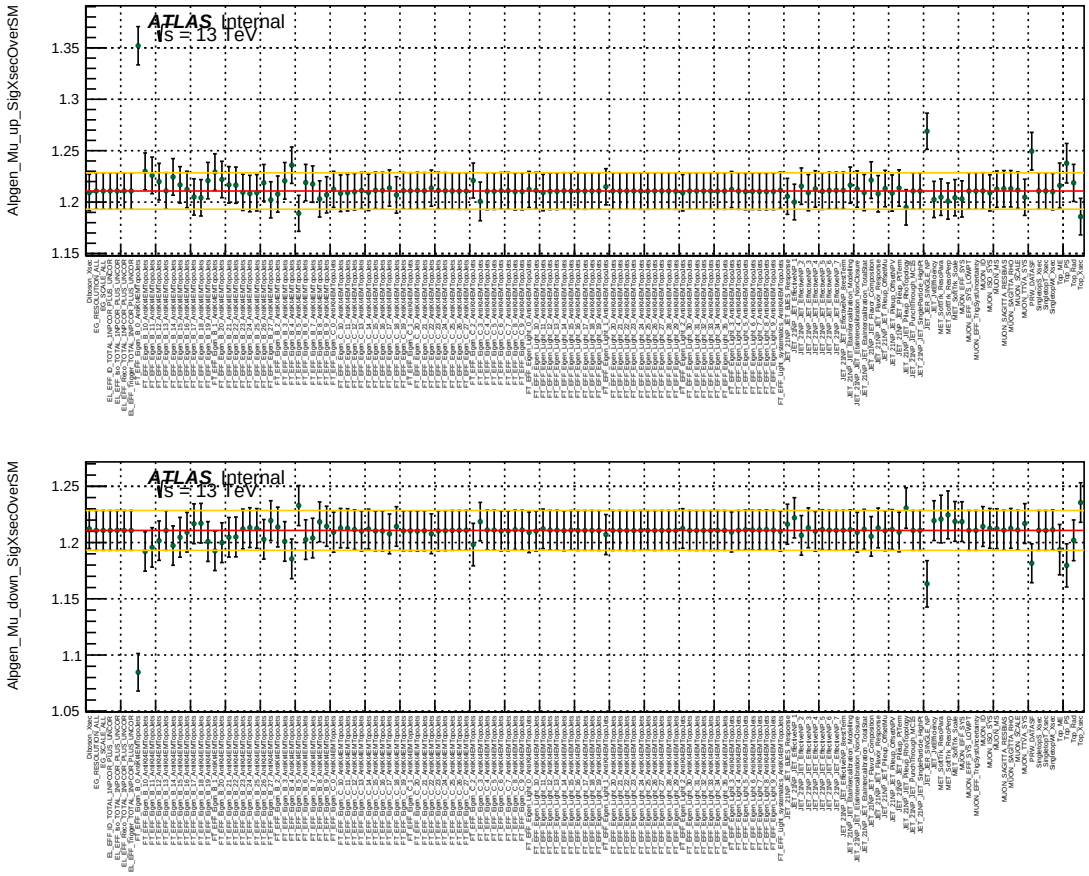

Figure B.15: Summary of scale factor obtained for the Z + bb component in the muon channel fit using Alpgen as the generator for the Z+jets processes, for all the up (left figure) and down (right figure) components of the systematic variations. The horizontal lines represents the fitted SF for the nominal case, i.e. no systematic applied, and the corresponding up and down variation from the statistical error of the fit. Each SF obtained for the different systematic variations is displayed by a point and its corresponding statistical error bar from the fit.

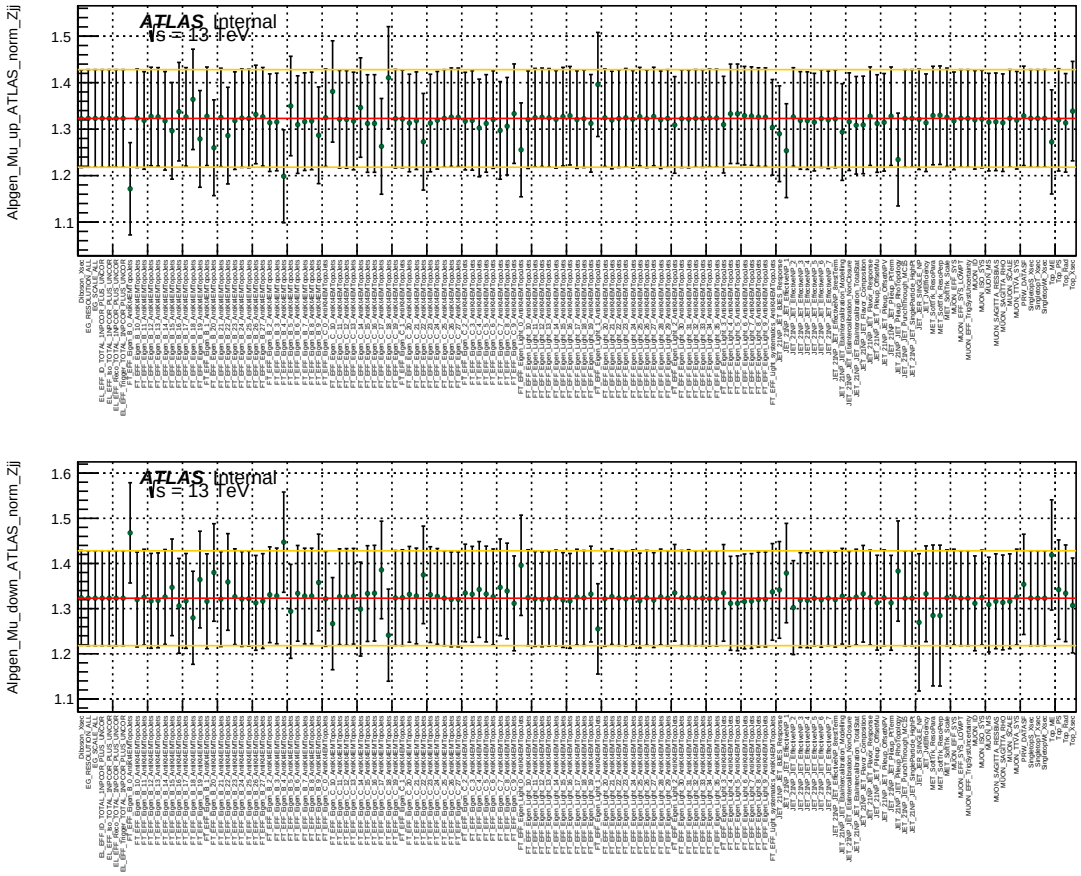

Figure B.16: Summary of scale factor obtained for the Z + jj component in the muon channel fit using Alpgen as the generator for the Z+jets processes, for all the up (left figure) and down (right figure) components of the systematic variations. The horizontal lines represents the fitted SF for the nominal case, i.e. no systematic applied, and the corresponding up and down variation from the statistical error of the fit. Each SF obtained for the different systematic variations is displayed by a point and its corresponding statistical error bar from the fit.

B.3 Post-Fit Yields of Systematic Variations for Sherpa Generator

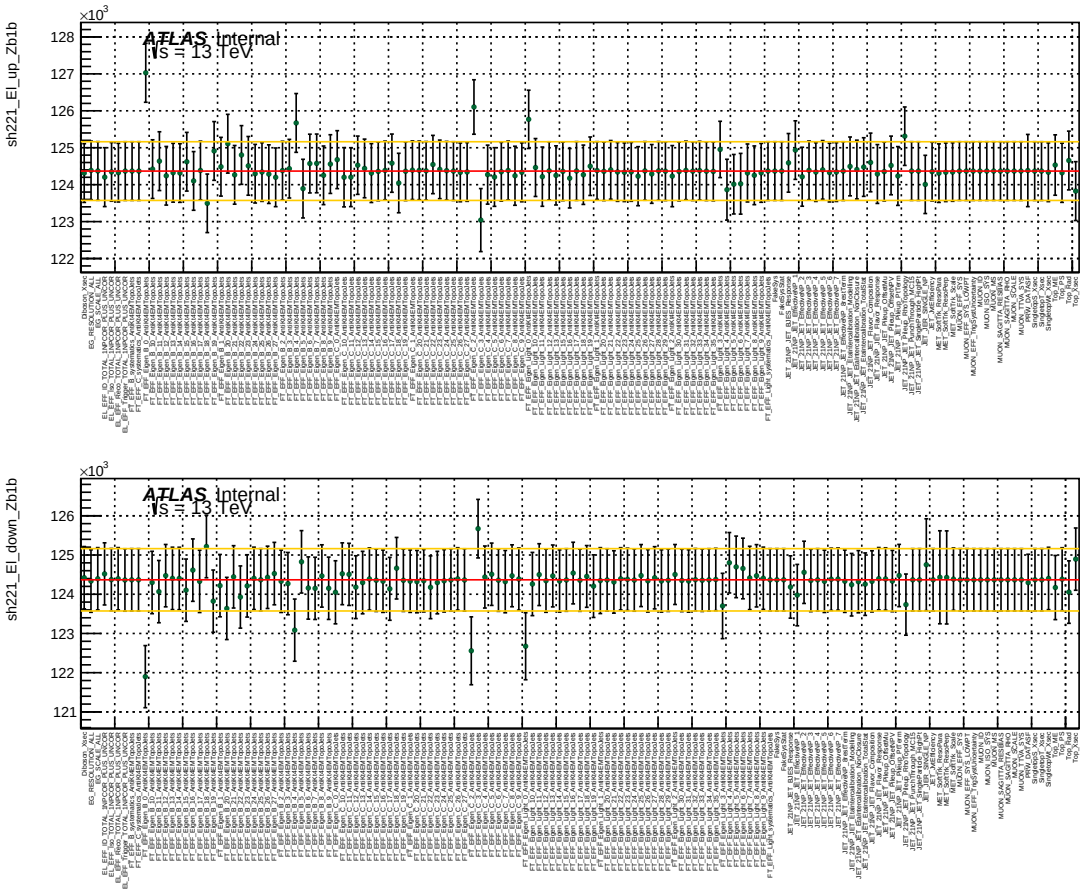

Figure B.17: Summary of the post-fit yields obtained for the Z + b-jets component in the electron channel fit using Sherpa as generator for the Z+jets processes, for all the up (left figure) and down (right figure) components of the systematic variations. The horizontal lines represents the fitted yield for the nominal case, i.e. no systematic applied, and the corresponding up and down variation from the statistical error of the fit. Each yield obtained for the different systematic variations is displayed by a point and its corresponding statistical error bar from the fit.

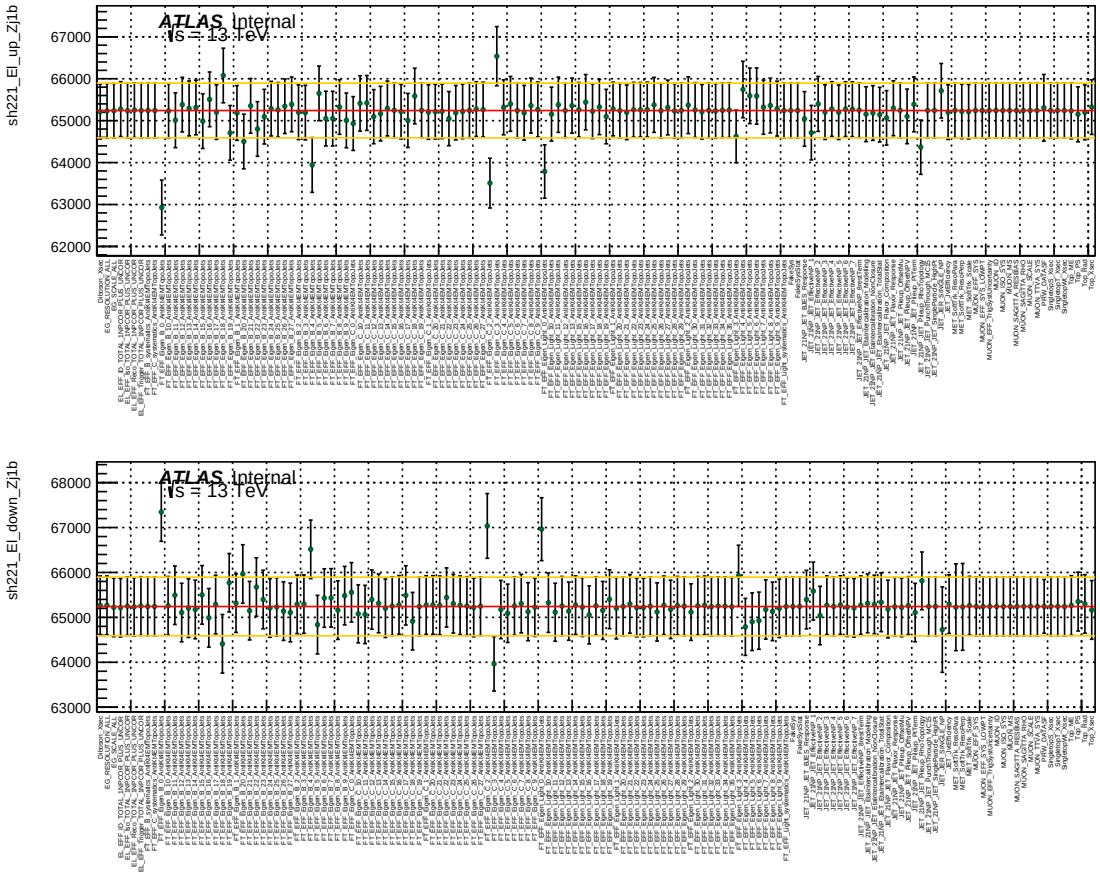

Figure B.18: Summary of the post-fit yields obtained for the Z + j component in the electron channel fit using Sherpa as generator for the Z+jets processes, for all the *up* (left figure) and *down* (right figure) components of the systematic variations. The horizontal lines represents the fitted yield for the nominal case, i.e. no systematic applied, and the corresponding up and down variation from the statistical error of the fit. Each yield obtained for the different systematic variations is displayed by a point and its corresponding statistical error bar from the fit.

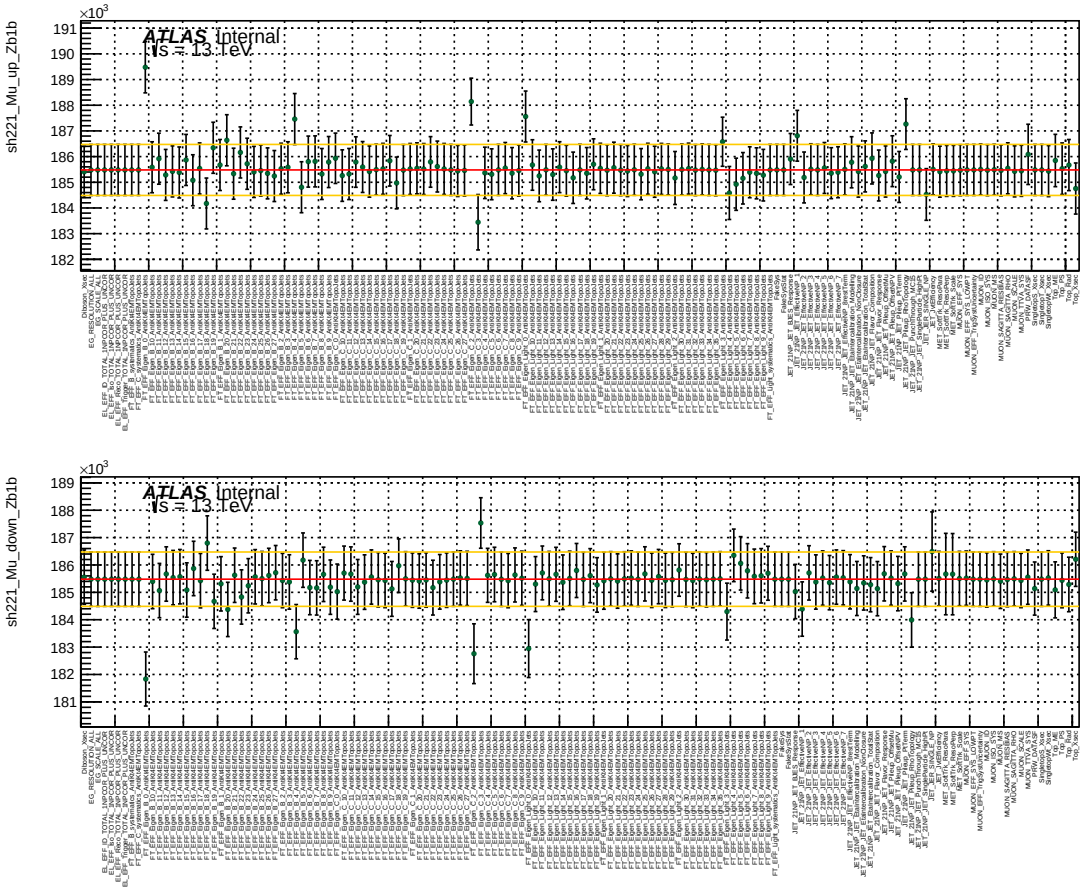

Figure B.19: Summary of the post-fit yields obtained for the Z + b-jets component in the muon channel fit using Sherpa as generator for the Z+jets processes, for all the up (left figure) and down (right figure) components of the systematic variations. The horizontal lines represents the fitted yield for the nominal case, i.e. no systematic applied, and the corresponding up and down variation from the statistical error of the fit. Each yield obtained for the different systematic variations is displayed by a point and its corresponding statistical error bar from the fit.

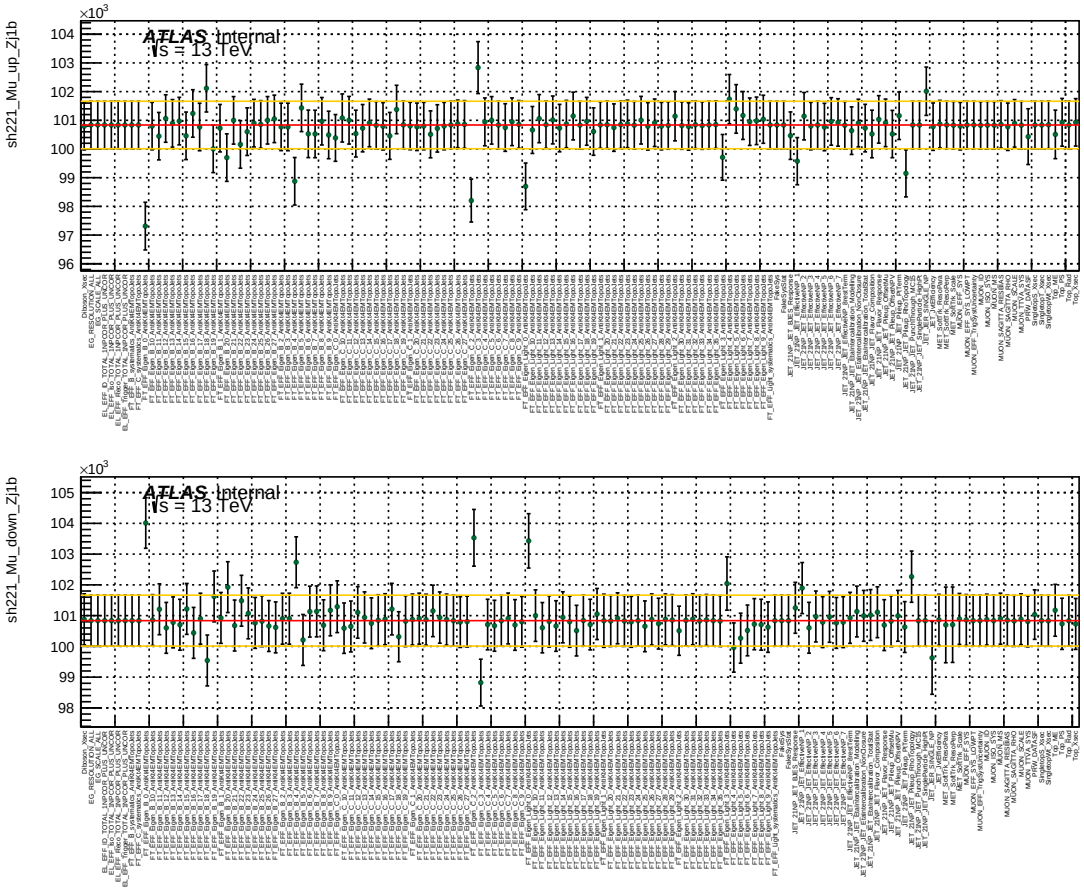

Figure B.20: Summary of the post-fit yields obtained for the Z + j component in the muon channel fit using Sherpa as generator for the Z+jets processes, for all the up (left figure) and down (right figure) components of the systematic variations. The horizontal lines represents the fitted yield for the nominal case, i.e. no systematic applied, and the corresponding up and down variation from the statistical error of the fit. Each yield obtained for the different systematic variations is displayed by a point and its corresponding statistical error bar from the fit.

APPENDIX C

TRUTH TAGGING

This chapter gives a brief description of the use of truth-tagging. The b-tagging algorithm was to developed to select b-jets while rejecting lighter jets (L and c-jets). However, in the 2B signal region, the b-tag selection is in a way too good. The high rejection power of the b-tagging selection for L and c-jets means that requiring two such jets to both pass the b-tagging selection will result in a very small fraction of events. This, together with possible large weights assigned to single events (ie MC weights, flavor-tagging calibration SFs, PU-weights) produces large statistical fluctuations in many of the kinematic distributions. This is shown in fig. C.1 which shows two examples of distributions where the MC predictions suffer from large statistical fluctuations originating from the Z+LF background in the Sherpa sample. Looking at the yield of the Z+LF component in the legends of the plots it shows the large statistical uncertainty on the light flavor component.

The truth tagging method addresses this by not applying the b-tagging selection based on MV2c10 score. Instead all events are kept and the event is given a truth weight, w_{TT}.

C.1 Truth Tagging Weight

This section will describe the determination of the truth tagging weight, w_{TT}. Consider an event with n jets in it. The number of combinations of m-tagged jets is then given by $\binom{n}{m}$ [1]. Let $\binom{n}{m}_i$ denote the i^{th} combination. The probability for the i^{th} combination to be b-tagged will be equal to the product of the efficiencies of b-tagging the m jets in the i^{th} combination multiplied by the products of the inefficiencies of b-tagging the $n-m$ jets not part of the

1. $\binom{n}{m}$ is the usual binomial coefficient: $\binom{n}{m} = \frac{n!}{m!(n-m)!}$

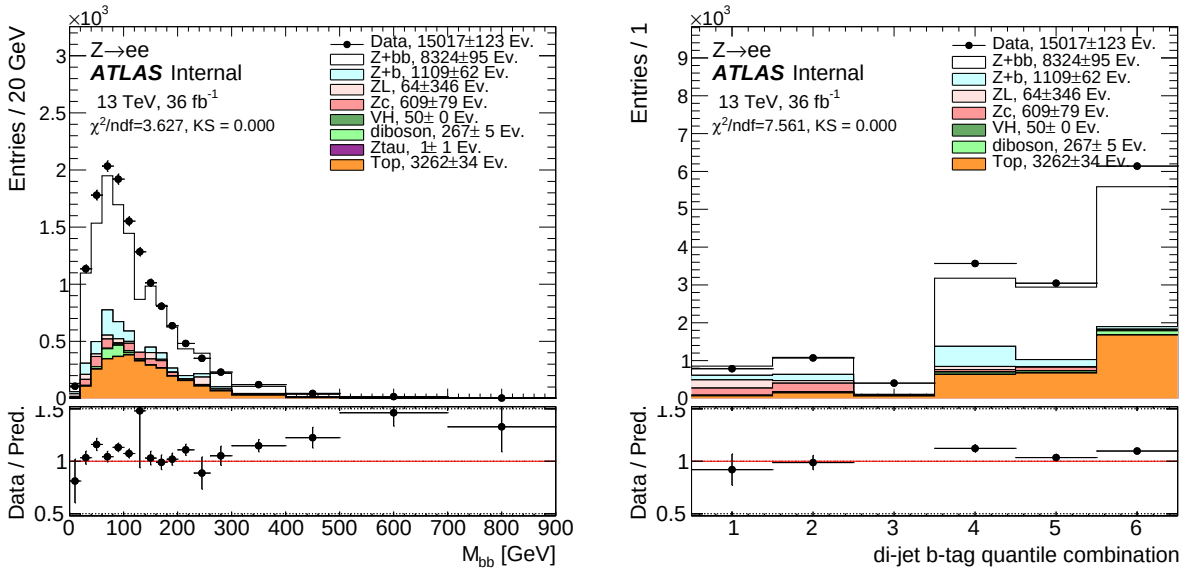

Figure C.1: Distributions of M_{bb} (left) and di-bjet WP Quantiles (right) in the $Z \to ee$ analysis channel where statistical fluctuations introduced by low MC statistics of the Z+LF background sample are visible. Only a few events, precisely 174, pass the 2-btag selection and are used for the Z+LF-jet background estimate, some of them having negative event weights. The legend summarizes the estimated yield for each process and the corresponding statistical uncertainty.

i^{th} combination. Write these products separately as the efficiency and inefficiency products:

$$\varepsilon(\binom{n}{m}_i, x) = \prod_{j \in m} \epsilon_x^f(j) \tag{C.1}$$

$$\varepsilon_{in}(\binom{n}{m}_i, x) = \prod_{j \in n-m} (1 - \epsilon_x^f(j)), \tag{C.2}$$

where $\epsilon_x^f(j)$ is the tagging efficiency for jet j of flavor f at an efficiency working point x. Summing over all $\binom{n}{m}$ possible combinations gives the truth weight:

$$w_{TT} = \sum_i^{\binom{n}{m}} P_i(x), \tag{C.3}$$

where

$$P_i(x) = \varepsilon(\binom{n}{m}_i, x)\varepsilon_{in}(\binom{n}{m}_i, x). \tag{C.4}$$

A random permutation of m b-tagged jets is then selected for the event according to the probability $P_i(x)/w_{TT}$. Each jet is also randomly assigned to a quantile of the MV2c10 distribution which depends on the fraction of jet-tagging efficiency belonging to a quantile.

C.2 Closure Check

A closure check is done by comparing the jet p_T and MV2c10 spectrum in events with exactly one jet passing the 70% b-tagging requirement when using truth-tagging (TT) to when using the standard b-tagging selection, referred to as direct tagging (DT). The closure is shown for LF-jets and c-jets for Sherpa and Alpgen in figs. C.2 and C.3, respectively.

C.3 Application of Truth Tagging

The truth tagging is only applied in the 2B signal regions, which is the region most affected by statistical fluctuations and large weights in the MC events. In fig. C.4 a few distributions are shown for the Z+L and Z+cc components of the Z+jet Sherpa samples in the 2B signal region for the electron channel comparing the results from the truth tagging method to the direct tagging method. The results show compatibility within the limited statistics of the samples. In order to account for a possible bias in the truth tagging yield and shape and assign a systematic associated with the use of the truth tagging method the Z+bb component of the MC samples was used. These components are not statistically limited and allow for a comparison between truth tagging yields and shape to the direct tagging yields and shape. For this component in the 2B signal region the yields were approximately 20% lower in the truth tagging compared to the direct tagging. The bias is roughly consistent in Sherpa and Alpgen and flat versus di-jet kinematic distributions. As a result an additional 20%

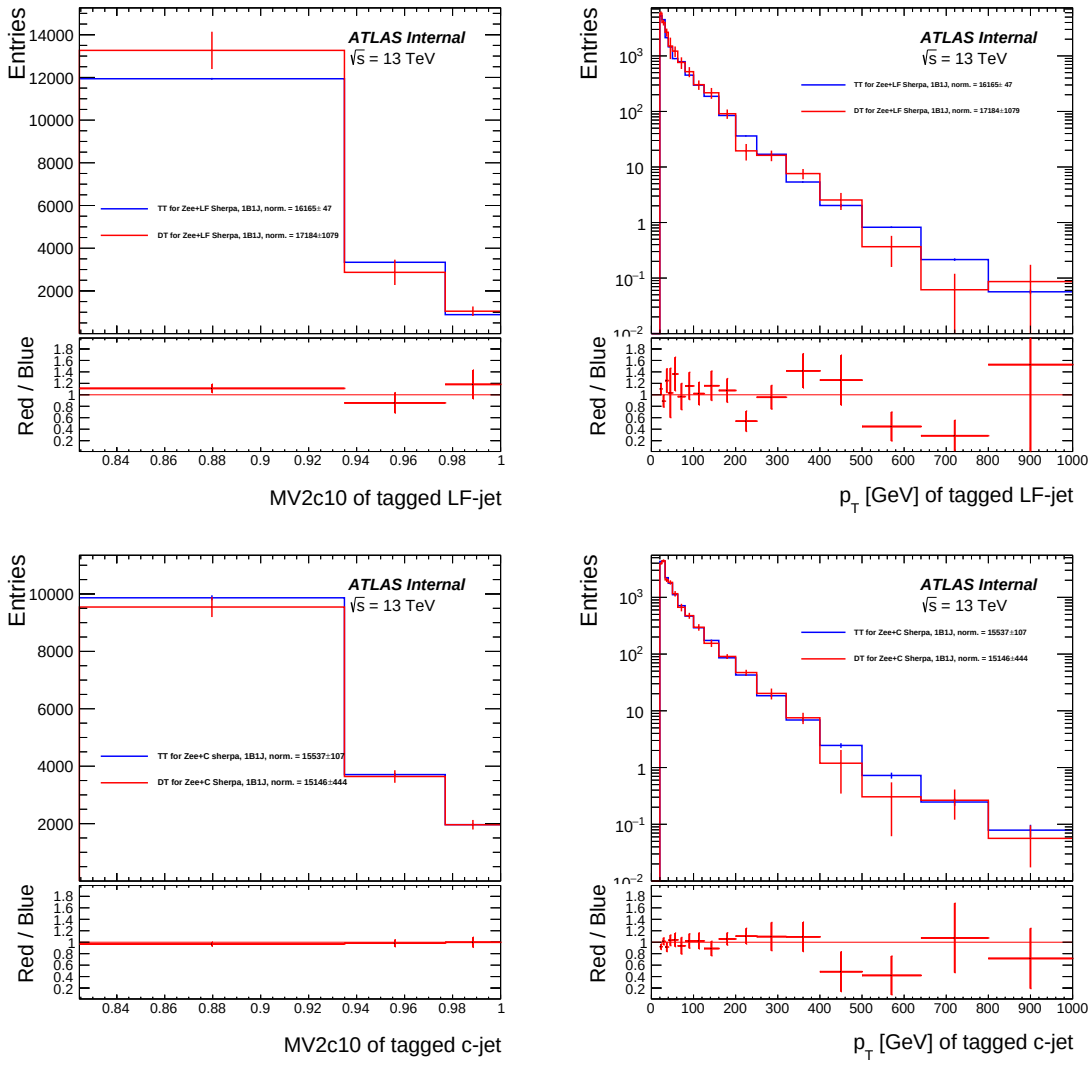

Figure C.2: Comparison of DT (red) and TT (blue) results for $Z \to ee$ Sherpa v2.2.1 events selected with exactly 1 jet and passing b-tag 70% WP. The comparison is shown for LF-jet (top) and c-jets (bottom) and for the MV2c10 score (left) and p_T of the selected jet (right). The two b-tagging evaluation methods agree within statistics.

systematic on rate of samples evaluated using truth taking is applied.

The truth tagging is only applied to the Z+L component of the Z+jet samples in this analysis. The resulting yields of this component are summarized in table C.1 comparing the direct tagging yields to the truth tagging yields. The distribution for the invariant mass of the two leading b-jets and working point quantiles are shown in fig. C.5 for the electron channel in the 2B signal region after applying truth tagging to the Z+L component of the

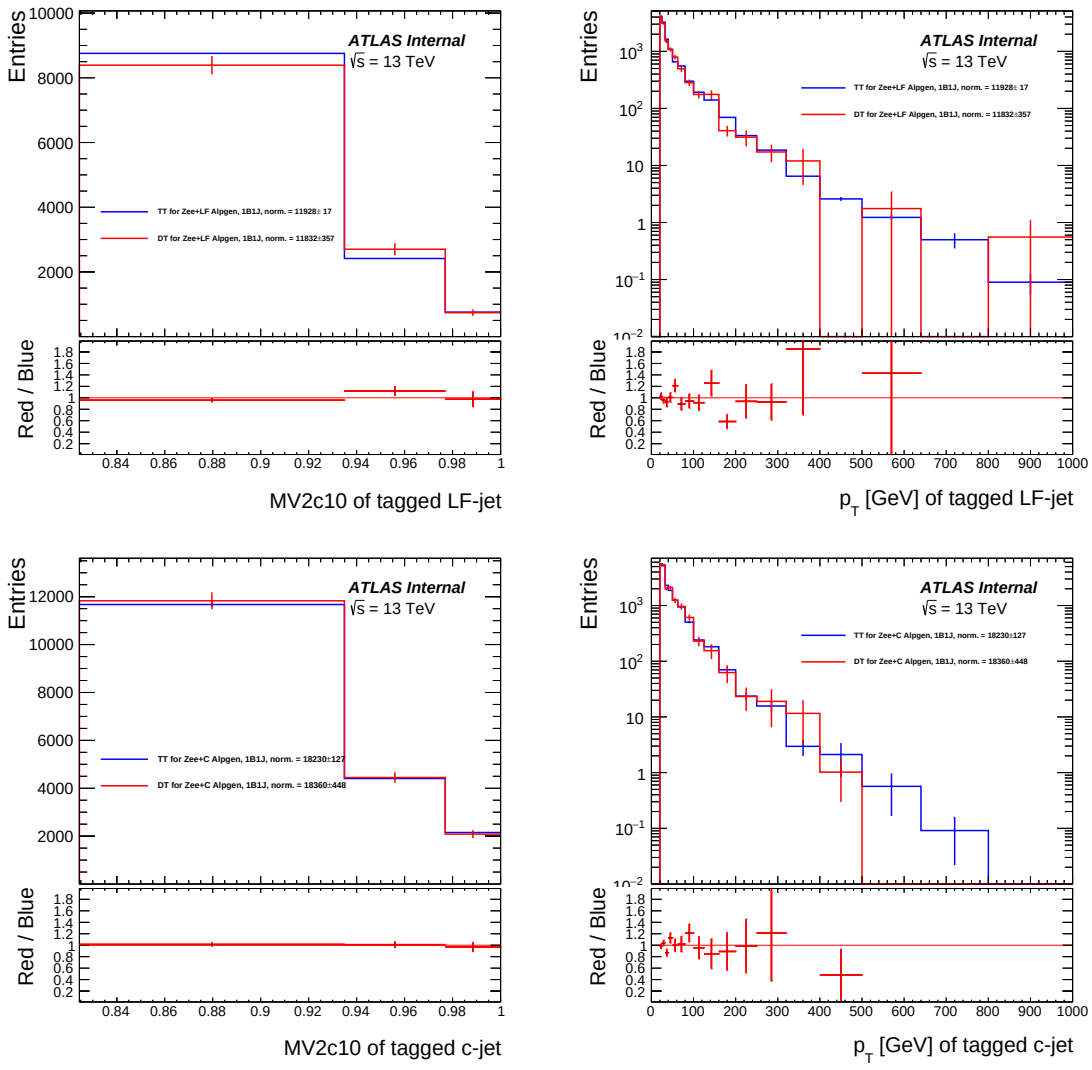

Figure C.3: Comparison of DT (red) and TT (blue) results for $Z \to ee$ Alpgen events selected with exactly 1 jet and passing b-tag 70% WP. The comparison is shown for LF-jet (top) and c-jets (bottom) and for the MV2c10 score (left) and p_T of the selected jet (right). The two b-tagging evaluation methods agree within statistics.

Z+jet sample. These same distributions were shown previously in fig. C.1 except in the previous plots the direct tagging method was used for the Z+L component.

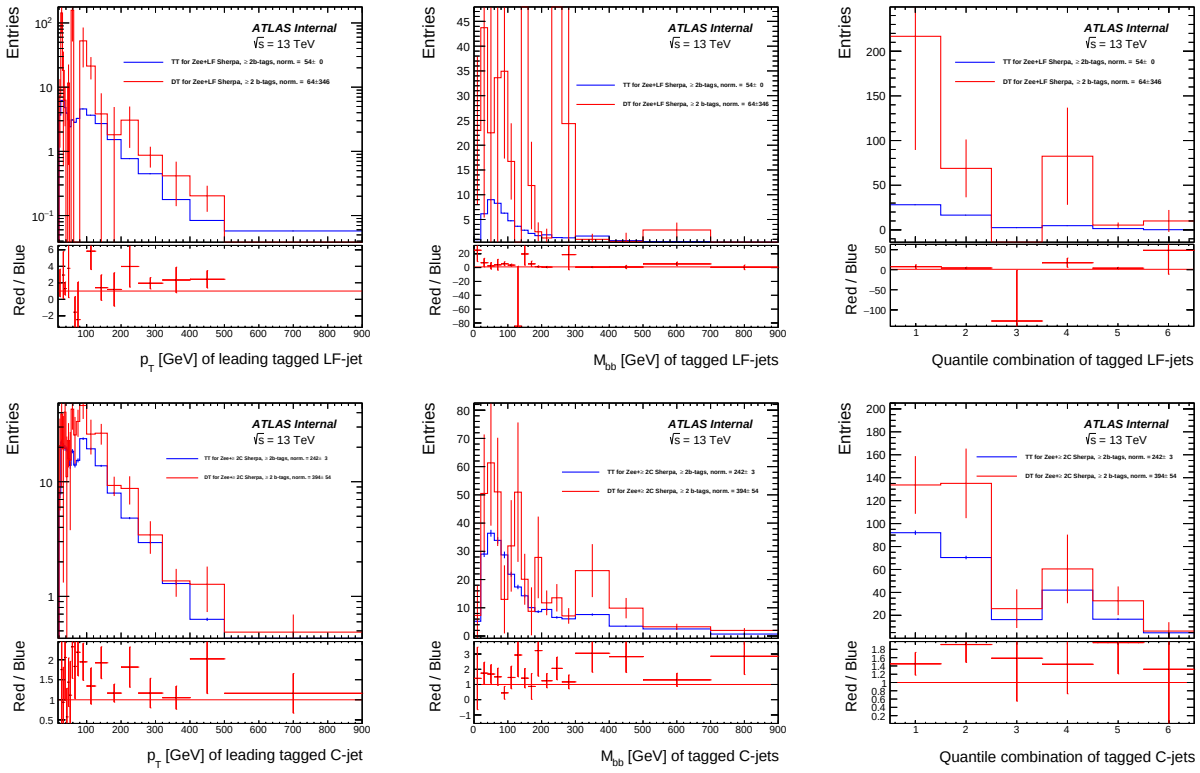

Figure C.4: Distributions, in the $\geq 2b$-tag signal region of leading b-jet p_T (left), the M_{bb} (center), and di-bjet working point quantiles (right) in the $Z \to ee$ analysis channel for the Sherpa MC, after the evaluation of the Z+LF-jet (top) and Z+$\geq$ 2c-jet (bottom) backgrounds using the DT (red) or the TT (blue) method. The legend summarizes the estimated yield for each process and the corresponding statistical uncertainty.

	DT Estimate	Fraction of Data	TT Estimate	Fraction of Data
$Z(\to ee) + LF$, $\geq$ 2b-tags, Sherpa	63.8 ± 346	$0.4 \pm 2\%$	53.5	0.35%
$Z(\to \mu\mu) + LF$, $\geq$ 2b-tags, Sherpa	588 ± 202	$2.7 \pm 0.9\%$	82.5	0.38%
$Z(\to ee) + LF$, $\geq$ 2b-tags, Alpgen	141 ± 38	$0.9 \pm 0.3\%$	26.5	0.18%
$Z(\to \mu\mu) + LF$, $\geq$ 2b-tags, Alpgen	411 ± 113	$1.9 \pm 0.5\%$	40.9	0.19%

Table C.1: Estimate of Z+L jet component in the $\geq 2b$-tag signal region for Sherpa and Alpgen MC samples using direct tagging and truth tagging. Statistical uncertainties on the direct tagging estimates are shown (truth tagging estimate has negligible statistical uncertainty). The fraction of the Z+L jet estimate in comparison to the selected data events is also shown.

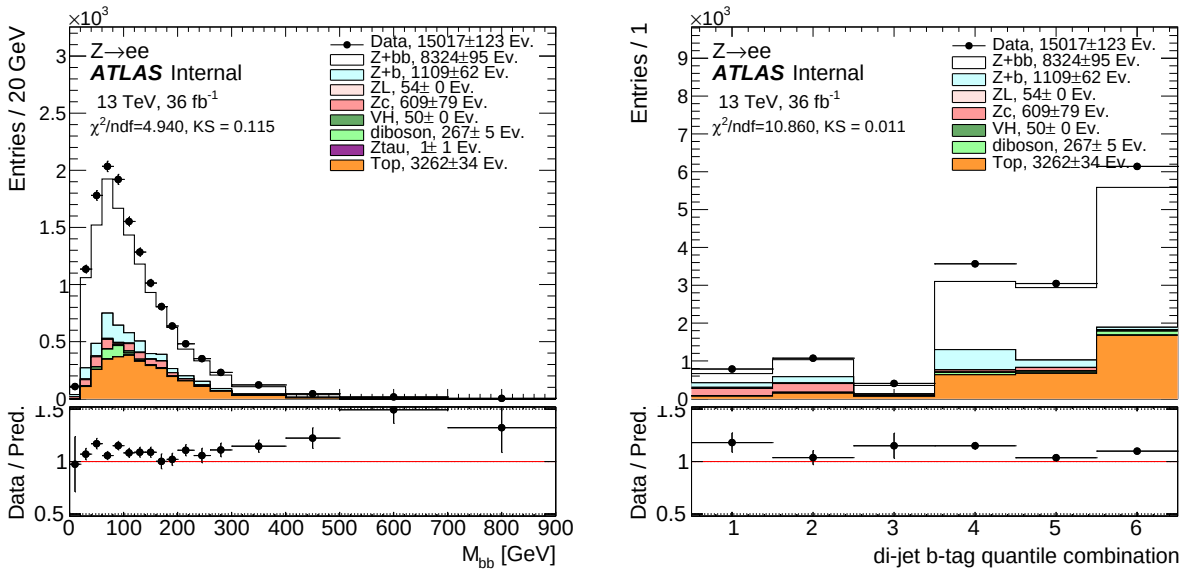

Figure C.5: Distributions of M_{bb} (left) and di-bjet working point quantiles (right) in the $Z \to ee$ analysis channel after the evaluation of the Z+L jet background component using the truth tagging method. The legend summarizes the estimated yield for each process and the corresponding statistical uncertainty.

APPENDIX D

UNFOLDING

D.1 Response Matrices

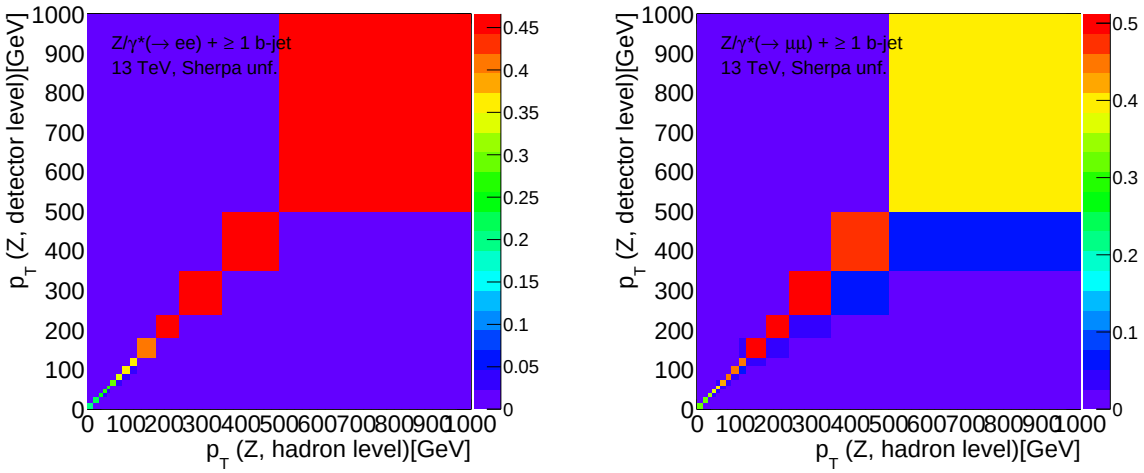

Figure D.1: Response matrix for the Z boson p_T for the Z + $\geq$ 1b-jet signal region in the electron channel (left) and muon channel (right) using Sherpa.

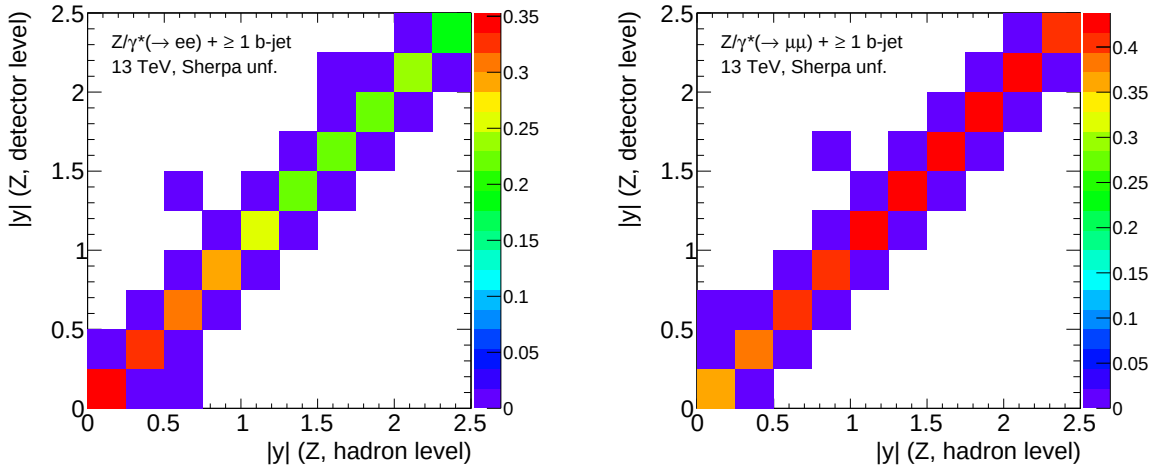

Figure D.2: Response matrix for the Z boson rapidity for the Z + $\geq$ 1b-jet signal region in the electron channel (left) and muon channel (right) using Sherpa.

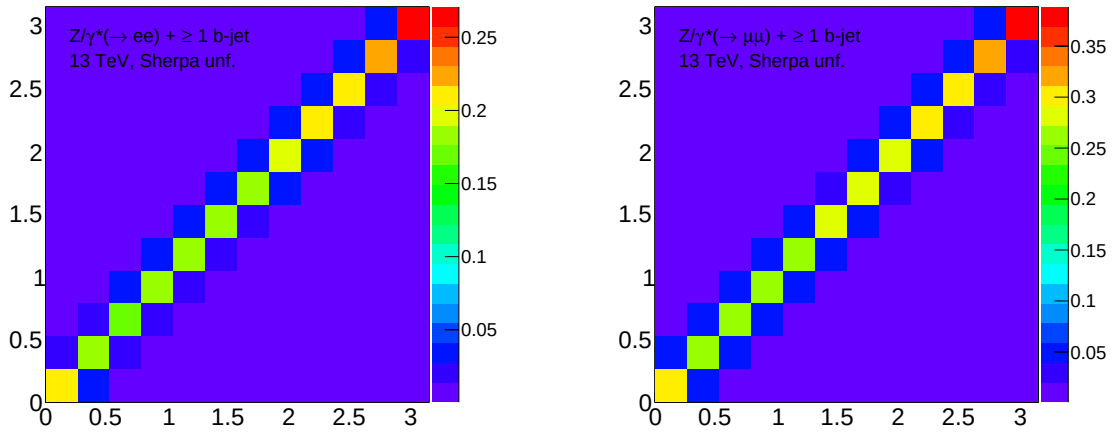

Figure D.3: Response matrix for $\Delta\phi$ between the Z boson and leading b-jet for the Z + $\geq 1b$-jet signal region in the electron channel (left) and muon channel (right) using Sherpa.

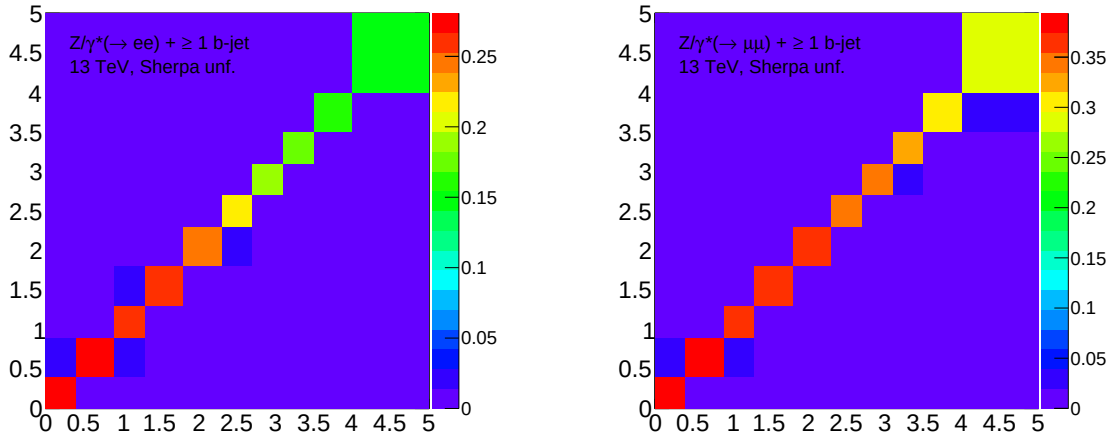

Figure D.4: Response matrix for ΔY between the Z boson and leading b-jet for the Z + $\geq 1b$-jet signal region in the electron channel (left) and muon channel (right) using Sherpa.

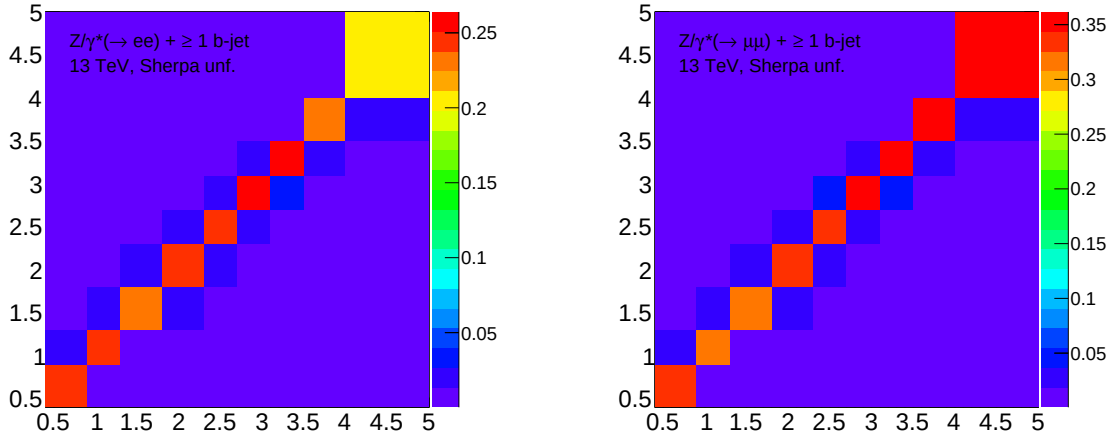

Figure D.5: Response matrix for ΔR between the Z boson and leading b-jet for the Z + $\geq 1b$-jet signal region in the electron channel (left) and muon channel (right) using Sherpa.

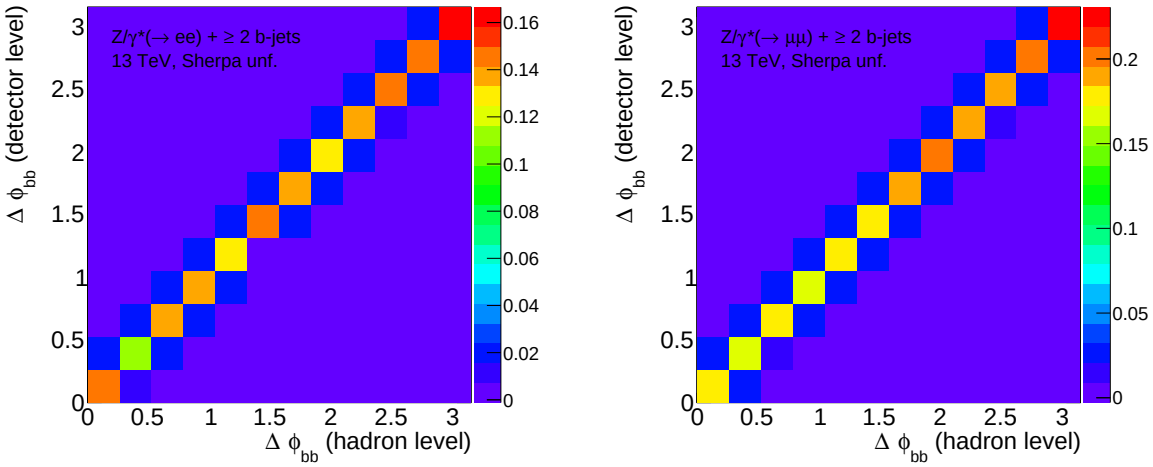

Figure D.6: Response matrix for $\Delta\phi$ between the two leading b-jets for the Z + $\geq 2b$-jets signal region in the electron channel (left) and muon channel (right) using Sherpa.

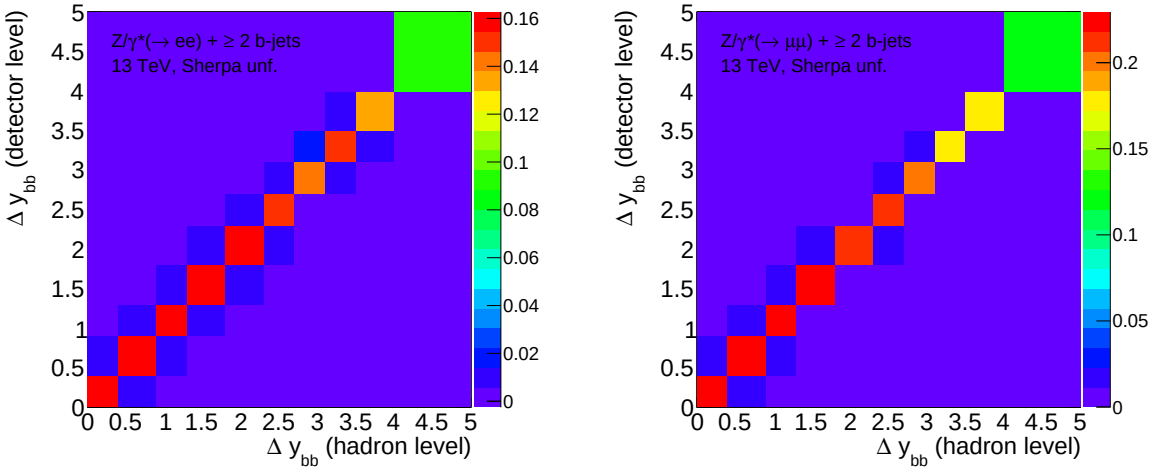

Figure D.7: Response matrix for ΔY between the two leading b-jets for the Z + $\geq 2b$-jets signal region in the electron channel (left) and muon channel (right) using Sherpa.

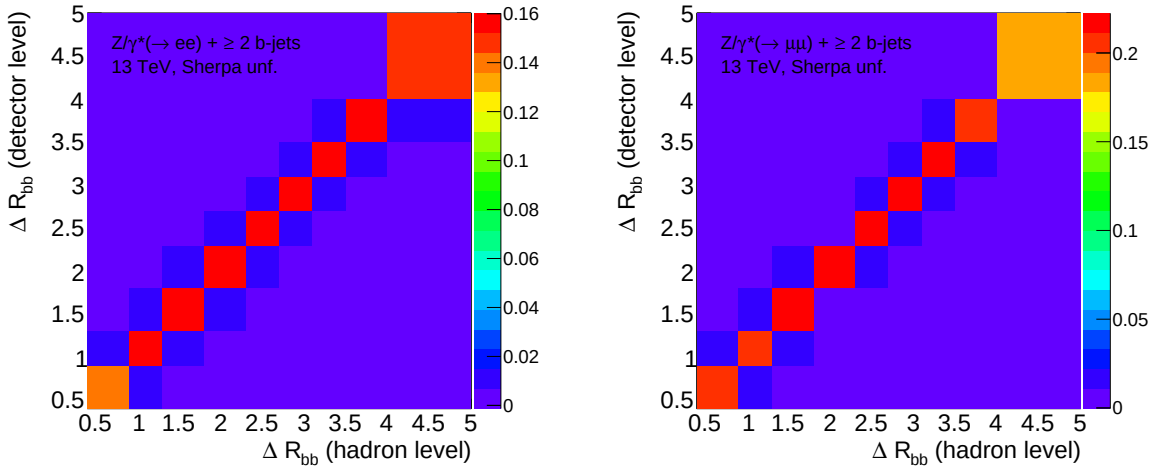

Figure D.8: Response matrix for ΔR between the two leading b-jets for the Z + $\geq 2b$-jets signal region in the electron channel (left) and muon channel (right) using Sherpa.

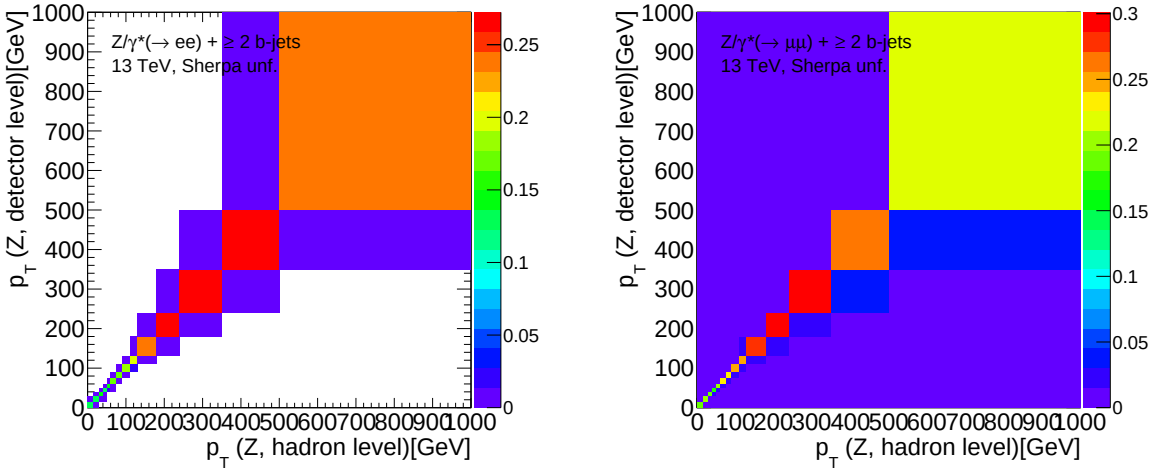

Figure D.9: Response matrix for the Z boson p_T for the Z + $\geq 2b$-jets signal region in the electron channel (left) and muon channel (right) using Sherpa.

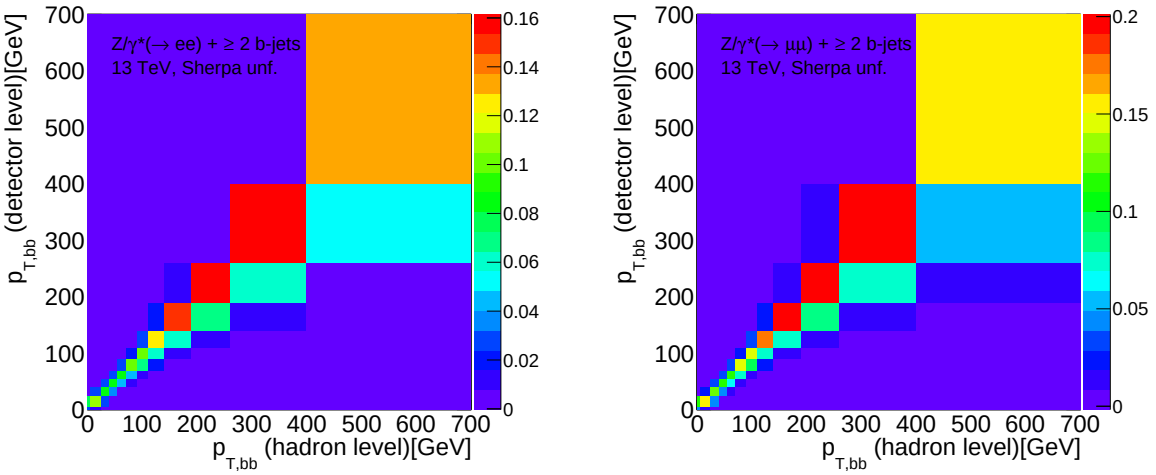

Figure D.10: Response matrix of the p_T of the sum of the two leading b-jets four-vectors in the Z + $\geq 2b$-jets signal region in the electron channel (left) and muon channel (right) using Sherpa.

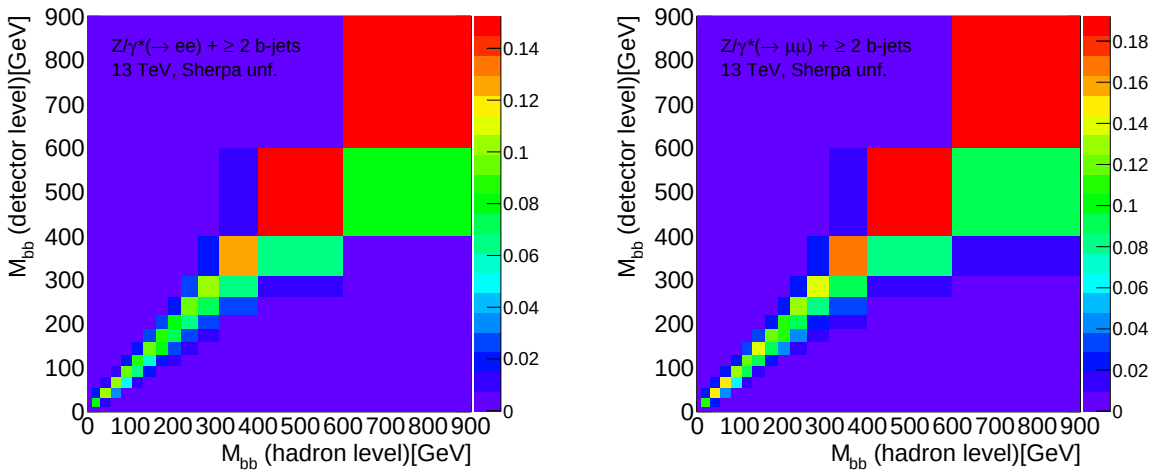

Figure D.11: Response matrix for the invariant mass of the two leading b-jets for the Z + $\geq 2b$-jets signal region in the electron channel (left) and muon channel (right) using Sherpa.

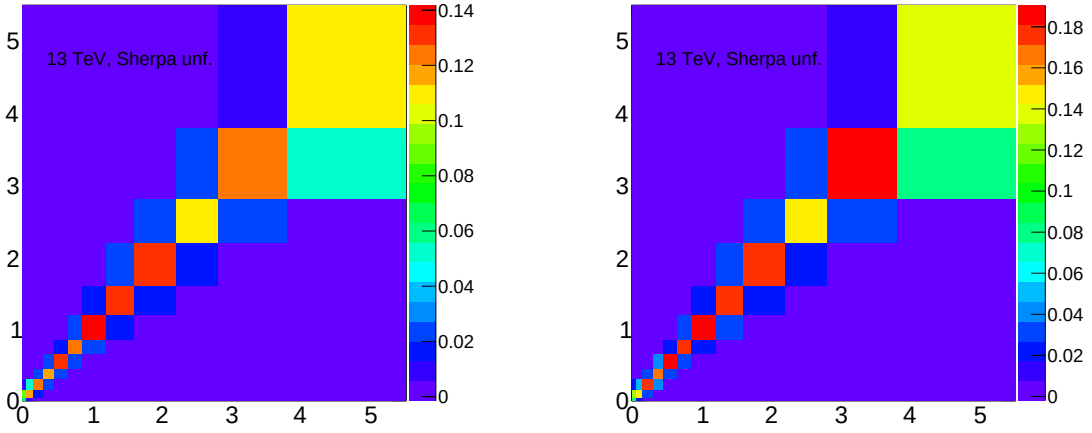

Figure D.12: Response matrix for p_T of the sum of the two leading b-jets four-vectors divided by the invariant mass of them in the Z + $\geq 2b$-jets signal region in the electron channel (left) and muon channel (right) using Sherpa.

D.2 Efficiencies

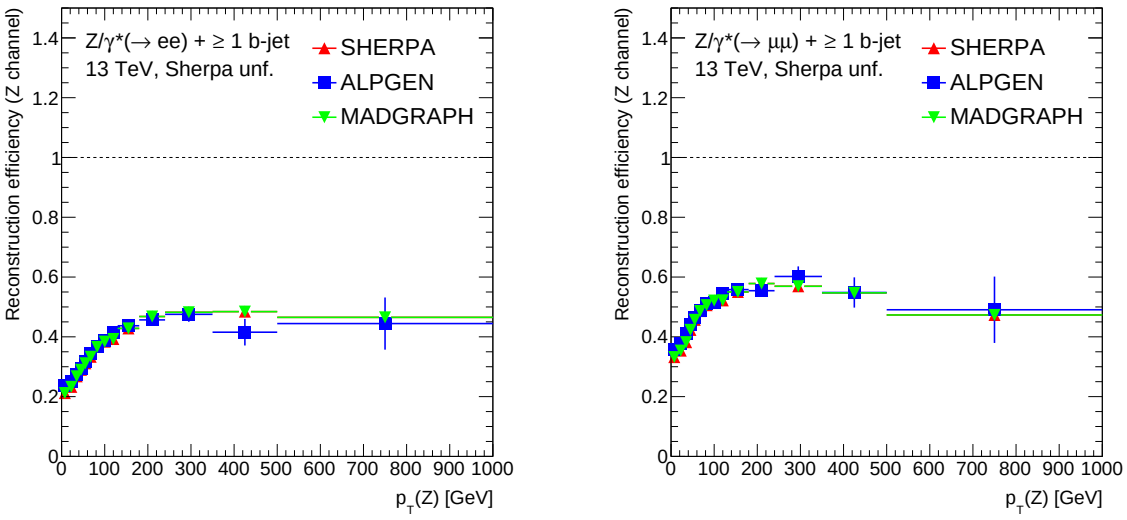

Figure D.13: Reconstruction efficiency of the Z boson p_T for the Z + $\geq 1b$-jet signal region in the electron channel (left) and muon channel (right) using Sherpa.

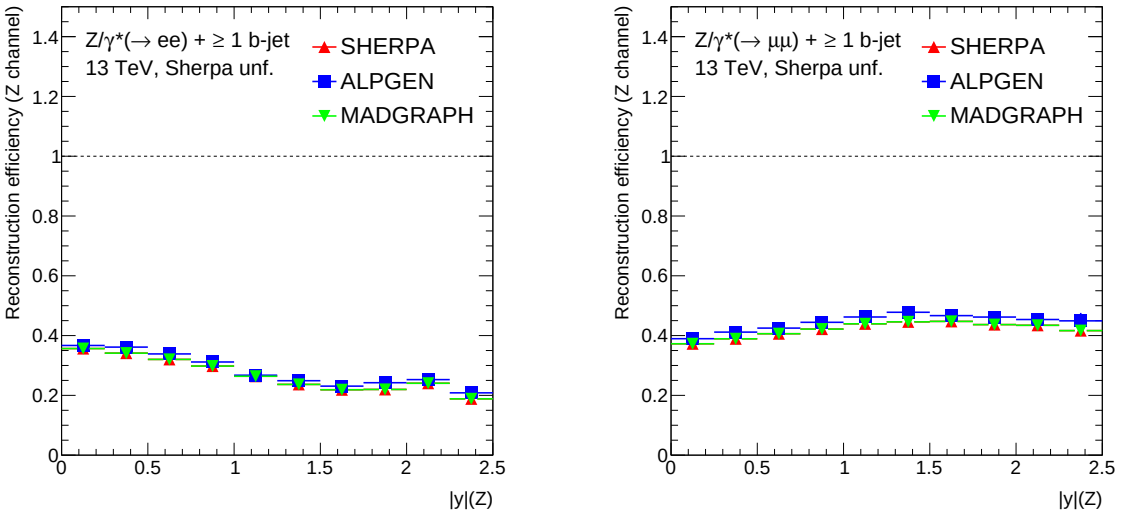

Figure D.14: Reconstruction efficiency of the Z boson rapidity for the Z + $\geq 1b$-jet signal region in the electron channel (left) and muon channel (right) using Sherpa.

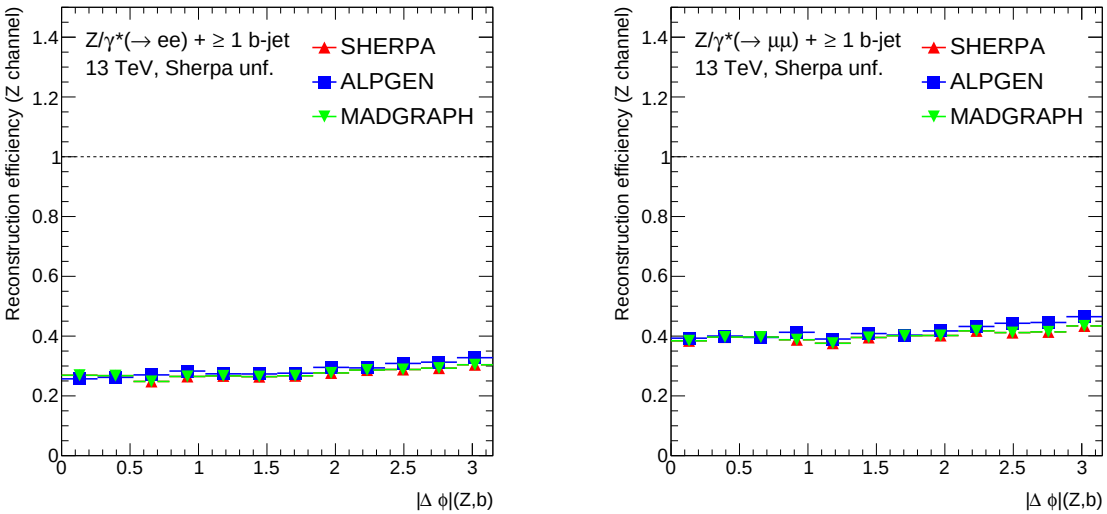

Figure D.15: Reconstruction efficiency of the $\Delta\phi$ between the Z boson and leading b-jet for the Z + $\geq 1b$-jet signal region in the electron channel (left) and muon channel (right) using Sherpa.

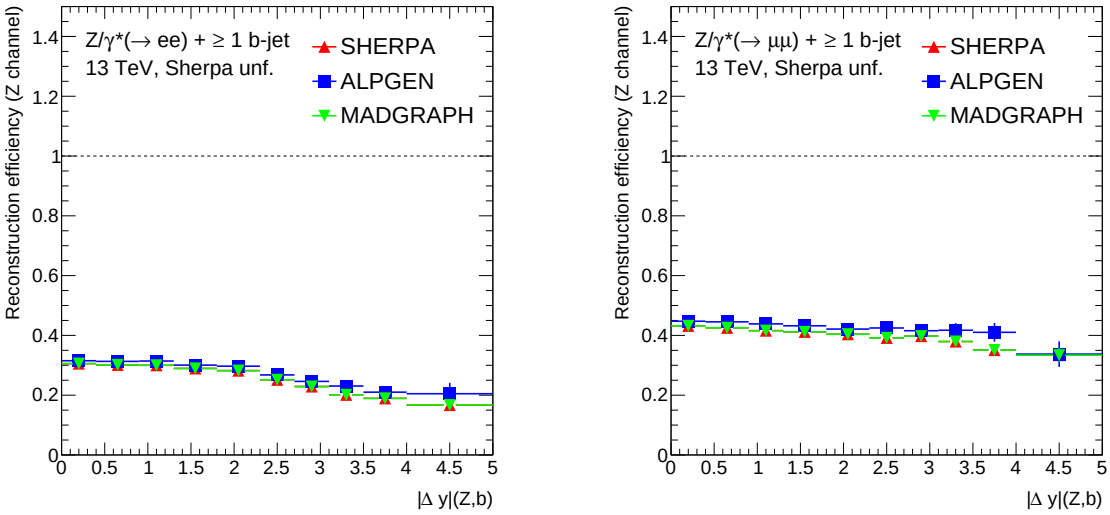

Figure D.16: Reconstruction efficiency of the ΔY between the Z boson and leading b-jet for the Z + $\geq 1b$-jet signal region in the electron channel (left) and muon channel (right) using Sherpa.

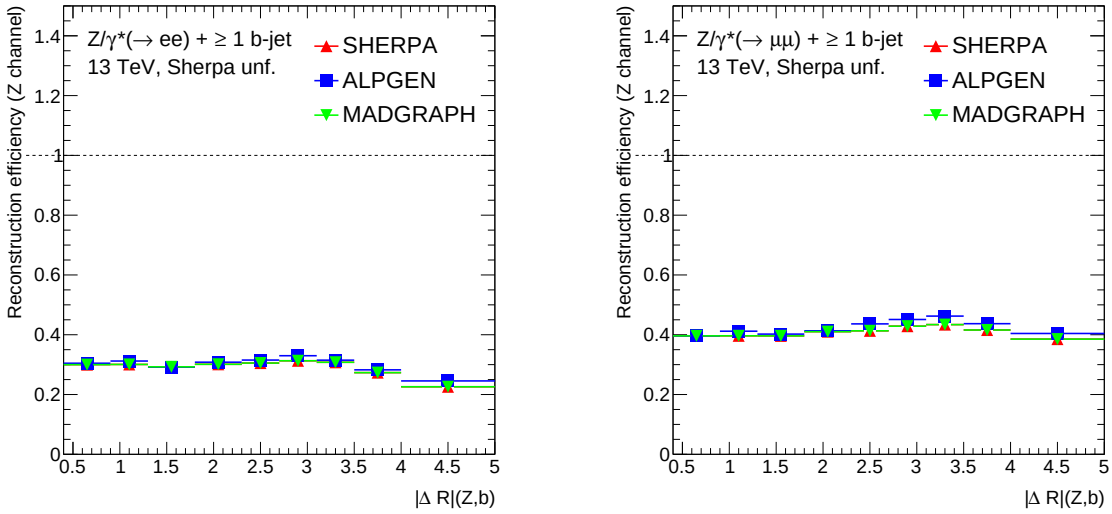

Figure D.17: Reconstruction efficiency of the ΔR between the Z boson and leading b-jet for the Z + $\geq 1b$-jet signal region in the electron channel (left) and muon channel (right) using Sherpa.

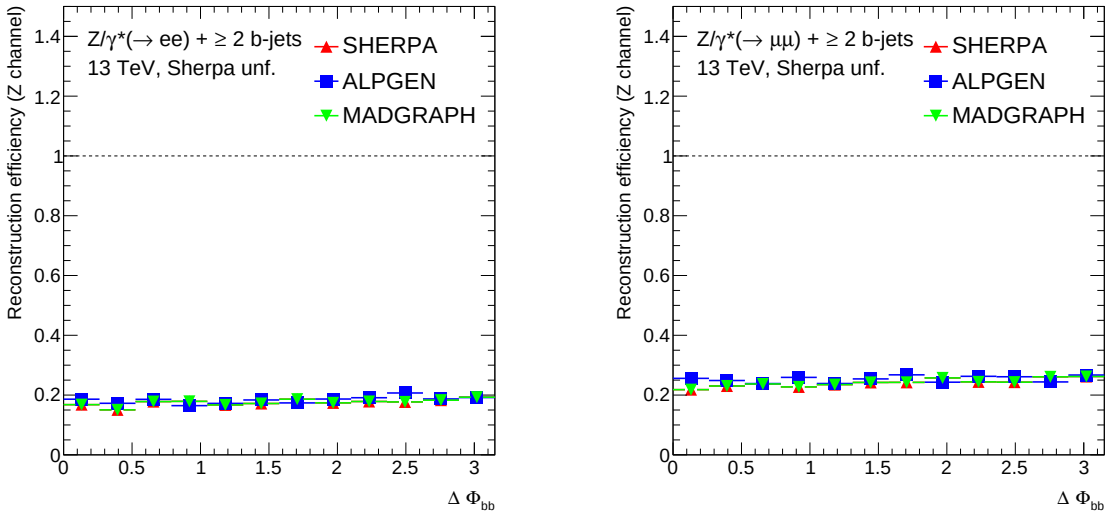

Figure D.18: Reconstruction efficiency of the $\Delta\phi$ between the two leading b-jets for the Z + $\geq 2b$-jets signal region in the electron channel (left) and muon channel (right) using Sherpa.

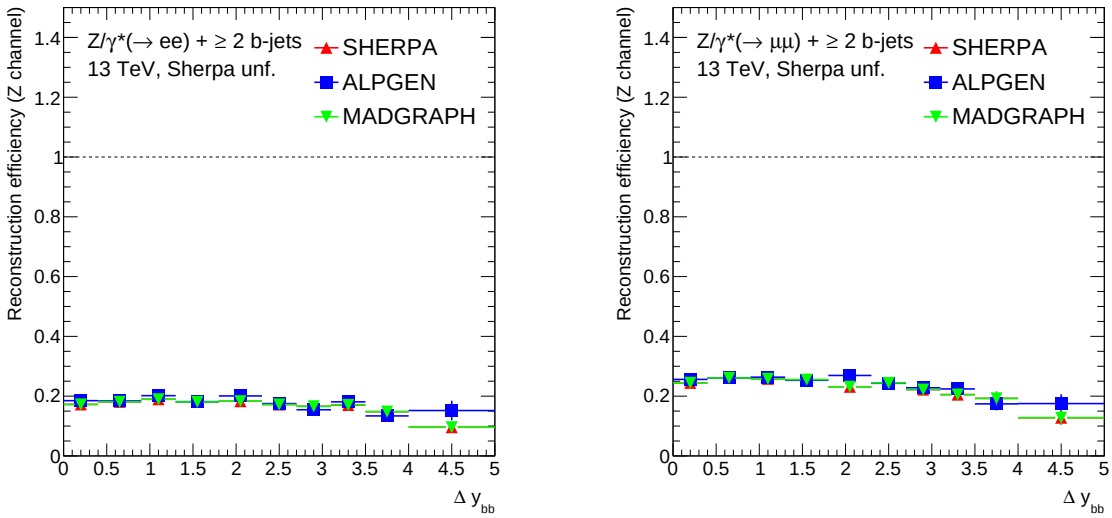

Figure D.19: Reconstruction efficiency of the ΔY between the two leading b-jets for the Z + $\geq 2b$-jets signal region in the electron channel (left) and muon channel (right) using Sherpa.

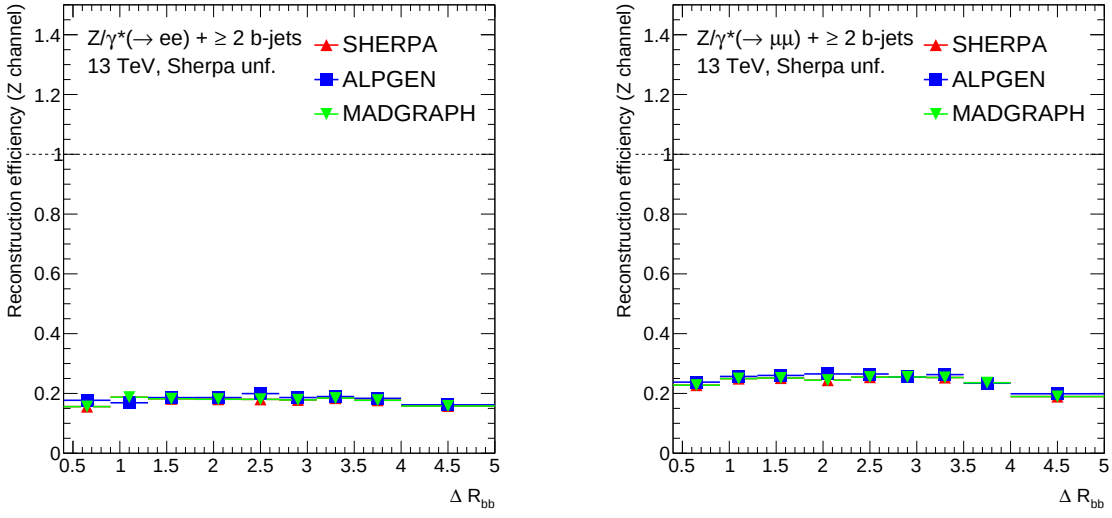

Figure D.20: Reconstruction efficiency of the ΔR between the two leading b-jets for the Z + $\geq 2b$-jets signal region in the electron channel (left) and muon channel (right) using Sherpa.

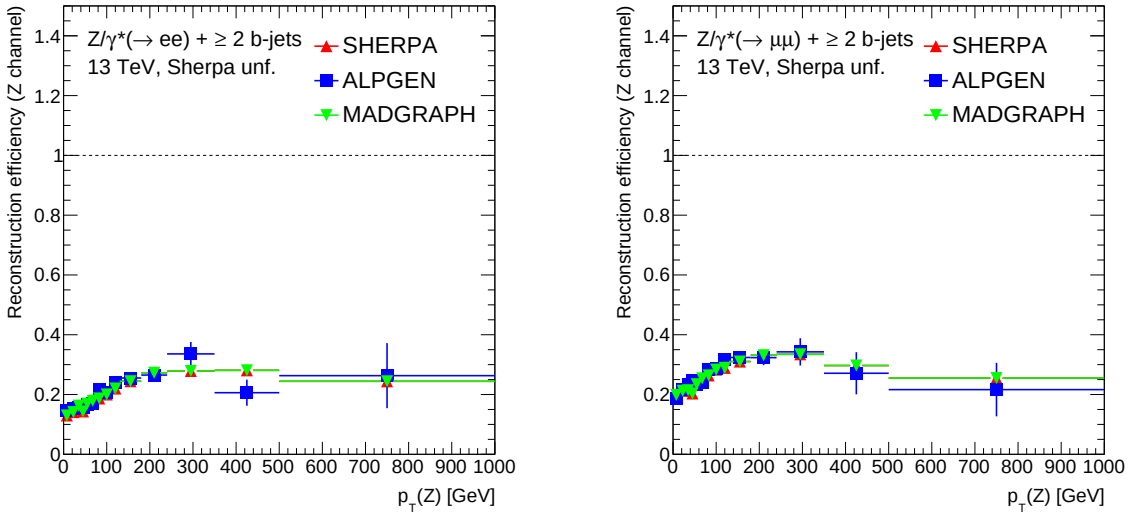

Figure D.21: Reconstruction efficiency of the Z boson p_T for the Z + $\geq 2b$-jets signal region in the electron channel (left) and muon channel (right) using Sherpa.

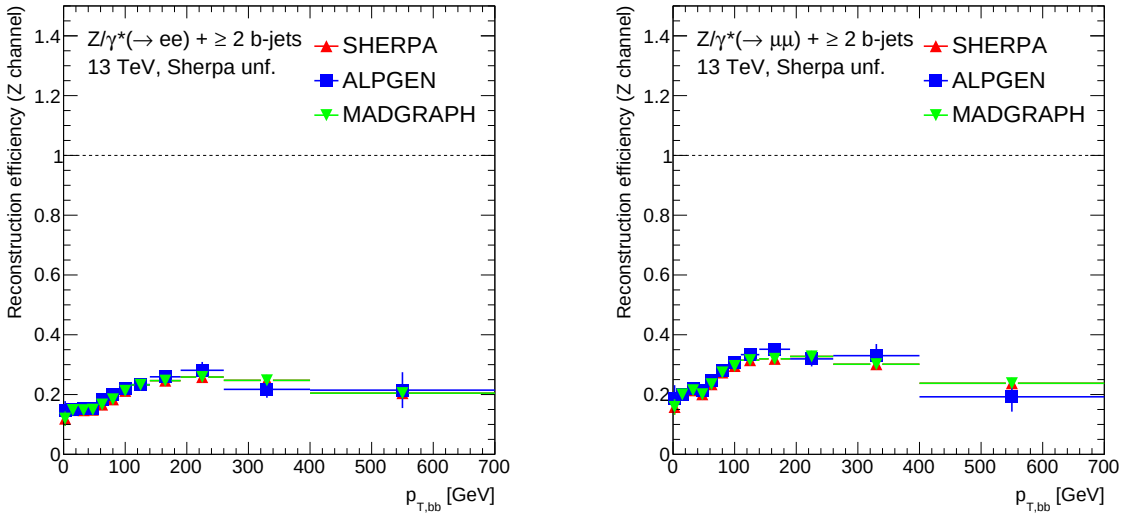

Figure D.22: Reconstruction efficiency of the p_T of the sum of the two leading b-jets four-vectors for the Z + $\geq 2b$-jets signal region in the electron channel (left) and muon channel (right) using Sherpa.

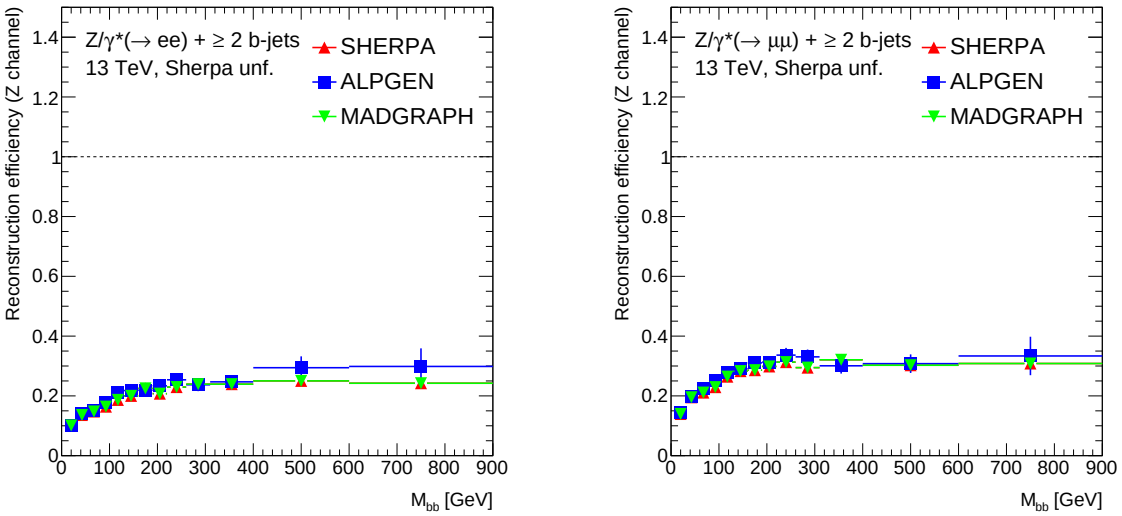

Figure D.23: Reconstruction efficiency of the invariant mass of the two leading b-jets for the Z + $\geq$ 2b-jets signal region in the electron channel (left) and muon channel (right) using Sherpa.

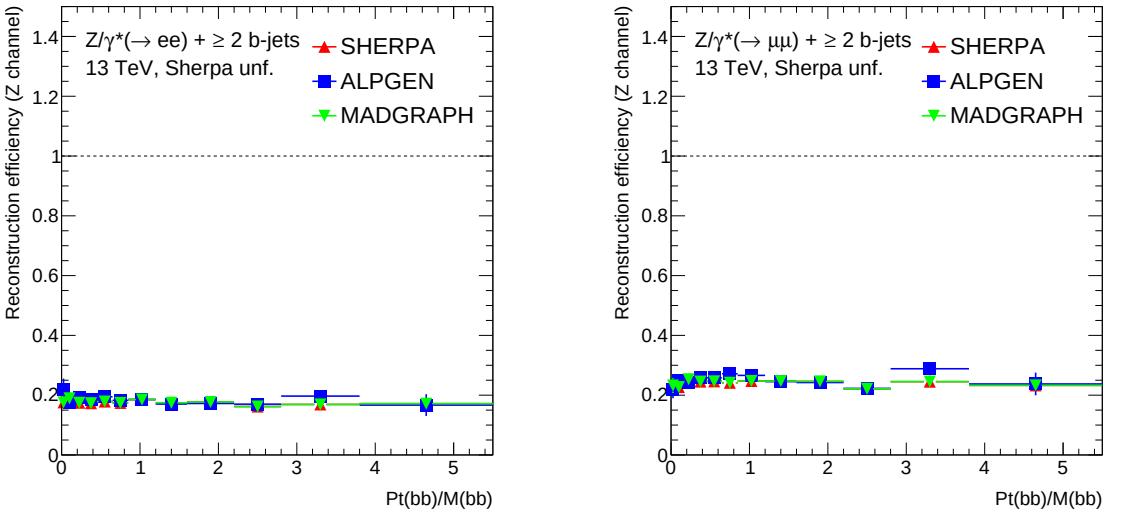

Figure D.24: Reconstruction efficiency of the p_T of the sum of the two leading b-jets four-vectors divided by the invariant mass of them for the Z + $\geq$ 2b-jets signal region in the electron channel (left) and muon channel (right) using Sherpa.

D.3 Fake Factors

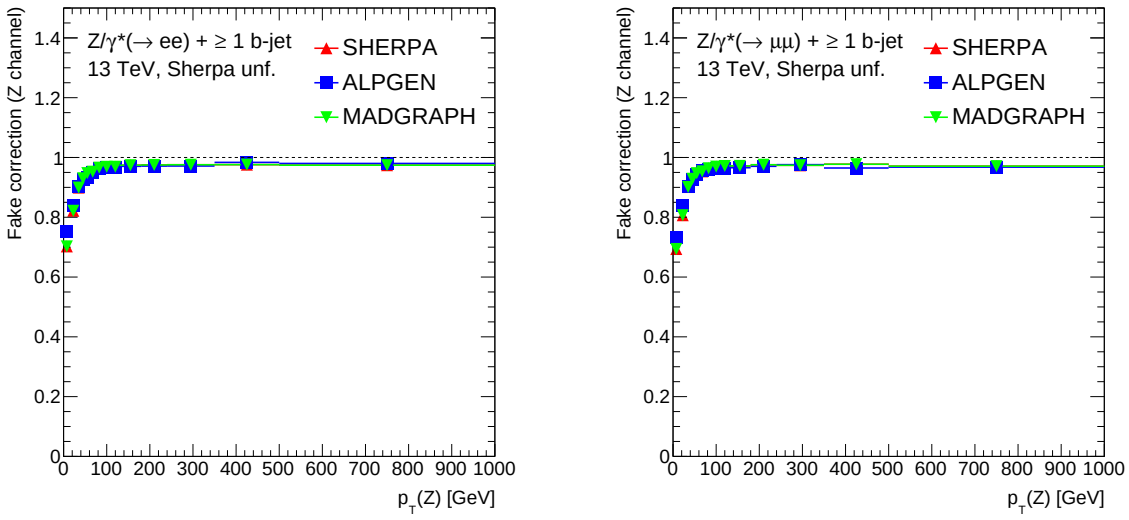

Figure D.25: Fake correction of the Z boson p_T for the Z + $\geq$ 1b-jet signal region in the electron channel (left) and muon channel (right) using Sherpa.

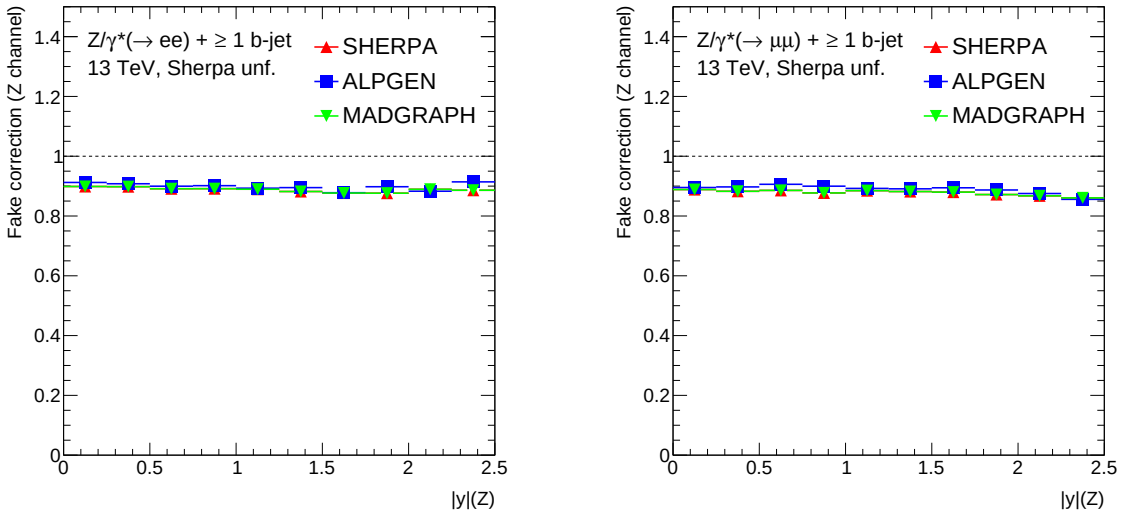

Figure D.26: Fake correction of the Z boson rapidity for the Z + $\geq$ 1b-jet signal region in the electron channel (left) and muon channel (right) using Sherpa.

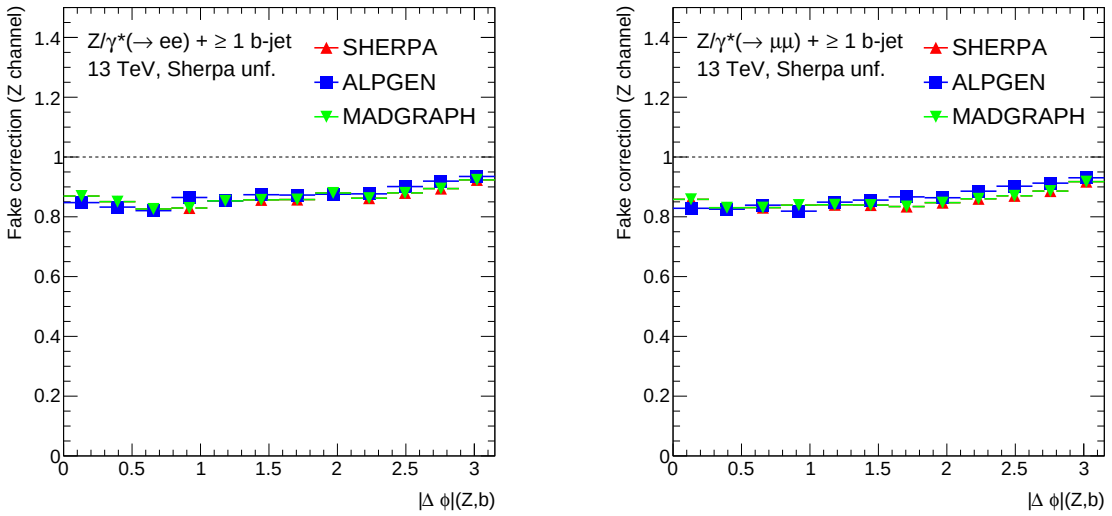

Figure D.27: Fake correction of the $\Delta\phi$ between the Z boson and leading b-jet for the Z + $\geq 1b$-jet signal region in the electron channel (left) and muon channel (right) using Sherpa.

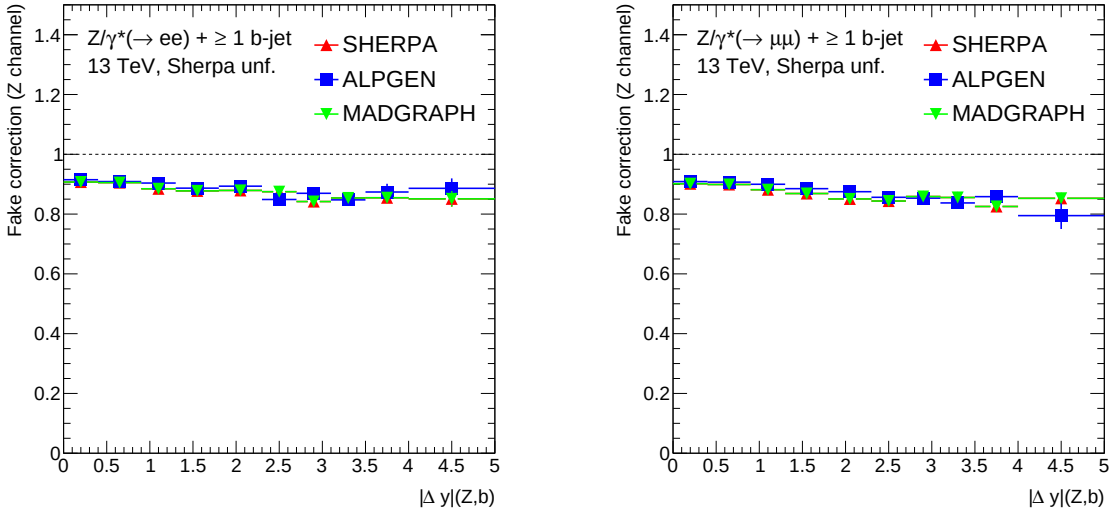

Figure D.28: Fake correction of the ΔY between the Z boson and leading b-jet for the Z + $\geq 1b$-jet signal region in the electron channel (left) and muon channel (right) using Sherpa.

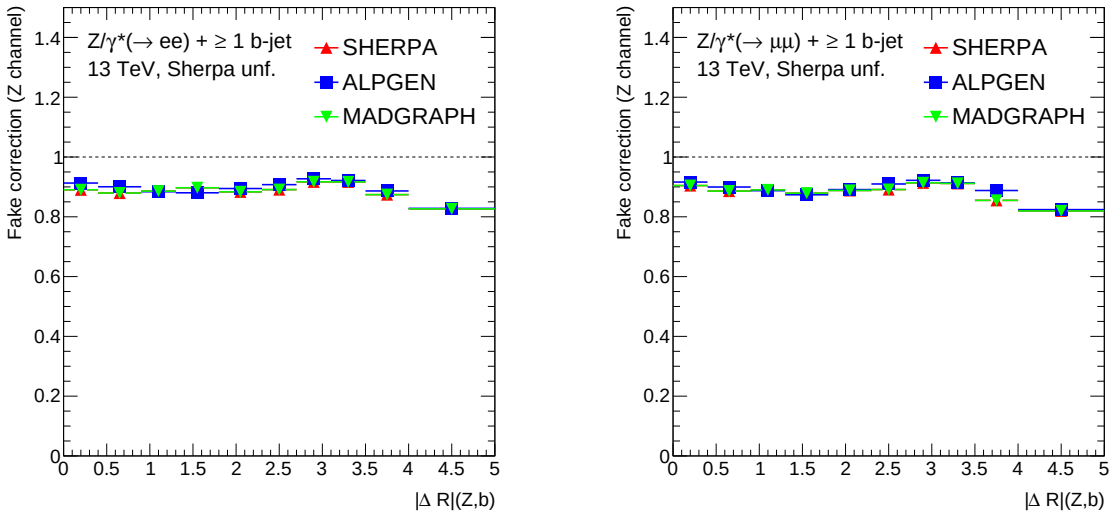

Figure D.29: Fake correction of the ΔR between the Z boson and leading b-jet for the Z + $\geq 1b$-jet signal region in the electron channel (left) and muon channel (right) using Sherpa.

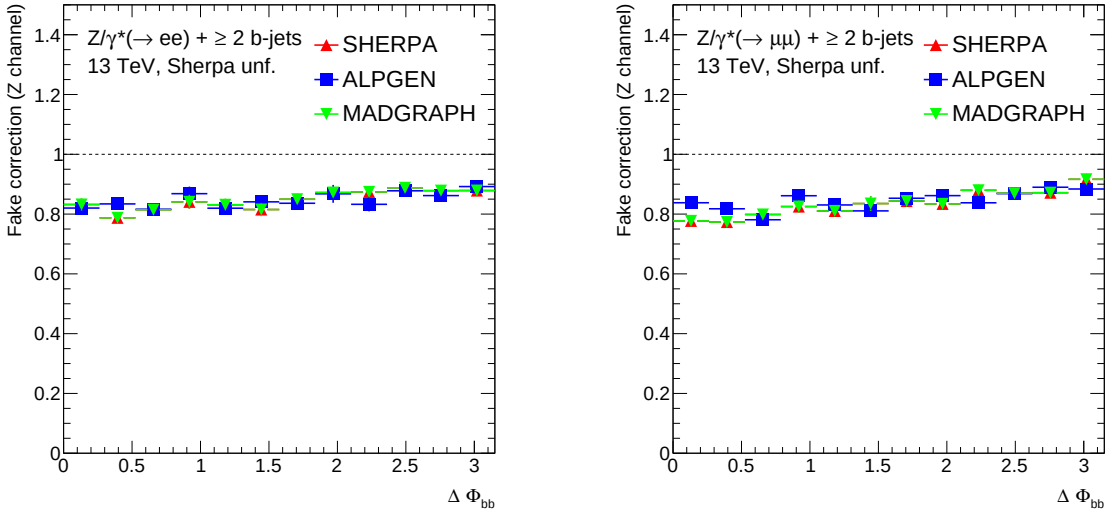

Figure D.30: Fake correction of the $\Delta\phi$ between the two leading b-jets for the Z + $\geq 2b$-jets signal region in the electron channel (left) and muon channel (right) using Sherpa.

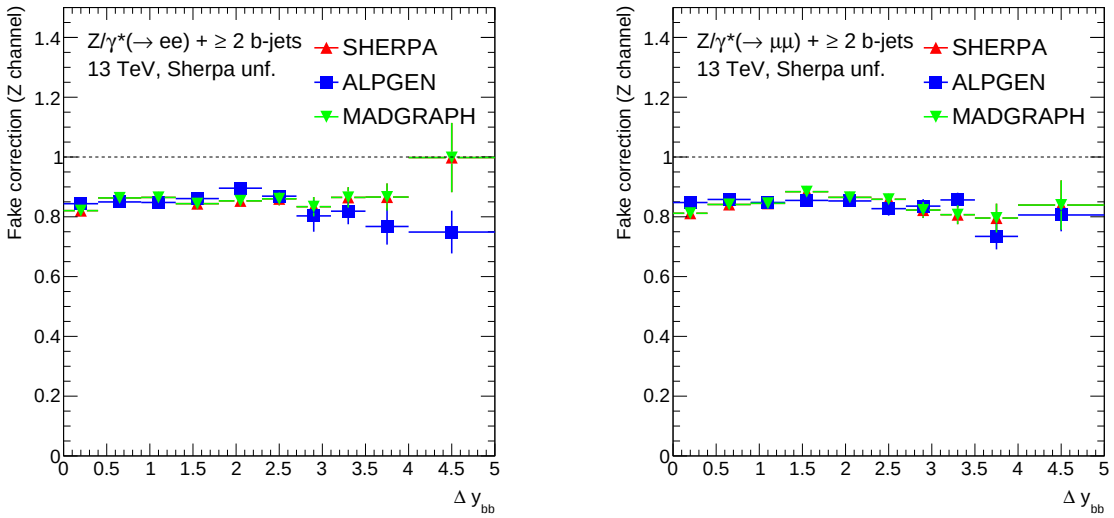

Figure D.31: Fake correction of the ΔY between the two leading b-jets for the Z + $\geq 2b$-jets signal region in the electron channel (left) and muon channel (right) using Sherpa.

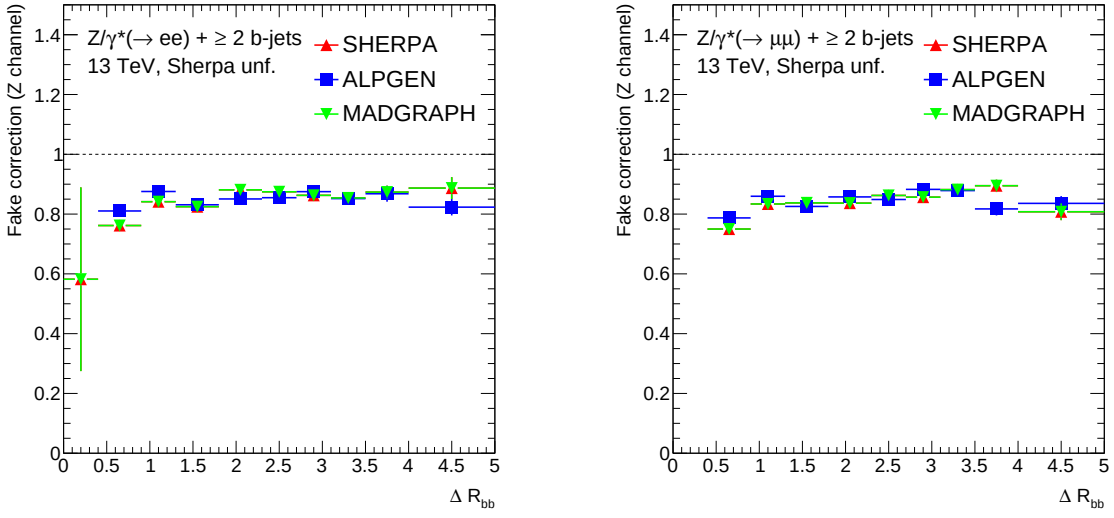

Figure D.32: Fake correction of the ΔR between the two leading b-jets for the Z + $\geq 2b$-jets signal region in the electron channel (left) and muon channel (right) using Sherpa.

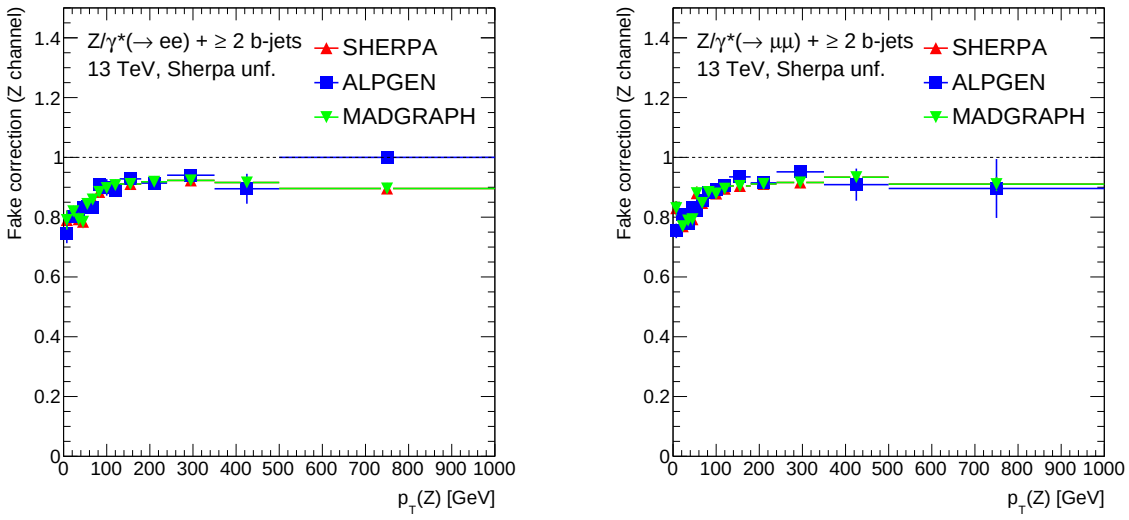

Figure D.33: Fake correction of the Z boson p_T for the Z + $\geq 2b$-jets signal region in the electron channel (left) and muon channel (right) using Sherpa.

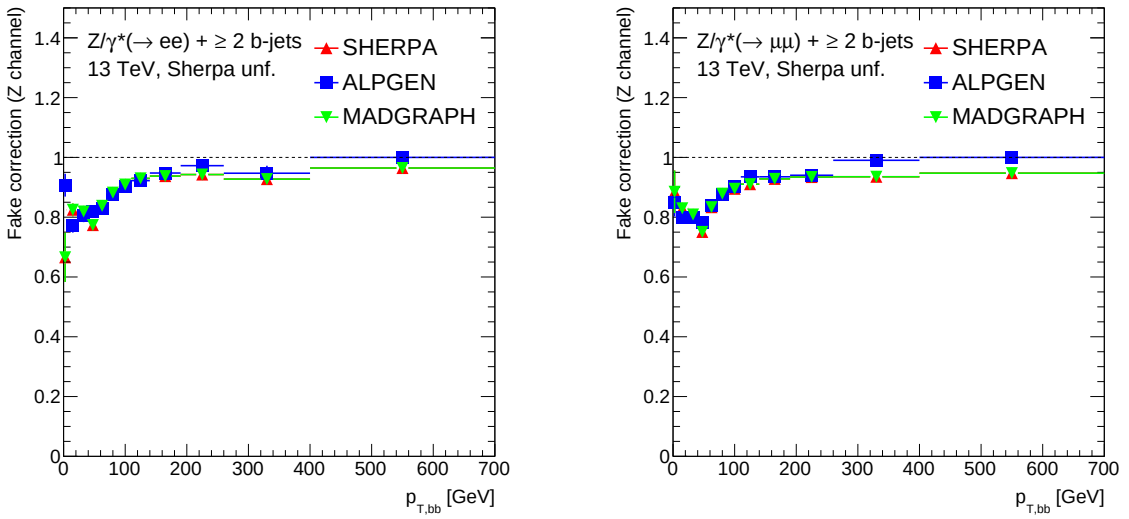

Figure D.34: Fake correction of the p_T of the sum of the two leading b-jets four-vectors for the Z + $\geq 2b$-jets signal region in the electron channel (left) and muon channel (right) using Sherpa.

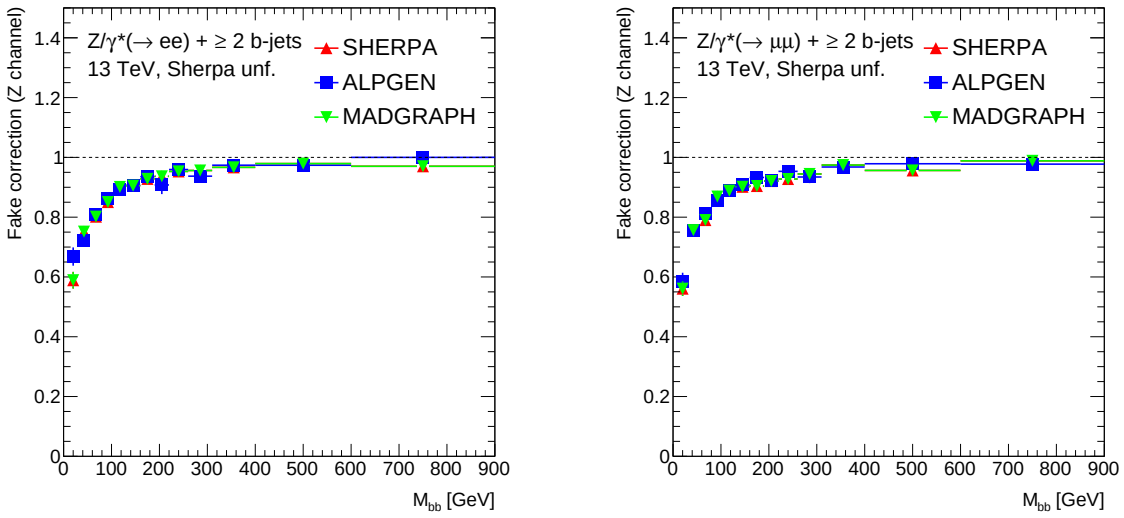

Figure D.35: Fake correction of the invariant mass of the two leading b-jets for the Z + $\geq 2b$-jets signal region in the electron channel (left) and muon channel (right) using Sherpa.

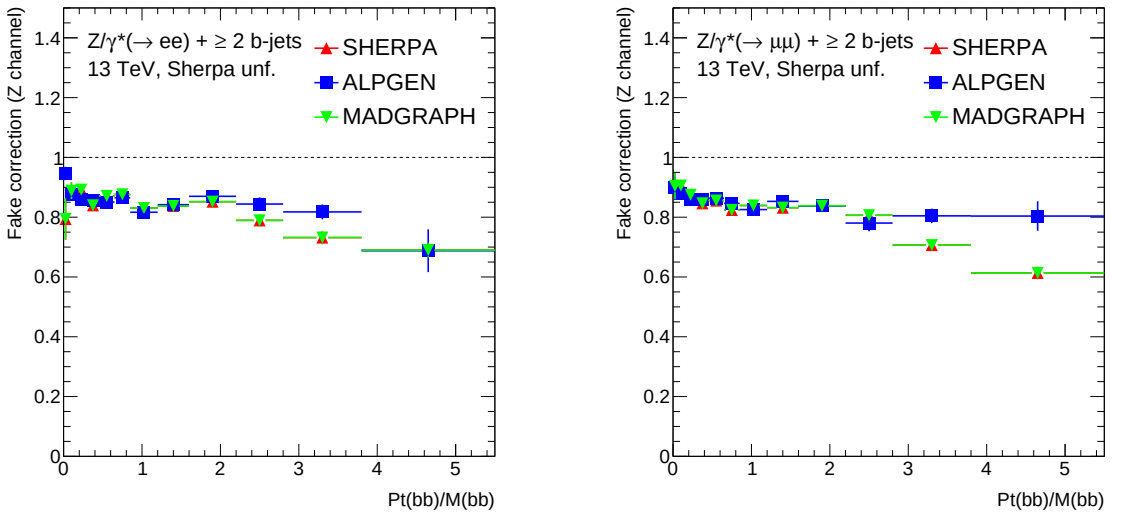

Figure D.36: Fake correction of the p_T of the sum of the two leading b-jets four-vectors divided by the invariant mass of them for the Z + $\geq 2b$-jets signal region in the electron channel (left) and muon channel (right) using Sherpa.

D.4 Breakdown of Unfolding Uncertainty

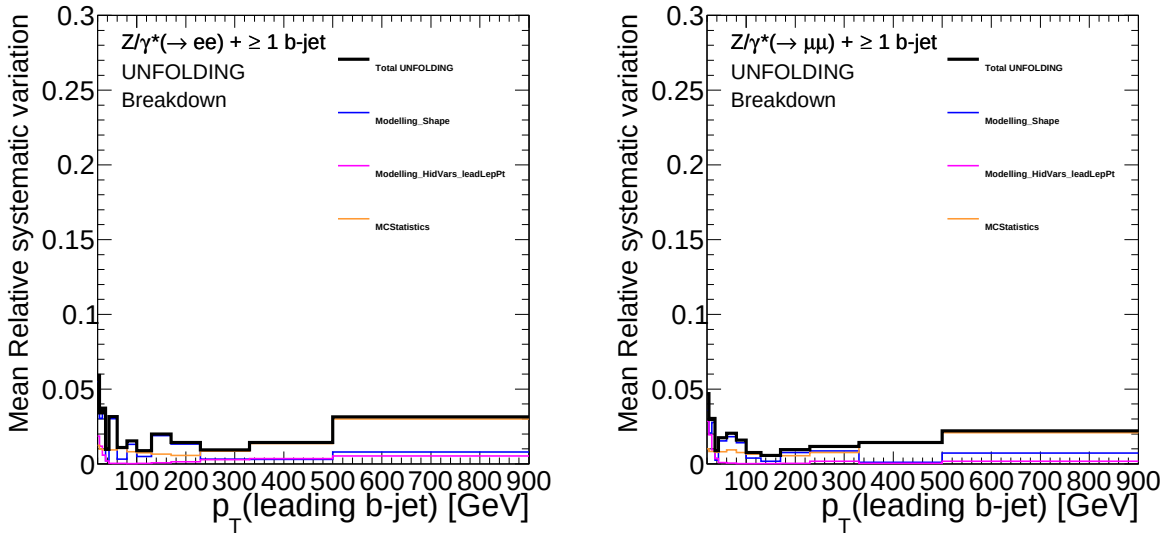

Figure D.37: Breakdown of the three components of the uncertainty on the unfolding method on the leading b-jet p_T for the electron channel (left) and muon channel (right) in the Z + 1b-jet signal region.

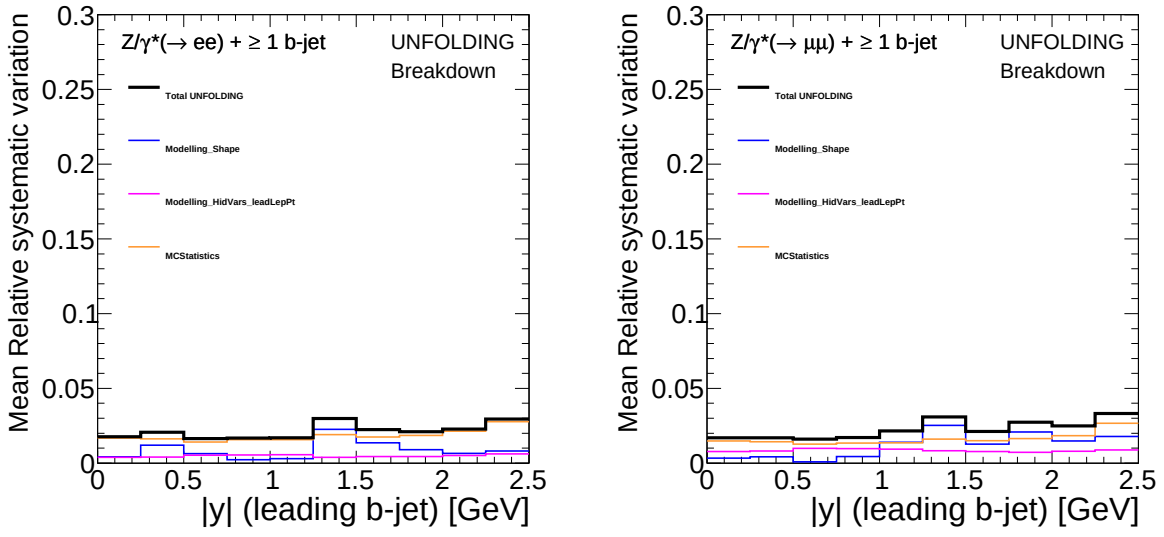

Figure D.38: Breakdown of the three components of the uncertainty on the unfolding method on the leading b-jet rapidity for the electron channel (left) and muon channel (right) in the Z + 1b-jet signal region.

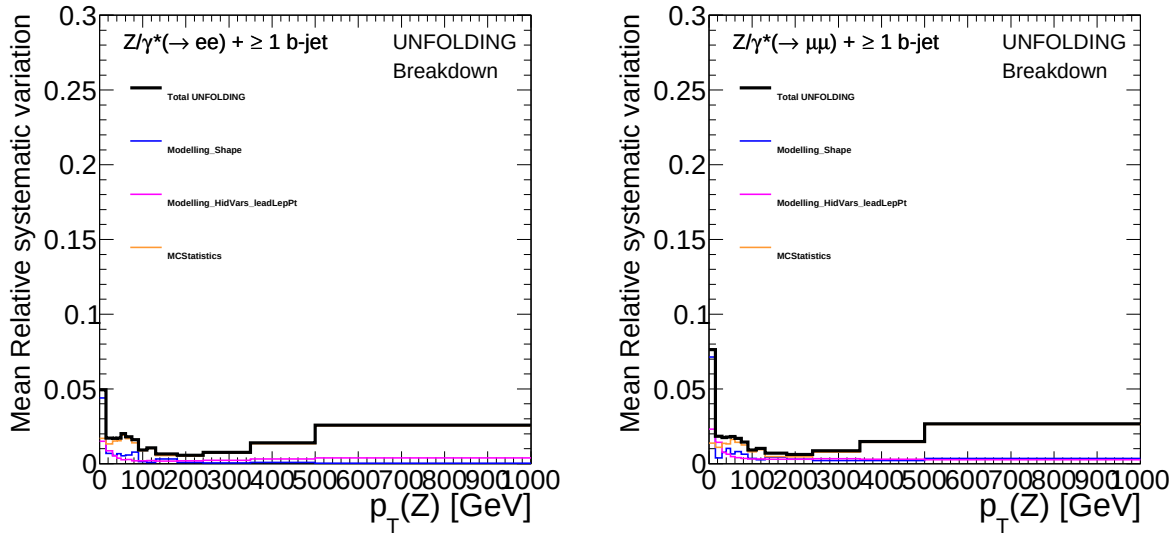

Figure D.39: Breakdown of the three components of the uncertainty on the unfolding method on the Z boson p_T for the electron channel (left) and muon channel (right) in the Z + 1b-jet signal region.

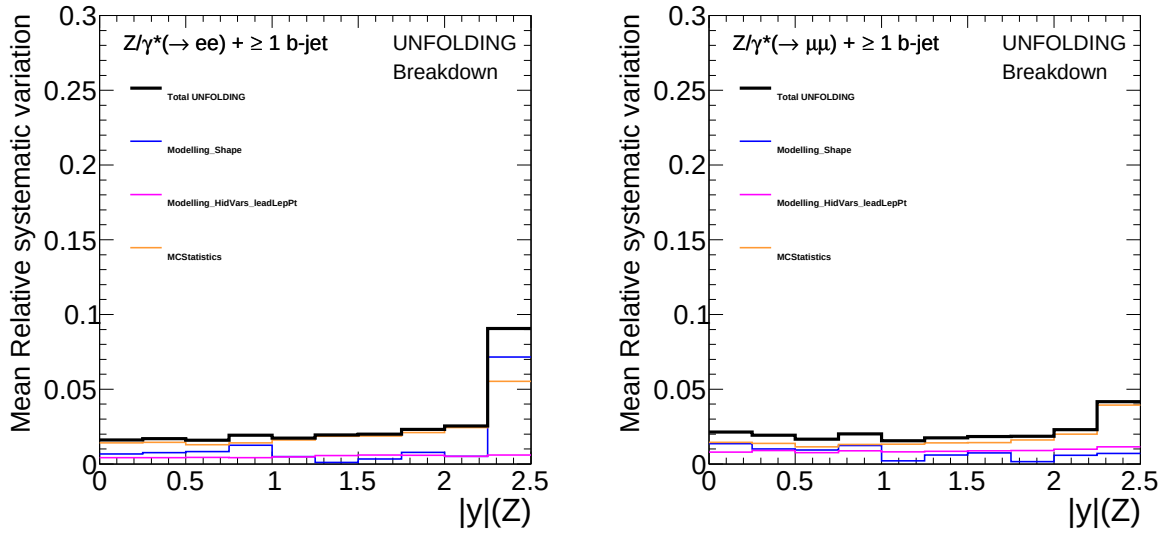

Figure D.40: Breakdown of the three components of the uncertainty on the unfolding method on the Z boson rapidity for the electron channel (left) and muon channel (right) in the Z + 1b-jet signal region.

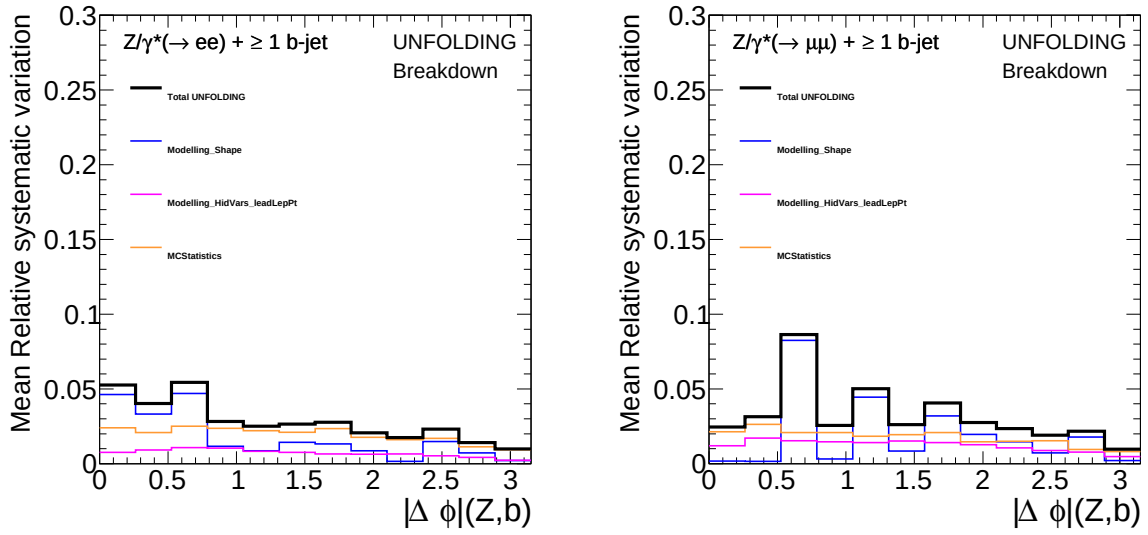

Figure D.41: Breakdown of the three components of the uncertainty on the unfolding method on the $\delta\phi$ between the leading b-jet and Z boson for the electron channel (left) and muon channel (right) in the Z + 1b-jet signal region.

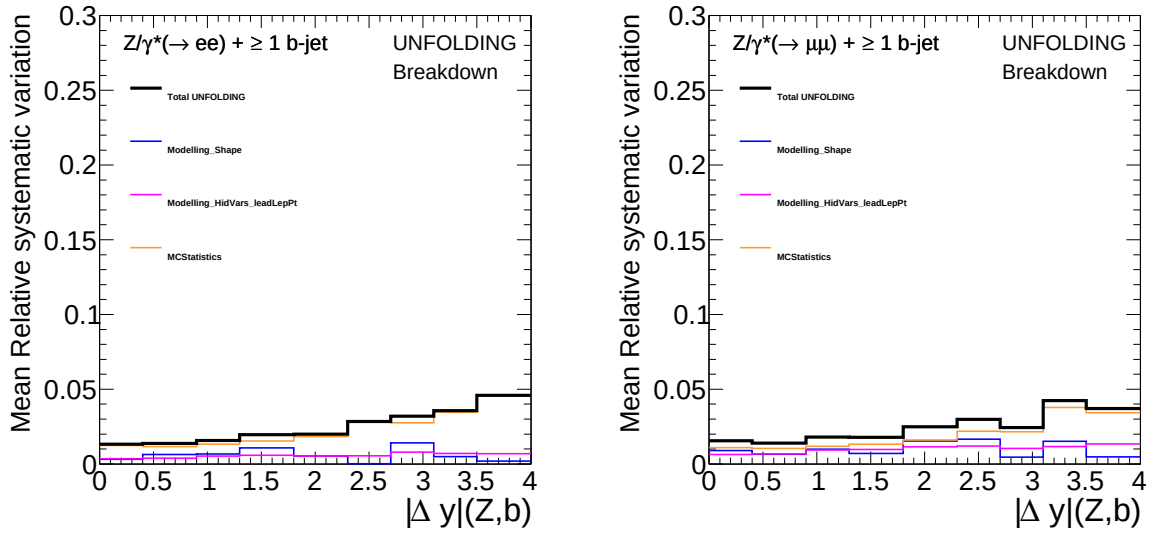

Figure D.42: Breakdown of the three components of the uncertainty on the unfolding method on the δY between the leading b-jet and Z boson for the electron channel (left) and muon channel (right) in the Z + 1b-jet signal region.

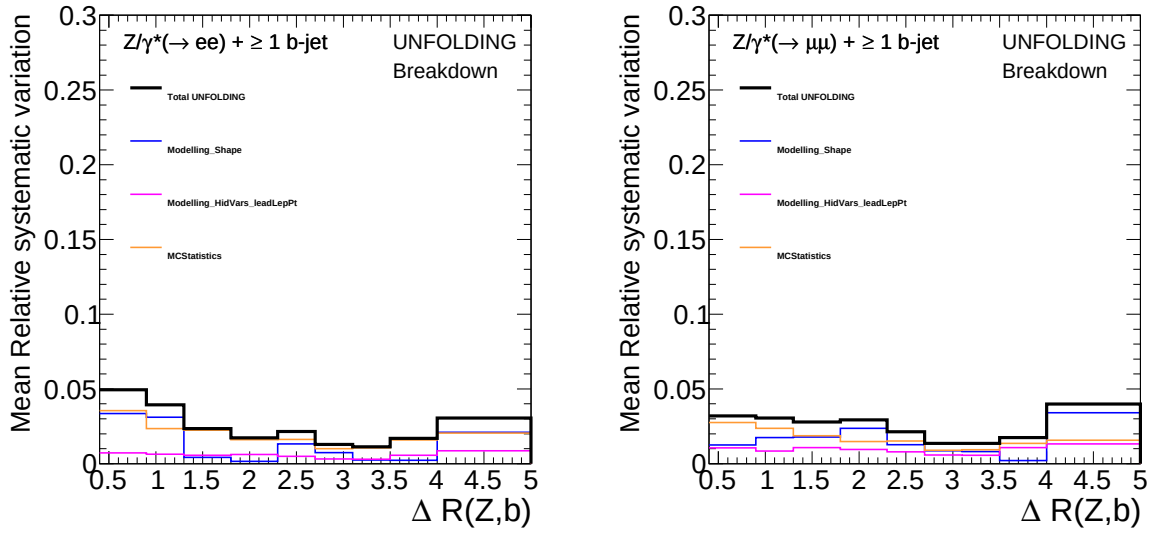

Figure D.43: Breakdown of the three components of the uncertainty on the unfolding method on the δR between the leading b-jet and Z boson for the electron channel (left) and muon channel (right) in the Z + 1b-jet signal region.

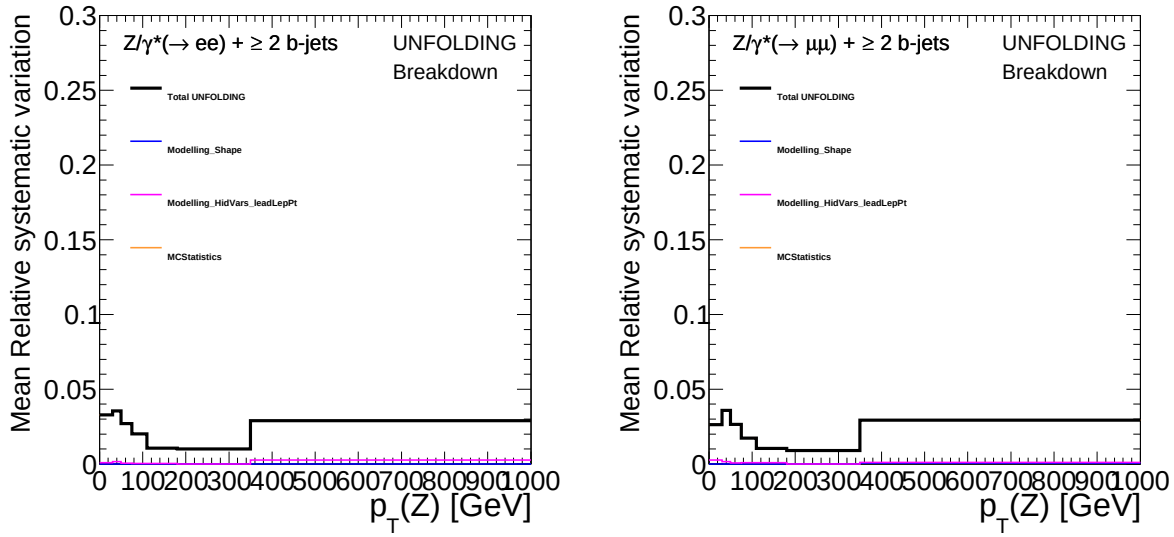

Figure D.44: Breakdown of the three components of the uncertainty on the unfolding method on the Z boson p_T for the electron channel (left) and muon channel (right) in the Z + 2b-jets signal region.

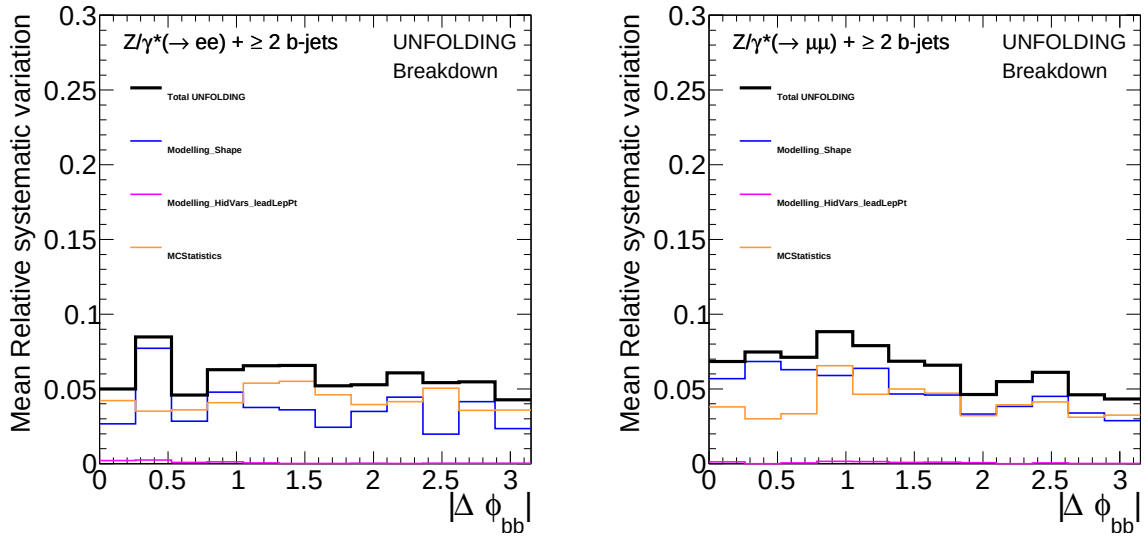

Figure D.45: Breakdown of the three components of the uncertainty on the unfolding method on the $\delta\phi$ between the two leading b-jets for the electron channel (left) and muon channel (right) in the Z + 2b-jets signal region.

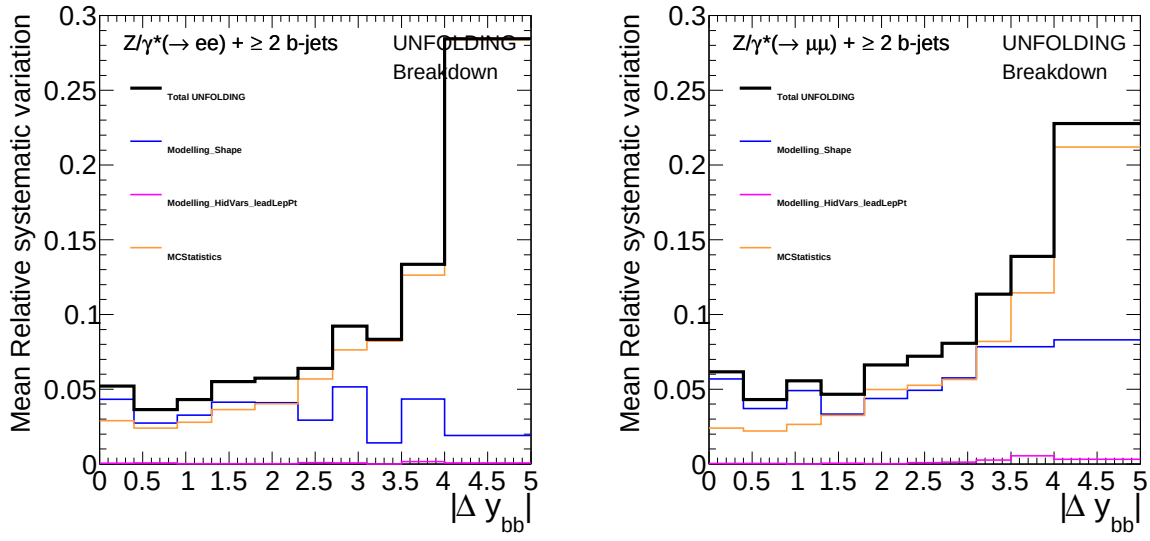

Figure D.46: Breakdown of the three components of the uncertainty on the unfolding method on the δY between the two leading b-jets for the electron channel (left) and muon channel (right) in the Z + 2b-jets signal region.

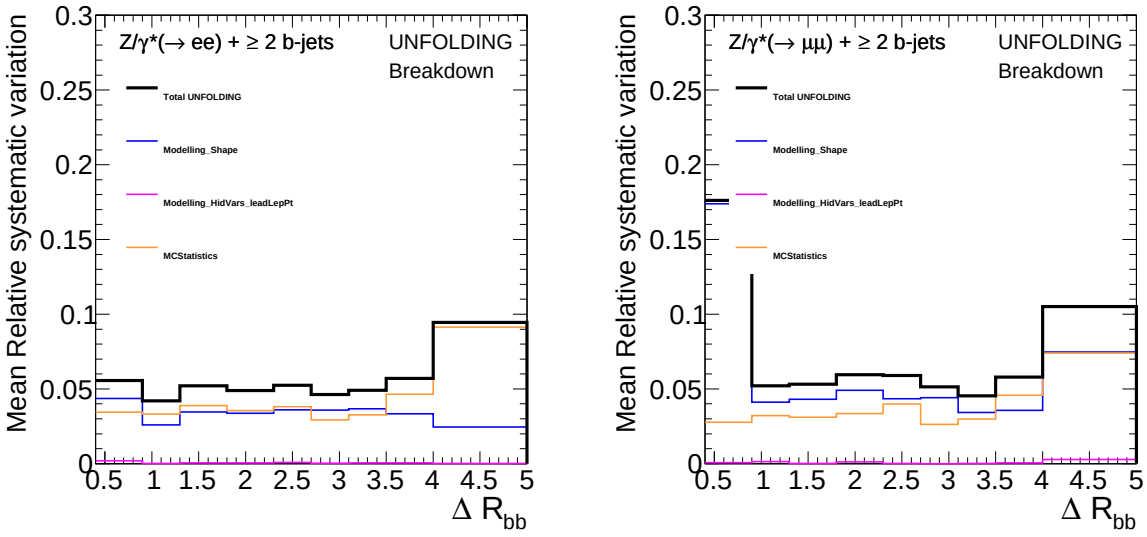

Figure D.47: Breakdown of the three components of the uncertainty on the unfolding method on the δR between the two leading b-jets for the electron channel (left) and muon channel (right) in the Z + 2b-jets signal region.

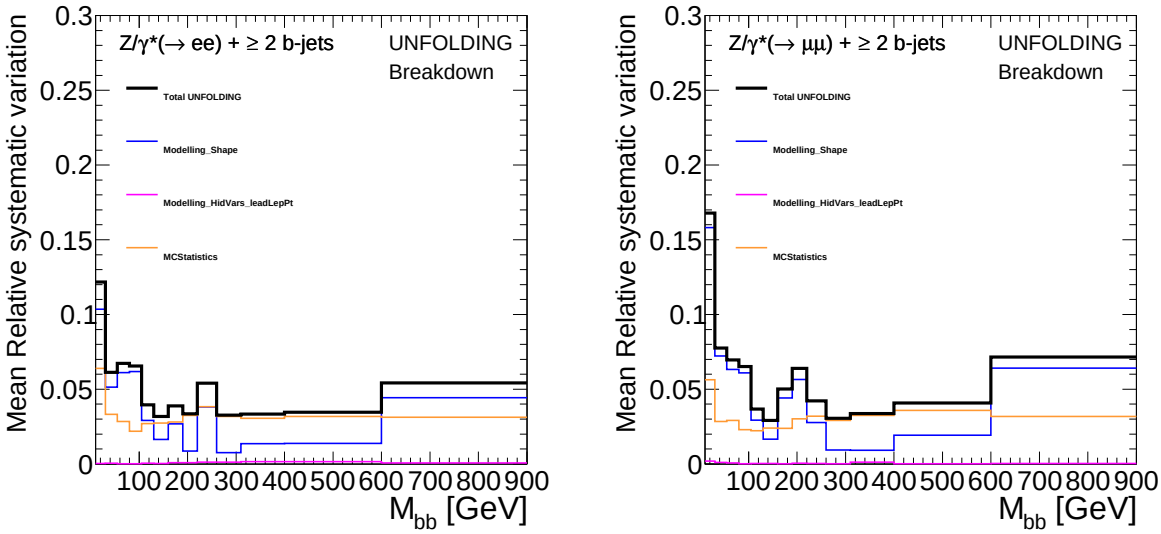

Figure D.48: Breakdown of the three components of the uncertainty on the unfolding method on the invariant mass of the two leading b-jets for the electron channel (left) and muon channel (right) in the Z + 2b-jets signal region.

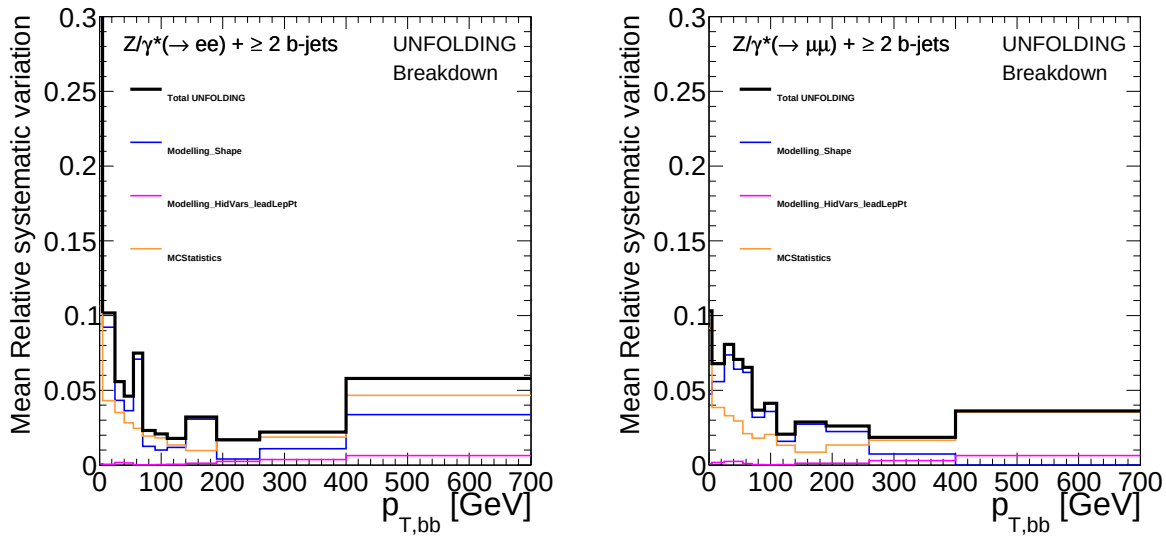

Figure D.49: Breakdown of the three components of the uncertainty on the unfolding method on the p_T of the sum of the two leading b-jets four-vectors for the electron channel (left) and muon channel (right) in the Z + 2b-jets signal region.

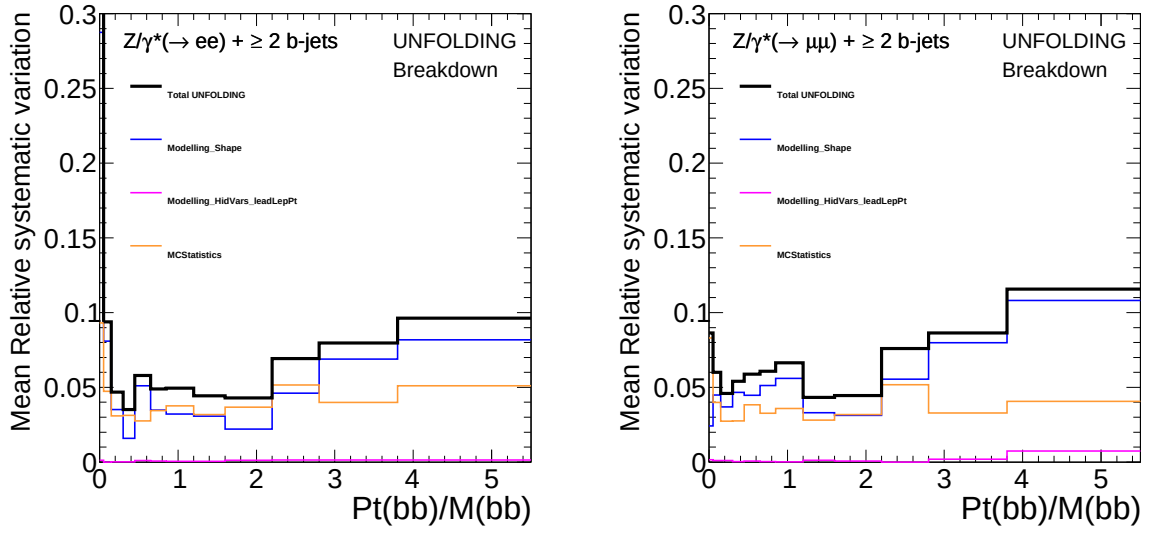

Figure D.50: Breakdown of the three components of the uncertainty on the unfolding method on the p_T of the sum of the two leading b-jets four-vectors divided by the invariant mass of them for the electron channel (left) and muon channel (right) in the Z + 2b-jets signal region.

APPENDIX E

CONTRIBUTIONS

This chapter briefly describes the contributions I made to the analysis presented in this thesis.

Performed in parallel to the Z boson analysis was the measurement of the W boson production in association with b-jets. The two different analyses used the same code except for different event selections. Top background is a much more significant background in the W analysis. The W+jets background flavor components are also much larger relative to the signal flavor component. As a result the signal regions are defined exclusively in the number of b-jets. The signal regions also apply a veto on the number of additional jets present in the event. This is necessary to reduce the amount of top background present.

The two analyses originally started using the 77% working point of the b-tagging algorithm MV2c10. I performed a study of the different working points and their effect on flavor components of the W+jets samples. As a result the working point for both analysis was changed to the 70% working point that is used in this thesis.

I had a large role in the development and running of the unfolding code. This included a bunch of debugging and validating that the systematics were implemented and being treated correctly in the unfolding procedure. I also worked on the top systematics. Producing the varied samples as well as implementing them in both the flavor fit code and the unfolding code. This allowed me to become familiar with and use/edit the main components of this analysis (Event selection that produces the detector level plots, the flavor fit, and the unfolding code).